

UNIVERSITÀ DEGLI STUDI
DI MODENA E REGGIO EMILIA

PhD Programme: Industrial Innovation Engineering

XXXVIII Cycle

Enhancing performance in Ultrafast Laser-based Manufacturing: the role of Adaptive Optics in improving quality and productivity

PhD Candidate: **Vincenzina Siciliani**

Supervisor: **Prof. Dr. Leonardo Orazi**

PhD Course Coordinator: **Prof. Dr. Franco Zambonelli**

Reggio Emilia, March 2026

a.y. 2024/2025

Abstract

Ultrafast laser-based manufacturing has become a pivotal technology across diverse industrial sectors, offering exceptional precision and flexibility in material processing. Despite its growing adoption, the scalability of this technique remains limited by fundamental physical constraints. Simply increasing laser power or pulse intensity does not proportionally enhance ablation rates due to saturation effects and material-specific thresholds, such as the maximum achievable groove aspect ratio. Similarly, raising scanning speeds at constant power reduces the laser-material interaction time, thereby hindering some processes and material transformations.

This thesis explores how integrating adaptive optics into ultrafast laser systems can address these limitations. The focus is on dynamic beam shaping, thus modifying the spatial characteristics of the laser beam to optimize energy distribution on the workpiece surface. This control is crucial, as the beam profile directly influences process efficiency, accuracy, and adaptability.

The research begins by establishing the theoretical and practical foundations of ultrafast laser processing, laser-matter interaction, and adaptive optics as a tool for real-time beam shaping. It then demonstrates how adaptive optics can enable higher processing speeds, decoupling this by the interaction time, thereby improving both throughput and quality.

A custom experimental setup was developed within the BrightLab laboratory at Tecnopolo in Reggio Emilia to support this investigation. This system integrates safety protocols, material compatibility considerations, beam quality monitoring, and an adaptive optics module for beam shaping. The setup enables processing across a wide range of scales, from macro to micro and nano, and materials, including those traditionally considered difficult or impossible to machine. These materials include glass, polymers, carbon fiber composites, zirconia, steel, aluminum, sintered titanium, and copper foils.

The thesis highlights several application areas, such as microfluidic channel fabrication, surface wettability tuning, biocompatibility enhancement, and selective

cleaning. It also establishes the foundational understanding of how adaptive optics can be used to dynamically modify the laser intensity distribution on the workpiece surface.

Experimental results show substantial productivity gains: by using elliptical beams with aspect ratios of 1:4 and 1:20, up to 70% faster processing for parallel and grid groove texturing, and over 93% faster for generating Laser-Induced Periodic Surface Structures (LIPSS) on AISI 420 stainless steel are reported. The adaptive optics system enables beam shape reconfiguration within milliseconds, offering high flexibility for industrial applications like large-area mold texturing. Finally, the thesis presents preliminary numerical simulations that integrate beam shaping, demonstrating their potential to predict and optimize system performance in advance. This approach supports the design of more efficient laser processing strategies, paving the way for scalable, high-throughput ultrafast laser manufacturing.

Sommario

Le lavorazioni con laser a impulsi ultracorti rappresentano oggi una tecnologia fondamentale in numerosi settori industriali, grazie alla loro precisione e versatilità. Tuttavia, gli sforzi per aumentarne la produttività incontrano un limite intrinseco: l'incremento dell'intensità dell'impulso non comporta un aumento proporzionale del tasso di ablazione, a causa di effetti di saturazione e compromessi nella qualità del processo. Ciò è dovuto principalmente ai limiti nella risposta del materiale, ad esempio nel massimo rapporto di forma del solco ablato. Allo stesso modo, l'aumentare della velocità di scansione a fluenza costante riduce il tempo di interazione, inibendo alcuni processi di trasformazione del materiale.

Questa tesi esplora l'integrazione dell'ottica adattiva nei sistemi laser ad impulsi ultracorti come strategia per superare tali limitazioni. L'attenzione è rivolta alla modellazione dinamica del fascio laser, ovvero alla modifica delle caratteristiche spaziali del fascio, al fine di ottenere una distribuzione energetica ottimizzata sulla superficie del pezzo. Questo controllo è cruciale, poiché il profilo del fascio influenza direttamente l'efficienza, l'accuratezza e la versatilità del processo.

La ricerca inizia con la definizione delle basi teoriche e pratiche della lavorazione laser ad impulsi ultracorti, dell'interazione laser-materia e dell'ottica adattiva come strumento per la modellazione dinamica del fascio. Viene poi dimostrato come l'ottica adattiva consenta di aumentare la velocità di lavorazione, disaccoppiandola dal tempo di interazione, migliorando così sia la produttività che la qualità.

Per supportare questa indagine è stato sviluppato ed implementato un sistema sperimentale avanzato efficace sulle diverse classi di materiale all'interno del laboratorio BrightLab, nel Tecnopolo di Reggio Emilia. L'impianto integra dispositivi di sicurezza, di monitoraggio della qualità del fascio e un modulo di ottica adattiva per la modifica della distribuzione del fascio, consente lavorazioni a diverse scale, dal macro al micro fino al nano, e su un'ampia gamma di materiali, inclusi quelli tradizionalmente difficili o impossibili da lavorare con metodi tradizionali. Tra questi: vetro, polimeri, compositi in fibra di carbonio, zirconia,

acciaio, alluminio, titanio sinterizzato e fogli di rame.
La tesi evidenzia diverse applicazioni, tra cui la fabbricazione di canali microfluidici, la modifica della bagnabilità delle superfici, il miglioramento della biocompatibilità e la pulizia selettiva. Vengono inoltre poste le basi teoriche per l'utilizzo dell'ottica adattiva come tecnica per modificare dinamicamente la distribuzione di intensità incidente sul pezzo.
I risultati sperimentali mostrano significativi incrementi di produttività: utilizzando un fascio ellittico con rapporti di forma pari a 1:4 o 1:20 si ottiene un aumento fino al 70% della velocità per la testurizzazione a griglia e parallela, e di oltre il 93% per la generazione di strutture periodiche indotte da laser (LIPSS) su acciaio inox AISI 420. Il sistema di ottica adattiva consente la riconfigurazione del fascio in millisecondi, offrendo un'elevata flessibilità per applicazioni industriali come la testurizzazione di stampi su larga scala.
Infine, la tesi presenta simulazioni numeriche preliminari che integrano la modulazione del fascio, dimostrando il potenziale di queste tecniche per prevedere e ottimizzare le prestazioni del sistema, supportando la progettazione di strategie di lavorazione laser più efficienti e scalabili.

List of Publications

Journal Articles

1. Caruso S., Saffioti M.R., **Siciliani, V.**, Zaniboni G., Umbrello D., Orazi L., Filice L. , *"Influence of Cutting Parameters and Tool Surface Texturing on Surface Integrity in Face Milling of AISI 1050 Carbon Steel."*, J. Manuf. Mater. Process, 2025.
DOI:/10.3390/jmmp9120415

2. **Siciliani V.**, Pelaccia R., Castagnetti D., Raimondi L., Donati L., Orazi L., Alfano M., *"Enhancing the shear strength of adhesive bonded compression-molded CFRP laminates using selective UV picosecond laser treatment"*, The International Journal of Advanced Manufacturing Technology, 2025.
DOI: 10.1007/s00170-025-16985-8

3. **Siciliani V.**, Pelaccia R., Mazzonetto M., Reggiani B., Orazi L., *"Increased productivity in laser texturing of molds through dynamic beam shaping"*, Optics and Laser Technology, 2025.
DOI: 10.1016/j.optlastec.2025.113440

4. Betti A., Ongaro C., Zardin B., Bertacchini J., Tagliaferri N., **Siciliani V.**, Orazi L., Borghi M., *"Evaluating Laser-Based Microfabrication in Microfluidics: An Experimental and Computational Trial"*, Advanced Engineering Materials, 2024.
DOI:10.1002/adem.202401105

5. Orazi L., Pelaccia R., **Siciliani V.**, Oubellaouch K., Mazzonetto M., Reggiani B., *"Ultrafast laser texturing to improve wettability of polyimide (Kapton) films"*, Journal of Manufacturing Processes, 2023.
DOI:10.1016/j.jmapro.2023.10.058

6. Sanguedolce M., Rotella G, Curcio F., Pelaccia R., **Siciliani V.**, Cassano R., Orazi L., Filice L., *"Effects of Ti6Al4V mechanical and thermal surface modification on the adhesion of a chitosan-bioactive glass coating"*, International Journal of Advanced Manufacturing Technology, 2023.
DOI:10.1007/s00170-023-10943-y

International Conferences

1. **Siciliani V.**, Benvenuto M., Mandolfino C., Reggiani B., Orazi L., *"Enabling the reuse of single-lap adhesive-bonded joints through laser cleaning"*, Esaform 2026 Conference. [Abstract accepted]

2. **Siciliani V.**, Pelaccia R., Alfano M. et al., *"Effect of surface preparation on adhesive bonding of CFRP compression molding laminates"*, Materials Research Proceedings, 2025.
DOI: 10.21741/9781644903599-236

3. Zaniboni G., Oubellaouch K., Pelaccia R., **Siciliani V.** et al, *"Optical scanning application for numerical calibration of strain analysis on injection molded rail fastening components"*, Materials Research Proceedings (2025).

DOI: 10.21741/9781644903599-262

4. Mazzonetto M., Saffioti M.R., Sanguedolce M., **Siciliani V.** et al., *"Development of micro-texture patterns of cemented carbide cutting tools to improve cutting performance"*, 13th CIRP Conference on Photonic Technologies LANE 2024, Furth, Germany.
DOI: 10.1016/j.procir.2024.08.184

5. Orazi L., **Siciliani V.**, Pelaccia R. et al., *"Adaptive optics solution to improve laser induced periodic surface structuring (LIPSS)*, Progress in Biomedical Optics and Imaging – Proceedings of SPIE (2024).
DOI:10.1117/12.3002613

6. Mazzonetto M., Pelaccia R., Greborio A., **Siciliani V.** et al., *"Ablation rate assessment of GHz femtosecond laser in burst mode through fast numerical simulation"*, Progress in Biomedical Optics and Imaging – Proceedings of SPIE (2024).
DOI: 10.1117/12.3002715

7. Orazi L., **Siciliani V.**, Pelaccia R. et al., *"Ultrafast laser micromanufacturing of microfluidic devices*, Procedia CIRP (2022).
DOI:10.1016/j.procir.2022.06.023

8. Sanguedolce M., Rotella G., Siciliani V. et al., Surface Characterization of Ultra-Short Laser Textured Titanium For Biomedical Application, Procedia CIRP (2022).
DOI: 10.1016/j.procir.2022.06.024

Contributions to Volumes

1. **Siciliani V.**, Yamini N., Pelaccia R. et al., *"Laser texturing of 3D Copper current collector for ultrafast Zinc metal plating"*, Materials Research Proceedings (2025),
DOI:10.21741/9781644903735-33

2. **Siciliani V.**, Yamini N., Pelaccia R. et al., *"3D copper current collector by laser texturing for quick zinc metal plating"*, Diciassettesima Giornata di Studio Ettore Funaioli, 18 luglio 2025, Reggio Emilia.

3. Zaniboni G., Oubellaouch K., Orazi L., **Siciliani V.** et al., *"Functionalization of polymeric surfaces for antibacterial purpose"*, Sedicesima Giornata di Studio Ettore Funaioli, 19 luglio 2024, Bologna.

4. Mazzonetto M., **Siciliani V.**, Pelaccia R. et al., *"Use of textured cutting tools to improve the machining stability"*, Sedicesima Giornata di Studio Ettore Funaioli, 19 luglio 2024, Bologna.

5. **Siciliani V.**, Zaniboni G., Pelaccia R. et al., *"Adaptive Optics to enhance LIPSS surface texturing"*, 13th International Workshop on Adaptive Optics for Industry and Medicine (AOIM 2024), 12-15 March, Padua.

6. Mazzonetto M., **Siciliani V.**, Orazi L. et al., *"Development of an automatic procedure to texture cutting tools with a complex geometry"*, Quindicesima Giornata di Studio Ettore Funaioli, 14 luglio 2023, Bologna, pag 35-38.

7. **Siciliani V.**, Orazi L., Pelaccia R. et al., *"Adaptive Optics for Laser Beam Shaping"*, Quindicesima Giornata di Studio Ettore Funaioli, 14 luglio 2023, Bologna, pag 31-34.

8. **Siciliani V.**, Betti A., Ongaro C. et al., *"UV picosecond laser processing for microfluidic applications"*, Materials Research Proceedings (2023).

DOI: 10.21741/9781644902714-40

9. Mazzonetto M., **Siciliani V.**, Pelaccia R. et al., *"Surface micro – texturing of tapping tools with complex geometry"*, Materials Research Proceedings (2023).
DOI:10.21741/9781644902714-43

10. Orazi L., **Siciliani V.**, Pelaccia R. et al., *"Ultrafast laser micro-manufacturing of glass based biomedical devices"*, Quattordicesima Giornata di Studio Ettore Funaioli, 15 luglio 2022, Bologna, pag 86-89.

11. Ongaro C, Betti A., **Siciliani V.** et al., *"An Alternative Solution for Microfluidic Chip Fabrication"*, Journal of Physics: Conference Series (2022).
DOI: 10.1088/1742-6596/2385/1/012029

Contents

Introduction **1**

1 Laser Technology Background **5**
1.1 Operating principles 6
1.2 Laser systems 16
1.3 Laser material processing 19
1.4 Ultrashort pulsed lasers 23
1.5 Surface functionalization 26

2 Laser-Matter Interaction **29**
2.1 Basic nature of light 31
2.2 Ray Optics 34
2.3 Wave Optics 38
2.4 Material properties 41
2.5 Non-linear effects 44

3 Laser beam shaping through Adaptive Optics **47**
3.1 Spatial and temporal laser beam shaping 48
3.2 Fundamentals of Adaptive Optics 51
3.3 Adaptive Optics Systems 53
3.4 Laser beam shaping through adaptive optics 59
3.5 Applications in laser processing 62

4 Design and Set-up of the laser processing system **67**
4.1 Laser safety elements 68
4.2 Laser processing cell at BrightLab 72
4.3 Beam Enlarger Analyzer for focused beam 77
4.4 Collimated and expanded beam analysis 80
4.5 Adaptive Optics system: deformable mirror 82
4.6 Hints of system integration 88

5 Case Studies with Results **93**
5.1 Characterization methods 97
5.1.1 Metallographic specimen preparation 97
5.1.2 Morphological characterization 98
5.1.3 Topographical characterization 99
5.1.4 Chemical characterization 102
5.1.5 Wettability and other functional characterization 104
5.2 Laser precise and selective microfabrication 105
5.2.1 Glass microfluidic device 105
5.2.2 Laser microtexturing for tribological applications 117
5.2.3 Micromanufacturing for Optics components 125
5.2.4 Colorization via Oxidation 133
5.2.5 Laser cleaning of metal-bonded joints 137
5.3 Laser-based surface functionalization 144
5.3.1 Tuning polymer and metal wettability 144
5.3.2 Improving titanium biocompatibility 150
5.3.3 Enhancing adhesive bonding strength 156
5.3.4 Enhancing electrochemistry: ion and solid-state batteries . . 161
5.3.5 Enhancing electrochemistry: electrolyzers and fuel cell 166
5.4 Adaptive Optics enhancing laser microprocessing and functionalization 170
5.4.1 Adaptive Optics approach for laser direct processing 170
5.4.2 Adaptive Optics approach for laser induced processing 175
5.4.3 Laser ablation simulation integrating beam shaping 179

6 Discussion **187**

Conclusions **191**

Appendix

A Zernike Polynomials **195**

Bibliography **207**

List of Figures

Figure 1 Laser operating principles [3]. 7
Figure 2 Laser source scheme. 8
Figure 3 Gaussian beam intensity profile, adapted from [3]. 10
Figure 4 Beam diameter evaluated at 13.5% intensity [3]. 11
Figure 5 TEM modes of the laser [3]. 12
Figure 6 Diagram of the parameters of a Gaussian beam [5]. 15
Figure 7 Laser system scheme [3]. 16
Figure 8 Laser applications as function of peak power and average power [4]. 18
Figure 9 Hierarchy of photonics models describing light phenomena [2]. 30
Figure 10 Wave characteristics [20]. 32
Figure 11 Wavefront of a point source [20]. 32
Figure 12 a) Linear polarization, b) circular polarization. 33
Figure 13 Electromagnetic spectrum: laser light can be located in the visible but also in the near infrared and ultraviolet. 34
Figure 14 Sperical versus Aspherical lens, adapted from [21]. 36
Figure 15 Refraction of an incident ray: Snell law. 37
Figure 16 Main laser-matter interaction: incident, reflected and transmitted waves [1]. 39
Figure 17 Young's experiment: interference of a diffracted wave. . . . 41
Figure 18 LIPSS formation as an electromagnetic interference phenomenon [4]. 46
Figure 19 Spatial beam shaping along a two-dimensional section. . . . 49
Figure 20 Temporal beam shaping. 50
Figure 21 Aberration scheme. 52
Figure 22 Adaptive optics system scheme. 54
Figure 23 Zernike Polynomials. 56

Figure 24 Shack-Hartmann Wavefront sensor principle, adapted from [33]. 57
Figure 25 Scheme (a) and real (b) piezoelectric deformable mirror from Dynamic Optics©. 58
Figure 26 Beam shaping through adaptive optics principle. 61
Figure 27 Transformation of a circular beam into an elliptical beam through modal correction. 62
Figure 28 Laser beam shaping applications [32]. 65
Figure 29 Laser risk to the different eye tissues depending on wavelength. 68
Figure 30 Laser risk to the skin as a function of wavelength. 69
Figure 31 3D model of the experimental laser system: on the left side is the working chamber, while the optical bench on the right represents the clean room. 73
Figure 32 a) Actual photograph of the laser processing cell inside the BrightLab laboratory: b) working chamber, c) clean room with visible laser optical path. 74
Figure 33 Laser system 2D scheme. 75
Figure 34 Beam Enlarger System scheme. 78
Figure 35 Reflective ND filters. 79
Figure 36 Gaussian beam profile from camera sensor. 80
Figure 37 IR, GR, UV beam dimensions from camera sensor. 80
Figure 38 Large beam profiler scheme. 81
Figure 39 Expanded beam profile from large beam profiler. 81
Figure 40 Non-expanded beam profile from 7 mm beam profiling camera for comparison. 82
Figure 41 Adaptive Optics system picture. 84
Figure 42 Theoretical wavefront sensor position calculation. 85
Figure 43 Real wavefront sensor position calculation. 86
Figure 44 Deformable mirror calibration: a) actuator modes, b) influence function, and c) different wavefront obtained in closed-loop configuration. 87
Figure 45 Beam shaping using adaptive optics example. 88
Figure 46 Example of integration of rotary-translational motion for machining threaded surfaces [40]. 91

Figure 47 Diagram of the machining operations to be performed at different heights of the tooth [40]. 91

Figure 48 Microfluidic channel on glass example [49]. 107
Figure 49 Micromixer with herringbone design [51]. 108
Figure 50 Micromixer functionality scheme [51]. 108
Figure 51 SEM images of herringbone micromixer device [51]. 109
Figure 52 CNF profiles of herringbone micromixer device [51]. 110
Figure 53 Mixing efficiency of herringbone device versus control device [52]. 111
Figure 54 CFD Simulations of herringbone micromixer, made by the fluid dynamics research group at DIEF, Modena [52]. 112
Figure 55 SEM images of vertical wall obstacles micromixer device. . . 113
Figure 56 CNF 3D topography of vertical wall obstacles micromixer device. 114
Figure 57 Vertical wall micromixer functionality assessed through litmus paper test. 114
Figure 58 Prototyping glass microfluidic devices flowchart. 115
Figure 59 Effective diffusion bonding test between two glass sliders [49].116
Figure 60 SEM images of textured tapping tool [40]. 119
Figure 61 Cutting tool textured morphology and profiles [58]. 121
Figure 62 Comparison of the average cutting forces for NT and textured inserts: FDBD rectangular dimples, WW stripe grooves parallel to the cutting edge, GG orthogonal, GR both, WG and GW are combined textures [58]. 121
Figure 63 Changes in cutting forces during dry cutting: a) NT, b) GG1, c) GR1 [58]. 122
Figure 64 SEM images of textured and coated cutting tool [59]. 123
Figure 65 Variation in cutting forces [59]. 123
Figure 66 Analysis of chip morphology: chip peak and chip pitch [59]. 124
Figure 67 Analysis of chip morphology: spiral pitch [59]. 124
Figure 68 Design of the thermo-optical lens prototype: the black lines are the resistive traces, while the color map represents the simulation of the temperature field by passing current. . . . 126
Figure 69 Spiral ablated track on the ITO. 127

Figure 70 Target (left) versus measured (right) aberration produced by the heated thermo-optics lens. 128
Figure 71 Zone plate design specifications: single zone plate from zone 1 to zone 4 (left), zone plate array covering a diameter of 50 mm (right). 130
Figure 72 Manufactured zone plate characterization: single zone plate measurements (left), zone plate array covering a diameter of 50 mm (right). 131
Figure 73 Zone plate functioning scheme. 131
Figure 74 Multiple focused spots from irradiating the zone plate. . . . 132
Figure 75 Experimental versus expected spot position profile. 133
Figure 76 Color palette on copper and brass. 134
Figure 77 Selective oxidation with different laser parameters. 134
Figure 78 a) Original PWM mode of the EKSPLA 50 laser, b) Analog mode implemented using AOM. 135
Figure 79 Power calibration curve to obtain shades. 136
Figure 80 Scanned bitmap example. 136
Figure 81 Untreated (a,c) versus laser cleaned (b,d) adherend surfaces. 139
Figure 82 Shear strength before and after laser cleaning, using different debonding methods (M1, M2, M3), and with respect to the control (CTRL). 140
Figure 83 Laser cleaning and texturing methodology scheme. 141
Figure 84 LIPSS structures on Aluminum surface. 141
Figure 85 Surface tension evaluation on untreated versus LIPSS textured Aluminum. 142
Figure 86 Shear strength and absorption energy for degreased (SG), abraded (AB), and textured (TXT) Aluminum substrates, before and after debonding. 143
Figure 87 SEM images of LIPSS on Kapton [94]. 145
Figure 88 AFM topography of LIPSS textured Kapton: KG1 sample with a line spacing of 40 μm, at different magnifications to analyze LIPSS [94]. 146

Figure 89 Contact angle measurement for evaluating wettability modification of Kapton: KP1-KP4 represent parallel lines with different energy per pulse, with the optimum in KP2 (0.84 μJ), while KG1-KG2 represent the combined structure of grid and parallel lines where the distance between the lines changes, with the optimum in KG1 (40 μm) [94]. . . . 147
Figure 90 Contact angle measurement of untreated Kapton and Kapton with parallel line texture "KP2" [94]. 147
Figure 91 SEM images of adhesive penetration into the texture on the Kapton surface. 148
Figure 92 SEM images of Titanium texturing for increasing bioactivity. 149
Figure 93 Contact angle measurements of textured Titanium. 150
Figure 94 Deposited droplet on untreated versus textured Titanium. . 150
Figure 95 CNF profilometer of wobble and grid texturing on Titanium [103]. 152
Figure 96 Raman spectrum wobble and grid texturing on Titanium [103]. 152
Figure 97 Profilometry of circular pockets on Titanium to increase bioactivity. 154
Figure 98 SEM images of LIPSS within circular pocket on titanium. . 154
Figure 99 CNF images of osteoblast (marked in red and blue) and endothelial (marked in green) cell culture on textured titanium. 155
Figure 100 SEM images of osteoblast (ovoid-shaped) and endothelial (elongated shape) cells deposited on textured titanium. . . . 156
Figure 101 Stereoscope images of laser cleaning and matrix ablation treatment on CFRP [110]. 158
Figure 102 EDS mapping of untreated, manual abrasion, laser cleaning, and matrix ablation treatment on CFRP: Silicon is in pink colour, while Carbon is in black [111]. 159
Figure 103 SEM images of LIPSS induced on the fiber of the CFRP composite [110]. 160
Figure 104 Shear strength of untreated versus cleaning and matrix ablation treatment on CFRP [110]. 160

Figure 105 Fracture surfaces of untreated versus cleaning and matrix ablation treatment on CFRP [110]. 160
Figure 106 Groove texturing on 100 μm copper surface. 162
Figure 107 Zinc deposition scheme [115]. 163
Figure 108 Mass percentage of Oxygen, Copper and Zinc of untreated and laser treated copper. 163
Figure 109 EDS mapping on untreated and laser-treated 100 μm copper [115]. 164
Figure 110 Profile and SEM images of 10 μm textured copper. 165
Figure 111 EDS mapping within glovebox to analyze Lithium deposition on untreated and textured Copper. 165
Figure 112 AFLMB battery performance of as-is and Lt laser textured copper. 166
Figure 113 SEM images of LIPSS textured sintered titanium. 168
Figure 114 Raman spectrum of "nt" untreated and I/II harmonic textured sintered titanium. 169
Figure 115 EDS elemental profile along the cross section: in pink is Carbon, in Red is Oxygen. 169
Figure 116 ECSA measurement of "O" untreated, and I/II harmonic treated sintered titanium: sample A and sample B are the two repetitions. 170
Figure 117 Circular versus 1:4 aspect ratio elliptical beam, adapted from [119]. 172
Figure 118 Measured intensity profile for the 42 μm-axis elliptical beam [119]. 172
Figure 119 Laser processing scheme to obtain parallel lines or grids using a circular or elliptical beam (scan step) [119]. 173
Figure 120 SEM images of the imprint left by circular (a) and elliptical beams (b) at different magnifications, adapted from [119]. . 174
Figure 121 SEM images of the grooves obtained by circular (a) and elliptical (b) beams [119]. 174
Figure 122 SEM images of grooves obtained at high power with circular beam [119]. 175
Figure 123 LIPSS texturing using circular or elliptical beam scheme, adapted from [120]. 176

Figure 124 Circular versus 1:20 elliptical beam, adapted from [119]. . . 177
Figure 125 SEM images of LIPSS texturing using circular or elliptical beam [119]. 178
Figure 126 DLOA distribution of LIPSS obtained by circular (SSC, NITIC) or elliptical beam (SSE, NITIE) on stainless steel (SS) or Nitinol alloy (NITI) [120]. 178
Figure 127 Mean and standard deviation of LIPSS orientations for circular (SSC, NITIC) or elliptical beam (SSE, NITIE) on stainless steel (SS) or Nitinol alloy (NITI) [120]. 179
Figure 128 3D and 2D representation of a laser pass for the circular beam (in red) and for the elliptical beam (light blue); xy plane is where laser simulation is done, yz plane is the other view. 181
Figure 129 Simulated intensity profile in COMSOL environment [119]. . 182
Figure 130 Heat Exchange Scheme and Mesh Refinement (top right) [119]. 184
Figure 131 Depth of the simulated groove using circular (left) and elliptical (right) beam. Lattice temperature scale at right [119]. 185
Figure 132 Plot of electron temperature (blue) and lattice temperature (green) over time, for circular (left) and elliptical (right) laser beam passage in COM SOL: ablation temperature in red [119]. 185
Figure 133 Example of groove section made with elliptical beam parallel scanning strategy [119]. 186

List of Tables

Table 1 Laser Safety Classes and Associated Risks. 70
Table 2 Laser system elements. 76

Table 3 Case studies matrix: non metallic materials. 94
Table 4 Case studies matrix: metallic materials. 96
Table 5 Laser parameter for herringbone micromixer. 109
Table 6 Laser parameters for tapping tool texturing. 119
Table 7 Laser parameters for texturing cutting tool. 120
Table 8 Laser parameters for milling cutting tool texturing. 123
Table 9 Laser parameters for ITO cutting and selective ablation. . . 127
Table 10 Laser parameters for zone plate selective ablation. 129
Table 11 Laser parameters for laser coloring. 135
Table 12 Laser parameters for laser cleaning. 138
Table 13 Laser parameters for texturing Aluminum substrates. 141
Table 14 Laser parameters for Kapton texturing. 145
Table 15 Laser parameters for Titanium texturing. 148
Table 16 Laser parameters for texturing titanium. 153
Table 17 Laser parameters for CFRP composite texturing. 158
Table 18 Laser parameters for 100 μm Copper texturing. 162
Table 19 Laser parameters for 10 μm copper texturing. 164
Table 20 Laser parameters for sintered Titanium texturing. 167
Table 21 Laser parameters for direct texturing using elliptical beam. . 173
Table 22 Laser parameters for LIPSS texturing using circular or elliptical beam. 177
Table 23 Material parameters for ablation simulation. 183
Table 24 Mean value and depth variance comparison between simulation and experiment case. 186

Introduction

Ultrafast laser-based manufacturing has emerged as one of the most advanced technologies for precision material processing. By delivering energy in femtosecond or picosecond pulses, these systems enable "cold ablation," where material removal occurs faster than thermal diffusion, minimizing heat-affected zones and preserving the integrity of the substrate. This capability has opened new opportunities in diverse fields, including microfluidics, biomedical implants, tribological surface engineering, and photonic device fabrication. The ability to process metals, polymers, ceramics, and even transparent dielectrics with high accuracy and minimal collateral damage makes ultrashort pulsed lasers indispensable for next-generation manufacturing. The maximum potential of lasers is found in the macro to nano measurement range.

Despite these advantages, the scalability of ultrafast laser processing remains a major challenge. Industrial applications demand high throughput and cost-effectiveness, yet current systems struggle to meet these requirements. Increasing pulse energy or average power does not proportionally enhance ablation rates due to saturation phenomena and material-specific constraints, such as the maximum achievable groove aspect ratio in a single-step process. Similarly, raising scanning speeds at constant fluence reduces interaction time, leading to insufficient energy accumulation and compromised surface morphology. These limitations are widely recognized in the state of the art, which emphasizes that productivity gains cannot rely solely on power scaling but require innovative strategies to optimize energy delivery and interaction dynamics.

Several approaches have been proposed to address these challenges. Burst-mode operation, beam splitting, and parallel processing have shown promise in improving throughput, but they increase complexity and cost, often requiring additional optical components or multiple sources. Beam shaping has emerged as a particularly promising solution. By modifying the spatial intensity distribution of the laser beam, beam shaping enables more uniform or application-specific energy de-

position, improving process efficiency in cutting, welding, and microstructuring. Techniques such as diffractive optics, spatial light modulators, and holographic methods have been employed to generate flat-top, Bessel, or multi-spot beams. However, many of these methods are static and cannot adapt to changing process conditions or complex geometries in real time, while the more flexible solutions are constrained by limited power.

Adaptive optics (AO) offers a transformative advantage in this context. Originally developed for astronomical imaging and high-power laser systems, AO enables dynamic wavefront modulation through deformable mirrors or liquid crystal devices, correcting aberrations and obtaining high-resolution images. In ultrafast laser manufacturing, AO provides the capability to reshape the beam in milliseconds, synchronizing its geometry with scanning trajectories or material features. By elongating the beam along the scanning direction, AO can increase the effective interaction length without reducing fluence, thereby boosting processing speed while preserving texture fidelity. Furthermore, AO facilitates advanced functionalities such as multi-focal structuring and aberration compensation during deep material processing, expanding the scope of ultrafast laser applications to complex three-dimensional surfaces.

The motivation for this thesis is to bridge the gap between the unique characteristics of ultrafast lasers and the productivity demands of industrial-scale manufacturing. By integrating adaptive optics into a custom-designed laser processing system, this work aims to demonstrate that real-time beam shaping can overcome fundamental limitations in throughput and quality. The research not only addresses practical challenges in mold texturing, surface functionalization, and microfabrication but also contributes to the theoretical understanding of light–matter interaction under dynamically modulated beam conditions. In doing so, it aligns with the current trajectory of the state of the art, which increasingly emphasizes hybrid solutions combining optical innovation, process modeling, and intelligent control to achieve scalable, high-performance manufacturing.

The methodology adopted in this research combines theoretical analysis, experimental validation, and computational modeling. The first step involves establishing the theoretical foundations of ultrafast laser–matter interaction and adaptive optics principles. This is followed by the design and implementation of a custom

experimental system within the BrightLab laboratory at the Tecnopolo in Reggio Emilia. The system integrates a picosecond pulsed laser source with multiple harmonics, galvanometric scanning heads, and an adaptive optics module equipped with deformable mirrors and real-time wavefront sensing. Advanced diagnostic tools, including beam profiling cameras and an in-house beam enlarger analyzer, ensure accurate characterization of focal intensity distributions.

Experimental tests were conducted on a wide range of materials, metals, polymers, glass, and ceramics, covering applications such as microfluidic channel fabrication, surface functionalization for wettability tuning and biocompatibility, and tribological enhancement through mold texturing. Complementary numerical simulations based on the Two-Temperature Model (TTM) were implemented in COMSOL Multiphysics® to predict ablation dynamics under varying beam profiles, providing a robust framework for process optimization. The scope of this research extends beyond incremental improvements. By demonstrating that adaptive optics can increase processing speed by up to 93% for LIPSS formation and 70% for groove texturing while maintaining or improving surface quality, this work establishes adaptive optics as a transformative approach for next-generation ultrafast laser manufacturing. It also enables flexible, real-time beam shaping for diverse industrial applications. These findings bridge the gap between laboratory-scale accuracy and industrial-scale productivity, paving the way for flexible, high-throughput solutions in advanced engineering and emerging technologies.

The thesis is structured to guide the reader from fundamental principles to advanced industrial applications, ensuring logical progression from theory to practice. The first chapter establishes the foundations of laser technology, covering operating principles, system architectures, and historical developments that shaped modern ultrafast laser systems.

The second chapter delves into laser–matter interaction mechanisms, emphasizing nonlinear phenomena such as multiphoton absorption and plasma formation, which dominate ultrafast regimes and enable precision processing with minimal thermal effects.

The third chapter introduces the fundamentals of adaptive optics, explaining wavefront control strategies, deformable mirror technology, and their role in dy-

namic beam shaping for real-time process optimization.
The fourth chapter details the design, integration, and calibration of the experimental AO-enabled laser processing cell developed at BrightLab, including safety considerations, diagnostic tools, and system automation for high reproducibility.
The fifth presents a comprehensive set of case studies demonstrating the benefits of AO-enhanced processing across diverse applications, such as microfluidics, tribology, biomedical implants, optical components, and electrochemical systems, supported by quantitative performance metrics and predictive simulations based on the Two-Temperature Model.
A dedicated section follows with an in-depth discussion of the results, where experimental findings are critically analyzed in relation to theoretical expectations. This discussion addresses productivity gains, quality improvements, and economic implications, highlighting how adaptive optics justifies its cost even when paired with expensive ultrafast sources. It also compares some case studies to identify common trends, limitations, and scalability potential, providing a holistic interpretation of the research outcomes.
Finally, the conclusions chapter synthesizes the findings and outlines future research directions, including industrial scalability and integration with machine learning for real-time process optimization.
By combining theoretical rigor, experimental innovation, and computational modeling, and a critical discussion of results, this thesis positions adaptive optics as a transformative enabler for ultrafast laser manufacturing, delivering precision, flexibility, and productivity to meet the evolving demands of Industry 4.0 and Industry 5.0 sustainable production paradigms.

1. Laser Technology Background

Lasers represent one of the most versatile and transformative technologies in modern science and industry. It is based on a fascinating interplay of quantum physics and engineering, originating in 1916 with an insight from Albert Einstein, who proposed its theoretical foundations by explaining the main physical principles involved [1].

The first demonstration was done in 1960 with the creation of a ruby laser prototype by Theodore Maiman at Hughes Research Laboratories in Malibu, California. This breakthrough extended coherent radiation into the optical spectrum, at a frequency five orders of magnitude higher than previous microwave sources (MASER) [2]. The 1960s and 1970s witnessed the rapid development of various laser types, including helium-neon, diode, CO_2, and Nd: YAG. Particularly, the development of the CO_2 laser by Kumar Patel at $AT\&T$ Bell Laboratories in 1963, which was significantly more cost-effective and efficient for high power, paved the way for the adoption of laser technology across various sectors and industries [3].

In the years following 1960, the invention of tunable dye lasers and nonlinear optics expanded the laser's versatility. Physicists demonstrated the generation of ultrashort pulses using organic dye lasers, despite their low efficiency and operability. These pioneering devices established theoretical groundwork for the first Ti-Sapphire mode-locked laser, which operated in the femtosecond regime by 1990, followed by the introduction of the first regenerative chirped-pulse amplifiers. In the early 2000s, fiber chirped-pulse amplifiers set new standards for compactness and operability, significantly increasing peak power from kilowatts to megawatts and gigawatts, thereby expanding possibilities in laser material processing [2, 4].

Thanks to its unique properties, since its invention, laser evolved from a novel curiosity into an indispensable tool across a vast spectrum of applications: from precise measurement and alignment to high-speed communication, advanced medical

procedures, industrial material processing, and everyday life [1, 2].
Lasers offer remarkable flexibility in both spatial and temporal domains, operating across dimensions from micrometers to centimeters and, with remote delivery systems, extending to meters. Their ability to emit either continuous or pulsed beams with adjustable power modulation allows for tailored interactions with materials, ranging from gentle heating to intense ablation. These interactions can be thermal, causing heating, melting, or evaporation, or non-thermal, enabling cold ablation and precise chemical bond disruption. The versatility of lasers is further enhanced by their ability to operate across a wide range of wavelengths, from infrared to ultraviolet. This spectral flexibility allows the selection of specific laser sources based on the absorption properties of the target material, enabling precise and efficient processing of diverse substances such as metals, ceramics, polymers, semiconductors, and composites.
Laser systems are not only powerful and precise but also highly integrable into automated and digital manufacturing environments. Their compact size, remote controllability, and compatibility with CNC systems, robotics, and CAD/CAM workflows make them ideal for modern production lines. This ease of integration, combined with their non-contact nature, positions lasers as one of the most adaptable and future-proof tools in industrial and scientific applications. Though a solid understanding of the physical principles and technologies that form the basis of laser science makes the more established and possible future applications possible.

1.1 Operating principles

Laser technology is based on the physical principle that gives it its name. The acronym LASER stands for “Light Amplification by Stimulated Emission of Radiation”, referring to the amplification of light through the stimulated emission of photons. The phenomenon can be understood in relation to the other two physical principles: spontaneous emission and absorption.
Absorption occurs when a photon is absorbed by an atom of matter, transferring its energy to the atom. Spontaneous emission occurs when an atom in an excited state, at an energy level E1 higher than the initial level E0, moves back to the

initial energy level E0, emitting a photon of energy. If an atom in the excited state is struck by an incident photon, stimulated emission occurs, resulting in the emission of a photon that share the same frequency, direction, and phase as the incident photon, see Figure 1.

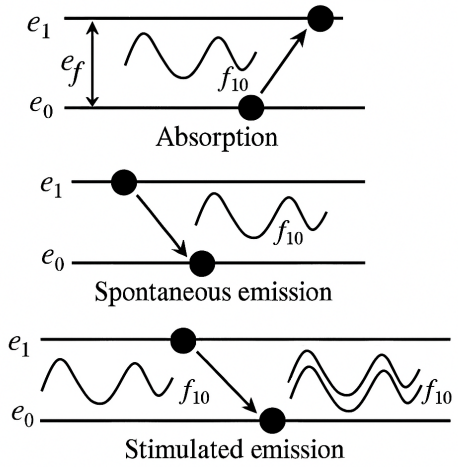

Figure 1: Laser operating principles [3].

If a material medium is subjected to energy pumping, stimulated emission can occur. Many materials exhibit the phenomenon of stimulated emission; however, only a select few possess significant power capabilities. A crucial requirement for this is the existence of the population inversion, where there are more atoms or molecules in the excited state than in the lower-energy state, enabling amplification rather than absorption. To achieve this condition, the lifetime of the excited species must be longer than that of the lower-energy state.
A resonant cavity can then amplify this phenomenon, generating a beam of sufficient intensity that can interact with the material, see Figure 2.

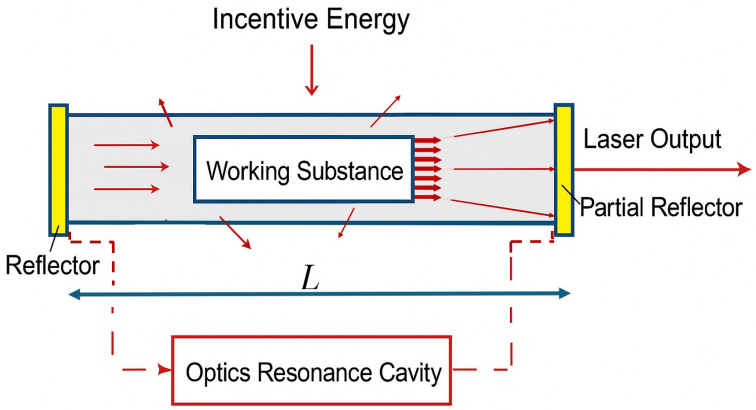

Figure 2: Laser source scheme.[1]

So, ultimately, the laser source must contain three essential components: an active medium, a pumping source, and an optical resonator. The active medium, which can be a solid, liquid, gas, or plasma, is the substance that emits light. The pumping source provides energy to excite the atoms or molecules within the active medium, elevating them to higher energy states. The optical resonator, typically composed of two mirrors facing each other, reflects light back and forth through the medium, reinforcing the stimulated emission process and creating the beam [1].

The gain of a laser, namely the measure of how much light is amplified, is determined by the population inversion and the properties of the active medium. When the gain exceeds the losses in the optical cavity, the system reaches the threshold for laser oscillation, producing a sustained and directed beam of light. Laser construction varies depending on the intended application and power requirements. Designs range from stable cavities for low-power lasers to unstable cavities for high-power systems. Cooling mechanisms are integral to laser design, as they prevent overheating and maintain performance. These include conduction cooling in rod-shaped lasers, convective cooling in gas flow systems, and area cooling in disc and waveguide lasers [1].

There are several types of laser sources, each with unique characteristics. Gas lasers, such as CO_2 and excimer lasers, are widely used in industrial and medical

[1] https://it.loshield.com/news/what-is-the-principle-and-working-of-lasers-67362795.html

applications. Solid-state lasers, including Nd:YAG and Yb:YAG, offer high peak powers and are often diode-pumped for improved efficiency. Fiber lasers, which guide light through doped optical fibers, provide excellent beam quality and compact design. Dye lasers are notable for their tunability across a wide range of wavelengths, while free-electron lasers generate light through synchrotron radiation rather than atomic transitions.

In all cases, the laser beam obtained consists of electromagnetic waves with a single frequency and a single phase, making it both temporally and spatially coherent, characterized by limited divergence. Temporal coherence is associated with the property of monochromaticity, while spatial coherence enables the production of unidirectional and collimated beams that remain almost parallel over long distances. Laser beams can be focused onto very small areas, on the order of micrometers; however, the diameter of the spot depends on various parameters such as wavelength and the numerical aperture of the optical system.

These characteristics distinguish laser emission from incoherent light and form the basis of the primary applications of lasers: the high irradiance is utilized in manufacturing processes such as cutting, engraving, and welding of metals; monochromaticity and coherence are employed in metrology, optical communications, and information transport.

The beam generated by the source has a specific brightness or power P measured in Watts. The energy Q transported by the beam over time t is:

$$Q = P \cdot t \tag{1.1}$$

And it is generally measured in Joules [J].

The fluence F of the beam is defined as the ratio:

$$F = \frac{Q}{S} \tag{1.2}$$

where S is the cross-sectional area of the beam in cm^2.

The irradiance I or power density is given by:

$$I = \frac{P}{S} \tag{1.3}$$

which represents the average value across the entire section of the laser beam, as it varies in the cross-section.
In particular, the most common spatial distribution profile for laser sources is axially symmetric Gaussian:

$$I(r, \theta) = I(r) = I_0 e^{-(\frac{r}{r_0})^2} \tag{1.4}$$

where I_0 is the power density on the beam axis and r_0 is a distribution parameter related to the beam radius, see Figure 3.

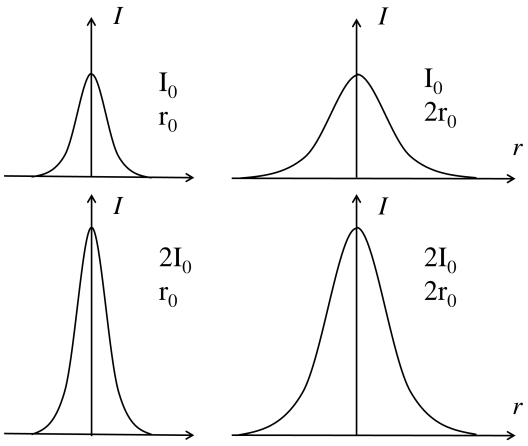

Figure 3: Gaussian beam intensity profile, adapted from [3].

Since the intensity of the beam varies continuously between its maximum value at the center and a zero value away from it, it is necessary to define a conventional diameter. According to UNI EN ISO 11146, the beam radius is calculated at a

power density equal to 13.5% of the maximum, see Figure 4. Therefore:

$$r_0 = \frac{d}{2\sqrt{2}} \tag{1.5}$$

and

$$I(d/2) = I_0 e^{-2} = 0.135 I_0 \tag{1.6}$$

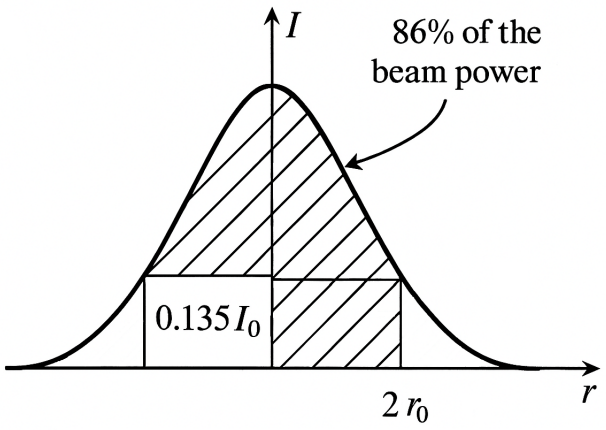

Figure 4: Beam diameter evaluated at 13.5% intensity [3].

The percentage of power contained in the beam is 86%. Alternatively, the radius can be defined at 36.8% in the same way. This power distribution allows for extremely high peak intensity values and can also be focused on very small sections, further increasing it.

The transversal distribution of power density *I(x,y)* is in a close relationship with the geometry of the resonant cavity. One way to characterize the spatial profile of the beam power intensity is through the Transverse Electromagnetic Mode *($TEM_{m,n}$)*, where m and n represent the number of power intensity minima on the section normal to the beam axis in the two orthogonal x and y directions. The Gaussian corresponds to $TEM_{0,0}$. A beam can also have multiple overlapping TEM modes (multimode laser), see Figure 5.

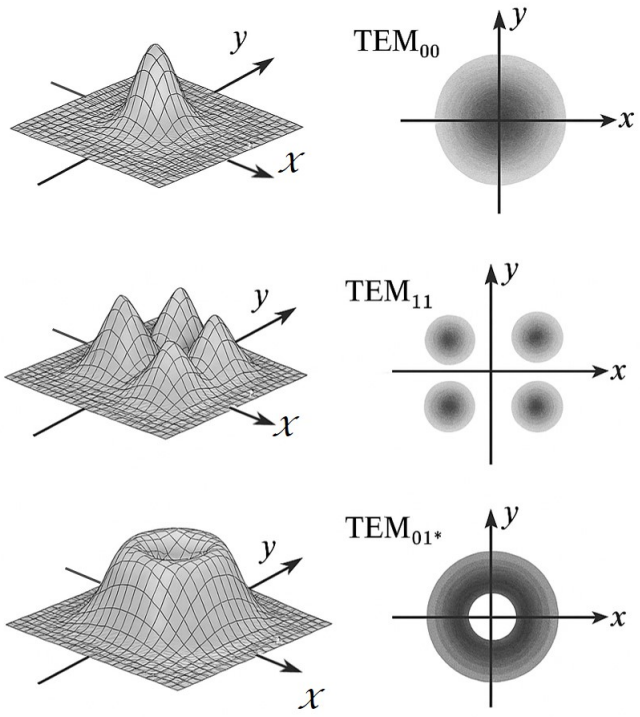

Figure 5: TEM modes of the laser [3].

In addition to the spatial profile, the temporal profile of the beam can also be defined, given that the sources can be continuous (CW) or pulsed (PW). The continuous mode emits power at a constant rate over time, while the pulsed mode emits power intermittently over time, resulting in very high peak power levels. Pulsed lasers are also characterized by pulse duration (τ), pulse repetition frequency ($f = 1/T$), and instantaneous power. The average power of the pulses in this case is:

$$P_{av} = f\tau P_k \tag{1.7}$$

where P_k is the average power of the single pulse. The pulsed regime can be obtained by pulsed excitation of the active medium (free running), in q-switch or mode-locking.

Electromagnetic waves consist of two fields: one electric and the other magnetic. Stimulated emission produces waves whose electric vectors are all aligned, meaning that the beam is polarized. The photons resulting from stimulated emission have the same polarization direction and propagate in the same direction as the wave that induced the atom to undergo this type of transition.
The polarization of the beam concerns the way in which electric and magnetic vectors propagate in space. If the two vectors lie in two planes parallel to the direction of propagation of the wave, the wave is said to have linear polarization. If, on the other hand, the two vectors rotate around the axis during propagation in the z direction (thus describing a spiral), the polarization is circular. Finally, if each ray constituting the beam has randomly oriented vectors, the polarization is random. [3]
The geometry that a laser beam assumes in the direction of propagation is convergent-divergent and has a point of minimum beam diameter (d_0). This point is called the beam focus, while the area straddling it is called the beam neck. In an area far from the neck, the beam has a conical geometry with straight generatrices and a vertex angle of 0.
For this type of beam, the following relationship applies:

$$\theta\, d_0 = k\, \lambda \tag{1.8}$$

where k is a positive constant. The product $\theta\, d_0$ is a characteristic parameter of the beam and, once the wavelength is fixed, remains constant if the beam interacts with perfect optical systems without restrictive elements (apertures). Even when generated, the beam assumes the geometry described, and therefore at the source output, the beam diverges at an angle θ, known as the angle of divergence. The value of this angle is linked to the construction factors of the source and is generally very small, of the order of milliradians. The divergence of the beam in an area far from the source is therefore equal to:

$$\theta = k\frac{\lambda}{d_0} \tag{1.9}$$

where d_0 is the minimum diameter of the beam and generally falls at a point inside the source. The value of the constant k depends exclusively on the power density distribution of the beam, i.e. on its spatial profile. For a Gaussian beam, we have:

$$k_g = \frac{4}{\pi} = 1.27 \tag{1.10}$$

and, due to diffraction, this is the smallest possible value for k. A beam for which the relationship holds is said to be diffraction-limited. The smallest value that can be observed for the divergence of a laser beam out of the source is obviously given by:

$$\theta_g = \frac{4\lambda}{\pi d_0} \tag{1.11}$$

In all other cases, $\theta > \theta_g$. The propagation factor of the beam K is then defined as the ratio:

$$K = \frac{\theta_g}{\theta} = \frac{k_g}{k} = \frac{4}{\pi k} \tag{1.12}$$

determined at the same d_0. Obviously, $0 < K \leq 1$, and the closer the value of K is to unity, the closer the irradiance distribution is to the Gaussian distribution. The beam propagation factor radically influences the characteristics of the beam in the focusing zone. In some cases, instead of the beam propagation factor, it is preferable to use the beam quality factor M^2 defined as:

$$M^2 = \frac{1}{K} \tag{1.13}$$

and in this case, $M^2 \geq 1$. The value of M^2, as will be described later, directly

influences the ability to focus the beam and, therefore, profoundly influences the machining result. [3]

The shape and intensity of the focal point of the laser beam after it has been focused by an optical system are described by caustics. The caustic equation for a Gaussian laser beam in Equation 1.14 describes the radius of curvature of the wavefront and the beam size as a function of distance, using parameters such as the waist radius (w_0) and wavelength (λ), often expressed in terms of the Rayleigh parameter ($z_R = \pi w_0^2/\lambda$), which defines the radius of curvature of the wavefront and the size of the linearly expanding beam, showing how the caustic (the envelope of the rays) forms at the focal point, where the beam is narrowest, and then diverges, with its maximum size (waist) and angular divergence depending on the beam quality (M^2).

$$d^2(z) = d_{0,focal}^2 + (z - z_0)^2\theta^2 \tag{1.14}$$

The schematic diagram of the parameters of a Gaussian beam is shown in Figure 6. A Gaussian beam has its highest intensity at the focus, where the waist radius is smallest, and as the defocus distance grows, the beam radius expands according to the Gaussian propagation formula, causing the energy to spread over a larger area. This means that by adjusting the defocus distance rather than the laser power, you can precisely control the energy density delivered to the material. In this way, defocusing acts as a robust and simple control mechanism for laser-material interaction.

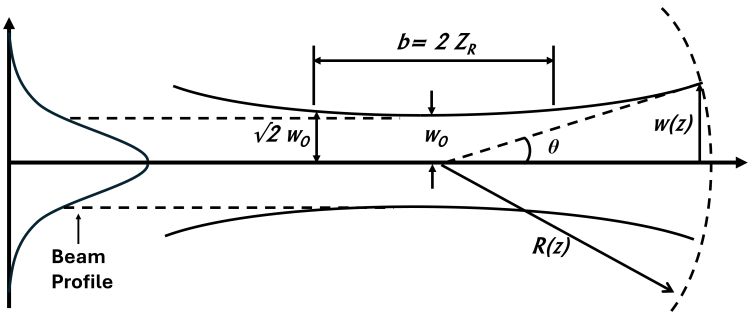

Figure 6: Diagram of the parameters of a Gaussian beam [5].

1.2 Laser systems

Laser source is not sufficient to obtain a tool for performing machine operations. A laser system is composed of several key components that work together to generate, model, and direct laser light where processing takes place, as in Figure 7.

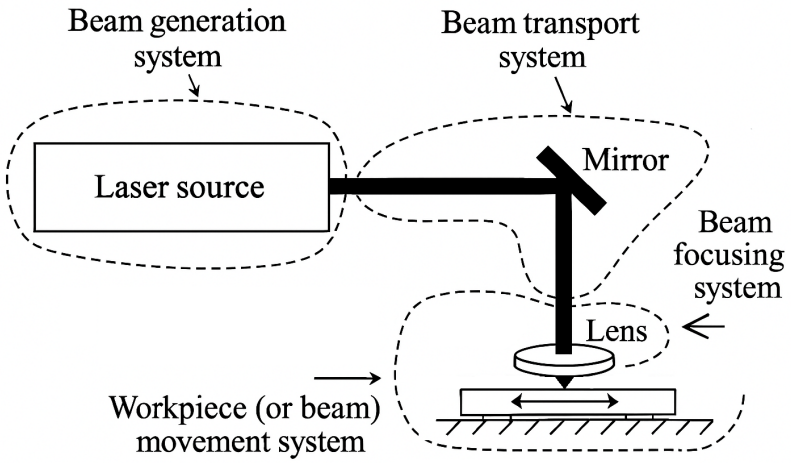

Figure 7: Laser system scheme [3].

At its core is the laser source, which includes the gain medium, the pump source (electrical or optical), and the resonator cavity with mirrors to amplify light through stimulated emission. A partially reflective mirror allows the emission and utilization of the generated beam.

Various laser sources are used in industrial and scientific applications, categorized primarily into gas lasers, solid-state lasers, excimer lasers, semiconductor lasers, dye lasers, and free-electron lasers.

Gas lasers include CO_2 lasers, which are widely used for cutting and welding due to their high power and efficiency. They operate at 10.6 μm and rely on vibrational transitions in CO_2 molecules, often enhanced by nitrogen excitation. Variants include slow flow, axial flow, and transverse flow designs, each with different cooling and discharge mechanisms. CO lasers, emitting at 5.4 μm, offer higher quantum efficiency but require cryogenic cooling, limiting their practicality. Excimer lasers, based on excited dimers of noble gas halides (e.g., KrF,

ArF), emit in the ultraviolet range and are used for high-precision applications like micromachining and lithography. They produce short, powerful pulses but have high maintenance costs due to gas degradation and optical component wear.
Solid-state lasers use doped crystals or glasses as the gain medium. The most common is Nd:YAG, emitting at 1.06 μm, suitable for both CW and pulsed operation. It can be pumped by flash lamps or diode lasers, with diode pumping offering higher efficiency and longer lifetimes. Variants include Nd:glass (better energy conversion but poor cooling), Yb:YAG (used in disc and fiber lasers for high power and beam quality), and Er:YAG (eye-safe applications). Fiber lasers, especially those doped with ytterbium, are compact, efficient, and capable of high beam quality, making them ideal for cutting and welding. Their design includes waveguiding and integrated Bragg reflectors for minimal alignment issues.
Semiconductor lasers, or diode lasers, are compact and highly efficient, converting electrical energy directly into light. They are used both as pump sources and for direct applications like welding and marking. Their structure involves p–n junctions with double heterostructures to reduce current density and improve performance. Emission wavelengths vary based on material composition, with GaAs and InGaAs being common.
Dye lasers are highly tunable and can operate from CW to femtosecond pulses. They use organic dyes excited by another laser source and emit over a broad spectrum, selectable via cavity tuning. Despite their versatility, they are inefficient and costly to maintain.
Finally, free-electron lasers generate radiation via synchrotron emission from relativistic electrons passing through magnetic wigglers. They cover a wide spectral range from infrared to X-rays and are used in advanced research applications. [1]
They are each tailored for specific applications. Gas and solid-state sources account for almost all industrial sources installed (Figure 8).

Once the laser beam is generated, it is directed using a beam transport system, which can include mirrors, beam expanders, optical fibers, and collimators to guide and shape the beam precisely.
Fiber optics enables flexible beam delivery. Step-index and graded-index fibers

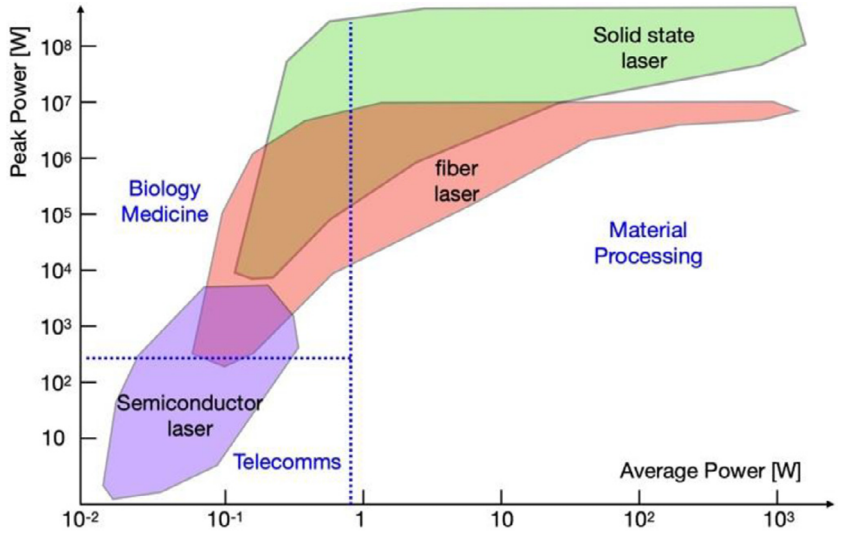

Figure 8: Laser applications as function of peak power and average power [4].

guide light via total internal reflection. Coupling efficiency depends on matching the beam's diameter and divergence to the fiber's numerical aperture. Scanning systems, using oscillating mirrors or rotating polygons, direct beams across surfaces for marking or engraving. Advanced systems use computer control for precise pattern generation.[1]

For applications requiring dynamic beam positioning, scanning heads are used, these can be galvanometric scanners (fast-moving mirrors for 2D/3D scanning), polygonal scanners (rotating mirrors for high-speed line scanning), or acousto-optic deflectors (using sound waves to steer the beam). Each scanning head type offers different advantages in terms of speed, precision, and field of view.

The laser beam comes out of the source almost collimated, with a certain amount of divergence. A focusing system is placed downstream of the chain and is fundamental in determining the precision, efficiency, and overall effectiveness of the beam-material interaction. Among the various optical components used for beam focusing, the f-theta lens stands out as a particularly advantageous solution in applications involving laser scanning. Unlike conventional lenses that produce a curved focal plane, an f-theta lens is specifically designed to maintain a focal point of constant size and shape across the entire scanning field, thanks to a linear relationship between the scanning angle (theta) and the position of the point, which is described by $x = f \cdot theta$, where f is the focal length. This

means that as the beam is deflected across the lens, typically by galvanometric mirrors, the focal point moves across the working plane, ensuring uniform spot size and consistent energy delivery. It is compatible with various wavelengths and beam diameters, and ideal for high-speed and high-precision operations.
In addition to the core components of a laser system, various auxiliary systems can be integrated to tailor the laser setup for specific industrial or scientific processes. For example, a gas supply system may be added to deliver inert assist gases like nitrogen or argon, which enhance cutting efficiency, reduce oxidation, and control the chemical environment during laser-material interaction. Similarly, a controlled atmosphere chamber with precise regulation of temperature, pressure, and gas composition is crucial for processes like laser welding of reactive metals or precision micromachining. These additions help optimize beam-material interaction, improve quality and repeatability, and enable processing of sensitive materials.
A workpiece manipulation system is responsible for precisely positioning and moving the material being processed. It can include motorized stages, robotic arms, conveyor systems, or CNC platforms, depending on the complexity and scale of the operation. These systems often operate in multiple axes (e.g., X, Y, Z, and rotational axes) and are controlled via software to synchronize with the laser's scanning or pulsing behavior. In high-precision tasks like micro- and nano-stereolitography, the workpiece manipulation system can ensure sub-micron accuracy and repeatability. When integrated with sensors and feedback loops, it can also adapt in real time to variations in material or process conditions, enhancing quality and efficiency.
Together, these components form a highly adaptable system capable of meeting diverse application requirements.

1.3 Laser material processing

Lasers are advantageous and versatile due to their ability to emit a concentrated, powerful beam of light that can be used to treat a wide range of materials and tissues in a precise and selective manner. This technology allows interaction with specific targets without physical contact, eliminating tool wear and reduc-

ing processing times, while adjusting the beam parameters, making it adaptable to different applications. In mechanical processing, the laser beam is utilized as an energy source, primarily of heat. The material irradiated by the beam undergoes rapid heating, which may result in it remaining solid, melting, or even vaporizing almost instantaneously.

The primary industrial processes achievable with lasers are diverse, including cutting, welding, heat treatment (e.g., tempering), marking, micro-drilling, and cladding. Each application necessitates a beam with specific characteristics, thus precluding the existence of a universal source applicable to all. Moreover, a comprehensive understanding of the characteristics of the various beams produced by different sources, as well as the processing techniques, is essential for effective technological application.

The evolution of laser systems and sources has been pivotal in shaping modern manufacturing and scientific applications. Industrial laser systems have grown into a multi-billion-dollar market [6], driven by their versatility in cutting, welding, marking, and micro-processing. This growth reflects a technological shift from traditional CO_2 lasers to high-power solid-state sources such as fiber and disk lasers, which offer superior energy efficiency and process stability. Concurrently, ultrashort pulse lasers, picosecond and femtosecond, are gaining prominence in precision applications, enabling material removal with minimal thermal impact and supporting advanced processes like glass cutting and microstructuring for electronics and photovoltaics.

Among the processes that have become established over time, laser cutting is noted for its excellent quality and process characteristics, and can be easily automated. The advantages of laser cutting include the ability to work with both metallic and non-metallic materials (ductile or brittle) and complex shapes; high speeds and flexibility; significant reductions in the heat-affected zone (HAZ) and noise; minimal or no tool wear; and the absence of the need for component clamping. The cut edge exhibits high quality, appearing smooth, clean, squared, and devoid of burrs. The laser can perform cuts in multiple directions depending on beam polarization, enabling blind cuts with very narrow openings, and can process, with some limitations, multiple overlapping parts. Cutting depth largely depends on laser power, with higher powers, combined with advanced machines,

allowing for the cutting of thick sheets.
Similarly, the drilling process benefits from laser technology, enabling high-speed perforation with reduced and controlled burrs. It can drill at nearly any angle and process all materials that absorb the specific wavelength, regardless of hardness. The shape and size of the hole vary depending on the laser employed. However, current limitations exist in drilling coated materials, where the properties of the coating significantly influence the final outcome.
At the micro scale, laser drilling offers significant advantages, for example, ultrafast laser drilling of alumina ceramic substrates is emerging as the most viable solution in microelectromechanical systems (MEMS), particularly when achieving high aspect ratios (depth-to-diameter) [7].
Laser welding is characterized by high energy density, melting the material to produce a good weld bead profile, often described as "keyhole", narrow and deep. This process is easily automated and is marked by speed, high accuracy, and reduced chemical contamination. It can be performed at ambient temperature, does not require filler material, reduces the heat-affected zone, and minimizes material evaporation, which is particularly advantageous for materials like magnesium. The depth of the weld depends on laser power. Notably, it allows for various applications, including the welding of dissimilar materials, such as lithium-ion battery connectors, and the welding of electrical windings in electric motors. However, near-IR lasers are less effective for welding reflective materials, for these applications green and blue lasers are currently employed.
Laser heat treatment processes enable low chemical contamination, control of the heat-affected zone, and thus low distortions, as well as precise thermal profile control and localization of treatment, reducing the need for post-treatment. These processes can be conducted remotely without contact and are easily automated, finding extensive applications in surface hardening or melting to homogenize materials.
Recently, laser forming, as an advanced non-contact manufacturing technique that utilizes laser energy to induce controlled thermal expansion and plastic deformation in metal sheets, has proven to be a highly promising alternative to conventional forming techniques, especially in shaping high-strength and brittle materials with minimal residual stresses, enhanced accuracy, and reduced tool

wear [8].

More generally, laser surface treatments involve generating surface structures, texturing, marking, and various micromachining processes. Recent applications include surface treatment on molds and dies to expedite component transfer in large-scale applications or directly on the component of interest. The small beam diameter facilitates high-precision micromachining without the need for molds or dies, eliminating force transfer to the workpiece and providing advantages such as reduced tool wear. However, this process is slower in material removal. Notable micro-scale applications include polymer cutting for stents, channel creation for microfluidics, and processing solar panels.

Ultrafast pulse lasers exhibit unique absorption modes and laser-material interactions that provide advantages in micromachining. The interaction between the laser beam and the material is the foundation of processing techniques and significantly influences the quality of the resulting work. The flexibility to control energy density allows for the creation of structured surfaces and bulk processing of various materials, even at the mesoscale. The principal advantage of femtosecond lasers is their ability to remove material with minimal thermal transport surrounding the work area.

Another significant application of lasers is in Laser Additive Manufacturing (LAM), in which a laser is used to selectively melt or sinter powdered material, typically metals or polymers, layer by layer to build up a three-dimensional object directly from a digital design. The laser's focused energy allows for localized melting, rapid solidification, and high-resolution control over the geometry and microstructure of the part being produced. LAM is particularly valuable for creating complex, customized components that would be difficult or impossible to manufacture using traditional subtractive methods. It enables lightweight designs, internal channels, and intricate lattice structures, which are especially beneficial in aerospace, automotive, and biomedical industries. The process also minimizes material waste and allows for rapid prototyping and on-demand production.

The energy of the laser beam can also be used to initiate or influence chemical reactions, depending on the wavelength, pulse duration, and intensity of the laser, as well as the nature of the target material. In laser-induced breakdown spec-

troscopy (LIBS), a focused laser pulse creates a plasma that reveals the chemical composition of a material, while in laser-induced mass spectroscopy (LIMS), it analyzes vaporized material. Lasers can also trigger photochemical reactions, such as breaking molecular bonds or activating photosensitive compounds, as seen in photodynamic therapy for cancer treatment. Additionally, techniques like Raman spectroscopy and fluorescence detection use laser light to identify chemical substances based on their unique spectral signatures.

1.4 Ultrashort pulsed lasers

As mentioned above, a laser source can generate pulsed light by emitting energy in short bursts rather than continuously. This is mainly achieved through techniques like Q-switching, which stores energy in the laser medium and releases it suddenly to produce high-intensity pulses, or mode-locking, which synchronizes multiple light waves (modes) within the laser cavity to interfere constructively at regular intervals, creating extremely short pulses. Ultrashort pulses, lasting picoseconds ($10^{-12}s$) to femtoseconds ($10^{-15}s$), are typically produced by passive mode-locking using a saturable absorber, a material whose absorption decreases with increasing light intensity. This favors the formation of short, intense pulses while suppressing continuous or long-pulse emissions.
Kerr-lens mode-locking is a nonlinear optical technique used in solid-state lasers like Ti: sapphire systems. It exploits the intensity-dependent refractive index of the gain medium to favor the formation of short pulses. The Kerr effect causes self-focusing of intense light, which helps to stabilize the pulse formation within the cavity.
Ultrashort pulses seeded by a mode-locking oscillator can then be amplified by means of Chirped Pulse Amplification (CPA), which was developed to overcome the limitations of amplifying ultrashort pulses directly. In CPA, a short pulse is first stretched in time to reduce its peak power, then amplified, and finally recompressed to its original duration. This technique allows for the generation of high-energy femtosecond pulses without damaging the amplification medium. CPA is foundational in many high-power ultrafast laser systems.
So, the terms "ultrafast" or "ultrashort" laser refer to lasers that operate with

pulse durations typically ranging from tens of femtoseconds to hundreds of picoseconds. Commonly, these are referred to as "femtosecond lasers" or "picosecond lasers". In the context of laser manufacturing, the definition of ultrashort pulses is based on the interaction phenomena between electromagnetic fields and the material being processed. Electromagnetic waves interact with the electronic system, which then transfers energy to the material lattice. An appropriate definition of an ultrashort pulse is one with a duration shorter than the coupling time between the electrons and the material lattice. This duration can vary significantly depending on the material's electronic structure, but usually falls within the range of a few to tens of picoseconds due to the strong nonlinear phenomena that occur at high pulse intensities.

Ultrafast laser processing of materials possesses distinct characteristics compared to processing with longer pulses, due to the ultrashort timescale of excitation. This enables the separation of the physical processes involved in the excitation of the electronic system, energy transfer to the lattice (including heating and melting), and material removal followed by solidification. Consequently, ultrafast lasers not only facilitate material processing but also provide insights into the underlying physics, thereby enhancing the understanding of light-matter interactions, which vary depending on the type of material (e.g., metals or dielectrics) [4].

Immediately after its discovery, researchers showcased the use of femtosecond lasers for material processing, enabling the ablation of polymeric materials with exceptionally clean edges and minimal HAZ [1, 4, 9]. Subsequently, the capability to operate within the volume of non-conductive optically transparent materials was demonstrated by altering the refractive index to create waveguides in glass and generating micro voids through nonlinear phenomena at high photon densities [2, 9, 10].

Modern ultrafast pulse lasers, which are also characterized by ease of use, robustness, and reliability, offer significant advantages and find applications in high-precision and fast temporal resolution processes. The unique attributes of ultrashort lasers were further employed in micro-stereolithography, utilizing near-infrared (IR) sources for two-photon polymerization of photo-curable resins. Additionally, the generation of quasi-periodic 3D structures, known as Laser In-

duced Periodic Structures (LIPSS), attracted significant research interest. LIPSS are formed when the laser's electric field interacts with surface electrons, generating periodic fluctuations in electron density that guide the propagation and scattering of the beam, resulting in highly regular surface patterns. Firstly observed on dielectric materials using various laser sources, the application of ultrashort pulses opened a wider range of possibilities concerning materials and applications. [4]

Among the various applications of ultrashort lasers are cutting, drilling, marking, additive manufacturing, and micro-milling in bulk processes. For example, it leads to significantly higher quality and precision in thin-film battery production or photovoltaic cells.

Ultrafast lasers are not only tools for high-precision manufacturing but also platforms for exploring and manipulating matter at its most fundamental levels. One of the most compelling aspects of ultrafast laser processing is its ability to induce structural transformations at the atomic level. For example, femtosecond laser irradiation can reshape metallic nanoparticles, alter their crystallinity, and even induce phase transitions in two-dimensional materials like MoS_2 [9, 11, 12, 13]. These transformations are driven by localized electric field enhancements and rapid electron dynamics, which can be simulated using finite-difference time-domain (FDTD) methods and two-temperature models. Such reshaping and ablation techniques are crucial for tailoring the optical, electronic, and catalytic properties of nanomaterials.

Ultrafast laser shock peening (LSP) is another advanced application, where high-pressure plasma plumes generated by femtosecond pulses induce compressive residual stresses and grain refinement. When combined with magnetic fields, LSP can significantly enhance the oxidation resistance and mechanical integrity of alloys used in aerospace and energy systems.

Moreover, ultrafast lasers are instrumental in the fabrication of micro-optical devices, including waveguides, microlens arrays, and metasurfaces. Techniques like two-photon polymerization allow for 3D printing of complex structures with sub-diffraction resolution. These devices are used in photonic circuits, lab-on-chip systems, and quantum technologies. [9]

Ultrafast lasers in reshaping, ablating, and interconnecting nanomaterials, as well

as fabricating advanced devices like photodetectors, metasurfaces, and supercapacitors, demonstrate the technology's potential across nanotechnology, photonics, and energy systems[9].
Then, it can be used in spectroscopy, microscopy, and tomography, and refractive surgery. It can also be used in nonlinear optics.

1.5 Surface functionalization

The vast and growing range of applications for ultrafast laser technology has led to a dynamic and evolving research landscape, particularly in the areas of surface texturing and functionalization. These processes are increasingly recognized for their ability to tailor material surfaces with high precision, enabling new functionalities and enhancing performance.
Surface texturing refers to the deliberate creation of micro- or nanostructures on a material's surface to alter its physical characteristics. The texture is a given surface finishing that repeats periodically. Using ultrafast lasers, this process exploits nonlinear absorption mechanisms such as multiphoton ionization and avalanche ionization to achieve sub-wavelength resolution with minimal thermal damage. The result is a highly localized modification of the surface, enabling the fabrication of intricate geometries that can span from nanometers to millimeters. These textures can be designed to mimic natural surfaces, such as lotus leaves or insect wings, resulting in biomimetic properties like superhydrophobicity, anti-reflectivity, or low friction. LIPSS, for example, are a well-known outcome of ultrafast laser texturing, where interference between incident laser light and surface plasmons leads to regular, tunable patterns. Such textures are widely applied in fields ranging from tribology and optics to biomedical engineering, where they can influence wettability, adhesion, and biocompatibility; therefore, the functionality of the surface [9, 11, 14, 15, 16, 17].
Surface functionalization involves modifying not only the physical properties of a surface, but also its chemical, electronic, or biological properties in order to improve its performance or introduce new functionalities. Ultrafast lasers enable this by inducing localized changes such as oxidation, doping, or the formation of surface defects, without affecting the bulk of the material. This precision

allows for selective activation of surface regions, which is particularly valuable in applications requiring spatial control, such as biosensing or catalysis. For instance, ultrafast laser processing has been used to induce strong metal-support interactions in catalytic systems like Pt/CeO_2, enhancing their activity and stability by modifying the interface at the nanoscale. In biomedical contexts, laser-functionalized surfaces can promote cell adhesion or inhibit bacterial growth, while in industrial applications, they can improve paint bonding, reduce wear, or create anti-corrosive coatings. [1]

For example, ultrafast laser irradiation of metallic surfaces like copper can induce complex microstructural transformations, including the formation of dislocation layers and phase transitions from FCC to BCC or HCP structures. These changes are driven by rapid electron excitation and subsequent lattice thermalization, which occur within tens of picoseconds. The resulting dislocation layers enhance mechanical properties such as hardness and wear resistance [9].

Ultrafast laser micromachining enables the fabrication of surface textures that influence wettability and optical properties. Hierarchical micro/nano structures can be engineered to produce superhydrophobic surfaces, anti-reflective coatings, or surfaces with controlled friction. These textures are often inspired by natural surfaces, such as lotus leaves or beetle wings, and are created through direct laser writing or the formation of LIPSS [12]. The integration of ultrafast laser texturing with functionalization strategies has also led to the development of advanced devices. Ultrafast lasers have been used to fabricate supercapacitors, photodetectors, and metasurfaces. These processes rely on precise control of surface geometry and chemistry, enabling the design of multifunctional surfaces with tailored electronic, optical, and catalytic properties [9]. The ability to control both the physical structure and chemical composition of surfaces at micro- and nanoscales continues to drive innovation.

2. Laser-Matter Interaction

A solid foundation in optics is essential for understanding laser processing because it provides a theoretical framework for how laser light behaves and interacts with materials. Key optical principles such as wave propagation, reflection, refraction, interference, and diffraction are fundamental for predicting and controlling the behavior of laser beams. These concepts help explain how light can be focused, directed, or manipulated to achieve specific effects on a material's surface or within its volume.

In addition to these basic optics principles, a deeper understanding of wavefront concept, coherence, and beam characteristics, such as intensity distribution, divergence, and polarization, is crucial for designing optical systems that can precisely shape and deliver laser energy. These parameters directly influence the efficiency, resolution, and repeatability of the process.

This knowledge becomes particularly important when working with ultrafast lasers, where the interaction between the electromagnetic field and the material occurs on extremely short timescales. Here, a strong background in optics ensures high-performance outcomes in both industrial and scientific applications.

The understanding of light has evolved through various theoretical models, each developed to explain increasingly complex optical phenomena. Isaac Newton proposed the corpuscular theory, suggesting that light consists of particles (corpuscles) that travel in straight lines. This model readily explained reflection but failed to account for refraction and diffraction. In contrast, Huygens introduced the wave theory, according to which light is a longitudinal wave whose wavefront results from the superposition of secondary wavelets. Huygens' theory explains reflection, refraction, diffraction, and interference, but it does not account for polarization or the photoelectric effect.

Young's double-slit experiment and Foucault's speed-of-light measurement eventually supported Huygens, leading to the wave theory's dominance. During the same historical period, Pierre de Fermat introduced Fermat's Principle, stating

that light follows the path of least time, at the basis of ray optics. Fermat's principle can be seen as a special case (minimization of time) of the wave phenomena described by Huygens.

Modern optics recognizes light as an electromagnetic wave, governed by the same principles as other forms of electromagnetic radiation, like radio waves and X-rays. This model, known as electromagnetic optics, describes light as two coupled vector fields, electric and magnetic. However, many optical phenomena can be approximated using scalar wave optics, which simplifies light to a single wavefunction.

When light interacts with objects much larger than its wavelength, its wave nature becomes less apparent, and ray or geometrical optics provides a sufficient approximation. Mathematically, ray optics is the limiting case of wave optics as the wavelength approaches zero.

Thus, the hierarchy of models is in Figure 9. Each model is valid within its domain and derives from the more general one above it. While electromagnetic optics offers the most complete classical description, some phenomena require quantum optics, or quantum electrodynamics, to be fully explained. Historically developed from ray to quantum, each was introduced to explain experimental results that previous models could not account for. The best model for a given situation is the simplest one that accurately describes the phenomenon, though determining the appropriate model often relies on experience [18, 19].

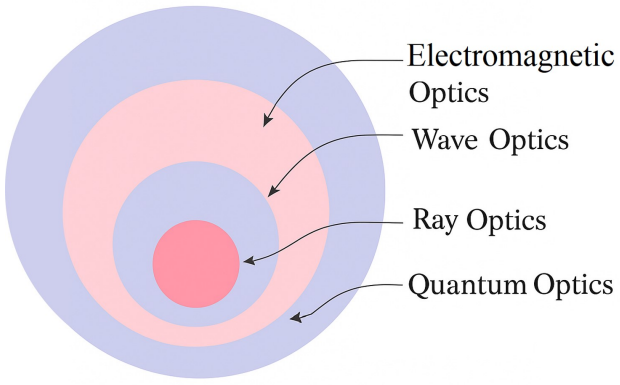

Figure 9: Hierarchy of photonics models describing light phenomena [2].

In laser processing, all models are important. Ray optics helps in designing the beam delivery system, such as focusing, collimating, and steering the laser

beam, while wave optics is crucial for understanding how the laser interacts with materials at micro- and nano- scales, particularly in ultrafast laser applications where interference and nonlinear effects dominate.

2.1 Basic nature of light

The fundamental nature of light as electromagnetic radiation is rooted in its dual behavior, exhibiting both wave-like and particle-like properties. As a wave, light propagates through space via oscillating electric and magnetic fields, which are perpendicular to each other and to the direction of propagation, forming a transverse wave, as described by Maxwell's equations. [1, 19]
The differential wave equation is a foundational tool in describing the propagation of laser light, which behaves as an electromagnetic wave. In its general form, the wave equation is expressed in Equation 2.1:

$$\frac{\partial^2 \psi}{\partial x^2} = \frac{1}{\nu^2} \frac{\partial^2 \psi}{\partial t^2} \tag{2.1}$$

where $\psi(x,t)$ represents the wave function, x is the direction of wave propagation, ν is the wave propagation speed, and t is the time. Solutions to this equation describe harmonic waves, which are sinusoidal as in Equation 2.2:

$$\psi(x,t) = A \sin k(x \mp \nu t) \tag{2.2}$$

Where k is the wave number, and A is the amplitude. They are characterized by some main parameters: wavelength (λ), from $k = 2\pi/\lambda$; period (τ), $\tau = \lambda/\nu$; frequency (f), $f = 1/\tau$; and phase (ϕ), $\phi = kx \mp \omega t$, where $\omega = 2\pi/\tau$ is the angular frequency [20]. In practice, the wavelength defines the spatial repetition of the wave, the period describes the temporal cycle, and the phase determines the wave's position in space and time, see Figure 10.

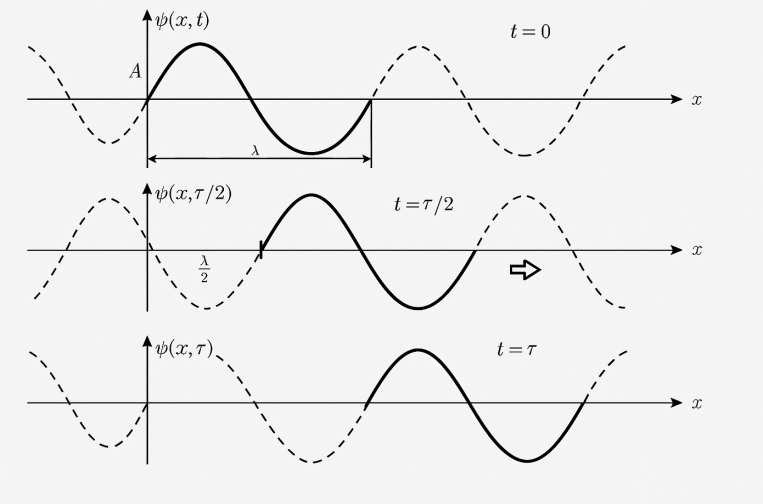

Figure 10: Wave characteristics [20].

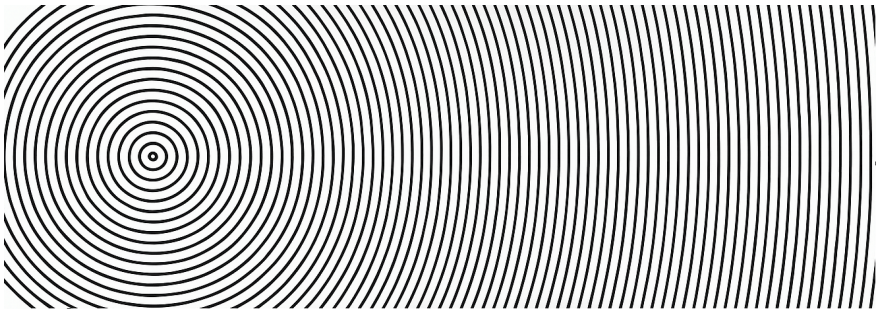

Figure 11: Wavefront of a point source [20].

A crucial concept in understanding laser light is the wavefront, which refers to the surface of constant phase across the propagating wave. In a plane wave, the wavefronts are flat and parallel, while in a spherical wave, they are concentric spheres. Laser beams typically exhibit curved wavefronts near the source and planar wavefronts in the far field, see Figure 11. The coherence and monochromaticity of laser light ensure that its wavefronts are well-defined and stable, which is essential for applications requiring precise focusing, interference, or beam shaping. The ability to manipulate wavefronts is central to controlling laser beam propagation and optimizing its interaction with matter.

The wave nature explains phenomena such as interference, diffraction, and polarization.

Polarization plays an important role in the reflection and diffusion of light. If the electric vector is constantly aligned in one direction, the beam is linearly

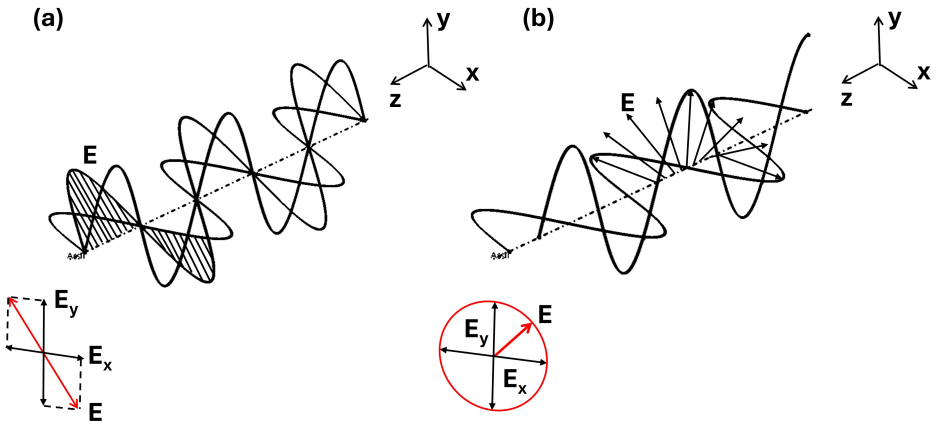

Figure 12: a) Linear polarization, b) circular polarization.

polarized, see Figure 12-a). If it has two perpendicular vector directions of equal intensity, it is circularly polarized (right or left), see Figure 12-b); if one vector is stronger than the other, it is "elliptically polarized".

It is interesting that birefringent crystals have fast and slow refractive indices for different states of polarization, or how some molecules, particularly quartz and sugars, can rotate the plane of polarization of transmitted beams. This becomes a degree of freedom with which to manage light.

As a particle, light consists of photons, discrete packets of energy, whose behavior is governed by quantum mechanics. The energy of a photon is proportional to its frequency, as described by Planck's equation, Equation 2.3:

$$E = h\nu \tag{2.3}$$

where h is Planck's constant and ν is the frequency. Based on the active material medium, this simple equation can be used to obtain the wavelength of the laser light that can be achieved.

This particle aspect is crucial in explaining effects like the photoelectric effect, where photons eject electrons from a material.

The duality of light becomes especially significant at different wavelengths, see Figure 13: longer wavelengths (e.g., radio waves) exhibit more wave-like behav-

ior, while shorter wavelengths (e.g., X-rays) reveal particle-like characteristics [1]. The behavior of laser light lies in between, since the possible wavelengths for industrial applications range between 10.6 μm (CO_2 laser) and roughly 200 nm (Excimer laser).

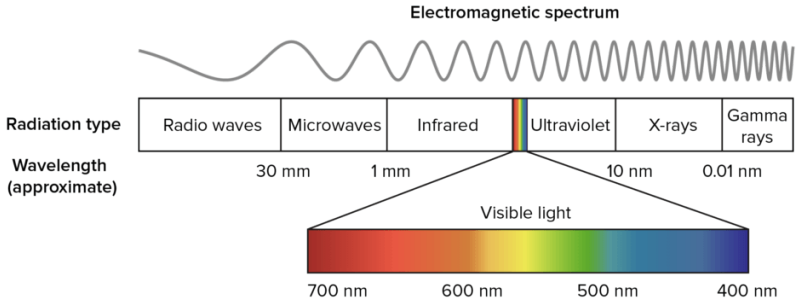

Figure 13: Electromagnetic spectrum: laser light can be located in the visible but also in the near infrared and ultraviolet.[2]

When a beam of electromagnetic radiation, such as laser light, encounters a material, it can be reflected, absorbed, or transmitted depending on the material's properties and the radiation's wavelength. At the microscopic level, the electric field component of the radiation interacts primarily with electrons in the material.

If the frequency of the radiation matches the natural resonance of the electrons, energy is absorbed, leading to excitation.

Laser light is unique due to its coherence and directionality. Coherence enables interference-based applications. The mode structure defines power distribution across the beam. Polarization affects reflection and absorption, especially for anisotropic materials or not hortogonal incident beam.

2.2 Ray Optics

Ray optics primarily concerns itself with the propagation of light as straight lines or rays. It is based on the approximation that light travels in straight paths and

[2] https://medium.com/@torthix7/all-about-light-e75684c48cd6

changes direction only when it encounters a boundary between different media. This model is particularly useful for analyzing systems involving lenses, mirrors, prisms, and optical fibers.
The action of focusing concentrates laser energy into a small spot, increasing the energy intensity. The focused spot size depends on the beam quality and lens parameters. Even with perfect lenses, it is not possible to focus light into an infinitely small point, but a spot with a certain finite size will always be obtained: there is a diffraction-limited spot size.
The beam quality factor M^2 quantifies deviation from an ideal Gaussian beam. A lower M^2 indicates better focusability. Depth of focus is the range over which the beam remains tightly focused. Spherical lenses can only approximately focus all rays to the same point. In this case, Spherical Aberration occurs.
The laser beam can be guided and modified by different optical components.

- Lenses focus or collimate the rays of the beam; they can be single, double, and aspherical lenses (Figure 14). Doublets and aspheric lenses reduce spherical aberration.
- Mirrors reflect beams; metallic mirrors (e.g., gold-coated copper) are preferred for high-power lasers (due to their high reflectivity and thermal conductivity).
- Beam expanders increase the beam diameter to reduce the intensity of the beam and increase the numerical aperture of the following optical components; they can be Galilean or Keplerian.
- Depolarizers convert linearly polarized light to circular or radial polarization.
- Diffractive optical elements, due to their microstructured surfaces, shape beams into complex patterns. Applications include beam splitting into multiple beams, uniform heating, and pattern projection [1].

Ray optics explains phenomena such as reflection, refraction, and image formation using simple geometric constructions and Snell's law, which will be explained below. It models the phenomena when the dimensions of the optical elements are

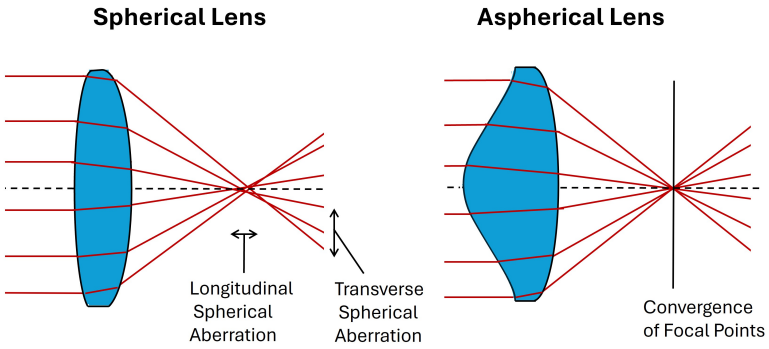

Figure 14: Sperical versus Aspherical lens, adapted from [21].

much larger than the wavelength of light, and it does not account for wave-based effects like interference or diffraction.

Reflection occurs when light encounters a surface and bounces back into the original medium. The law of reflection states that the angle of incidence equals the angle of reflection, and both rays lie in the same plane defined by the incident ray and the surface normal. This principle is derived from Hero's principle, which asserts that light follows the path of least distance in a homogeneous medium. Mirrors, whether planar, spherical, or paraboloidal, utilize this principle to redirect light. Paraboloidal mirrors focus parallel rays to a single point, making them ideal for collimating light from sources like LEDs. Spherical mirrors, while easier to fabricate, approximate paraboloidal behavior only for paraxial rays, those close to the optical axis, allowing for simplified image formation under the paraxial approximation.

Refraction, on the other hand, occurs when light passes from one medium into another with a different refractive index. The change in speed causes the light to bend, a phenomenon described by Snell's law, in Equation 2.4. This bending depends on the relative indices of the two media and the angle of incidence. When light travels from a medium of higher refractive index to one of lower index, i.e., from air (θ_1) to glass (θ_2), the angle relative to the normal of the incident wave (n_1) is greater than the angle relative to the normal of the refracted wave (n_2), and light has a lower phase velocity in the second medium (ν_2) respect to the first one (ν_1), see 15.

If the angle of incidence exceeds a critical value, total internal reflection occurs. This principle is fundamental in optical fibers and prisms, where light is effi-

ciently guided or redirected without loss.

$$\frac{sin\theta_2}{sin\theta_1} = \frac{\nu_2}{\nu_1} = \frac{n_1}{n_2} \tag{2.4}$$

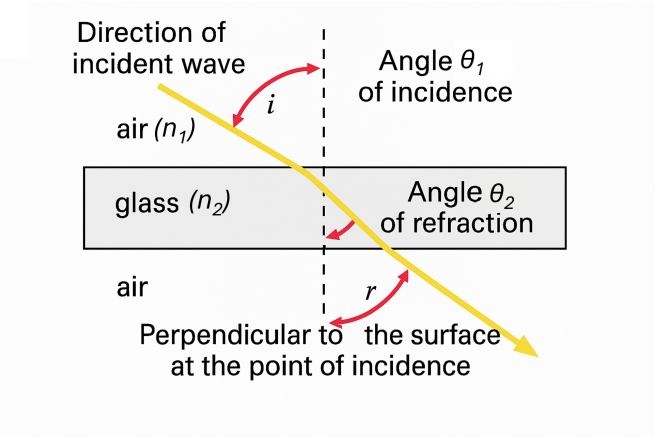

Figure 15: Refraction of an incident ray: Snell law.[3]

Image formation is the process by which a three-dimensional scene is projected onto a two-dimensional plane, such as a screen or digital sensor, using optical elements like lenses or mirrors to manipulate light rays. It arises from the controlled redirection of light rays by optical components. In ray optics, an image is formed when rays from each point of an object converge to a corresponding point. Spherical mirrors and lenses can form images by reflecting or refracting paraxial rays. The imaging equations derived from these systems relate object and image distances to the focal length of the component. For instance, a spherical mirror with radius R has a focal length $f = R/2$, and the imaging condition is given by $1/z_1 + 1/z_2 = 1/f$, where z_1 and z_2 are the object and image distances. Similarly, thin lenses follow analogous rules, with their focal length determined by the curvature of their surfaces and the refractive index of the material.
A conjugate plane in optics refers to a location where an image of an object is formed by a lens or mirror system. The principles of image formation and conjugate planes are fundamental to understanding key components of laser-based

[3] https://www.chimica-online.it/fisica/legge-di-snell.htm

systems, such as beam expanders and Shack-Hartmann sensors of adaptive optics systems [22, 23].

2.3 Wave Optics

As light radiation propagates in a solid material, the electromagnetic field generates a force on charged particles, inducing oscillatory motion that is transferred from electrons to atoms. The mode of energy transfer from electrons to atoms depends on the type of irradiated material. Since the temperature increase in a solid is related to the amplitude of atomic vibrations, the ultimate effect of laser radiation is temperature elevation. Consequently, energy absorption occurs, and at the same time reflection phenomena occur at the interface, which, in the case of rough real surfaces, may be both specular and diffuse, see Figure 16. Although reflectivity influences energy efficiency, its impact becomes considerably less significant at elevated temperatures and further diminishes once the material reaches the liquid phase. In non-melting operations, alternative methods can be employed to enhance the absorption coefficient. The interaction time between the material and the laser light, as well as the magnitude of thermal flux, characterize the various processing techniques.

The absorbed energy can manifest as heat, cause molecular vibrations, or even lead to ionization if the intensity is high enough. In metals, free electrons oscillate in response to the electric field, leading to high reflectivity. In dielectrics, the interaction is more complex and can involve scattering, fluorescence, or nonlinear effects at high intensities.

The extent of each portion depends on the material's properties and the light's wavelength. At dimensions sufficiently larger compared to wavelength, absorption follows the Beer–Lambert law, Equation 2.5:

$$I = I_0 e^{-\beta z} \tag{2.5}$$

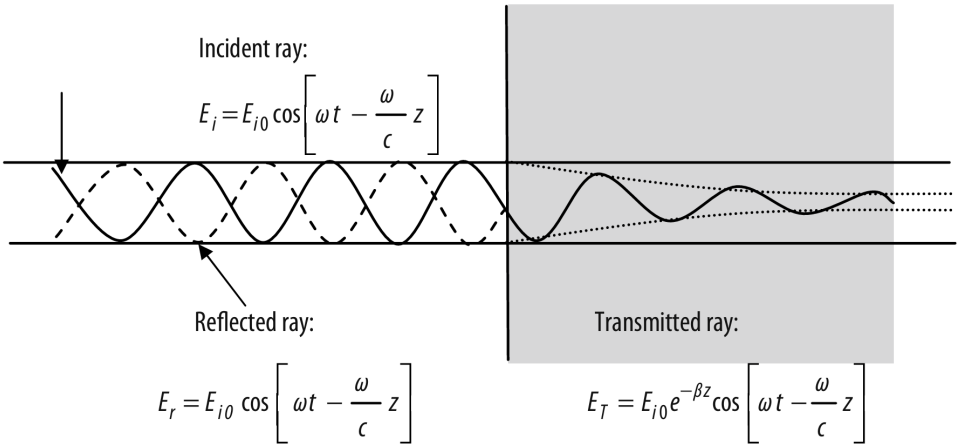

Figure 16: Main laser-matter interaction: incident, reflected and transmitted waves [1].

where β is the absorption coefficient of the material and z is the depth. Absorbed energy excites electrons, which may re-radiate (reflection/transmission) or transfer energy to the lattice (absorption), resulting in heating, melting, or vaporization. At high intensities, materials can form plasmas, which strongly absorb laser energy.
Reflection occurs when light bounces off the surface. Metals, with free electrons, reflect most incident light. The reflectivity R and absorptivity A are the corresponding complements to 1 of the other: $R = 1 - A$.
Other phenomena involving light waves are described as follows.

Diffraction refers to the bending and spreading of light waves when they encounter obstacles or apertures. It is a direct consequence of the wave equation and becomes significant when the dimensions of the obstacle are comparable to the wavelength of light. For a circular aperture, the minimum spot size due to diffraction is:

$$d_{min} = 2.44\frac{f\lambda}{D} \tag{2.6}$$

where f is the focal length λ the wavelength, and D is the beam diameter. While a true laser beam has a theoretical minimum beam quality with a Gaussian intensity profile, any real-world optical system focusing it will be limited by

diffraction, preventing resolution of details smaller than roughly half the wavelength of light. [24]
Diffraction patterns arise from the interference of secondary wavelets emitted from different parts of the aperture, as described by Huygens' principle. In laser beam shaping, diffraction is used to control the spatial profile of the beam, for example through the use of diffractive optical elements like gratings or zone plates. These components modulate the phase or amplitude of the beam to produce desired intensity distributions. In ultrafast laser–material interaction, diffraction effects influence how tightly a beam can be focused, which in turn affects the intensity and localization of energy deposition in the material.
Interference occurs when two or more coherent light waves overlap in space and time, resulting in a redistribution of optical intensity due to constructive or destructive superposition, see Figure 17. This effect depends critically on the relative phase between the waves. When the phase difference leads to constructive interference, the resulting intensity can be significantly higher than the sum of the individual intensities; conversely, destructive interference can lead to complete cancellation. This principle is exploited in interferometers, which are used to measure small changes in distance, refractive index, or optical phase with high precision. In holography, interference between a reference beam and an object beam encodes spatial information into an intensity pattern that can later reconstruct the wavefront of the original object. The interference of multiple monochromatic waves with equal phase differences can also produce ultrashort optical pulses, a principle used in mode-locking lasers to generate femtosecond pulses.

Polarization describes the orientation of the electric field vector of a light wave and is inherently a vector property, requiring electromagnetic optics for a complete description. Although scalar wave optics does not fully capture polarization effects, they are crucial in laser applications. Polarization determines how light interacts with anisotropic materials, how it reflects or transmits at boundaries, and how it can be manipulated using waveplates or polarizers. In ultrafast laser processing, polarization can influence the efficiency of nonlinear interactions, the

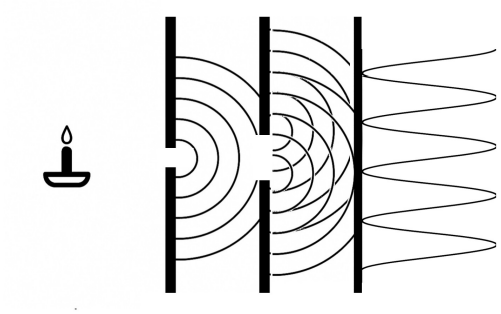

Figure 17: Young's experiment: interference of a diffracted wave.

formation of surface structures, and the directionality of ablation. For example, linearly polarized femtosecond pulses can induce anisotropic surface textures due to polarization-dependent absorption and field enhancement.

2.4 Material properties

The interaction between laser radiation and materials is a complex phenomenon governed by both fundamental physical principles and practical considerations. At the microscopic level, this interaction involves the behavior of charged particles, primarily electrons, within the material when exposed to electromagnetic fields. The laser beam, modeled as a sinusoidal electromagnetic wave, exerts forces on these particles, initiating energy transfer processes that vary significantly depending on the material's electronic structure, thermal properties, and phase state.

In metals, the presence of free electrons allows for efficient energy absorption through electron excitation. In metals, free electrons enable efficient energy absorption through electron excitation. Under ultrashort laser pulses, this interaction is accurately described by the Two-Temperature Model (TTM), which distinguishes the rapid heating of the electron subsystem from the slower thermal response of the lattice. This concept will be explained in detail in the following sections. However, metals also exhibit high reflectivity, particularly in the infrared range, which can limit energy coupling unless the surface is modified or the laser wavelength is carefully selected. Once absorbed, the energy diffuses rapidly due to high thermal conductivity, leading to melting or vaporization, effects that

are harnessed in industrial processes like laser cutting and welding.
Non-metallic materials, including semiconductors and transparent dielectrics such as glass, lack free electrons in their conduction bands. As a result, they require nonlinear absorption mechanisms, such as multiphoton ionization or tunnel ionization, to initiate interaction. Once free carriers are generated, avalanche ionization can lead to optical breakdown and permanent structural changes. These materials are particularly suitable for internal modifications, such as the creation of waveguides or microchannels, without affecting the surface. Glass, for instance, is transparent to many laser wavelengths, but at high intensities, nonlinear effects enable femtosecond laser micromachining that allows for sub-diffraction precision and minimal collateral damage [10].
Polymers and bio-materials are highly sensitive to thermal effects due to their low thermal and electrical conductivity. They tend to absorb laser energy more efficiently in the ultraviolet and visible ranges, often undergoing photochemical reactions rather than thermal melting. This can result in clean ablation or decomposition, which is advantageous for applications requiring minimal thermal damage, such as microelectronics or biomedical device fabrication. Ultrafast lasers, particularly those operating in the femtosecond and picosecond regimes, are especially effective for processing these materials, enabling precise structuring while preserving their functional integrity.
Ceramics, characterized by their opacity, brittleness, low thermal conductivity, and high melting points, present additional challenges. Their response to laser irradiation is highly dependent on composition and microstructure. Absorption leads to localized heating, but due to their low thermal diffusivity and mechanical fragility, thermal stresses can easily induce cracking. Therefore, laser processing of ceramics demands careful control of pulse duration, energy, and interaction time to avoid damage and ensure precision.
Laser-based technologies that combine physical and chemical processes have been used for precise surface treatment and functionalization of diamond, not only at the nanoscale but even at the atomic level [13].
Composite materials, which combine multiple phases, such as fibers embedded in a matrix, introduce further complexity. Each constituent may respond differently to laser irradiation, and their interfaces can lead to non-uniform energy distribu-

tion and stress accumulation. For example, in polymer matrix composites, the matrix may absorb UV light efficiently, while the fibers (e.g., carbon or glass) may reflect or conduct heat differently, potentially causing delamination or uneven ablation. In ceramic or metal matrix composites, differences in absorption thresholds and thermal conductivities between phases require precise tuning of laser parameters to prevent microcracking or phase separation. Ultrafast lasers are particularly beneficial for composite processing, as they enable localized energy deposition with minimal thermal diffusion, allowing for clean and controlled modification even across heterogeneous interfaces. Laser processing of composite specimens is a suitable preparation method for bonding, sealing or encapsulation of structures technology [25] .

In real-world industrial applications, ideal conditions are rare. Surfaces are often microscopically irregular or contaminated, which affects the energy absorption and reflection. Therefore, technological descriptions of laser–material interaction must account for practical variables such as surface roughness, contamination, and ambient conditions. The absorption coefficient plays a central role in determining how much energy is effectively used for processing. While solid materials often exhibit low absorption coefficients, these values increase significantly during phase transitions, from solid to liquid to gas, becoming nearly unitary in the gaseous state. This behavior is critical during laser processing, especially when melting is undesirable, as uneven absorption can lead to unintended thermal effects.

Interaction time, the duration for which the material is exposed to the laser beam, is another key factor. It influences the temperature profile within the material and, together with irradiance, determines the extent of melting, vaporization, or ablation. Ultrafast laser pulses, by depositing energy faster than thermal diffusion can occur, enable non-thermal processing with minimal heat-affected zones. This capability is transformative for precision manufacturing, allowing for micro- and nano-scale structuring across a wide range of materials. [4, 18]

2.5 Non-linear effects

The interaction of electromagnetic radiation with matter undergoes a profound transformation when ultrafast lasers, emitting pulses in the femtosecond to picosecond range, are applied. Ultrashort laser pulses interact with materials in a fundamentally different way compared to conventional lasers. While traditional lasers deposit energy gradually, allowing thermal diffusion and equilibrium between electrons and the atomic lattice, ultrafast lasers deliver energy so rapidly that electrons absorb it before the lattice can respond. This results in a pronounced non-equilibrium state where electron temperatures rise sharply while the lattice remains relatively cool. Such conditions suppress thermal conduction and confine energy to extremely short timescales, enabling highly localized and controlled material modifications. These dynamics allow non-thermal melting, solid-state plasma formation, and precise ablation with minimal heat-affected zones. In metals, this behavior is accurately described by the Two-Temperature Model (TTM), which distinguishes the rapid heating of the electron subsystem from the slower lattice response. The resulting non-equilibrium conditions drive ultrafast phase transitions such as spallation, phase explosion, and cold ablation mechanisms essential for achieving high-quality surface finishes and precise material removal in ultrashort laser processing.

At the heart of nonlinear optics is the relationship between the electric field of the light and the induced polarization in the medium. In linear media, this relationship is proportional, meaning the polarization density is directly related to the electric field via a constant susceptibility.

At these high peak intensities, ultrafast lasers trigger a range of nonlinear optical effects, where the material's response becomes intensity-dependent and the polarization is no longer linearly proportional to the electric field.

One of the most prominent nonlinear effects is self-focusing, which occurs when the refractive index of a material increases with light intensity (the Kerr effect). This causes the laser beam to act like a lens, focusing itself as it propagates through the medium. If the peak power exceeds a critical threshold, the beam collapses into a narrow filament, a phenomenon known as filamentation. This self-guided propagation allows ultrashort pulses to maintain high intensity over

long distances, even in dispersive media like air, water, or glass. Filamentation is not only a striking demonstration of nonlinear optics but also a practical tool for applications such as internal glass modification, waveguide writing, and even atmospheric sensing [1, 4]. Filamentation together with Bessel beam generation are key technologies currently employed for realizing high aspect-ratio laser processing, with applications in many fields, such as optics, biological manipulation, and microelectronics [26].

Another critical nonlinear phenomenon is phase conjugation, where an incoming distorted wavefront is reflected as its exact time-reversed replica. This is achieved through a mechanism called degenerate four-wave mixing, where three laser beams interact in a nonlinear medium to produce a fourth beam that retraces the path of the original, correcting any distortions.

Second-harmonic generation is a second-order nonlinear effect where two photons of the same frequency interact within a nonlinear crystal to produce a new photon with twice the energy and half the wavelength—effectively doubling the frequency of the incident light. For example, a Nd:YAG laser emitting at 1064 nm can be converted to green light at 532 nm using a crystal like lithium niobate ($LiNbO_3$). Efficient SHG requires phase matching, when the phase velocities of the fundamental and second-harmonic waves are equal, often achieved using birefringent crystals carefully oriented and temperature-controlled.

The ability to generate the second harmonic expands the applications of laser processing for the same materials that respond differently, and to achieve unique results, as they depend on the wavelength of the laser that generates them.

In addition, the nonlinear effects are foundational to advanced beam shaping and adaptive optics applications.

Laser-Induced Periodic Surface Structures (LIPSS) are nanoscale surface patterns formed through the interaction of ultrafast laser pulses with solid materials. Their generation is fundamentally governed by nonlinear optical phenomena, particularly multiphoton absorption and strong-field ionization, which occur when the laser intensity exceeds the material's linear absorption threshold, see Figure 18. In dielectrics and semiconductors, these nonlinear effects promote electrons to the conduction band, enabling localized energy deposition and material modification. The ultrashort duration of femtosecond pulses allows for precise control

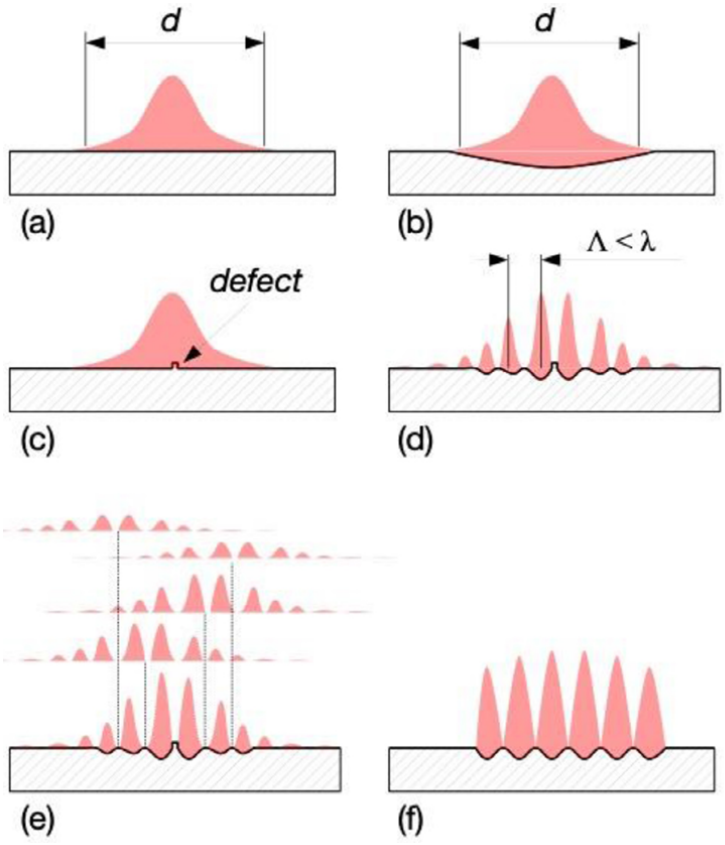

Figure 18: LIPSS formation as an electromagnetic interference phenomenon [4].

over energy delivery, minimizing thermal diffusion and enabling sub-wavelength structuring. LIPSS formation is influenced by factors such as laser polarization, fluence, and pulse number, and is often explained through models involving surface electromagnetic wave excitation, surface plasmon polaritons, and thermally induced Marangoni instabilities.

These structures offer unique advantages for industrial applications, including wettability control, tribological enhancement, and optical functionality, making LIPSS a powerful tool in laser-based surface manufacturing. The periodicity of LIPSS varies between $\lambda/2$ and λ for Low Spatial Frequency LIPSS (LSFL) resulting in the sub-micron range for the usual laser wavelengths. High Spatial Frequency LIPSS (HSFL) are shorter as they are shorter than $\lambda/2$ and usually lie in the 100 nm and sub-100 nm range. They generally appear by applying a high number of pulses at low fluence. [4]

3. Laser beam shaping through Adaptive Optics

Laser beam shaping refers to the process of modifying the spatial or temporal characteristics of a laser beam to achieve a desired intensity distribution or an energy delivery pattern. It enables more precise control over how laser energy is delivered to a workpiece, with the aim to improve performance, efficiency, and quality in laser-based manufacturing processes. Modulating the beam can reduce thermal gradients, prevent overheating, and improve the uniformity of the treated area. This technique has emerged as a transformative approach across a wide range of industrial applications, where it is now essential in laser cutting, welding, or additive manufacturing, as the interaction between the laser and the material can be significantly influenced by the beam's shape.

By tailoring the spatial, temporal, and polarization characteristics of laser beams, or by modifying the wavefront phase of the laser light, beam shaping achieves a desired intensity or phase distribution at the target surface. In particular, intensity shaping focuses on what happens to the light's energy at a specific plane, whereas phase shaping focuses on how the light travels and interacts with its environment. They can be done using devices such as spatial light modulators, deformable mirrors, diffractive optical elements, or acousto-optic and electro-optic modulators.

Dynamic beam shaping using adaptive optics offers several compelling advantages in laser materials processing. Adaptive optics refers to systems that can actively and precisely modify the wavefront of a laser beam in real time. These systems respond to changing conditions or desired outcomes, enabling highly flexible and optimized energy delivery.

One of the key benefits is the ability to tailor the laser beam to match the specific requirements of a process at any given moment. This means that the beam can be reshaped dynamically to adapt to variations in material properties, surface geometry, or environmental factors, enhancing the process efficiency and quality. So, the use of adaptive optics supports real-time feedback in a closed-loop

control. By integrating sensors and monitoring systems, the beam can be continuously adjusted based on live data from the process. This leads to smarter, more autonomous manufacturing systems capable of self-optimization and error correction.

3.1 Spatial and temporal laser beam shaping

Traditionally, laser beams have been employed in their fundamental Gaussian or top-hat profiles, but recent advances have introduced a variety of complex beam shapes, such as ring, donut, Bessel, and multi-spot configurations, each tailored to specific processing goals and obtained by several techniques.
First of all, there are two main approaches to shape the beam: static and dynamic beam shaping. Static beam shaping involves using fixed optical components, such as diffractive optical elements or specially designed lenses, to transform the beam into specific profiles like top-hat, elliptical, or annular shapes. These configurations are predetermined and do not change during operation. Dynamic beam shaping introduces time-dependent modulation of the beam's position or intensity. Dynamic beam shaping mainly uses programmable Diffractive Optical Elements (DOE) and Spatial Light Modulators (SLM). It includes linear longitudinal oscillations, circular or elliptical oscillations, where the beam follows a curved path to distribute energy more uniformly; spiral patterns, which are useful for gradually increasing energy exposure over a surface; and Lissajous patterns, which result from combining two perpendicular oscillations at different frequencies to create complex, uniform coverage. Additionally, some systems use pseudo-random or non-repetitive modulation to avoid thermal accumulation and improve surface quality. Another approach involves modulating the focal position along the optical axis, known as focus plane oscillation, which helps balance energy delivery through the depth of the material. Temporal pulse shaping is also considered a form of dynamic beam shaping, where the pulse duration, spacing, or intensity is varied over time to match the thermal response of the material. In some advanced systems, even the polarization state of the beam is dynamically adjusted to influence how energy is absorbed by different materials.

Beam shaping can also be categorized into spatial, temporal, and polarizational modalities, each influencing the process through distinct physical mechanisms. These can be done either statically or dynamically.
Spatial beam shaping modifies the intensity distribution across the beam cross-section, often using devices like liquid crystal on silicon spatial light modulators (LCoS-SLMs), deformable mirrors (DMs), or DOEs. These devices can dynamically alter the wavefront to produce flat-top, elliptical, or multi-focal patterns, improving uniformity and reducing defects such as heat-affected zones or spatter formation [27]. An example of different spatial beam profiles is shown in Figure 19, where, for simplicity, axially symmetric configurations are represented.

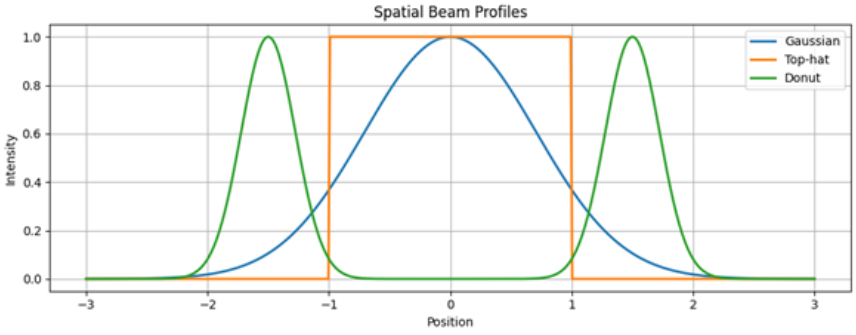

Figure 19: Spatial beam shaping along a two-dimensional section.

DOEs improve processing efficiency by splitting beams into multiple sub-beams for parallel operations, reducing thermal effects, and enhancing uniformity. In this context, computational design, numerical modeling, and artificial intelligence accelerate design cycles, improve phase profile shaping, and allow real-time adaptive control [28].
Temporal beam shaping, on the other hand, adjusts the power or frequency of the laser over time, allowing synchronization with transient material responses. Techniques such as chirped pulse amplification (CPA), pulse bursts, and modulation via electro-optic or acousto-optic modulators enable control over ablation efficiency, heat accumulation, and phase transitions [29]. For instance, in ultrashort pulsed laser processing, temporal shaping can enhance selective etching in glass or optimize the formation of laser-induced periodic surface structures. An example of different temporal beam profiles is shown in Figure 20.

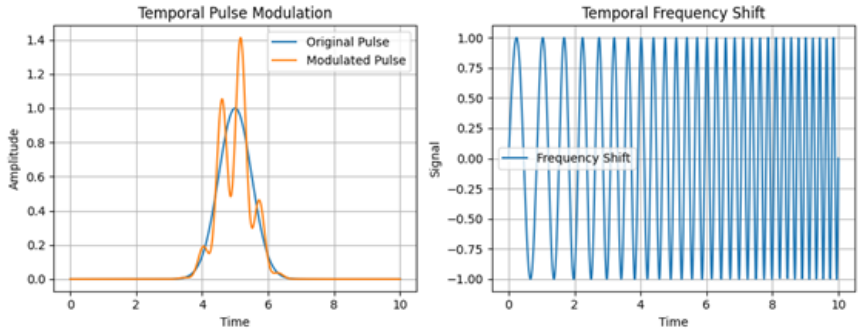

Figure 20: Temporal beam shaping.

Polarizational beam shaping, though less commonly exploited, plays a critical role in processes involving oblique incidence or plasmonic effects, where the orientation of the electric field vector influences absorption and material excitation. Radial and azimuthal polarizations have demonstrated improved cutting performance and ablation efficiency in metals and dielectrics [30, 31].

Importantly, the effectiveness of beam shaping is not solely determined by the shape itself but by its synchronization with the characteristic time scales of the underlying physical processes. This concept of "synchronous energy coupling" suggests that optimal results are achieved when the modulation frequency of the beam matches the dynamic response of the material, be it melt pool convection, keyhole formation, or solidification kinetics.
Consequently, dynamic beam modeling has emerged as the dominant strategy for this purpose.
However, this also creates significant challenges, for example, the importance of selecting appropriate beam size metrics when implementing beam shaping in ultrafast laser processing. As beam profiles evolve from simple Gaussian shapes to complex, non-centrosymmetric distributions, traditional metrics such as the 86% power containment or $1/e^2$ intensity threshold fail to accurately predict process outcomes. For conduction-mode processes, the second moment metric is most representative, and Knife-edge also performed well and is simpler to implement experimentally, but cautions that other regimes (e.g., keyhole welding or short-pulse ablation) may require different or multiple metrics.[30]

3.2 Fundamentals of Adaptive Optics

While temporal and polarization state shaping may depend strictly on a type of processing and can be defined upstream, the spatial shape may need to be changed in-process, so it is worth analyzing dynamic spatial beam shaping through an adaptive optics system.

Adaptive optics (AO) is a system technology that achieves the desired goal of adding or removing aberrations to or from light wavefronts, to improve image clarity and resolution for delivery to a vision system, biological or machine. Aberrations are effects caused by optical elements and non-linear phenomena, such as the refraction index dependent on wavelength, intensity, or geometrical issues. They cause light to scatter in space, instead of focusing on a point, and produce wavefront deviations from flat to deformed (curved or irregular), thus blurred or distorted images, see Figure 21.

AO is a multidisciplinary field in science and engineering aimed at enhancing the performance of optical systems by compensating for environmental and system-induced distortions in real time. It applies to both imaging and laser systems, using feedback mechanisms to correct wavefront aberrations. AO is typically considered a subset of active optics, characterized by closed-loop, real-time control, though broader definitions include intensity correction, multi-conjugate approaches, and applications in incoherent imaging.

A natural example of this technique is the human visual system, where the eye–brain mechanism continuously adjusts focus, aperture, and direction to optimize image clarity, demonstrating phase-only and intensity-based corrections. In lay terms, AO can be described as a method for automatically keeping light in focus when it becomes distorted [22].

The principles of AO rely on modifying optical systems by adding, removing, or adjusting components to approach the diffraction limit, despite the inherent nature of diffraction governed by Maxwell's equations. AO compensates for additional distortions caused by mechanical or thermal imperfections, minimizing their impact through dynamic correction strategies.

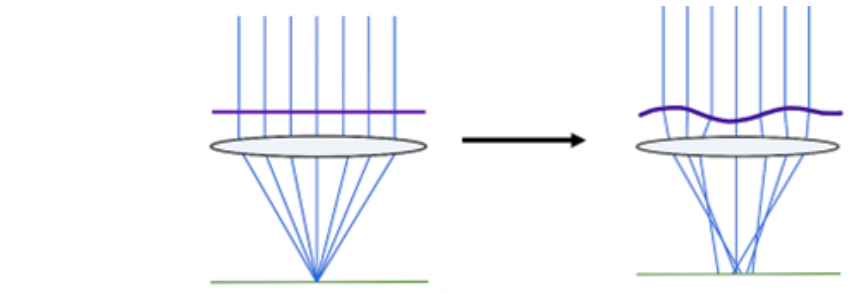

Figure 21: Aberration scheme.

In laser resonators, aberrations are amplified due to their multi-pass nature, leading to intensity fluctuations and degraded beam quality. Common issues include misalignments, tilts, defocus, and astigmatism, which can prevent lasing. Aberrations also arise from the gain medium, whether solid, liquid, gas, or plasma, due to inhomogeneities and turbulence. Some resonator designs, like unstable annular resonators, are less sensitive to misalignments but suffer from edge effects that introduce high spatial frequency aberrations. AO systems have been successfully implemented both intracavity and externally, especially in high-power and ultrafast lasers, to correct these distortions [22].
The most common AO configuration includes wavefront sensors, electronic controls, and corrective optics, operating in a closed-loop system. Passive and unconventional methods also exist, such as spatial filtering and the use of non-linear optical materials. Real-time correction is essential, as post-processing often fails due to low modulation transfer function (MTF) and poor signal-to-noise ratio (SNR).
A key technique in AO is phase conjugation, which reverses the phase of a distorted wavefront, allowing it to retrace its path. Phase-conjugated mirrors exploit this effect to automatically compensate for aberrations in optical systems. This process requires some specifications:

- Precise spatial correction: the mirror or optical element must introduce a phase shift equal in magnitude but opposite in sign to the distortion.
- Temporal accuracy: especially for dynamic aberrations, the correction must be applied at the right moment.
- Complex conjugation: mathematically, the distorted field is multiplied by

its complex conjugate, restoring a plane wavefront.

Though conceptually simple, implementing phase conjugation is challenging due to the need for exact spatial and temporal matching. In laser material processing, AO has revolutionized precision and efficiency, since it can corrects aberrations in laser systems, adjusts the focal spot inside materials, generates multiple foci, varying phase and depth, and enables optimal 3D structuring. Modern AO tools include liquid crystal spatial light modulators (SLMs), MEMS micromirrors, and deformable mirrors (DMs), allowing control over beam shape, pulse duration, and orbital angular momentum.

A notable application is the direct writing of waveguides in glass for photonic integrated circuits, where AO reduces spherical aberration during deep writing, enabling uniform waveguides at depths up to 1000 μm through open-loop corrections and laser parameter optimization. AO also supports beam shaping (e.g., flat-top, Bessel, vortex beams) and parallelization, crucial for waveguide lattices, microfluidics, and high-aspect-ratio drilling [32].

Beyond conventional adaptive optics (AO) systems, there is the concept of non-inertial and nonlinear AO, where materials respond to electric fields without requiring any mechanical motion. These unconventional methods are based, for example, on the Pockels effect, whereby the change in refractive index is directly proportional to the intensity of the applied electric field [22].

AO in laser technology is a transformative approach that enhances precision, efficiency, and flexibility, particularly in ultrafast laser applications. It enables diffraction-limited focusing at varying depths, consistent feature quality, and reduced energy thresholds. Integration with machine learning further enhances real-time optimization and compact aberration correction. Despite challenges like system complexity and power handling, AO continues to push the boundaries of laser fabrication and light–matter interaction control [32, 23].

3.3 Adaptive Optics Systems

AO systems are designed to enhance the performance of larger optical setups by dynamically correcting wavefront distortions in real time. Effective AO design

requires careful consideration of three core aspects: the system's performance requirements, the properties of the optical beam to be corrected, and the integration strategy within the host optical environment. There is no universal design formula; instead, engineers must balance cost, complexity, and performance using modeling tools such as atmospheric turbulence simulators and phase screen generators to guide specifications and reduce development time.

Significant design parameters include spatial bandwidth (related to the number of correction zones), temporal bandwidth (servo control speed), and disturbance amplitude, which influence the choice between deformable mirrors and beam-steering components. Beam characteristics, such as size, shape, intensity distribution, and power level, also affect component selection. For example, high-power beams require robust optics, while small beams with complex aberrations may need magnification. Wavelength selection is driven by scientific goals and detector capabilities, with visible light preferred for sensing and infrared for imaging.

Typically, an adaptive optics system consists mainly of three basic elements: a wavefront sensor, a wavefront corrector, and a control system, see Figure 22.

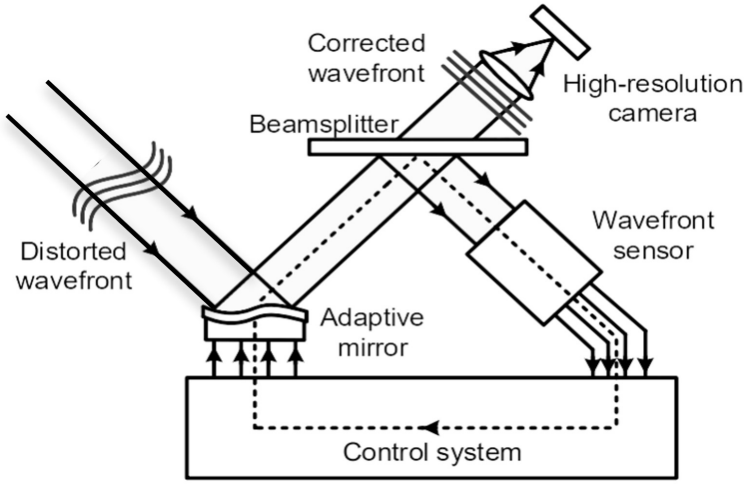

Figure 22: Adaptive optics system scheme. [4]

In adaptive optics, the wavefront is usually the entity that is meant to be mod-

[4] Adapted from: https://encyclopedia.pub/entry/23057

ified to alter the propagation characteristics of the beam. A mathematical representation of a complex wavefront is given by Zernike polynomials, a sequence of continuous functions orthogonal on a unit circle, which allows mathematical manipulations of wavefronts, such as addition, subtraction, translation, rotation, and scaling. They also have good relationships with classical aberrations, including astigmatism, coma, and spherical aberration. They can be divided into even (Z_n^m) and odd (Z_n^{-m}) polynomials as follows:

$$\phi(x, y) = \sum a_i Z_i(x, y) \tag{3.1}$$

and

$$\begin{cases} Z_n^m(\rho, \phi) = R_n^m(\rho) cos(m\phi) \\ Z_n^{-m}(\rho, \phi) = R_n^m(\rho) sin(m\phi) \end{cases} \tag{3.2}$$

Where $\phi(x, y)$ is a generic wavefront, n and m are integer numbers, ϕ is the azimuthal angle, ρ is the radial distance, and R_n^m are radial Zernike polynomials which can be described as factorial ratios. The first 21 Zernike polynomials, ordered vertically according to radial degree and horizontally according to azimuthal degree, are shown in Figure 23. A more detailed discussion of their mathematical expressions is provided in the Appendix A.

Wavefront sensing is central to AO systems, requiring high spatial resolution and fast response to correct dynamic aberrations. Sensing methods include:

- Direct approaches, which explicitly measure phase or optical path difference (OPD).
- Indirect approaches, which infer phase-related information without full reconstruction.

In the direct approach, a critical requirement is the ability to determine OPD

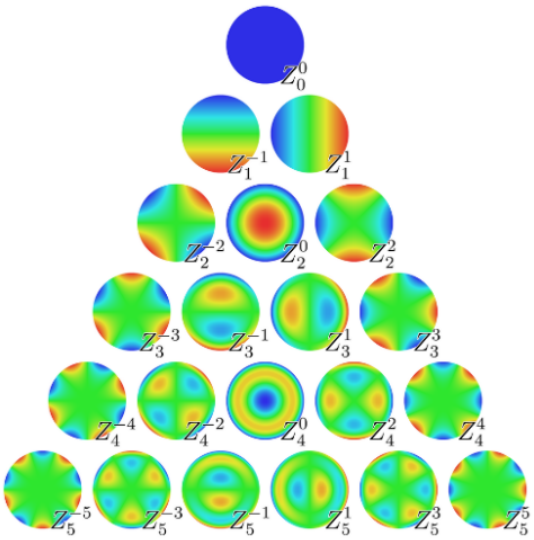

Figure 23: Zernike Polynomials.[5]

independently of intensity, especially under non-uniform illumination. Broadband light is often used when single-wavelength measurements are insufficient. Advanced direct phase retrieval techniques include:

- Zernike-based retrieval, using electric field patterns and the Gerchberg-Saxton algorithm.
- Differential Optical Transfer Function (dOTF), a non-interferometric method using point spread function (PSF) image differences to compute pupil plane phase and amplitude.
- Shack-Hartmann wavefront sensor (WFS), which measures local wavefront slopes through the displacement of focal spots created by a microlens array. From these slopes, the wavefront phase is reconstructed using numerical integration or fitting methods

After Shack-Hartmann measures slopes, the reconstructed wavefront can be expressed in Zernike polynomials for analysis as a post-processing step, but the sensing principle is different. Shack-Hartmann WFS is widely used for real-time wavefront measurement. It consists of a lenslet array and a CCD detector, measuring local wavefront tilt via focused spot positions, as can be seen

[5] https://it.wikipedia.org/w/index.php?title=Polinomi$_di$Zernikeoldid = 145034910

in Figure 24. The major advantages include wide dynamic range, high optical efficiency, compatibility with white light, and support for pulsed or continuous sources. Modern implementations address challenges like subaperture size tradeoffs, anisoplanatism, and spot distortion. Enhancements include optical binning, image intensification, rotated quadcells, and digital micromirror devices (DMDs) for scanning.

Centroid estimation is vital for precise wavefront reconstruction because it directly determines the local tilt of the wavefront in each subaperture of a wavefront sensor. The combined set of local tilts measured across the aperture provides a gradient map of the wavefront. From this, the full wavefront phase can be reconstructed using mathematical techniques such as Zernike polynomial fitting or Fourier-based methods. Errors in centroid estimation propagate into the phase reconstruction, reducing accuracy.

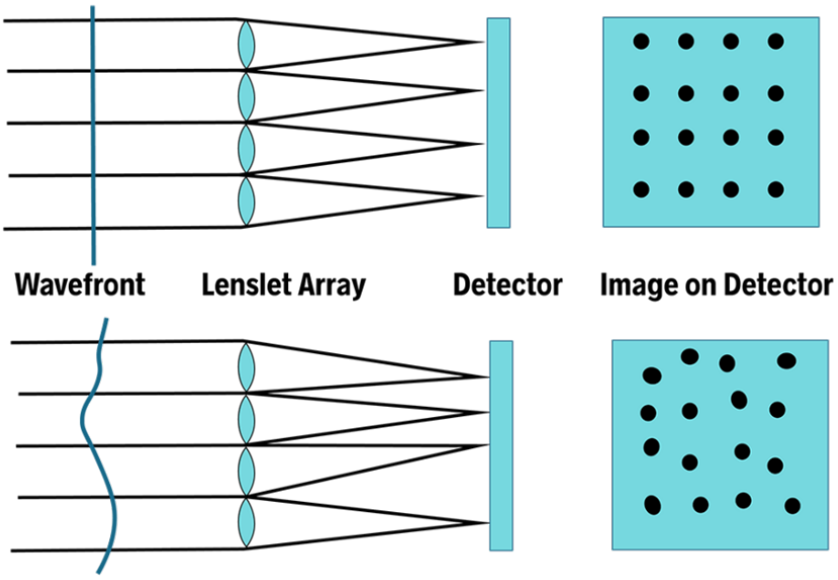

Figure 24: Shack-Hartmann Wavefront sensor principle, adapted from [33].

Wavefront correction in AO is based on optical phase conjugation, where distortions introduced by one optical element are reversed by another. AO systems use modal (specific aberration modes) and zonal (localized regions) correction strategies. The most common correction devices are active mirrors, especially deformable mirrors (DMs), which can be:

- Continuous surface mirrors (e.g., membrane or bimorph mirrors)
- Discrete actuator mirrors, with actuators behind or at the edges.

These mirrors are capable of correcting high spatial frequencies and are essential in high-energy laser systems. Actuators are classified by output type (constant displacement or constant force) and mechanism (piezoelectric, ferroelectric, Lorentz force, electrostatic, magnetostrictive). The choice depends on system requirements like bandwidth, stroke, correction zones, and field of view. An example is in Figure 25.

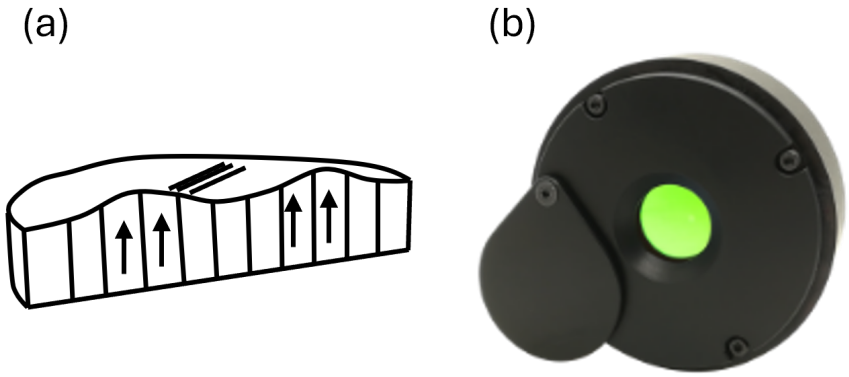

Figure 25: Scheme (a) and real (b) piezoelectric deformable mirror from Dynamic Optics ©.[6]

However, there is a trade-off between spatial and temporal frequency capabilities. Fast tilt mirrors correct low-order modes quickly but lack spatial resolution. Large active mirrors correct high spatial frequencies but respond more slowly. Multi-actuator DMs offer a balanced solution for general-purpose correction.
Reflective correctors benefit from a factor-of-two angular gain, unlike single pass refractive devices such as liquid crystal modulators. Real-time correction devices were demonstrated as early as the 1970s, initially for atmospheric turbulence compensation. Before DMs, tilt and scanning mirrors were used for beam steering, laying the foundation for modern AO systems.
Wavefront sensors include not only opto-mechanical components but also electro-optical elements and processing algorithms, which are equally critical for accurate

[6] https://www.dynamic-optics.it/

wavefront representation. Innovations in lenslet array manufacturing, including 3D printing techniques, and the integration of liquid crystal displays as both lenslet arrays and correctors, continue to expand AO capabilities. These developments, combined with faster detectors and processors, are driving the evolution of AO [22].

3.4 Laser beam shaping through adaptive optics

By using adaptive optics, not with the goal of correction, but to introduce aberrations and wavefront modification, ultrashort laser beams with different energy distributions in the focal point can be obtained.
Laser beam shaping by means of flexible mirrors represents a powerful and versatile approach to control the spatial characteristics of laser radiation, particularly in high-precision and high-power applications. Flexible mirrors, especially bimorph deformable mirrors, are adaptive optical elements capable of dynamically modifying the phase front of a laser beam within the resonator or in extracavity configurations. These mirrors consist of piezoceramic layers bonded to a substrate, and their shape can be precisely controlled by applying voltages to segmented electrodes. This enables the mirror surface to deform in a controlled manner, allowing compensation for wavefront aberrations and the generation of tailored irradiance profiles such as super-Gaussian or annular beams.
In particular, the deformable mirror employed in this work belongs to the class of bimorph deformable mirrors, whose design follows specific criteria to ensure adequate performance in the presence of high-energy laser beams [34]. These devices consist of a thin glass substrate bonded to a piezoelectric (PZT) actuator, whose deformation arises from the expansion or contraction of the piezoceramic material when a voltage is applied. The geometry and layout of the actuators—typically defined through micromachining of the electrode—are chosen based on the spatial characteristics of the aberrations to be reproduced or corrected. The mirror response is well described by the Poisson equation, which links the applied voltage distribution to the resulting deformation of the reflective surface, enabling accurate numerical modeling of the device. During the design phase, parameters

such as maximum required deformation (stroke), spatial frequency content of the aberrations, and temporal evolution of thermally induced distortions are carefully evaluated. Furthermore, the ratio between substrate thickness and PZT plate thickness, as well as the number and distribution of actuators, is optimized to ensure both adequate correction capability and compatibility with manufacturing constraints, including limitations on the achievable aspect ratio of the mirror substrate. Thermal effects and coating-induced stresses, potential sources of unwanted curvature, are also considered and may be mitigated through symmetric dielectric coatings or dedicated mounting techniques. These considerations together allow the realization of deformable mirrors with high stability, linear response, and large dynamic range, suited for operation in high-power laser systems where significant thermal aberrations develop [34].

Unlike static beam shaping methods, such as graded reflectivity or phase mirrors, which are fixed and optimized for specific conditions, flexible mirrors offer real-time adaptability. This is particularly valuable in environments where thermal effects, mechanical stress, or active medium inhomogeneities can distort the beam. Flexible mirrors can correct these distortions and maintain beam quality, even under varying operational conditions. Their ability to reproduce low-order aberrations like defocus, astigmatism, coma, and spherical aberration with high fidelity makes them ideal for both beam homogenization and mode control [35]. Flexible mirrors also support closed-loop control systems when integrated with wavefront sensors, enabling automatic correction of dynamic aberrations. Their design can include water-cooling channels to manage thermal loads in high-power lasers, ensuring surface stability and preventing deformation due to temperature fluctuations. Materials like PKR-7M piezoceramics offer high sensitivity and low hysteresis, making them suitable for precise control, although care must be taken to avoid depolarization at high voltages.

Experimentally, flexible mirrors have been used to shape laser beams into fourth-, sixth-, and eighth-order super-Gaussian profiles, as well as annular (doughnut-like) beams. These profiles are beneficial in applications such as metal hardening, atmospheric transmission, and nonlinear optics, where uniform or specialized irradiance distributions are required. The ability to form such beams without introducing additional optical losses or compromising mode purity highlights the

effectiveness of flexible mirrors in beam shaping [35].

The laser beam shaping through adaptive optics operating principle can be explained by the scheme in Figure 26. Suppose a beam with a flat wavefront (PWF) having a Gaussian intensity distribution (GD) is incident on the deformable mirror (DM). Deformation of the mirror surface changes the wavefront of the incident collimated light from flat to deformed (DWF). When the light with the deformed wavefront is focused by a lens (L), point-by-point interference (ID) occurs, and the desired modified intensity distribution (FD) appears in the focus. In three-dimensional space, the intensity distribution created on the focal plane is reflected in a different beam cross-section.

The actuators can be controlled directly by adjusting the values of the single

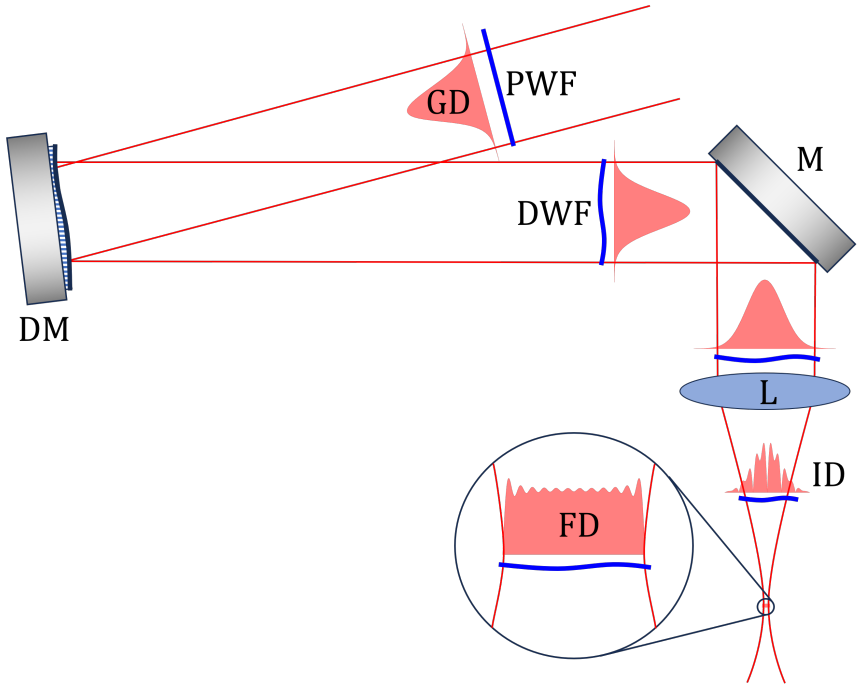

Figure 26: Beam shaping through adaptive optics principle.

Zernike decomposition contributions: by changing the coefficient values, the positions of the actuators are modified accordingly, and then different combinations of aberrations and beam shapes can be obtained. The different shapes that can be obtained can be generally complex, but at an industrial level, a simple yet effective one is the elliptical shape, with a variable ratio between the axes, see Figure 27.

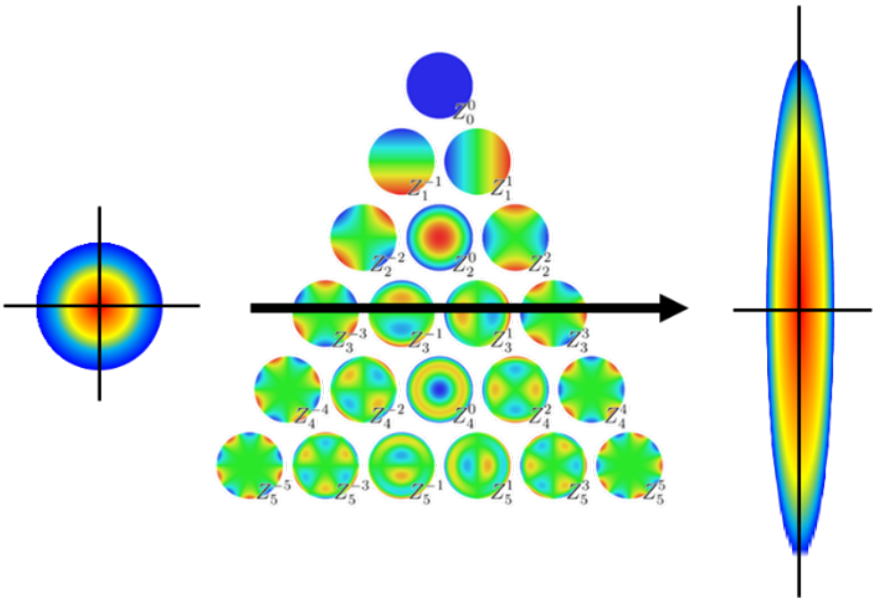

Figure 27: Transformation of a circular beam into an elliptical beam through modal correction.

To generate a linear or highly elliptical focal spot, the adaptive optics system must impose a cylindrical wavefront on the incoming beam. A cylindrical wavefront corresponds to a curvature introduced along only one axis (e.g. 0° or 45°), producing an elongated focal region after the focusing optic. This deformation can be obtained by combining a small set of low-order Zernike modes, primarily those associated with defocus and vertical or oblique astigmatism. Astigmatism introduces different radii of curvature along orthogonal axes, while defocus shifts the overall focal position and preserves symmetry.

3.5 Applications in laser processing

The versatility of spatial beam shaping has led to its adoption across a wide range of applications. One of the purposes of beam shaping is in ultrashort pulsed laser processing, further enhancing the advantages of ultrashort pulses. In this context, this thesis aims to demonstrate that adaptive optics–enabled dynamic beam shaping bridges the gap between the precision of ultrafast lasers and the productivity required for industrial-scale manufacturing, by enabling real-time control of energy distribution, improving throughput, and ensuring superior surface quality

Using flat-top beam profiles in surface patterning processes is shown to significantly improve ablation efficiency and structure quality compared to conventional Gaussian beams. Gaussian beams often lead to uneven energy distribution, causing excessive heating at the center and insufficient energy at the edges, which can degrade the performance of components such as solar cells or carbon-based coatings.

In surface and bulk structuring, spatial beam shaping enables parallel micromachining, reducing operation time and enhancing precision. Applications include surface texturing for tribological improvements, anti-reflective coatings, and functional microstructures in glass and metals. Bulk structuring benefits from controlled energy deposition for internal modifications, such as waveguide writing and photonic crystal fabrication [36]. SLM-generated multi-spot arrays have been used for microsurgery, enabling multi-site ablation with minimal collateral damage [36]. Holographic beam shaping using SLMs has facilitated the fabrication of intricate patterns such as Fresnel zone plates and data-matrix structures, while also enabling high-throughput surface texturing and marking [29].
Furthermore, simulation-based optimization of beam shaping parameters can predict the number of holograms required to achieve the desired structure quality. This predictive capability is valuable for process planning and quality assurance in laser micromachining.[27]
In additive manufacturing spatial beam shaping enhances the precision and efficiency of laser-based additive manufacturing. It enables the creation of complex 3D structures with tailored properties, supports multi-material processing, and improves throughput through parallelization [36].
In processes like Laser Powder Bed Fusion (LPBF) and Direct Energy Deposition (DED), beam shaping serves both as a process enabler and an optimization tool. Static beam shaping using top-hat profiles has been shown to improve melt pool stability, reduce porosity, and prevent cracking in materials such as Inconel 939. Dynamic beam shaping, achieved through cascaded systems involving acousto-optic deflectors and mechanical scanners, allows for real-time modula-

tion of beam profiles, which enhances build rates and part quality. For example, dynamic control of laser power in multilayer DED has enabled the fabrication of porous metals with consistent melt pool sizes, contributing to the development of advanced functional materials [31].

In this context, flat-top beams improve uniformity in ablation and deposition processes, while vortex beams are used for chiral microstructure fabrication and polarization-sensitive surface patterning. Bessel beams, with their non-diffractive propagation characteristics, are particularly effective for high-aspect-ratio drilling and deep material processing [37].

Adaptive wavefront shaping also plays a crucial role in compensating for optical aberrations during deep material processing. This is especially relevant in femtosecond laser sculpting of transparent materials such as diamond and silicon, where aberration correction enables precise energy deposition at depth, improving the fidelity of internal structuring .

In cutting and drilling of glass, non-diffractive beams such as Bessel and Airy beams, shaped via axicons and SLMs, have demonstrated superior performance in glass cutting and drilling. These beams offer extended depth of focus and self-healing properties, allowing for high-aspect-ratio machining and reduced cracking [36, 38].

In cutting, a single-mirror dynamic beam shape system offers a robust and efficient alternative to conventional setups, with the added benefits of compactness and ease of integration. The system already demonstrates substantial gains in speed and dross reduction [39] .

Beam shaping also plays a crucial role in wavelength conversion, which is essential for generating extreme ultraviolet (EUV) radiation used in lithography. By tailoring the temporal amplitude distribution of laser pulses, researchers have achieved up to 30% improvements in conversion efficiency. This has implications not only for semiconductor manufacturing but also for high-resolution imaging and spectroscopy. [31]

By way of example, Figure 28 shows three-dimensional images of Gaussian (a), flat (b), and inverted Gaussian (c) laser beam profiles. Representative two-dimensional and three-dimensional fabrication using parallel processing are shown: (d) the array of microletters “N” fabricated with 28 exposure points

in two dimensions through a magnifying glass with a focal length of 150 mm; and (e) a three-dimensional array of microsprings manufactured with the magnifying glass with a focal length of 80 mm (the corresponding insets focus on the individual structures). Schematic of dynamic ring fabrication (f) and corresponding images of the same circular trajectories fabricated at depths of 1 μm (g) and 7 μm (h) both with and without simultaneous aberration compensation [32].

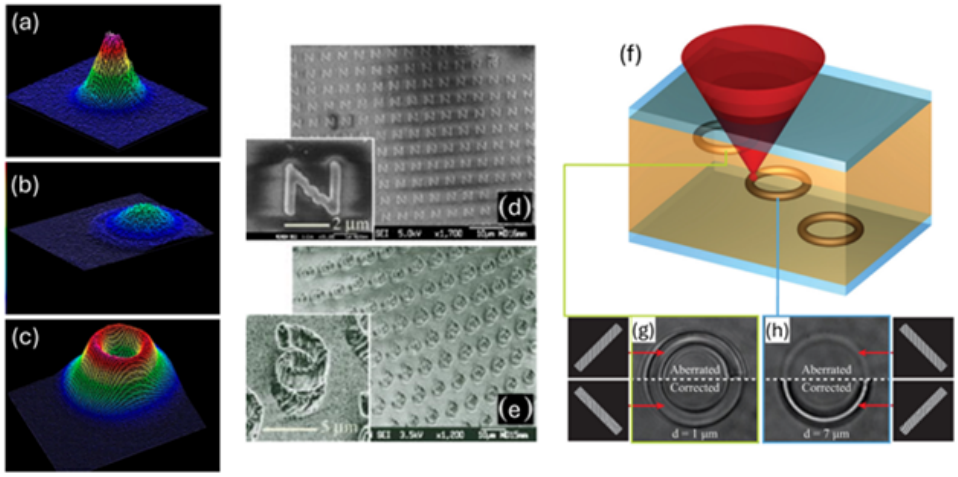

Figure 28: Laser beam shaping applications [32].

4. Design and Set-up of the laser processing system

The design and configuration of a laser processing system are central to achieving high precision, flexibility, and productivity in ultrafast laser-based manufacturing. This chapter presents the architecture of the experimental laser processing cell developed during the PhD program, for the proposed research, which integrates all the main components required for direct and induced laser processing. At the core of the system is a three-harmonics Class 4 ultrashort pulse laser source, selected for its ability to deliver high peak power and ultrashort pulses suitable for nonlinear interactions with materials. The beam delivery path includes specific optics components, adaptive optics elements, and scanning systems, all aligned using physical principles to ensure optimal energy distribution on the workpiece. The workpiece itself is positioned and moved precisely across the working area using motorized stages, enabling dynamic and repeatable processing.

Each subsystem, ranging from beam shaping and wavefront sensing to motion control, is governed by dedicated control software, which has been unified into a custom-developed interface to streamline operation and experimentation. The processing cell also includes diagnostic tools for beam characterization and process monitoring, as well as innovative components such as deformable mirrors for adaptive optics, which can be integrated or reconfigured depending on the experimental requirements.

Additional features under development include inert gas supply systems and structural enhancements to support advanced processing scenarios. Safety is ensured through comprehensive collective and individual protection systems, making the setup compliant with industrial and laboratory standards. The rationale behind each design choice is detailed, and how the integrated system supports the goals of enhancing quality and productivity in ultrafast laser manufacturing

is clarified.

4.1 Laser safety elements

Laser safety is a vital discipline in environments where lasers are used, particularly in industrial material processing. Lasers, by their nature, concentrate large amounts of energy into narrow beams of light, which can pose significant hazards if not properly controlled.

The most critical risk is to the human eye. Because the eye's lens can focus laser light onto the retina, even low-power visible or near-visible lasers can cause permanent damage, see Figure 29. This is especially true for lasers like Nd:YAG or He–Ne, which operate in or close to the visible spectrum and are therefore more likely to be focused by the eye. The damage can occur in fractions of a second, often faster than the blink reflex can protect against.

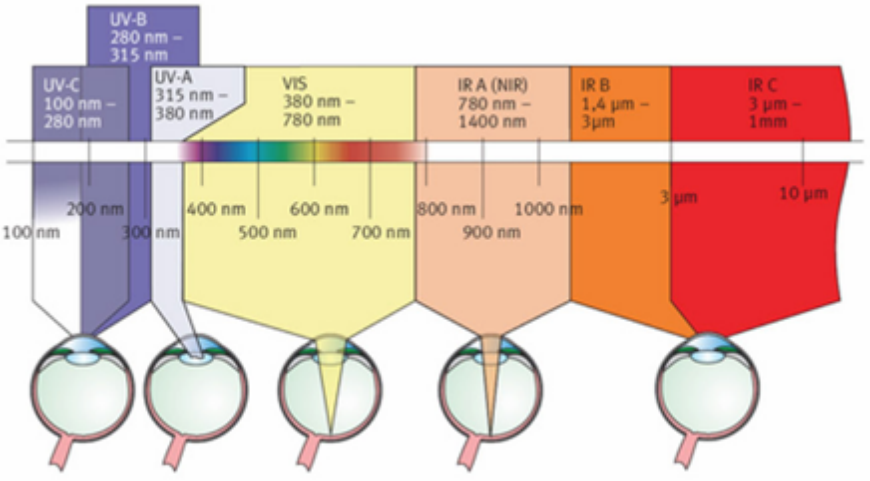

Figure 29: Laser risk to the different eye tissues depending on wavelength.[7]

Skin exposure to laser radiation is generally less dangerous but still important. High-power lasers can cause burns or cuts, and while these injuries are typically clean and healable, they should not be underestimated, see Figure 30. The laser

[7] $https://www.safetygroupitalia.it/news/wp-content/uploads/2010/12/slideroa_safety.pdf$

beam should never be allowed to contact the skin directly, and adjustments to the beam path should always be made using tools or by handling optical components from the edges.

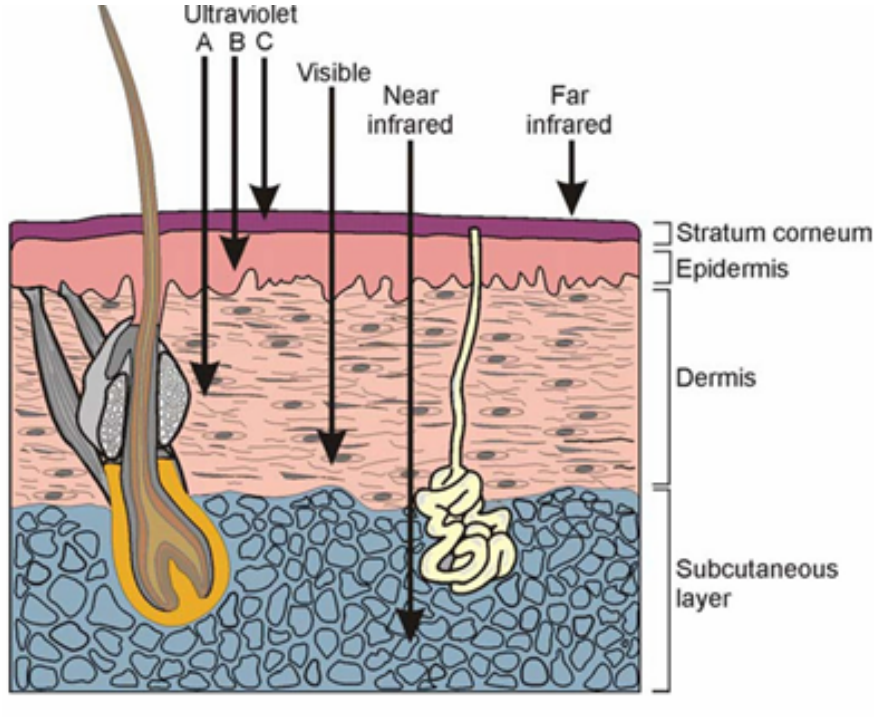

Figure 30: Laser risk to the skin as a function of wavelength.[8]

Many industrial lasers, such as CO_2 and Excimer lasers, require high-voltage power supplies, sometimes up to 30,000 volts. These systems can retain lethal charges even after being powered down, due to large capacitors in the circuitry. Therefore, strict procedures must be followed when servicing or maintaining laser equipment, including discharging capacitors and using interlocks and panic buttons to prevent accidental exposure.

Fume hazards are also significant, particularly when lasers are used to cut or engrave organic or synthetic materials. The intense heat can vaporize substances, releasing toxic or carcinogenic compounds such as hydrogen chloride, benzene, and hydrogen cyanide. Proper ventilation and fume extraction systems are essential to maintain a safe working environment.

To manage these risks, national and international standards have been developed.

[8] $https://www.ap-publishing.com/wp-content/uploads/2010/10/124_ROA.pdf$

The IEC 825 and its European counterpart EN 60825 provide comprehensive guidelines for laser safety, including classification systems that categorize lasers based on their potential to cause harm. The American ANSI Z136.1 standard offers similar guidance, with some differences in labeling and exposure limits. These standards define Maximum Permissible Exposure (MPE) levels, which are the thresholds below which laser radiation is considered safe. They also introduce the concept of the Nominal Hazard Zone (NHZ), which is the area around a laser where the intensity exceeds the MPE and protective measures are required. Lasers are classified into four main categories, whose risks are summarized in Table 1. Class 1 lasers are considered safe under all conditions of normal use, often because the laser is fully enclosed. Class 2 lasers emit visible light and are safe due to the natural blink reflex. Class 3 lasers are more hazardous, especially if viewed directly, and Class 4 lasers, used in most industrial applications, pose serious risks to both eyes and skin and can also be a fire hazard. These systems require rigorous safety protocols, including the use of protective eyewear, restricted access, warning signs, and the appointment of a Laser Safety Officer (LSO) to oversee compliance [1].

Table 1: Laser Safety Classes and Associated Risks.

Class	Risk Level	Description
1	Safe	No risk under normal use (e.g., CD players)
2	Low	Visible lasers, blink reflex protects eyes
3R/3B	Medium	Direct viewing hazardous, skin risk low
4	High	Dangerous to eyes and skin, fire risk

Laser safety eyewear and observation windows are critical components designed to mitigate the risks associated with accidental exposure to laser radiation. These devices function by attenuating or redirecting the incident laser energy, thereby preventing damage to the human eye.

Laser safety glasses are classified and certified according to the European standards EN207:2017 and EN208:2009. EN207 governs general protection against accidental exposure across a broad spectral range (180 nm to 1 mm), while EN208 specifically addresses alignment tasks involving visible lasers (400–700 nm), allowing partial visibility of the beam under controlled conditions.

The protective capability of these devices is quantified by their optical density (OD), which represents the logarithmic attenuation of transmitted power at a given wavelength. OD values are determined using spectrophotometric measurements and are critical for selecting appropriate eyewear based on the laser's operational parameters.

Two primary technologies are employed in the fabrication of laser safety filters: absorptive and reflective or interference-based systems. Absorptive filters incorporate chemical dyes into polymeric substrates such as polycarbonate or acrylic, selectively absorbing specific wavelengths and converting the energy into heat. Reflective filters, on the other hand, utilize multilayer dielectric coatings deposited on optically flat glass surfaces to reflect laser radiation through interference effects. While reflective filters offer high selectivity, their performance is sensitive to the angle of incidence, necessitating compliance with angular tolerance specifications.

Observation windows, typically integrated into laser processing machines, serve a dual purpose: enabling visual monitoring of the process while providing effective shielding against laser radiation. These windows are generally fabricated using absorptive filter technology and are certified under EN12254:2010. Unlike safety glasses, observation windows are subjected to more stringent stability tests, requiring resistance to direct laser exposure for durations up to 100 seconds. The determination of the appropriate protection level involves calculating the expected power or energy density under fault conditions, as defined by risk assessment protocols (e.g., EN60825-4), and comparing these values against standardized thresholds.

For pulsed and ultrafast laser systems, additional considerations apply. The energy density per pulse and the cumulative effect of multiple pulses must be evaluated, often incorporating correction factors based on pulse repetition frequency and beam diameter. The highest resulting protection level from these calculations is used to define the required scale number for certification.

4.2 Laser processing cell at BrightLab

All the laser processing operations described in this thesis were carried out using the laser workstation located in the BrightLab, within the university laboratories at the Tecnopolo of Reggio Emilia.
The workstation consists of two main areas:

- The clean room, which houses the laser source along with its chiller, the optical path with the reflective mirrors and other optical components. Everything is arranged on two optical tables, which are vibration control platforms. This area is accessed for maintenance, modifications, and testing of the laser's optical path when no work is being performed on the parts.
- The working chamber, where the scanning heads, final focusing lenses, and the workbench with the motor axes are located. This area is used to perform the actual machining operations on the parts.

Only the laser beam paths connect the two areas, which are fully shielded and isolated from the rest of the working chamber as they enter the scanning heads. The laser system is depicted schematically in Figure 31 and an actual photograph is shown in Figure 32.

The infrastructure includes the following components:

- Nextema protective panels equipped with safety windows;
- Clean air blower from outside;
- Internal air conditioning systems;
- Extractor hoods and fume extractors;
- Optical tables;
- Lenses and mirrors;
- Galvanometric scanning heads;
- Granite base table;
- Linear motion axes;
- Lifting system and rotational spindle;

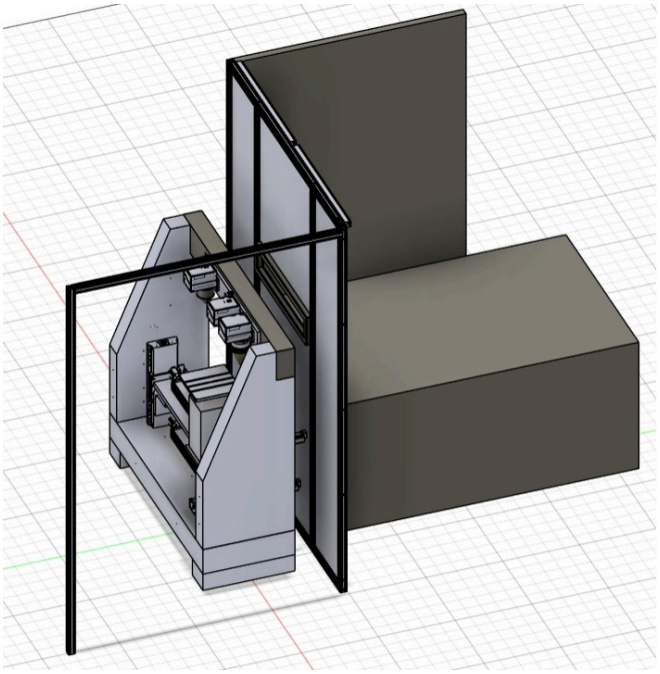

Figure 31: 3D model of the experimental laser system: on the left side is the working chamber, while the optical bench on the right represents the clean room.

- Personal protective equipment (PPE) such as safety goggles and masks with optical filters.

A Vortex blower connects the external environment and the clean area: it continuously blows clean air into the cell, creating an overpressure to prevent dust from settling on the optical components, which would significantly reduce the laser's power transmission and damage optical components. Inside the clean cell, two air recirculating hoods further decrease the amount of airborne particulate. This part of the cell is constantly air-conditioned and kept at a temperature of 22°C, which is the optimal ambient temperature at which the source chiller operates without malfunctioning.
Two Vortex fume extractors are installed in the working chamber to remove the particulate matter and volatile substances produced by the most demanding processes. This part of the cell is air-conditioned to keep the air dehumidified. In the working chamber, infrastructure has been set up for the supply of inert gas near the processing area: for example, argon or nitrogen.
Without distinguishing between the two areas of work, the fundamental components that comprise them, with their key characteristics, are listed in Table 2

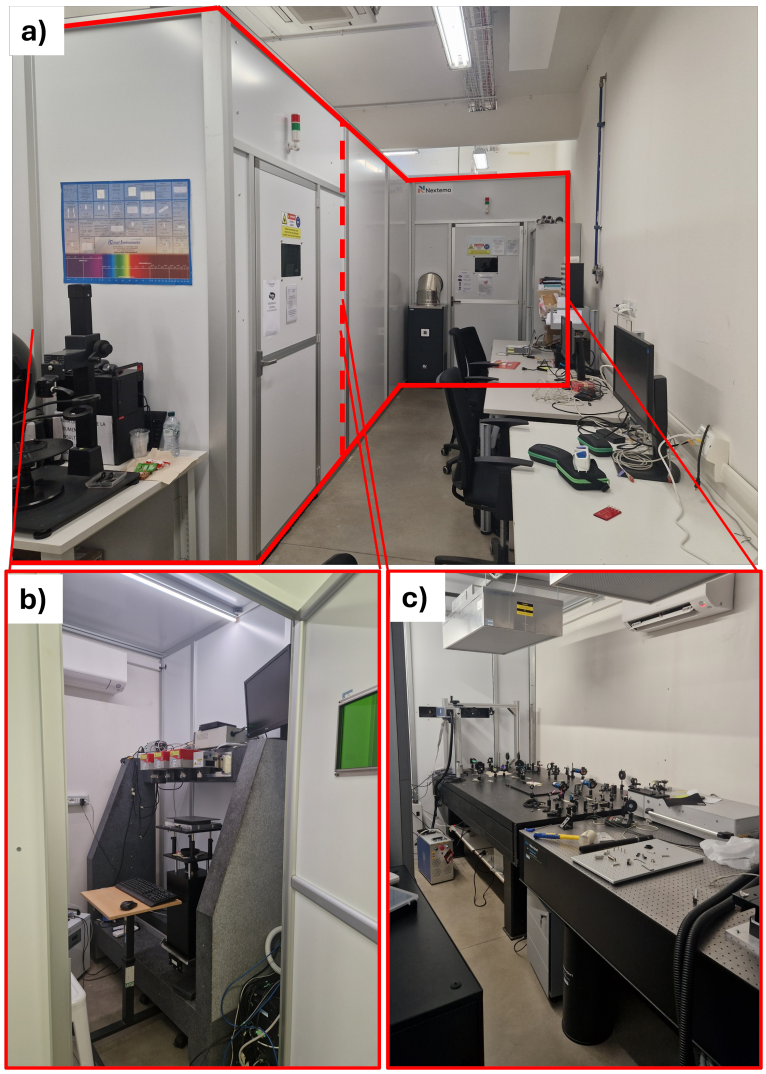

Figure 32: a) Actual photograph of the laser processing cell inside the BrightLab laboratory: b) working chamber, c) clean room with visible laser optical path.

and summarized in Figure 33.

The source is a picosecond laser amplifier Atlantic 50 of EKSPLA, which holds three different beamlines (1064, 532 and 355 nm) with a pulse duration of about 10 ps. The beam output from the source is approximately 2 mm in diameter. A lens system that creates a Keplerian beam expander is located upstream of the scanning head.

The movement of the IR laser beam over the workpiece is obtained by means of a Raylase Superscan V galvanometric scanner, with a 15 mm aperture, coupled with a 104 mm F-theta lens. This assures a maximum working area of 46 $\times$ 46 mm^2 on the sample surface and a focused beam diameter of about 10 μm at

$1/e^2$ intensity, with an ellipticity of 90%. Similarly, the characteristics for the other processing lines are shown in Table 2. However, since the laser system is integrated with a 3-axis movement system, it is possible to integrate the work-table movement to increase the working area during the laser treatment. It is also possible to integrate focusing lenses with longer focal lengths, thanks to the system's height adjustment feature.

The beam monitoring systems are mobile and can be used both in the middle of the optical path and downstream in the working area.

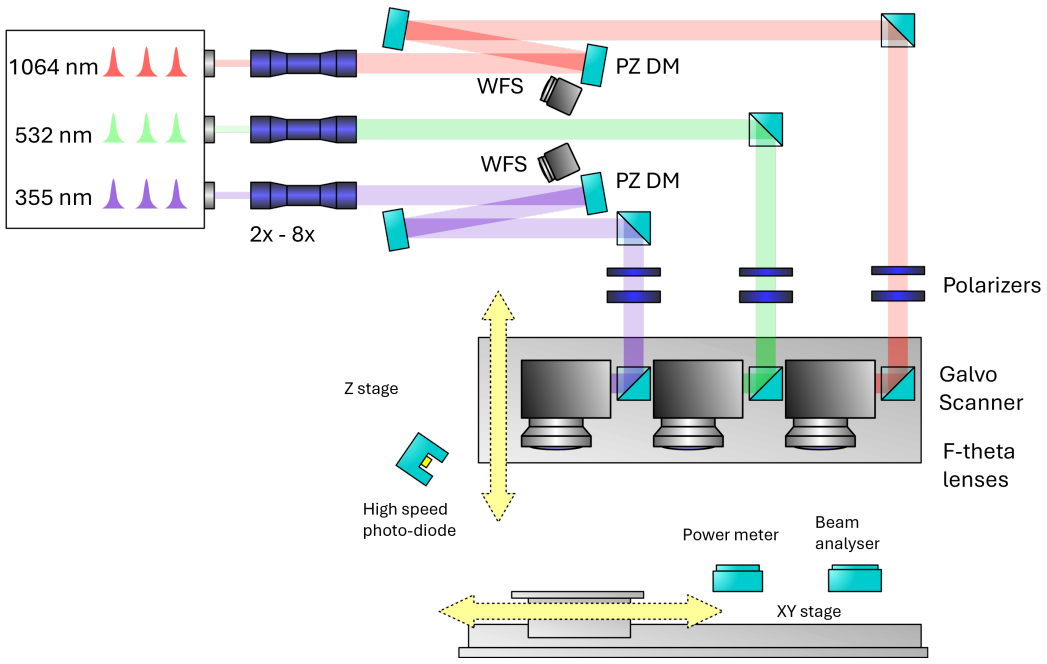

Figure 33: Laser system 2D scheme.

Table 2: Laser system elements.

Component	Model, Manufacturer	Characteristic	Value/Type
Picosecond Laser Source	Atlantic 50, Ekspla, Lithuania	Pulse Width [ps]	10
		Beam dimension [mm]	2
		Wavelength [nm]	(I) 1064 (II) 532 (III) 355
		Mazimum Power [W] @ 300 kHz	(I) 50 (II) 25 (III) 18
		Repetition Rate [kHz]	300-1000
Galvanometric scanning system	Superscan IV / V, Raylase, Germany	Deflection units	2-axis
		Max linear speed [m/s]	4.5
Focusing lens	S4LFT0080/121-126; 4401-509-000-21 F-Theta Lenses, Quioptiq / SillOptics, Germany	Aperture [mm]	15
		Type	Telecentric
		Working area [mm]	(I) 39x39 (II) 49x49 (III) 46x46
Rayguide Software	v2.14 2024, Raylase, Germany	Object	Dxf, bitmap, text, codes
		Mode	MOTF
Motion axes	Linear AEV120LB, Damo, Italy	X,Y [mm]	809, 309
		Max linear speed [mm/s]	30
	Optoprim, Italy	Z [mm]	300
		Max linear speed [mm/s]	3.5
	Rotational, Zolix, Japan	θ [°]	N*360
Beam Analysis Tools	BeamPro, Edmund Optics, USA	CMOS Beam Profiler	4.2 MP, 7mm
	Thermal Power Detector, Edmund Optics (R), USA	Power Meter, max power [W]	30
	Moku:Go, Liquid Instruments, Australia	Oscilloscope res. [GHz]	2
Adaptive Optics System	Dynamic Optics (c), Italy	Bimorph Deformable Mirror, Piezoelectric	32 radial actuator
		Wavefront Sensor	Shack-Hartmann
		Controller	Proportional-Integrative
		Photon Loop software	v2.2.3

A microprocessor-based laser power and energy meter designed for use with a wide range of detector heads, including photodiode power detectors from the PH series. It supports measurements from as low as 4 picowatts up to 30 watts, with selectable scales tailored to the sensitivity of the connected detector. The device provides ±0.5% accuracy from 20% to full scale and supports data transfer rates up to 15 Hz at 24-bit resolution. Its analog output is user-configurable, delivering a voltage proportional to the measured power, with a maximum output of 2.0 V and a refresh rate of 50 Hz.
Then, the Moku:Go of Liquid Instruments, a compact and portable FPGA-based test tool, integrates 14 instruments into a single device, including an oscilloscope, can be used to measure the repetition rate of the pulsed laser, view the general pulse train, and analyze pulse characteristics like peak voltage and rise/fall times. To analyze laser beam profiles across a wide spectral range, a Beamage beam profiling camera from Gentec-EO, a high-resolution CMOS-based instrument, is used. It has 4.2 megapixels and a 7 mm aperture, enabling precise measurements of beam shape, size, and stability. The camera supports UV, visible, and infrared wavelengths. To analyze high-power beam lines, filters that reflect part of the power can be placed in front of the sensor. Its software provides 2D, 3D, and cross-sectional displays, ISO-compliant measurements, and advanced features like background subtraction, beam tracking, M^2, and divergence angle analysis. This tool allows you to analyze the distribution of the collimated, i.e., unfocused beam, if not enlarged.

4.3 Beam Enlarger Analyzer for focused beam

The in-house system for analyzing beam distribution in the focal plane deserves a separate description. This is essential to obtain real feedback on the change in intensity distribution in the focal plane itself, given that the interference produced by a given shape cannot be measured elsewhere (see Chapter 3). Measuring the diameter and distribution of a very small focal spots in the focal plane is quite challenging. Using a CMOS camera directly for this purpose has two major drawbacks. First, there's a risk of damaging the camera sensor due to the high intensity of the beam, even when operating at low power. Second, the camera's

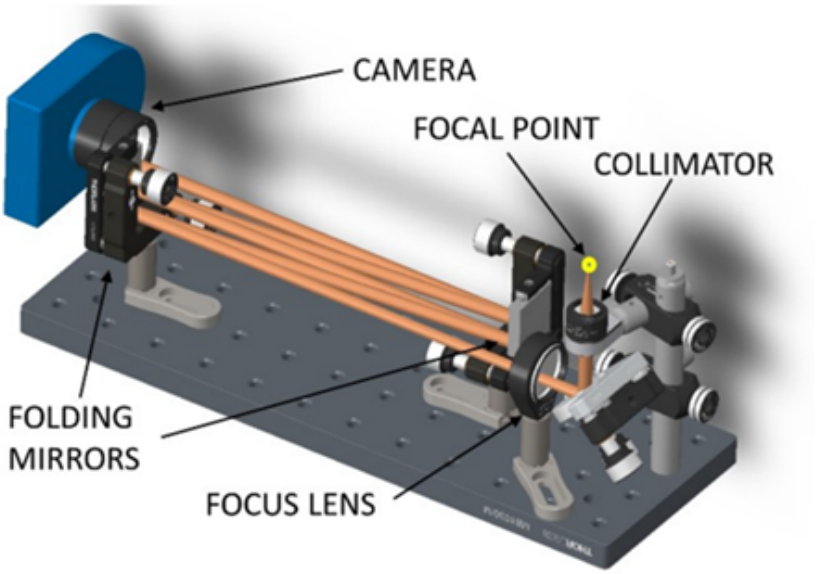

Figure 34: Beam Enlarger System scheme.

resolution is limited; its pixel size, typically between 3 and 5 micrometers, is nearly the same as the size of the focal spot, making accurate measurement difficult. To overcome these issues, a beam enlarger system was designed to allow for the precise evaluation of the beam's actual size and distribution. This system is built on a 100 × 300 mm² breadboard and includes several optical components: a collimating lens with a 30 mm focal length, a mirror to redirect the beam, a magnification lens with a 1000 mm focal length, two metallic folding mirrors to keep the setup compact, and a camera to capture the magnified beam (as shown in Figure 34). By applying a calibration factor of 1/30, i.e. 33x, and knowing the virtual pixel dimension of 181.5 nm, the system enabled accurate measurement of the beam's dimensions and shape. The system can be used with any wavelength based on the characteristics of the first collimating lens and the second focusing lens. Using an achromatic lens that focuses different wavelengths onto a single point makes the system very versatile. In this way, all three laser beams were measured accurately. To withstand different minimum powers, specific filters can be placed in front of the lenses, such as Reflective Neutral Density Filters with different optical densities from 0.1 to 4.0, see Figure 35.

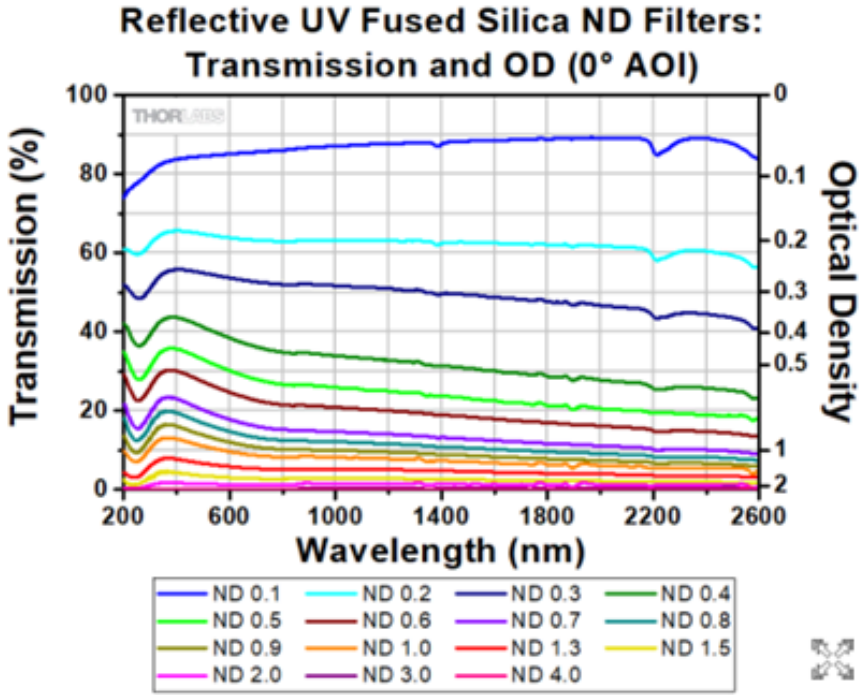

Figure 35: Reflective ND filters.[9]

It is essential to rationally adjust the exposure camera parameters, background noise removal, and laser beam power to obtain accurate measurements. Once a compromise has been found to display the beam distribution clearly, the Beamage camera software first fits the beam distribution with a Gaussian curve. The diameter can be measured using various methods, such as 4σ, FWHM, the $1/e^2$ method, 86%, or a custom method. The most used method in research is $1/e^2$, which measures the diameter that contains 86% of the total power, excluding the tails of the Gaussian distribution. Furthermore, it shows the actual intensity distribution of the beam as a percentage, fitted by a Gaussian curve, see Figure 36.

The results confirmed for almost all three wavelengths that the focused beam waist is approximately 10 μm over the workpiece, with a slight decrease for the green beam, with a certain ellipticity. In particular, IR shows an average diameter in two perpendicular directions of 10.9 μm and an ellipticity of 98%; green shows 8.4 μm with 82%, and UV shows 9.7 μm with an ellipticity of 90%,

[9] https://www.thorlabs.com/unmounted-uv-fused-silica-reflective-nd-filters?tabName=Overview

as illustrated in Figure 37. The quality of the first harmonic beam is generally higher, as it is not affected by secondary generation systems.
It is important to note that the intensity distribution of the beam can also be compromised by incorrect alignment, so it depends on the entire laser system. This is also the reason why interference fringes are evident around the main beam.

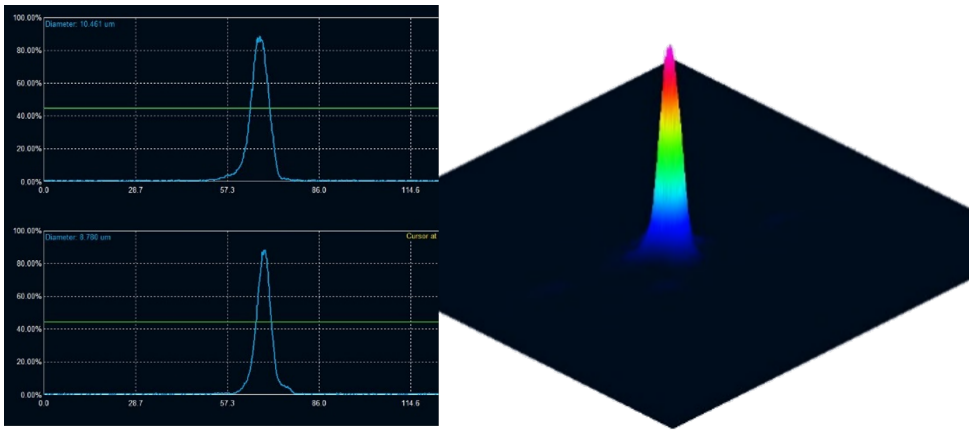

Figure 36: Gaussian beam profile from camera sensor.

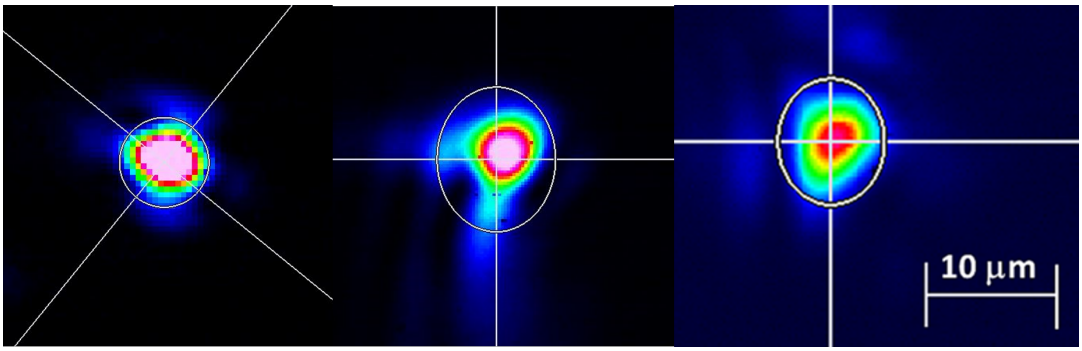

Figure 37: IR, GR, UV beam dimensions from camera sensor.

4.4 Collimated and expanded beam analysis

The Beamage beam profiling camera with an aperture of 7 mm cannot measure the 15 mm collimated beams. To overcome this limitation, a specific device is designed and implemented. To demonstrate the methodology of measuring the intensity of the 15 mm expanded collimated beam, the IDS UI3140-CP Camera is used in the system presented in Figure 38, which comprises a 16 mm Edmund Optics Macro lens, an adapter, and a Light diffuser. "Stitching Master" in-house

software is used to acquire the images, which is capable of reconstructing the beam profile from images acquired with different exposures to optimize the Signal to Noise Ratio for both the distribution peaks and the tails. In these cases, a total of 4 images are used.

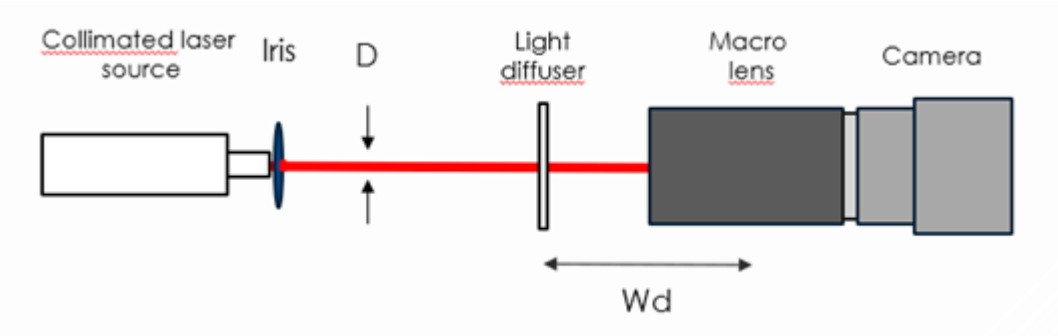

Figure 38: Large beam profiler scheme.

On the first harmonic, the results are in Figure 39, showing how the beam appears after the beam expander. The characteristic dimensions of the beam are asymmetrical, and the maximum is approximately 15 mm, so that it can enter the scanning head.

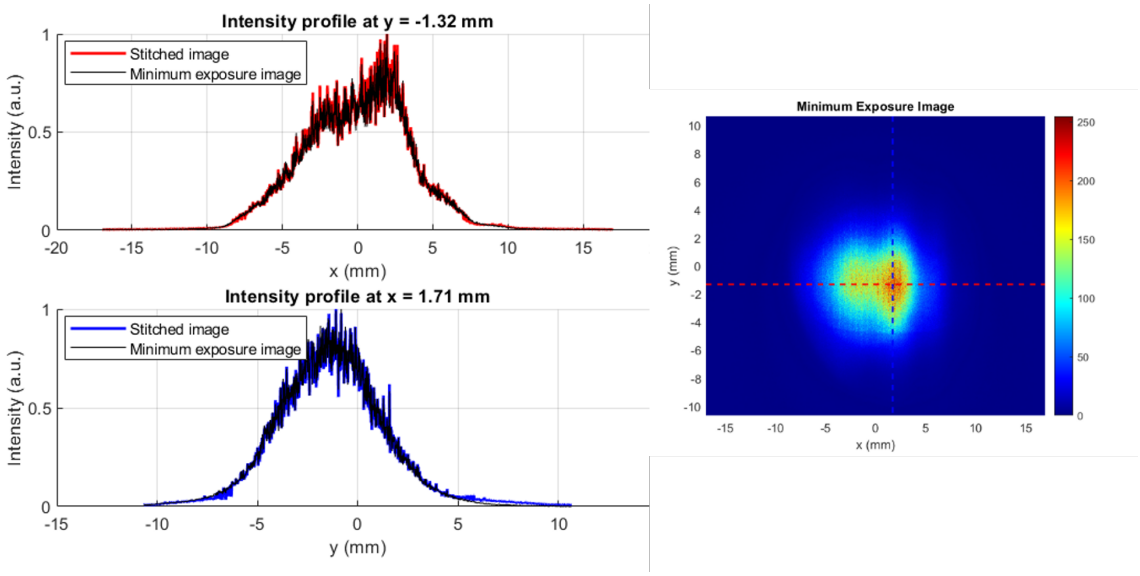

Figure 39: Expanded beam profile from large beam profiler.

To evaluate any changes in beam intensity due to the use of the beam expander, the profile obtained with the enlarged beam characterization system can be compared with the profile obtained by the 7 mm beam profiling camera before the beam expander. The profile recorded directly after exiting the laser with the 7 mm beam profiling is presented in Figure 40.
The intensity distribution of the beam is still highly asymmetrical. Apart from along the direction in which it fringes, the output beam remains 2 mm. This proved the methodology for characterizing the enlarged beam. These measurements were taken several months after those of the focused beam, and there is clear evidence of misalignment within the source, resulting in a beam that is no longer Gaussian. Interference patterns are created around the more energetic beam.

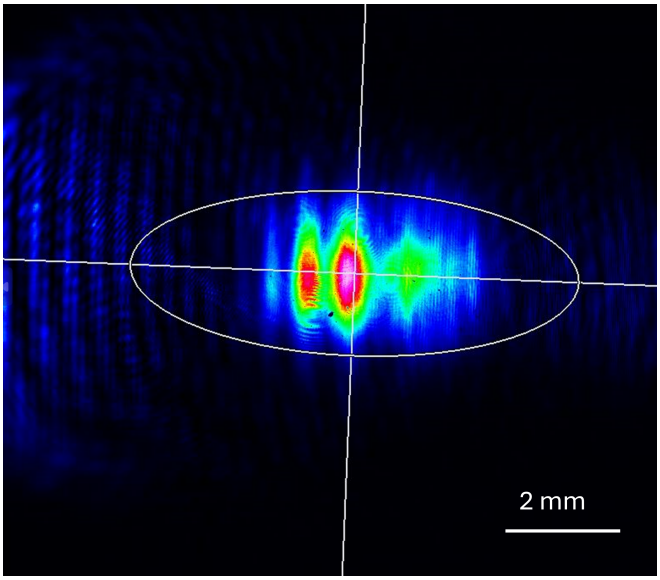

Figure 40: Non-expanded beam profile from 7 mm beam profiling camera for comparison.

4.5 Adaptive Optics system: deformable mirror

The adaptive optics system available comprises a deformable mirror (PZ DM), the wavefront sensor Monochrome Camera IDS UI-3060CP (WFS), the driver control, and the control software Photon Loop, from Dynamic Optics ©. Specifically, the wavefront sensor is equipped with a monochrome silicon-based detector,

without any color filters, ensuring high sensitivity across the visible and near-infrared spectrum. Figure 41 shows a photograph of the actual system on the optical table.
The deformable mirrors are piezoelectric bimorph DM_3215_1030 and the DM_-3215_355, respectively usable with the first and third harmonics to work the two extreme classes of materials. They have a reflective continuous surface controlled by 32 radial actuators. Mirror coating damage threshold guarantees operability with a high-power ultrashort laser, up to 1 kW without cooling, with a maximum of 15 mm diameter collimated incident beam. Soon, the deformable mirror will also be implemented on the second harmonic.
The wavefront sensor features a lenslet array with a 150 μm pitch and 5.2 mm focal length, enabling high-speed measurements at up to 500 frames per second, with an optional upgrade to 1 kHz. It operates with a 7 mm aperture and communicates via USB 3.0, supporting external triggering. The deformable mirror control system uses a Proportional-Integrative controller, calibrated through influence functions and Hadamard methods, and supports both open and closed loop configurations. The system is programmable via TCP-IP and compatible with deformable mirrors from other manufacturers.

The system is inserted into the optical path of the different wavelengths as follows:

- the deformable mirror is positioned like the other reflective mirrors;
- after the deformable mirror, the beam strikes a mirror at 0° which returns the beam to the path to the scanning head
- at the rear of the 0° mirror, a lens captures 0.5% of the transmitted beam power, further attenuated by a special filter, and focuses it at the focus of another lens;
- a second lens collimates the beam to a diameter that fits entirely within the wavefront sensor;
- finally, the wavefront sensor detects the wavefront of the beam in real time.

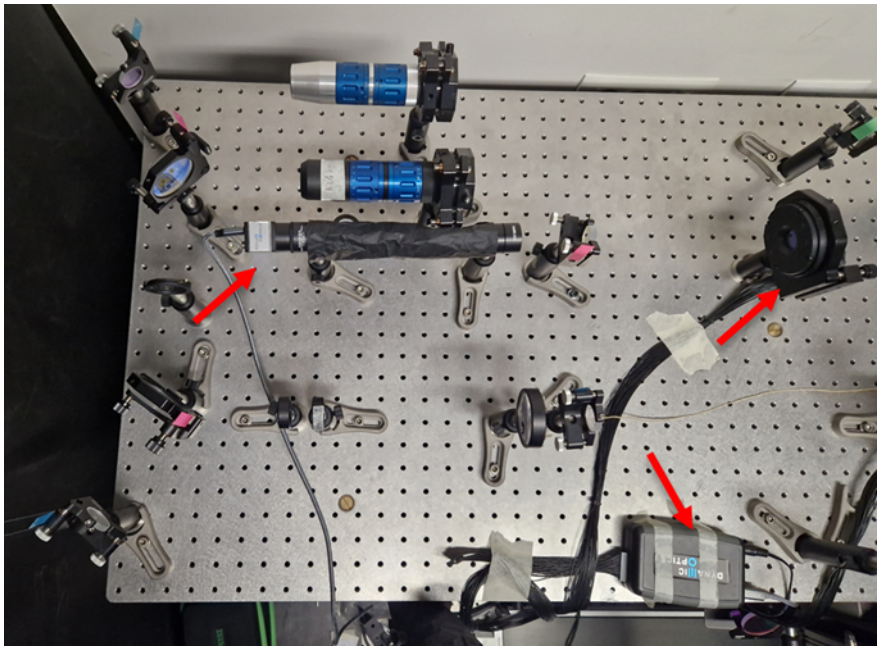

Figure 41: Adaptive Optics system picture.

As can be seen from Figure 41, the deformable mirror is connected to the driver, which in turn is connected to the PC on which the software is installed; the wavefront sensor is also connected to the PC. It is important that the beam points at the center of the deformable mirror, in order to follow a theoretical modeling of the beam, and that the surface of the mirror is entirely covered by the beam, so as to be able to modulate all the available actuators; in this way, we can work in optimal conditions. The deformable mirror can normally be used when switched off, with the surface completely "relaxed," and switched on only when a specific beam shape is required. However, when fully operational, it is useful to keep it switched on at all times and modify the beam shape as needed.
When implementing the optical path containing the adaptive optics system, it is necessary to calculate the position of the wavefront sensor to ensure that the wavefront is analyzed at the correct focal point for measurement. The optical system employed is based on a deformable mirror, two lenses that act as a telescope and point at the sensor. Specifically, the deformable mirror acts as the wavefront source, while the telescope creates the final image on the sensor, whose position depends on the distance between the lenses and their focal lengths. If the first lens forms an intermediate image, the second lens takes it as an object

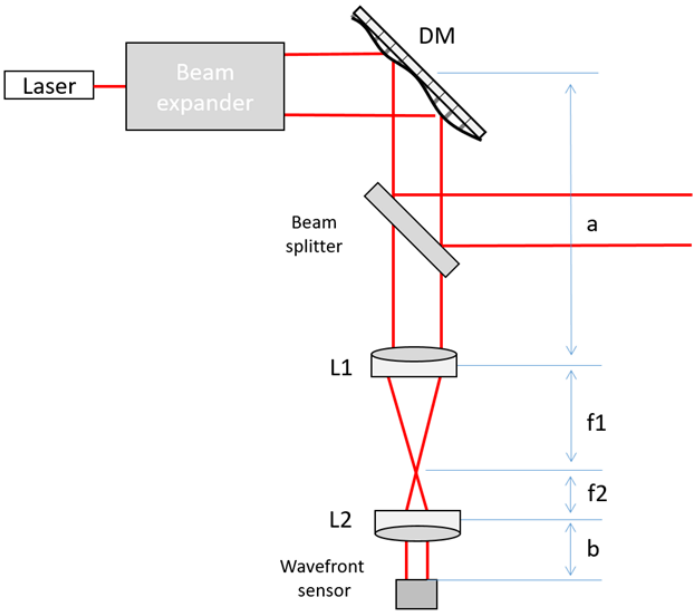

Figure 42: Theoretical wavefront sensor position calculation.

and forms the final image on the sensor, see Figure 42 and Equation 4.1.

$$b = \frac{f2(f1+f2) - f1f2\frac{a}{(a-f1)}}{f1 - f1\frac{a}{(a-f1)}} \tag{4.1}$$

Furthermore, to use the same wavefront sensor for all three harmonics, the sensor position can be calculated taking into account the translation of the wavefront through the optical system, the distance between sources that influence the geometry of the system, and the angular simplification that makes the calculation more direct, using the following formulas in the equations, as in Figure 43 and Equation 4.2.

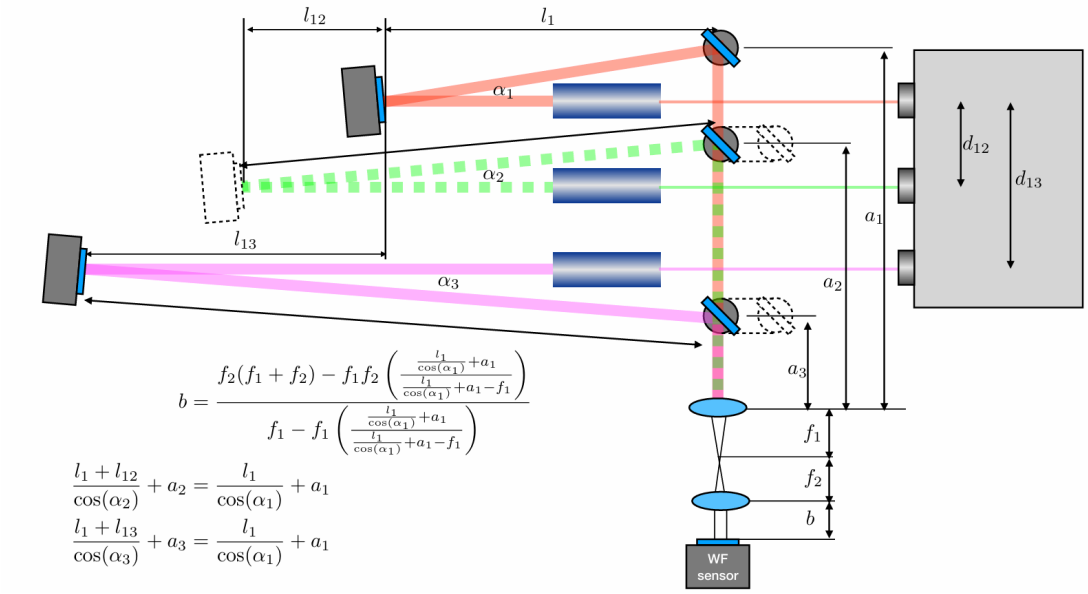

Figure 43: Real wavefront sensor position calculation.

$$\begin{cases} \alpha_1 \approx \alpha_2 \approx \alpha_3 \rightarrow \cos \alpha_i \approx 1 \\ b \approx \frac{f_2(f_1+f_2) - f_1 f_2 (\frac{l_1+\alpha_1}{l_1+\alpha_1-f_1})}{f_1 + f_1 \frac{l_1+\alpha_1}{l_1+\alpha_1-f_1}} \\ l_{12} \approx d_{12} \\ l_{13} \approx d_{13} \end{cases} \tag{4.2}$$

The beam shaping step-by-step procedure consists of turning on the deformable mirror, firing the laser into the deformable mirror and so in the beam enlarger analyzer, and live evaluating the shape of the focused beam through the software of the camera. Meanwhile, using the PhotonLoop software, the live wavefront can also be seen. Before using, the deformable mirror must be calibrated, and then the actuators can be moved to correct the wavefront.

After a first calibration performed by applying a small single-actuator excitation (commonly referred to as a "poke"), using a 50% dynamic range, an average over 20 frames, and a settling time of 0.1 seconds, the actuator modes, the corresponding influence functions, and a set of representative wavefronts generated in closed-loop configuration are reported in Figure 44. This figure provides a visual

summary of the calibration results: part (a) shows the individual actuator modes, each representing the localized deformation produced when a single actuator is excited, allowing verification of actuator uniformity and surface responsiveness; part (b) illustrates the influence functions, which describe how each actuator's deformation propagates across the continuous mirror surface and interacts with neighboring regions—information essential for constructing the control matrix; finally, part (c) displays examples of wavefronts generated in closed-loop operation, demonstrating the system's ability to accurately reproduce typical aberration modes once calibration is complete.

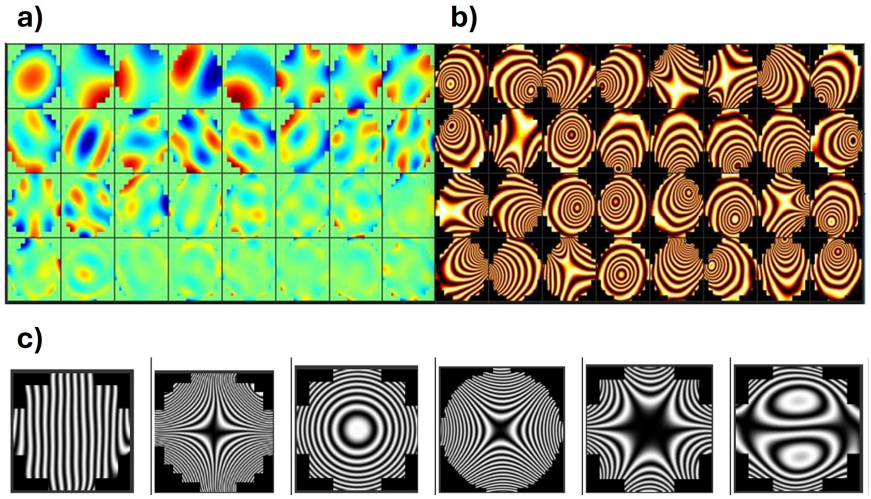

Figure 44: Deformable mirror calibration: a) actuator modes, b) influence function, and c) different wavefront obtained in closed-loop configuration.

Each time the mirror is used for the first time, it must be calibrated or reset, as its performance strictly depends on the shape of the beam, which is sensitive to even the slightest variations in ambient temperature and other factors. Alternatively, a calibration can be loaded if you are certain that the beam has not undergone any changes. After the calibration, the modes of the analyzed wavefront can be seen. Modes that are not well defined by the system can be removed, while the remaining ones can be used. Operating in open or closed loop control, it is possible to act directly on the actuators, modulating the values of the individual contributions of the Zernike decomposition through the RMS (root mean square) wavefront error in terms of wave fractions.

An example is shown in the figure, where the third harmonic ultraviolet beam has been deformed from Gaussian to an asymmetrical elliptical, characterized by a cylindrical wavefront. The offset values set are:

- **0.10 waves of defocus;**
- **0.49 waves oblique astigmatism;**
- **-0.57 waves vertical astigmatism.**

From the beam enlarger analyzer camera, it can be seen that the obtained beam has dimensions of 5.4x45.7 μm, with an ellipticity of 11.9%, see Figure 45.

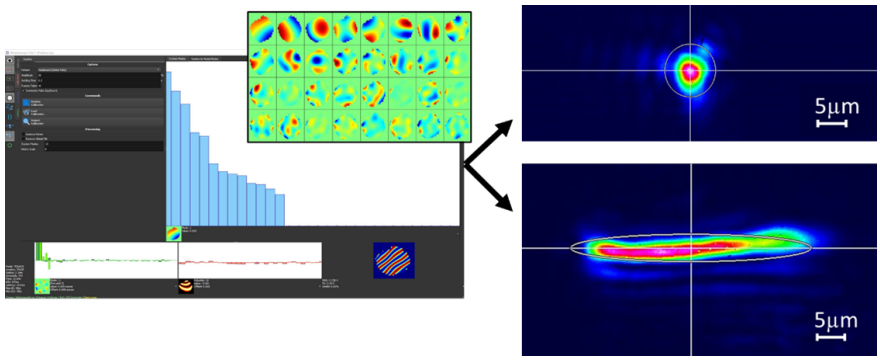

Figure 45: Beam shaping using adaptive optics example.

4.6 Hints of system integration

Everything that is achieved in Brightlab's experimental work cell is made possible by a considerable amount of system integration work.
The integration of ultrashort pulse laser systems for surface processing applications, such as marking and texturing, requires a precise orchestration of optics, electronics, and software components to ensure high fidelity and repeatability. Central to the system's control architecture is the SP-ICE-3 card, a high-performance controller developed by RAYLASE, which enables real-time coordination of laser emission and scanning head movement. It supports up to two axes and provides high-resolution position control via SL2-100 or RL3-100 protocols, with a step period of 10 μs and 20-bit resolution. The SP-ICE-3 also facilitates dynamic modulation of laser parameters based on velocity and po-

sition, making it ideal for precision applications such as microstructuring and ablation. Laser parameters are managed through a separate software interface, while custom software solutions developed in LabVIEW and Visual Studio C# bridge communication gaps, particularly in the absence of standardized connectors like X907. This integration facilitates automated execution of complex processing routines, including dynamic adjustment of pulse frequency, attenuation, and burst mode settings. The system architecture supports real-time power monitoring via a power meter, ensuring consistent output across varying environmental conditions. The modularity and programmability of the system allow for flexible adaptation to diverse experimental protocols, making it a robust platform for advanced laser processing.

An example is the generation of the “Rayguideexec” program developed within the LabVIEW environment, which serves as a bridge between the RAYGUIDE software suite and the SP-ICE-3 control card, enabling dynamic coordination of laser parameters and scanning head operations during real-time material processing. The program is designed to read and execute scanning project files generated by RAYGUIDE software, which contain geometric definitions and laser path trajectories. Each object within the project is associated with specific laser settings, referred to as "pens", that define parameters such as pulse frequency and attenuation. These pens can be independently assigned to object outlines and fillings, allowing for differentiated processing strategies within a single job.

Upon initialization, Rayguideexec performs a series of preparatory steps: it interrogates the SP-ICE-3 card to retrieve the IP address and correction file corresponding to the connected scan head, determines the appropriate harmonic based on the head type, and establishes communication with the laser source. This ensures that the laser operates with parameters coherent with the physical configuration of the system. The program then parses the scanning software file, extracting the laser settings for each object and executing them sequentially. Before each marking operation, the relevant laser parameters are set via direct communication with the laser control interface, overcoming the hardware limitation posed by the absence of an X907 connector in the experimental laser system. The execution logic is structured to handle both outline and filling operations separately, with parameter updates preceding each marking cycle. This modular

approach allows for precise control over proper energy delivery and spatial modulation, essential for achieving high-resolution surface features. At the conclusion of the job, the laser is safely disarmed, and all memory instances are cleared to prevent residual data conflicts. The Rayguideexec program thus provides a robust and scalable solution for integrating laser control with scan head coordination, significantly enhancing the flexibility and reliability of ultrashort pulse laser processing workflows.

To carry out one of the processes presented in the case studies, the use of automated firing and axis movement software was essential. The final application of the integrated approach was the surface texturing of tapping tools to enhance functional properties such as friction control, wear resistance, and fluid interaction.

The process involves the generation of rectangular dimples with controlled dimensions and depth, distributed across the circumferential and longitudinal development of the tool's thread, which will be addressed in section 5.2.2. These dimples are designed to enhance lubrication retention and tribological performance during machining.

The key facility lies in the software-driven coordination between laser firing and axis movement. The system integrates the laser source, scanning head, and multi-axis motion platform via C# libraries and LabVIEW, allowing synchronized control of the beam and mechanical positioning. This integration is fundamental for following the helical path of the thread, maintaining optimal focal height, and ensuring consistent dimple geometry across inclined surfaces, without doing it manually. First, position the rotator under the scan head, at the height corresponding to the focal plane on the material to be processed, as shown in Figure 46. Then, the process is executed in two stages: first, the laser textures the thread crest using a multi-level Z-axis approach, as shown in Figure 47; then, the tool is rotated incrementally while the X-axis shifts to follow the thread's helix, enabling full coverage of the surface. This method reduces mechanical repositioning and execution time, demonstrating the importance of software integration in achieving high-precision laser texturing on complex 3D surfaces. This approach demonstrated the system's capability to execute complex, multi-pass texturing routines on cylindrical components, validating its suitability for industrial ap-

plications requiring high precision and repeatability. This work was completed quickly, thanks to the teamwork and the interns at the Brightlab laboratory.

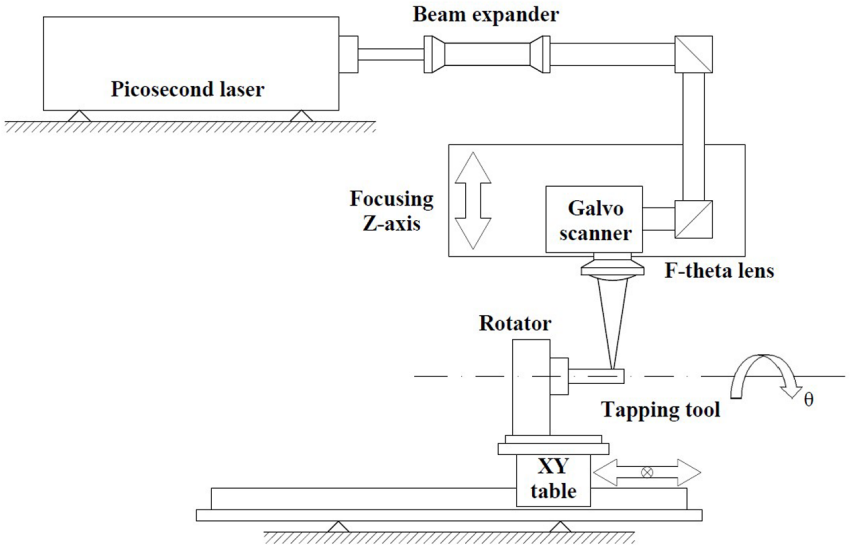

Figure 46: Example of integration of rotary-translational motion for machining threaded surfaces [40].

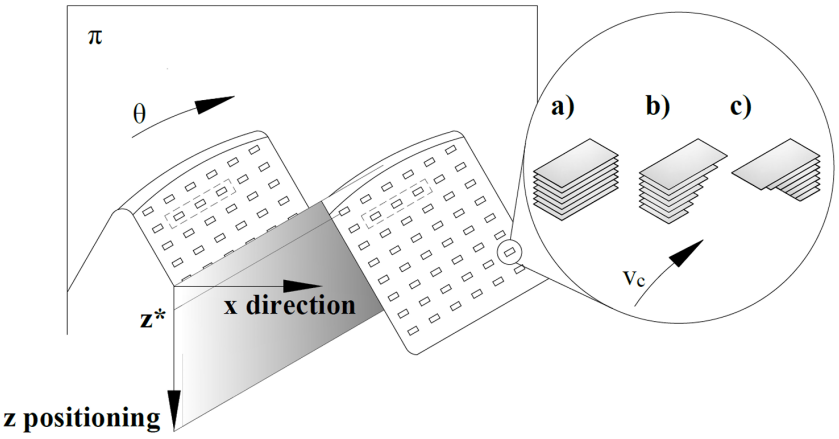

Figure 47: Diagram of the machining operations to be performed at different heights of the tooth [40].

5. Case Studies with Results

This chapter presents ten different case studies exploring the applications of the ultrashort picosecond laser system at the BrightLab laboratory at the Reggio Emilia Technopole in the processing of different classes of materials, each selected for its relevance to specific industrial and scientific objectives.

Thanks to the three wavelengths laser source available, the materials studied include metals, glass, polymers, ceramics, and biomaterials, processed under customized conditions to obtain functional results in tribology and biomedicine, microfluidics and optics, and computational modeling of ablation dynamics. For example, in tribological applications, laser-induced surface texturing is used to improve wear resistance and friction behavior, in particular through the generation of micro- and nano-scale patterns, such as dimples and grooves. In the biomedical field, ultrafast lasers are used to modify surfaces in order to improve cell adhesion, antibacterial properties, or controlled drug release, exploiting the precision and minimal thermal impact of ultrashort pulses. In the industrial sector, specific laser-textured surfaces are commercially available, as are industrial patents relating to the laser texturing process.

Additionally, ablation experiments are conducted to validate and refine numerical models that simulate laser-material interaction, providing predictive insights into energy deposition, material removal rates, and groove-morphological evolution

The case studies are presented in a matrix classification divided into metallic and non-metallic materials for ease of reading, see Table 3 and Table 4. In the two tables, the rows represent the different applications covered, while the columns represent the different materials processed.

Table 3: Case studies matrix: non metallic materials.

Applications \ Non metallic materials		Glass	Polymer	Zirconia/ Alumina	CFRP composites	Coated glass	CER-mets
Microprocessing (M)	Microfluidics	**355; direct**	355; direct	-	-	-	-
	Optics / Electronics Components	355; direct	**355; direct**	-	-	**532/ 1064; direct/ induced**	-
	Laser cleaning	355; direct	355; direct	355; direct/ induced	**355; direct/ induced**	-	1064; direct
Functionalization (F)	Modifying wettability	355; direct	**355; direct/ induced**	355/ 1064; direct	355/ 1064; direct/ induced	-	1064; direct
	Biocompatibility	355; direct	355; direct/ induced	355/ 1064; direct	-	-	-
	Tribology	-	-	355/ 1064; direct	-	-	**1064; direct**
	Adhesive bonding strength	-	**355; direct/ induced**	**1064; direct**	**355/ 1064; direct**	-	-
Both (M&F)	Mold microprocessing using AO	-	-	**355; direct**	-	-	-

The elements of the matrix contain information relating to the machinability conditions of a material for a given application: wavelength of the laser used, direct or induced machining. The solutions addressed in the case studies of this thesis are highlighted in bold; in other cases, where possible, a working hypothesis is provided. The last row of the matrix, for both non-metallic and metallic materials, represents the cases in which adaptive optics were actually used to increase productivity and processing quality, the results of which are reported in the last section of this chapter. However, it should be noted immediately that it can be used for all the proposed applications; therefore, the improvements are transferable to all the applications mentioned in the case studies.
The case studies are then classified into two broad families of laser processes for mere microfabrication, or for surface functionalization. However, the distinction is very blurry, as surface texturing for functionalization often involves surface micromachining. Indeed, the last application proposed incorporates both concepts, and adaptive optics has been applied to it as an example.
The numerous projects were made possible thanks to collaboration with other research groups within and outside the university, as well as various companies. The contribution of each will be specified on a case-by-case basis for clarity. These include the Fluid Dynamics Group, the Machine Design Group, the Medicine and Dentistry Group from the University of Modena and Reggio Emilia, the Machine Design Group from the University of Bologna, the Photonics Research Institute of Padua, the Technical University of Denmark, the University of Genoa, and the University of Calabria.

Table 4: Case studies matrix: metallic materials.

Applications \ Metallic materials		Bulk Titanium alloy	Steel	Brass	Copper	Aluminum	Magnesium	Sintered Titanium
Microprocessing (M)	Colorization via oxidation	1064; direct	**1064; direct**	**1064; direct**	**1064; direct**	**1064; direct**	1064; direct	**1064; direct**
	Laser cleaning	1064; direct	1064; direct	1064; direct	1064; direct	**1064; direct/ induced**	1064; direct	1064; direct
	Simulation	**1064; direct**	**1064; direct**	1064; direct	1064; direct	**1064; direct**	1064; direct	-
Functionalization (F)	Modifying wettability	**1064; direct/ induced**	**1064; direct/ induced**	1064; direct	1064; direct/ induced	**1064; direct/ induced**	1064; direct	532/ 1064; direct/ induced
	Biocompatibility	**532/ 1064; direct/ induced**	**532/ 1064; direct/ induced**	-	-	-	1064; direct	1064; direct
	Tribology	532/ 1064; direct/ induced	**532/ 1064; direct/ induced**	1064; direct	1064; direct	1064; direct	1064; direct/ induced	-
	Adhesive bonding strength	532/ 1064; direct/ induced	532/ 1064; direct/ induced	532/ 1064; direct/ induced	1064; direct/ induced	**1064; direct/ induced**	**1064; direct/ induced**	532/ 1064; direct/ induced
	Enhancing electrochemistry	-	532/ 1064; direct/ induced	-	**1064; direct/ induced**	-	-	**532/ 1064; direct/ induced**
Both (M&F)	Mold microprocessing using AO	532/ 1064; direct/ induced	**532/ 1064; direct/ induced**	-	-	-	-	-

5.1 Characterization methods

Characterization plays a pivotal role in understanding the effects of laser micromachining and surface modification, as it provides the link between processing parameters, induced micro/nanostructures, and the resulting functional properties. Laser texturing can significantly alter surface morphology, chemistry, and wettability, which in turn influence adhesion, tribological behavior, and other application-specific performances. Therefore, a comprehensive characterization strategy is essential to capture these multi-scale and multi-physics changes.
An effective approach integrates morphological, chemical, and functional analyses to establish correlations between surface features and material performance. Morphological evaluation reveals the geometry and hierarchical structure generated by laser interaction, while chemical analysis identifies compositional changes such as oxidation or phase transformations. Functional characterization assesses properties like wettability and adhesion, which are critical for practical applications.
To achieve this, complementary techniques are employed, which will be explained below. By combining these methods, it is possible to holistically understand how laser-induced surface modifications influence material properties and optimize processing strategies for targeted functionalities.

5.1.1 Metallographic specimen preparation

Sample preparation typically followed the metallographic procedures, including cutting, polishing, and cleaning. The cutting machine used is a Remet compact bench-top cutting machine, model TR 80 E, featuring a stainless steel structure and a maximum cutting diameter of 80 mm.
After cutting and hot-mounting, sequential polishing using abrasive papers and smooth cloths to achieve a mirror-like finish is done. High-quality SiC or Al2O3-based grinding paper Akasel Rhaco Grit are used for soft and ductile material: from P80-P320 are used for plane grinding, while from P600-P1200 are used for fine grinding. For mirror polishing, polishing cloths with 2-in-1 diamond suspension are used, carefully balanced mixtures of diamond suspension and lubricant with median values of 9-3-1 μm.

Finally, ultrasonic cleaning allows the removal of any contaminants such as grease, oil, polishing paste, and dust from metal and non-metal samples. The liquids used for cleaning are distilled water, acetone, ethanol, and isopropanol, chosen according to the material to be cleaned.
When cross-sectional analysis was required, samples were embedded in polymer resin using hot mounting. The embedding machine used is a Remet IPA 30, pneumatically operated. It quickly produces compliant inclusions of metallographic samples with any type of thermosetting or thermoplastic resin. The entire work cycle is managed by an easily programmable microprocessor, in which the maximum temperature to be reached and the time to remain at that temperature are set. It is also possible to adjust the compaction and cross-linking pressure slightly from the standard setting of 6-7 bar.

5.1.2 Morphological characterization

Morphological characterization was performed at multiple scales: stereoscopic inspection and an optical microscope with up to 1000x digital magnification were used as initial feedback on board, while high-resolution imaging was achieved with a scanning electron microscope.
The Zeiss Stemi 2000-C stereo-microscope has a zoom range of 0.65x -5.0x. The trinocular viewing head allows for adding a camera to this microscope. This comes on a plain focusing stand. Stereoscopic viewing gives the sensation of relief with the observation of flat images alone. In addition, color images retain the original chromatic information, which is useful in applications such as laser colorization.
Nikon Eclipse LV100ND industrial optical microscope is equipped with Nikon CFI60-2 optical system, which combines high numerical aperture (NA) with long working distance objectives to deliver bright, high-contrast images while minimizing chromatic aberration. This configuration supports multiple observation modes, including brightfield, darkfield, differential interference contrast (DIC), polarizing, epifluorescence, and two-beam interferometry, enabling versatile analysis of diverse surface conditions. The microscope features a modular design with motorized or manual nosepieces and illumination systems, allowing quick adaptation to different sample types and inspection requirements. Illumi-

nation is provided by a centered halogen or LED lamp, optimized for uniform light distribution and enhanced contrast. Objective lenses range from 5x to 100x magnification, offering flexibility for both low-magnification overview and high-magnification detail inspection. Integrated compatibility with Digital Sight cameras and NIS-Elements imaging software enables real-time image acquisition, extended depth-of-focus imaging, and basic measurement functions such as line distance and area calculation. These capabilities make the LV100ND an ideal tool for immediate visual assessment of laser-textured surfaces directly at the processing station, ensuring fast feedback on morphology, defect detection, and process consistency without the need for sample transfer to high-end analytical instruments.

Detailed surface morphology and compositional analysis were performed using a Nova NanoSEM 450 Field Emission Gun (FEG) Scanning Electron Microscope (FEI Company – Bruker Corporation). This instrument provides high-resolution imaging down to the nanometer scale ($\approx$1 nm) through electron beam scanning, enabling detailed visualization of micro- and nano-structures generated by laser processing. The system is equipped with multiple detectors for versatile imaging and analysis: In-lens SE (TLD-SE) and BSE (TLD-BSE) detectors for secondary and backscattered electron signals in both high and low vacuum modes, a solid-state BSED (GAD) for low vacuum operation, and a STEM detector for transmission electron imaging. Additional capabilities include IR-CCD for infrared imaging and a 6-channel EBIC detector for electrical contrast analysis in conductive and semiconductor samples. The microscope supports high vacuum mode for conductive samples and low vacuum mode ($\leq$ 1.5 Torr) for non-conductive specimens without prior metallization, using gas ionization for charge compensation. This feature is essential for analyzing glass, polymeric, and composite materials without introducing artifacts.

5.1.3 Topographical characterization

Surface topography and nanoscale characterization were performed using an Autoprobe CP Atomic Force Microscope (Veeco – 2M Strumenti), which enables high-resolution imaging of surface morphology and physicochemical properties through probe–sample interactions. The system is equipped with interchange-

able scanners providing measurement ranges of 5 μm and 100 μm, allowing both localized and extended area analysis. Vertical resolution is below the angstrom scale, while lateral resolution can reach the order of angstroms, making the instrument suitable for detecting nano-structured features. The AFM supports multiple operational modes, including contact, non-contact, and tapping mode, as well as advanced techniques such as lateral force microscopy, force and phase modulation, and Kelvin probe microscopy for mapping surface potential. Dedicated kits enable magnetic and electrical property measurements, while a liquid cell allows imaging of samples immersed in fluids, expanding its applicability to polymeric and biomedical materials. Sample positioning is facilitated by an integrated optical microscope with a color camera, and measurements are stabilized by a Newport SHP anti-vibration table to minimize environmental noise. Data acquisition and analysis are managed through PROSCAN software, enabling quantitative extraction of roughness parameters, phase contrast, and force curves. These capabilities are essential for correlating micro/nanostructures with functional properties such as wettability and adhesion.

For the initial studies, when nanometric vertical resolution was not required, three-dimensional surface characterization and optical analysis were performed using a Leica TCS SP8 confocal microscope, equipped with advanced modules for super-resolution and fluorescence lifetime imaging. The system is built on a Leica DMi8 inverted research platform with motorized XYZ stage and adaptive focus control (AFC), supporting high-precision positioning and automated acquisition. Objectives range from 10x to 100x oil immersion, enabling flexible magnification and high numerical aperture for optimal resolution. The scanning head integrates four fluorescence detection channels (PMT and HyD hybrid detectors) and one transmitted light channel, combined with an Acousto-Optical Beam Splitter (AOBS) for programmable spectral separation and an Acousto-Optical Tunable Filter (AOTF) for independent laser line attenuation. The system includes a white light laser (WLL) providing up to eight simultaneous excitation lines between 470–650 nm, and a 405 nm diode laser for UV excitation. Spectral analysis is supported by Lambda and Lambda^2 scanning with 10 nm resolution, allowing precise emission profiling. For super-resolution imaging, the instrument features STED 3X technology with a pulsed depletion laser at 775

nm, achieving lateral resolutions below 100 nm and enabling 3D (xyz) nanoscale visualization of complex surface structures. Additionally, the FLIM module (PicoQuant) provides fluorescence lifetime imaging on two simultaneous channels, offering chemical and environmental information. The system supports multicolor analysis, time-lapse experiments, and mosaic imaging, making it suitable for reconstructing large areas and performing dynamic studies. These capabilities are particularly relevant for obtaining high-resolution three-dimensional profiles of structures created with lasers, but even more so for evaluating the optical properties or biological functionality modified by the processing.

Subsequently, surface topography in more than one study was quantified using a Confovis structured light confocal profilometer integrated with a Nikon Eclipse LV150N optical microscope, an instrument designed to provide 3D maps and roughness parameters according to ISO 25178. It employs Structured Illumination Microscopy (SIM) technology for high-precision, non-contact 3D measurements. The profilometer provides true three-dimensional imaging of the specimen surface, which is processed using MountainsMap® software (Digital Surf) for quantitative evaluation of roughness parameters according to ISO 25178-2:2021 Geometrical Product Specifications (GPS). An automated XYZ motorized stage allows accurate positioning and repeatability. The system includes an adjustable confocal pinhole and a structured illumination camera to minimize optical aberrations and enhance depth resolution. Surface profiles can be filtered using a robust Gaussian filter to separate large-scale waviness from fine-scale roughness. The primary parameter considered was the arithmetic mean height (Sa), the maximum height (Sz), the root-mean-square height (Sq), the skewness (Ssk), and the kurtosis (Sku), which are calculated as the average of multiple measurements per sample.

Finally, profilometry for 3D surface mapping was performed using a Keyence VHX digital microscope equipped with an autofocusing module and advanced structured illumination capabilities. This system provides a digital resolution of 0.1 μm, enabling high-definition visualization of microgrooves, hierarchical textures, and fine surface details that are often undetectable with conventional optical microscopy. The instrument supports magnifications ranging from 100× to 2500× through two high-resolution objectives (100–500× and 500–2500×), al-

lowing flexible observation of both micro-scale and nano-scale features. The VHX microscope integrates multi-directional illumination modes to enhance contrast and reveal subtle surface irregularities, combined with a fully motorized stage for automated scanning and image acquisition. Its large 300 mm sample platform accommodates wafers and oversized components, making it suitable for industrial and research applications. The system includes advanced imaging functions such as metallurgical analysis, elemental inspection, image comparison, and automated measurement routines, supported by proprietary software for real-time image processing and data management. Although the instrument does not provide standardized roughness parameters according to ISO norms, its capability to generate high-resolution 3D reconstructions and depth profiles makes it an effective tool for automated quantitative assessment of surface topography.

5.1.4 Chemical characterization

Chemical and crystallographic characterization of laser-treated surfaces was performed using the Bruker QUANTAX-200 EDS system integrated into the Nova NanoSEM 450 platform. The EDS system employs an XFlash 6 silicon drift detector (10 mm^2 active area, 126 eV energy resolution), enabling high-sensitivity detection of elements with atomic number $Z > 8$. This configuration supports qualitative and quantitative elemental analysis, global spectra acquisition, and advanced mapping and line scan functionalities. Global EDS spectra were acquired over different integration periods, while elemental mapping was conducted for several minutes per area, repeated across multiple regions to ensure representativeness. These measurements provide detailed information on laser-induced chemical modifications such as oxidation or contamination.

For crystallographic analysis, the SEM is equipped with an EBSD module (Bruker QC-200i) featuring an e-Flash1000 detector, which enables phase identification and orientation mapping at high spatial resolution. EBSD data were processed using the Quantax ICSD database, allowing correlation between microstructural changes and laser processing parameters. The combined EDS–EBSD approach offers a comprehensive understanding of both chemical composition and crystallographic texture, which is essential to evaluate the functional impact of laser-induced surface modifications.

While EDS is used to evaluate the presence of individual chemical elements, Raman spectroscopy is used to reveal the chemical formula of the compounds present on the surface. For this reason, chemical characterization also included Raman spectroscopy using a LabRAM HR Evolution Raman spectrometer (Horiba), a high-performance system designed for confocal Raman imaging and spectroscopy. The instrument is equipped with multiple excitation sources to cover a broad spectral range and optimize analysis of diverse materials: a solid-state diode laser at 473 nm (25 mW), an Nd:YAG laser at 532 nm (100 mW), a He-Ne laser at 632.81 nm (21 mW), and a solid-state laser at 785 nm (100 mW). This configuration enables flexible selection of excitation wavelengths to minimize fluorescence interference and maximize Raman signal intensity for different sample types. The spectrometer incorporates high-resolution diffraction gratings (600 and 1800 g/mm) and a confocal pinhole adjustable from 0 to 1500 μm, ensuring precise depth discrimination and spatial resolution for microstructural analysis. Coupled with an Olympus BXFM-ILHS microscope featuring objectives from 5x to 100x (including long working distance options), the system supports detailed imaging and mapping of surface features. A motorized XYZ stage enables automated acquisition of 3D Raman maps and line profiles, while the autofocus function (optical or spectral) ensures optimal focus during extended scans. Detection is achieved through a front-illuminated CCD detector (spectral range 200–1100 nm) with Peltier cooling for low-noise performance, providing high sensitivity for weak Raman signals. The system also includes a multipass cell holder for liquid or bulky samples and an epifluorescence module, expanding its versatility for complex materials. Advanced software allows spectral deconvolution, baseline correction, and quantitative analysis of vibrational modes, enabling identification of chemical phases, crystallinity, and stress states. These capabilities allow correlation between processing parameters and chemical modifications such as oxide formation, phase transitions, and molecular structure changes at the microscale.

5.1.5 Wettability and other functional characterization

Wettability was assessed through two complementary approaches: qualitative tests using ethanol-based test inks and quantitative sessile drop measurements using a Dataphysics SCA20 contact angle system.
Surface energy evaluation was performed using Plasmatreat GmbH ethanol-based test inks, prepared according to DIN 53914/ISO 304:1985 standards. This method provides a rapid and reliable estimation of the wettability of solid substrates by determining their critical surface tension. The inks are available in a calibrated series with defined surface tension values (e.g., 28–72 mN/m), enabling stepwise assessment of surface energy. The procedure consists of applying a thin stroke of test ink to the treated surface using the integrated brush applicator. If the stroke contracts within two seconds, a lower surface tension ink is applied until a stable stroke is observed for at least two seconds. The surface energy of the material is considered equal to the last ink value that exhibited stable wetting. This approach allows precise determination of wettability immediately after laser processing, providing essential feedback on surface activation and functionalization. Plasmatreat inks are suitable for a wide range of substrates, including polymers, metals, glass, ceramics, and composite materials, and are widely used in industrial applications for adhesion promotion and quality control. To ensure accuracy, inks were used in their original, uncontaminated form and stored according to manufacturer recommendations to prevent evaporation-related changes in composition. This qualitative method offers a fast and standardized evaluation of surface energy.
Surface wettability was quantitatively assessed using a Dataphysics OCA20 contact angle goniometer, a precision instrument designed for static and dynamic contact angle measurements. The system operates by depositing a liquid droplet of known volume onto the sample surface using a high-precision dosing needle, ensuring reproducibility and control over droplet size. An integrated high-resolution imaging system captures the droplet profile immediately after deposition and during its evolution over time, enabling accurate determination of left and right contact angles through advanced image analysis algorithms. The measurement principle is based on the balance between adhesive and cohesive

forces at the solid–liquid interface, expressed as the contact angle. Surfaces exhibiting low contact angles (<90°) are classified as hydrophilic, indicating high wettability, whereas high contact angles (>90°) correspond to hydrophobic or superhydrophobic behavior. This parameter provides a direct quantitative indicator of surface functionality, particularly relevant for evaluating the effects of laser texturing on wetting properties. The OCA20 system supports time-dependent studies, allowing monitoring of droplet spreading or absorption, and can be configured for sessile drop, tilting plate, and dynamic measurements.
More specific functional analyses used to validate the various case studies were entrusted to research groups both within and outside the university, as well as to a number of companies, with whom the various projects were carried out in collaboration. These will be explained in detail in the relevant sections.

5.2 Laser precise and selective microfabrication

5.2.1 Glass microfluidic device

Microfluidic technology has revolutionized biomedical and pharmaceutical research by enabling precise manipulation of fluids at the microscale for applications such as drug delivery systems, point-of-care diagnostic kits, nanoparticle synthesis, and organ-on-chip platforms. These devices typically incorporate channels and chambers ranging in size from a few micrometers to hundreds of micrometers, allowing for the controlled transport, mixing, and reaction of fluids. Their versatility supports critical processes in nanomedicine, including high-throughput screening and controlled encapsulation of biomolecules, making them indispensable in modern healthcare and chemical engineering.
Despite their potential, conventional fabrication methods, such as photolithography, wet etching, and molding, pose significant limitations. Glass and silicon, which are historically used for microfluidic chips, require cleanroom environments, lithographic masks, and hazardous chemicals, resulting in high costs and lengthy lead times. Polydimethylsiloxane (PDMS) emerged as a popular alternative due to its ease of molding and optical transparency; however, PDMS suffers from gas permeability, limited solvent compatibility, and mechanical instability, restricting its use in aggressive chemical environments or high-temperature

applications [41, 42]. For instance, PDMS-based microreactors cannot reliably handle highly soluble organic solvents, necessitating the use of glass or silicon for certain drug formulation processes. Glass substrates, in contrast, offer superior chemical resistance, thermal stability, and dimensional accuracy, making them ideal for robust microfluidic systems, particularly in diagnostics and pharmaceutical manufacturing [43, 44]

To address the limitations of traditional techniques, ultrafast laser micromanufacturing has emerged as a transformative solution. Ultrafast lasers operating in the picosecond or femtosecond regime enable direct writing of microchannels on glass without masks or chemical etchants, drastically reducing process complexity and environmental impact. Their ability to induce multiphoton absorption in transparent materials allows precise ablation with minimal heat-affected zones, ensuring high geometric accuracy and preserving material integrity [4, 45]. Furthermore, laser texturing can tailor surface properties such as wettability, which is critical for controlling capillary-driven fluid flow in microchannels [46]. Complex geometries—such as Y-shaped mixers, forked channels, and multi-depth reservoirs—can be fabricated with quasi-vertical sidewalls, enabling advanced designs for microfluidic mixing and droplet generation [44, 47].

Beyond channel creation, laser-based processes integrate seamlessly with thermal diffusion bonding, eliminating adhesives and intermediate layers that risk contaminating channels or obstructing fluid flow. This approach ensures chemical purity and mechanical strength, paving the way for scalable production of sealed glass microfluidic devices [47, 48]. By combining precision, flexibility, and speed, ultrafast laser micromanufacturing bridges the gap between rapid prototyping and industrial-scale production, positioning itself as a cornerstone technology for next-generation microfluidic systems.

The first case study evaluates a rapid, maskless process chain for prototyping a glass microfluidic micromixer fabricated by picosecond laser ablation and sealed by plasma bonding with pre-cured silicone. The aim is to quantify fabrication accuracy, bonding robustness, and mixing efficiency (ME) under laminar flow, and to benchmark experimental results against CFD simulations for design validation in biomedical contexts (e.g., protein assays and acid–base mixing). Devices were fabricated on standard glass slides (76x26x1 mm).

Different complex geometries typical of microfluidic devices can be obtained on the glass slider, as visible in Figure 48.

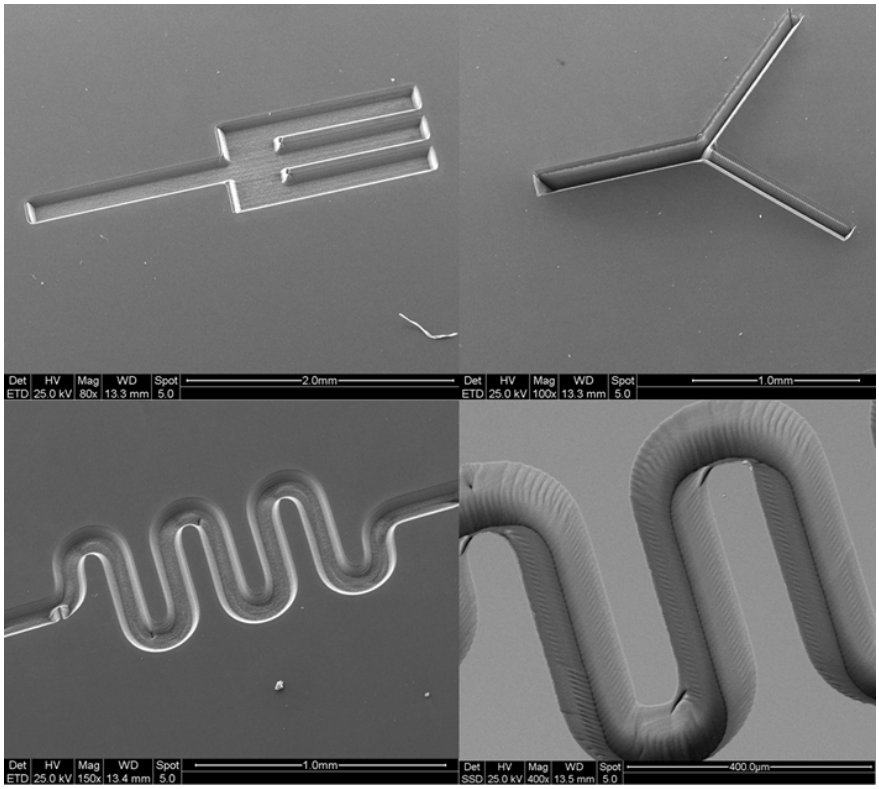

Figure 48: Microfluidic channel on glass example [49].

The chosen device design included a staggered herringbone geometry, a well-established passive mixing strategy that promotes chaotic advection in laminar flows, thereby enhancing mixing efficiency without external actuation. It consisted of a 200 μm-wide main channel with Staggered Herringbone (SH) grooves (groove height $\approx$ 30 μm, pitch $\approx$ 45 μm, angle $\approx$ 60°), flanked by Y-shaped inlet and outlet branches; inlet/outlet through-holes ($\approx$2 mm ϕ) were laser-drilled directly in the glass. The design is presented in Figure 49, while the functionality is explained in Figure 50

A similar SH geometry and dimensional ranges (channel depth 70–80 μm; groove height 30–35 μm) were realized in prior experiments and used as the basis for CFD model derivation [50].

The microfluidic circuit, including “herringbone” structures, was engraved di-

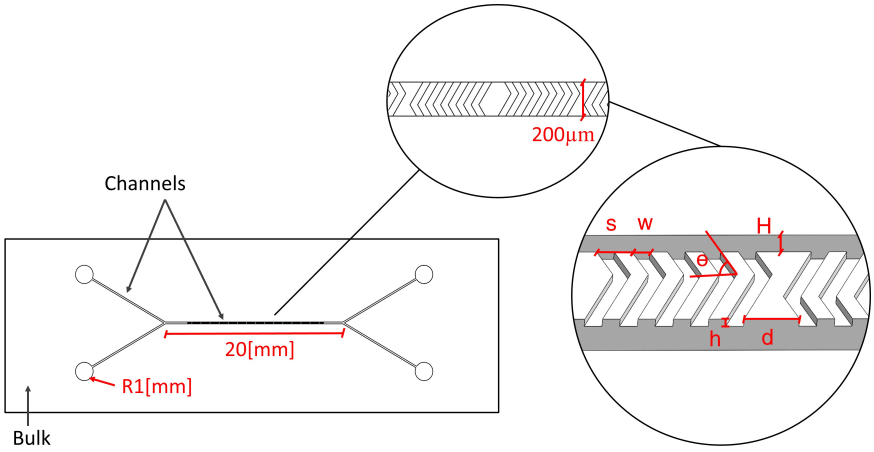

Figure 49: Micromixer with herringbone design [51].

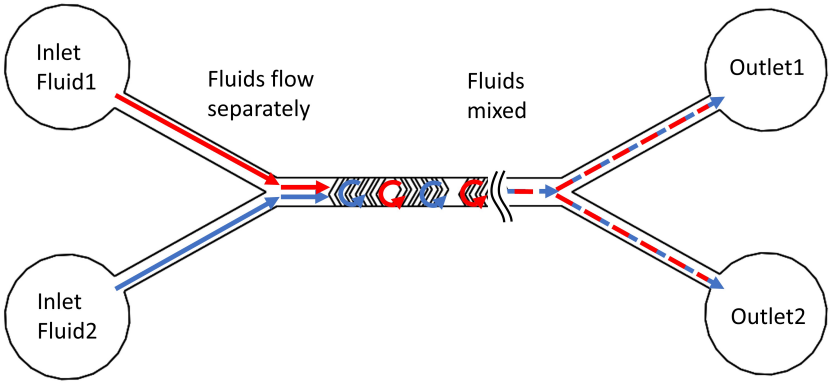

Figure 50: Micromixer functionality scheme [51].

rectly onto the glass substrate using the 355 nm wavelength laser light, which is easily absorbed by glass. For the main channels, the laser parameters chosen are 100 kHz of repetition rate, a pulse energy of 7 μJ, a scan strategy made of parallel longitudinal lines 3 μm spaced, and a scan speed of 300 mm/s to equally distribute the energy along and between the scanlines, all repeated for 11 passes. For the herringbones, the same parameters were chosen, but with 6 passes. The total process time is about 5 minutes: the seats are the largest and slowest feature to manufacture. The drilled holes are made on the 1 mm thick glass using a 5 μm spaced spiral scanned at 2500 mm/s, 300 kHz, and 16 μJ in about 1.5 minutes per drill. They are summarized in Table 5. The automated procedure consists of slowly lowering the scan head while performing the spiral

Table 5: Laser parameter for herringbone micromixer.

UV (355 nm)	**Scanning strategy**	**Frequency [kHz]**	**Mark speed [mm/s]**	**Overlap [%]**	**Power [W]**	**Passes [-]**	**Fluence [J/cm^2]**
Main Groove	Parallel lines	100	300	70	0.77	11	9.8
V groove	Parallel lines	100	300	70	0.77	6	9.8
Holes	Spiral	300	2500	50	4.8	Cont.	20.38

to change the focal height and achieve breakage. Furthermore, in this way, all the processing steps are made on a single glass slide. The process is carried out by holding the glass suspended to avoid unwanted reflections.

Engraved features were assessed by SEM to confirm edge sharpness and wall quality, and by confocal microscopy to reconstruct cross-sections and measure depths and wall inclination. Surfaces exhibited micro-/sub-micrometer roughness characteristic of ultrashort-pulse ablation, as visible in Figure 51; typical measured depths were ≈ 80 μm (main channel) and $\approx$ 30–35 μm (SH grooves), with wall inclinations on the order of $\approx 25°$ for narrow grooves, see Figure 52. Laser-ablated channels demonstrated a U-shaped profile with some deviation from the ideal CAD geometry due to wall inclination and surface roughness of the laser-treated material.

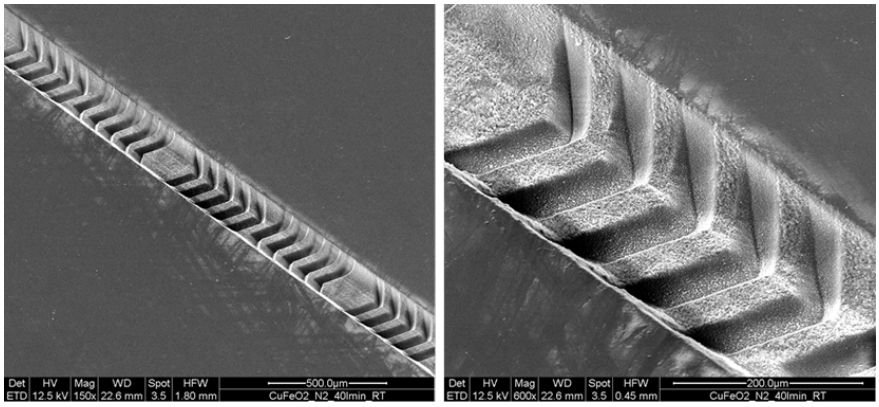

Figure 51: SEM images of herringbone micromixer device [51].

The circuits were sealed by plasma bonding a 3 mm pre-cured silicone layer (L/SF Silicone FDA) to the laser-processed glass. Surface activation (air plasma,

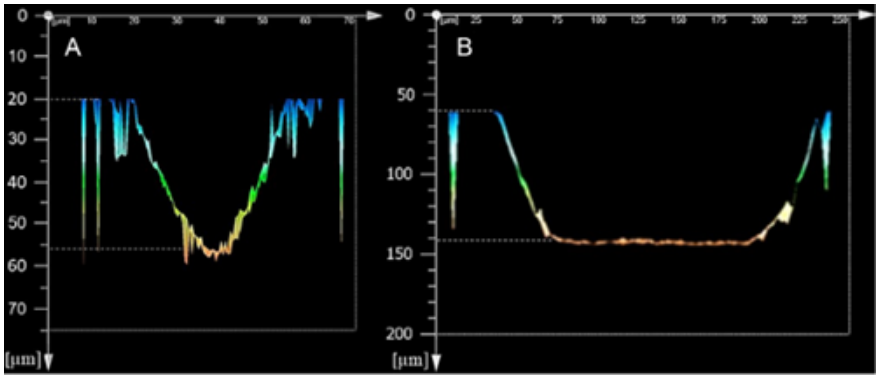

Figure 52: CNF profiles of herringbone micromixer device [51].

0.3 mbar) generated Si–OH groups on both interfaces, enabling formation of Si–O–Si covalent bonds upon contact; parameter sweeps (power 32–80 W; exposure 30–120 s) identified an optimal diagonal trade-off between power and time. Bonding robustness was validated by hydrostatic (up to 1600 mm H_2O) and pneumatic (0.1 MPa) pressure tests, meeting or exceeding typical microfluidic requirements [45]. This step is done in collaboration with the Engineering Department Enzo Ferrari of Unimore, in Modena [50, 52].
Two complementary assays quantified mixing performance under laminar flow (Re = 0.5, 1.0, 2.0):

- Qualitative pH assay: Distilled water (pH ≈7) and acetic acid (pH≈2.5) were co-injected at matched flow rates; litmus readouts at both outlets indicated mixed or segregated streams;
- Quantitative protein assay (Bradford): Distilled water and 1 mg mL^{-1} BSA were co-injected. Outlet samples (n = 9 pairs per Re) were analyzed in 96-well plates with Coomassie reagent (595 nm absorbance), and ME computed as $ME = 2Cw/(Cb+Cw)$, where C_b and C_w are outlet concentrations on the BSA and water sides, respectively. Statistical significance was tested via Student's t test.

This test was done at the Department of Surgery, Medicine, Dentistry and Morphological Sciences with Interest in Transplant, Oncology and Regenerative Medicine of Unimore, in Modena.
Control experiments employed an identical glass device without SH grooves to isolate the contribution of herringbone-induced advection.

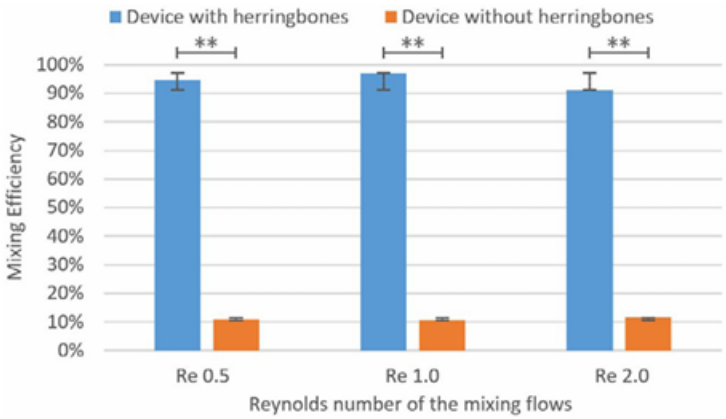

Figure 53: Mixing efficiency of herringbone device versus control device [52].

Figure 53 compares the mixing efficiency of the herringbone micromixer (HMD), shown in blue, with that of the control device (CTR), shown in orange, across all tested flow rates. For every flow condition, HMD achieved a significantly higher efficiency, averaging 94.1%, compared to only 11.0% for CTR. These results are consistent with the performance of state-of-the-art devices fabricated using conventional technologies, which typically reach values close to 100% for similar channel designs.

Furthermore, a 3D CFD model (ANSYS Fluent) was built for the mixing channel (excluding branches), with laminar, isothermal flow and velocity-inlet boundary conditions corresponding to Re = 0.5, 1.0, 2.0, as visible in Figure 54. Mesh independence was verified using poly-hexcore meshes (≈2.2 M elements), and a tracer patch method quantified outlet concentrations. A “real geometry” (RG) model incorporated U-shaped cross-sections and wall inclination derived from confocal/SEM to assess sensitivity to fabrication deviations, alongside an ideal geometry (IG) benchmark [46]. The simulations were done at the Engineering Department Enzo Ferrari of Unimore, in Modena.

The experimental campaign demonstrated that ultrafast laser micromachining of glass substrates, combined with plasma bonding to pre-cured silicone, enables rapid and accurate fabrication of microfluidic devices with complex geometries such as staggered herringbone micromixers. Morphological analyses confirmed

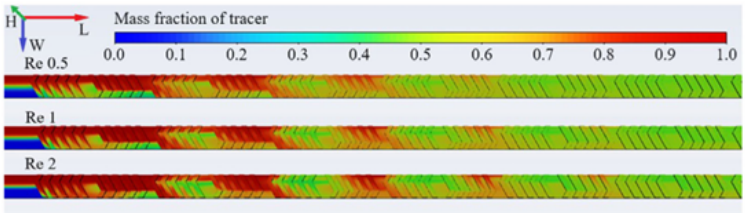

Figure 54: CFD Simulations of herringbone micromixer, made by the fluid dynamics research group at DIEF, Modena [52].

high dimensional fidelity, with channel depths around 80 μm and groove depths near 30 μm, while SEM and confocal imaging revealed sharp edges and quasi-vertical sidewalls despite minor U-shaped deviations. Plasma bonding produced robust seals capable of withstanding pressures up to 0.1 MPa without leakage, validating the mechanical integrity of the assembly. Functional tests showed excellent mixing performance: qualitative pH assays indicated complete homogenization, and quantitative Bradford protein assays yielded an average mixing efficiency of approximately 94%, significantly outperforming control devices without herringbones. CFD simulations corroborated these findings, predicting near-complete mixing and confirming that minor geometric deviations introduced by laser processing do not compromise fluid dynamic performance. Overall, the process chain achieved high-quality devices in less than 30 minutes, representing a substantial improvement over conventional replica molding workflows.

Once the procedure for prototyping micromixers has been validated, it is further developed through another project involving the creation of devices with obstacles along the vertical walls of the main channel rather than in depth. This allows the device to be created as a single scanning object, which can be immediately optimized programmatically. In this case, the hypothetical geometry in which obstacle features, position, and dimensions are modified is validated numerically, and laser ablation is used to generate microchannels of the desired geometry in the glass, subsequently sealing them with a layer of silicone.

Microfluidic channels designed for passive micromixing can exhibit diverse geometries, including serpentine paths, curved profiles, variable depths, or convergent–divergent cross-sections, all intended to induce chaotic flow and enhance mixing efficiency. In contraction–expansion array (CEA) microchannels, secondary flow phenomena such as inertial lift forces, Dean vortices, and localized

recirculation zones not only promote fluid mixing but also enable particle manipulation, broadening their functional applications. CEA channels typically consist of alternating narrow (contracting) and wide (expanding) sections, which generate convective secondary flows and microvortices within the 2D channel plane. Depending on the design, these channels can be symmetric or asymmetric, each configuration influencing flow behavior and mixing performance. Additional complexity can be introduced by incorporating recurring sharp-edged features along one or both channel walls. For this study, a straight microchannel configuration was selected. The design integrated grooves to create expansion–contraction regions, aiming to induce controlled vortices. The development process began with evaluating the size of the obstacles and their placement along the main channel relative to the flow direction. Based on these assessments, a "sawtooth" geometry was chosen. This design was subsequently compared with an alternative featuring similar dimensions but a different obstacle profile, as well as with a cyclic asymmetric configuration.
SEM images demonstrate the accuracy of the micrometer-scale geometries (Figure 55). Depth values and design geometries are validated through confocal profilometry (Figure 56).

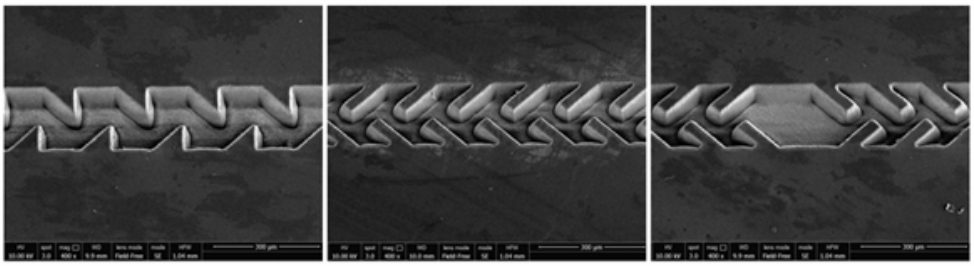

Figure 55: SEM images of vertical wall obstacles micromixer device.

The functionality of the device is qualitatively assessed through a litmus paper test: by inserting two fluids, one with a pH of 6 and one with a pH of 1, a pH of 3 is measured in the two outlets, see Figure 57.

These findings underscore again the suitability of ultrafast laser processing for the development of microfluidic lab-on-chip in applications ranging from biological screening and chemical synthesis to simulation-driven design optimization.

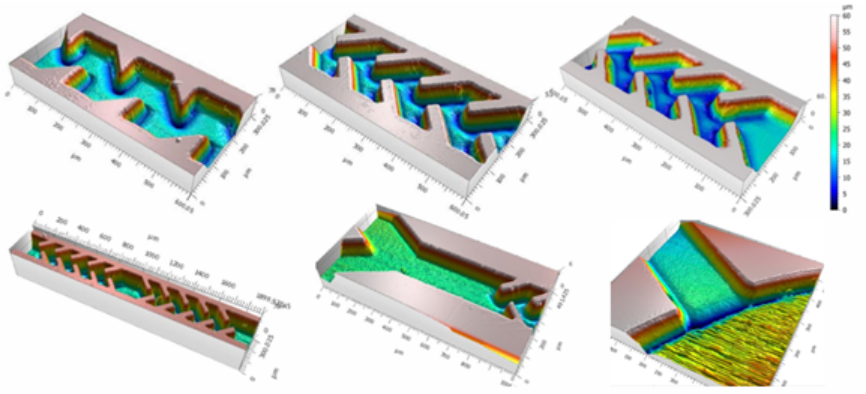

Figure 56: CNF 3D topography of vertical wall obstacles micromixer device.

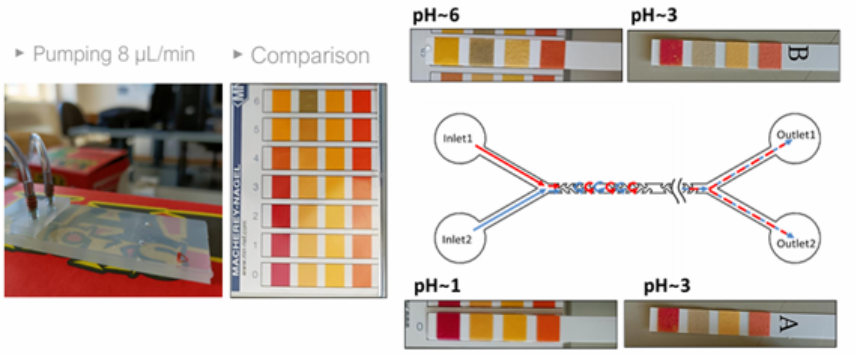

Figure 57: Vertical wall micromixer functionality assessed through litmus paper test.

Depending on the specific case and design constraints, a new geometry can always be created, simulated, and realized, following the flowchart in Figure 58. In further development, quantitative evaluation of mixing efficiency by microprobe pH, as well as numerical phase simulation for microparticle generation, can be introduced to refine the assessment of the right geometry.
The use of adaptive optics in the laser system could compensate for field-dependent aberrations, ensuring diffraction-limited focusing across large scan areas and improving dimensional accuracy, sidewall verticality, and surface finish. These improvements are expected to reduce the number of passes required for target depths and further increase productivity.

Additional developments in creating channels directly on glass provide an opportunity to pair this process with diffusion bonding, enabling the fabrication of fully glass-based microfluidic devices.

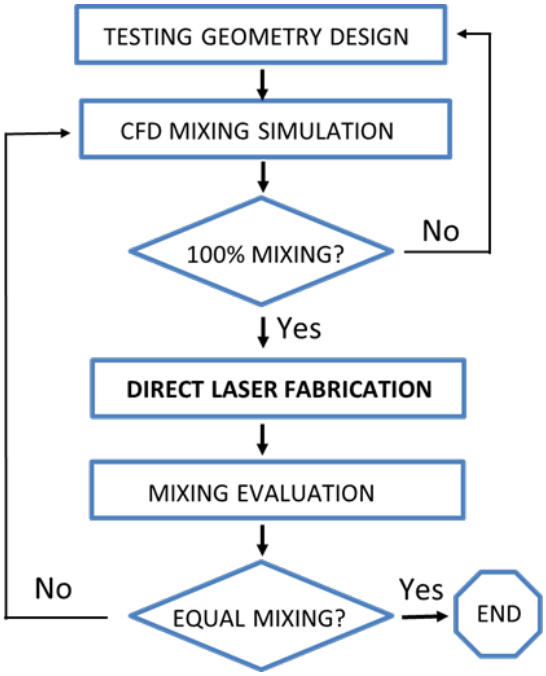

Figure 58: Prototyping glass microfluidic devices flowchart.

Traditional bonding methods, including adhesive bonding and anodic bonding, present significant drawbacks: adhesives risk contaminating or clogging microchannels, while anodic bonding often requires intermediate layers and complex setups [53]. These limitations compromise device reliability and increase manufacturing complexity. Diffusion bonding offers a compelling alternative by enabling the direct joining of glass substrates under controlled heat and pressure without introducing other materials. This approach ensures strong, hermetic seals that maintain chemical resistance and structural integrity, making it ideal for microfluidic systems exposed to aggressive solvents or high-pressure conditions [44]. Furthermore, diffusion bonding aligns with scalable and clean manufacturing practices, reducing contamination risks and simplifying the process chain compared to adhesive-based methods [54]. Its compatibility with ultrafast laser micromachining for channel creation positions diffusion bonding as a key enabler for producing robust, high-performance microfluidic devices for biomedical and industrial applications.

Diffusion bonding has been explored as a practical solution for sealing laser-machined microchannels in glass-based microfluidic devices. After creating channels on float glass using a UV picosecond laser, the bonding process aimed to

join the structured glass with a flat cover plate without adhesives or intermediate layers, which are common sources of contamination and flow obstruction in conventional methods [53]. The methodology involved heat treatment above the glass transition temperature (approximately 574 °C), with bonding trials conducted at Tg + 75 °C and Tg + 100 °C. Samples were placed in a muffle furnace under ambient air, with a refractory weight applied to ensure uniform pressure during the thermal cycle. Each cycle consisted of a controlled ramp-up to the target temperature, a 30-minute hold, and gradual cooling to room temperature. This test is done in collaboration with the Engineering Department Enzo Ferrari of Unimore, in Modena.

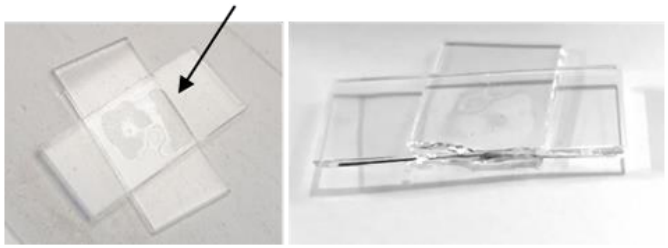

Figure 59: Effective diffusion bonding test between two glass sliders [49].

The results demonstrated successful glass-to-glass bonding at both tested temperatures, producing joints strong enough that the bonded samples could not be separated without fracture, see Figure 59.
This confirmed the feasibility of diffusion bonding for creating hermetically sealed channels suitable for microfluidic applications. Diffusion bonding is a clean, reliable, and scalable approach for manufacturing entirely glass-based microfluidic devices, offering superior chemical resistance and structural stability compared to adhesive bonding or anodic bonding. However, the proposed bonding method should be assessed by testing its applicability on glass slides with fabricated channels and verifying its capacity to withstand the fluid pressure within the microchannels.

5.2.2 Laser microtexturing for tribological applications

The growing demand for sustainable and high-performance manufacturing processes has driven significant interest in surface engineering techniques that enhance tribological properties of tools without relying on harmful lubricants. Conventional machining often suffers from excessive friction, heat generation, and rapid tool wear, particularly under dry cutting conditions, which compromises tool life and surface quality while increasing energy consumption and environmental impact. Traditionally, cutting fluids have been employed to mitigate these issues; however, their ecological and health hazards have prompted the search for cleaner alternatives. Laser surface texturing (LST) has emerged as a promising solution, offering precise control over micro- and nano-scale patterns that reduce friction, improve wear resistance, and enable self-lubricating behavior at the tool–chip interface, with surface features such as dimples, grooves, and periodic structures that can reduce the Coefficient Of Friction (COF), enhance wear resistance, and improve lubrication retention [55]. The use of ultrashort-pulsed lasers, particularly femtosecond and picosecond lasers, enables the creation of textures with minimal thermal damage, thereby preserving the integrity of the substrate while achieving superior tribological properties [56]. Several studies have demonstrated that LST can reduce COF by up to 68% and wear rates by over 50% compared to untextured surfaces, owing to mechanisms such as hydrodynamic lift, debris entrapment, and the formation of self-lubricating films [57]. Furthermore, the integration of LST with solid lubricants like MoS_2, WS_2, or h-BN has shown synergistic effects, significantly enhancing tool life and reducing energy consumption in dry and high-temperature environments [55]. These advantages translate into reduced cutting forces, lower temperatures, and enhanced tool life.

The first case study addresses the challenge of reducing friction, heat generation, and lubricant consumption during tapping operations by introducing microtextures on tool surfaces. The approach leverages the picosecond laser technology to create controlled dimples on complex geometries, aiming to improve lubrication retention and tribological performance under Minimum Quantity Lubrication (MQL) conditions. The work began with preliminary tests on planar

samples to optimize laser parameters for generating rectangular dimples. The infrared wavelength at 1064 nm was employed, at 400 kHz with an average power of 0.82 W and a pulse energy of 2.05 μJ per pass, see Table 6. Dimples were designed with dimensions of 30 $\times$ 60 μm and a target depth of $\approx$10 μm, arranged to cover 15% of the tool surface. Three depth profiles were implemented: flat-bottom, positively inclined, and negatively inclined relative to the chip flow direction. These were achieved by overlapping seven progressively narrower rectangles, filled with a 5 μm hatch spacing to ensure uniform energy distribution and avoid recast layers.

Transitioning from flat surfaces to the helical threads of commercial TiN-coated tapping tools required an advanced kinematic strategy. The system integrated an automated roto-translator, enabling synchronized X, Z, and rotational movements to follow the thread helix while maintaining the right focal position. Calculations of beam waist (11.6 μm) and Rayleigh length ($\approx$100 μm) confirmed the feasibility of texturing inclined surfaces without significant deviation from planar results. Dimples were distributed along the thread crest and root through a multi-step Z approach combined with incremental rotations of 4.5°, optimizing coverage and reducing processing time. SEM analysis validated the methodology, showing regular dimples with consistent geometry across both planar and inclined surfaces, see Figure 60. On flat samples, depths reached the designed 10 μm, while inclined surfaces achieved $\approx$8 μm, maintaining shape integrity despite angular adjustments. The dimples were uniformly distributed even in the conical inlet zone, critical for lubrication during high-depth tapping. No evidence of recast material or irregular energy deposition was observed, confirming the robustness of the laser parameters and motion strategy. The successful implementation of micro-textures on complex tool geometries demonstrates the potential of picosecond laser processing for tribological enhancement. Dimples act as lubricant reservoirs, potentially reducing friction and adhesion while enabling MQL conditions. However, it is important to note that laser microtexturing remains far from being a mass-production solution due to its relatively low throughput and high cost. For a few high-value or specialized components, the benefits in performance and durability may justify the investment, but their industrial adoption will likely remain limited to niche applications. Rather than claiming scalability,

Table 6: Laser parameters for tapping tool texturing.

GR (532 nm)	Scanning strategy	Frequency [kHz]	Mark speed [mm/s]	Overlap [%]	Power [W]	Passes [-]	Fluence [J/cm^2]
Dimples	Parallel lines	400	1000	50	0.82	2-14	2.61

the automated procedure should be viewed as a step toward improving process repeatability and precision for specialized manufacturing scenarios, where quality and functionality outweigh cycle time constraints. Future work will involve cutting tests to quantify reductions in thrust force and wear compared to conventional tools, validating the tribological benefits under real machining conditions [40].

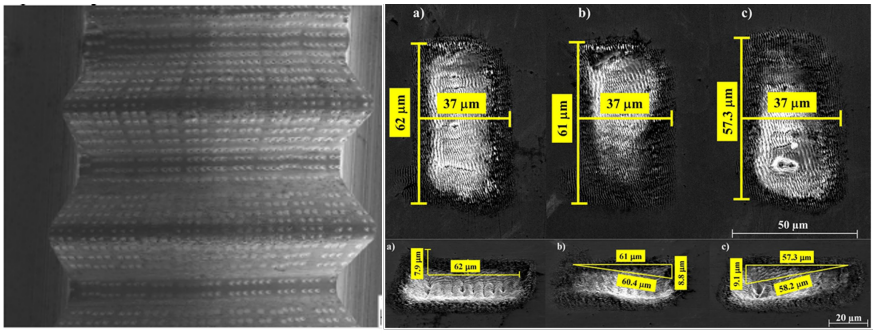

Figure 60: SEM images of textured tapping tool [40].

The second case study explores the use of picosecond laser ablation to create micro-textures on cemented carbide cutting inserts, aiming to improve tribological performance during dry cutting operations. The motivation lies in reducing friction, chip adhesion, and cutting forces when lubrication is absent. Commercial triangular carbide inserts (grade H13A) were selected to be textured. The surfaces targeted were both rake and flank faces, starting from the cutting edge. Four main texture strategies were developed: rectangular dimples (30 × 60 μm), parallel grooves, orthogonal grooves, and combined grid patterns. The textured area measured 5 × 3 mm, with a depth of approximately 20 μm to minimize adhesion while preserving texture integrity during machining.

Laser ablation was performed using the 532 nm wavelength with 10 ps pulse duration, 400 kHz frequency, and 0.44 W average power. Laser parameters are summarized in Table 7. Dimensional accuracy of textures was verified using structured light profilometry and optical microscopy, see Figure 61.

Table 7: Laser parameters for texturing cutting tool.

GR (532 nm)	**Scanning strategy**	**Frequency [kHz]**	**Mark speed [mm/s]**	**Overlap [%]**	**Power [W]**	**Passes [-]**	**Fluence [J/cm^2]**
Grooves and dimples	Parallel lines	400	1000	80	0.44	14	1.40

To predict cutting behavior, a finite element model (SFTC Deform 2D®) simulated orthogonal cutting under dry conditions. The model incorporated a shear friction approach and fine meshing near the cutting edge. Experimental validation involved orthogonal dry cutting tests on E235 steel tubes using a CNC turning center at 150 m/min cutting speed and 0.05 mm/rev feed. Cutting and thrust forces were recorded via a six-component piezoelectric dynamometer. The experiments revealed that texture design significantly influences cutting performance. Inserts with grid and orthogonal groove patterns exhibited improved process stability, evidenced by reduced fluctuations in cutting forces, see Figure 63. However, these strategies also increased average cutting forces by up to 20%, attributed to changes in contact area and frictional behavior, see Figure 62. Conversely, parallel grooves slightly reduced force components but promoted built-up edge formation, indicating higher adhesive effects. Dimples showed a negligible impact compared to non-textured tools.

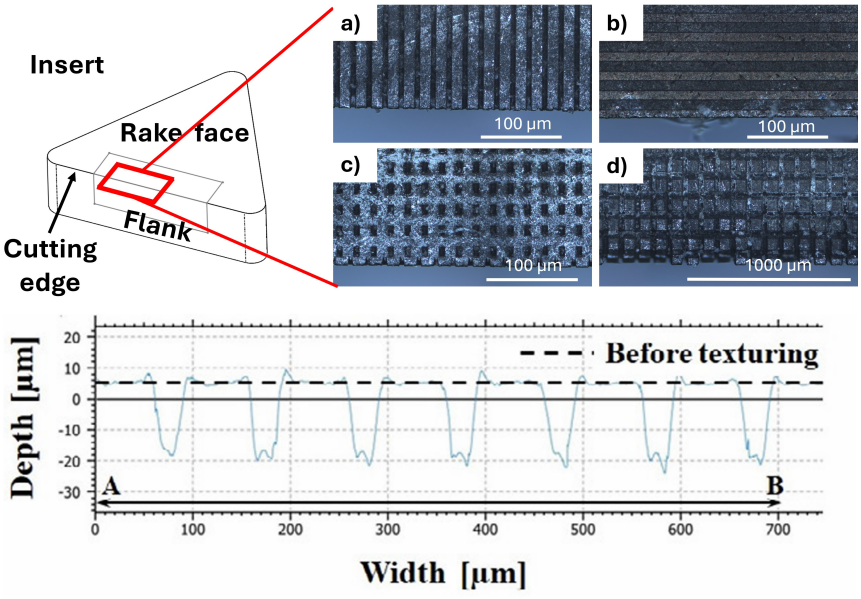

Figure 61: Cutting tool textured morphology and profiles [58].

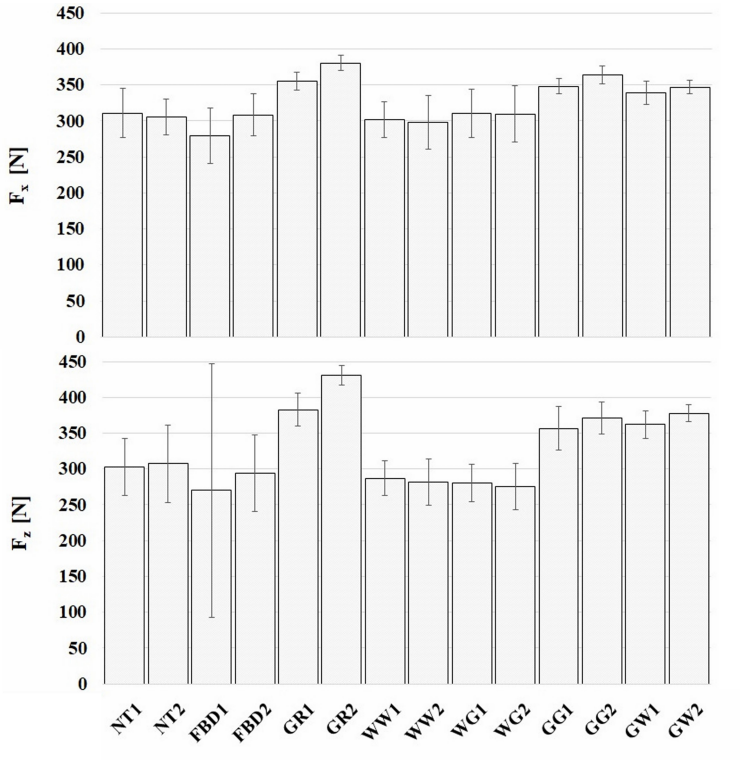

Figure 62: Comparison of the average cutting forces for NT and textured inserts: FDBD rectangular dimples, WW stripe grooves parallel to the cutting edge, GG orthogonal, GR both, WG and GW are combined textures [58].

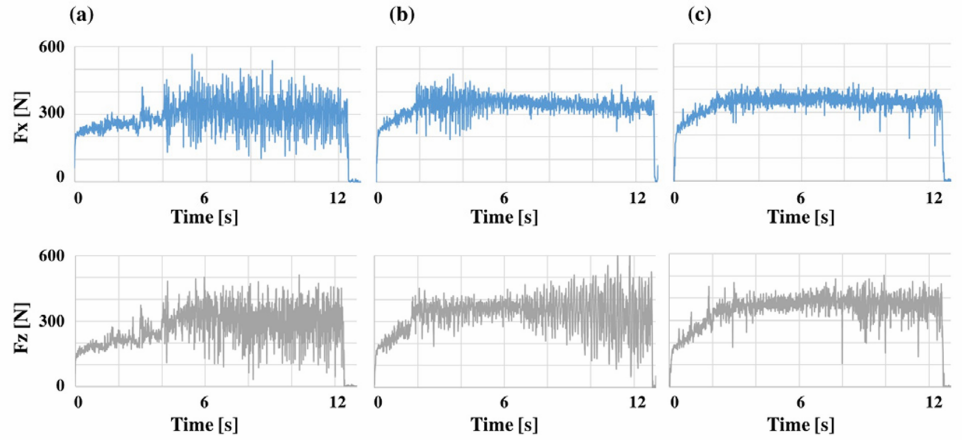

Figure 63: Changes in cutting forces during dry cutting: a) NT, b) GG1, c) GR1 [58].

Numerical simulations performed at the University of Calabria correlated well with experimental measurements, validating the predictive capability of the finite element model for force estimation. Overall, the results confirm that laser-generated micro-textures can have an effect on cutting performance under dry conditions [58]. Future work will focus on refining texture design to maximize anti-adhesion properties and minimize cutting forces without compromising process stability. Additional studies will explore the influence of cutting speed variations and the integration of advanced surface characterization to better understand wear mechanisms.

The third case study focused on enhancing face milling performance of AISI 1050 steel by applying laser-induced microtexturing to the cutting tools. The original coating was removed from carbide inserts, which were then textured using the 1064 nm wavelength. The grooves created were approximately 12 μm wide and 3 μm deep, spaced at 60 μm. Two configurations were tested: grooves parallel and grooves orthogonal to the chip flow direction. Due to the highly irregular surface of the cutting edges, it was decided to mark the textures at different focal heights to cover the entire surface. Laser parameters are in the Table 8. After texturing, tools were recoated with TiN to ensure coating conformity, see Figure 64. Milling tests were conducted on a CNC center under wet cooling conditions, using three axial depths of cut (1.5, 2.0, and 2.5 mm) and two cutting speeds (200 and 220 m/min), replicated for both texture orientations. Cutting forces

Table 8: Laser parameters for milling cutting tool texturing.

IR (1064 nm)	Scanning strategy	Frequency [kHz]	Mark speed [mm/s]	Overlap [%]	Power [W]	Passes [-]	Fluence [J/cm^2]
Grooves	Parallel lines	500	500	70	0.95	4	2.42

were measured with a piezoelectric dynamometer, while surface roughness (Ra and Rz) was assessed using a Mitutoyo SJ-410 tester. Chip morphology and tool wear were analyzed via optical microscopy.

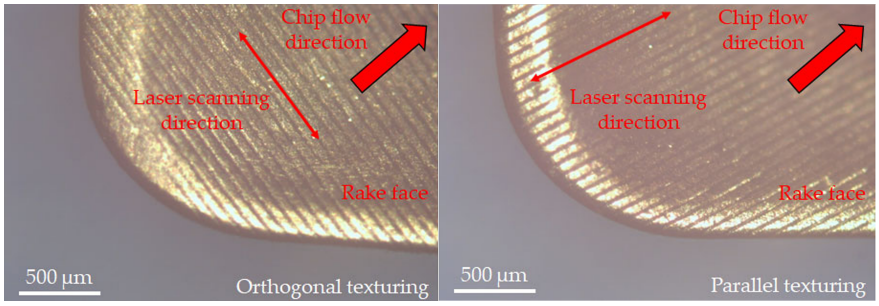

Figure 64: SEM images of textured and coated cutting tool [59].

Laser texturing again shows an effect on tribological behavior at the tool–chip interface. Orthogonal grooves improved chip evacuation and coolant penetration, reducing cutting forces by up to 3% compared to parallel grooves, particularly at lower speeds and depths, see Figure 65. Higher cutting speeds (220 m/min)

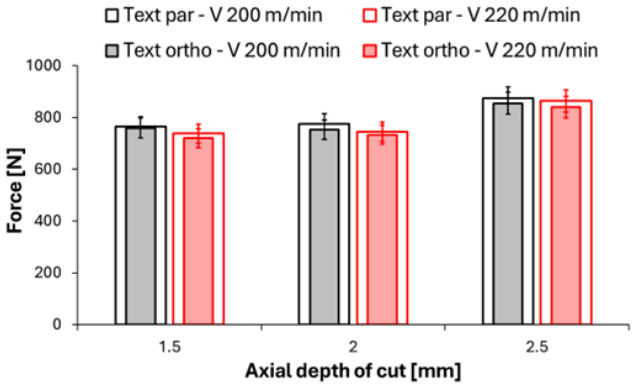

Figure 65: Variation in cutting forces [59].

further decreased cutting forces and improved surface finish due to thermal softening, while increased depth of cut raised forces and roughness markedly. Surface roughness analysis revealed that orthogonal texturing reduced Ra and Rz by ap-

proximately 40–45% compared to parallel orientation, confirming its potential in minimizing friction and adhesion. Chip morphology showed that orthogonal grooves produced larger peak and pitch values, indicating better segmentation and controlled chip breakage, whereas parallel grooves yielded smaller, continuous chips but slightly higher cutting loads, as visible in Figure 66. Spiral pitch lengths were shorter for orthogonal textures, reflecting efficient chip control, see Figure 67. No significant tool wear was observed, suggesting good coating integrity and durability under the tested conditions. All the cutting tests were carried out at the University of Calabria.

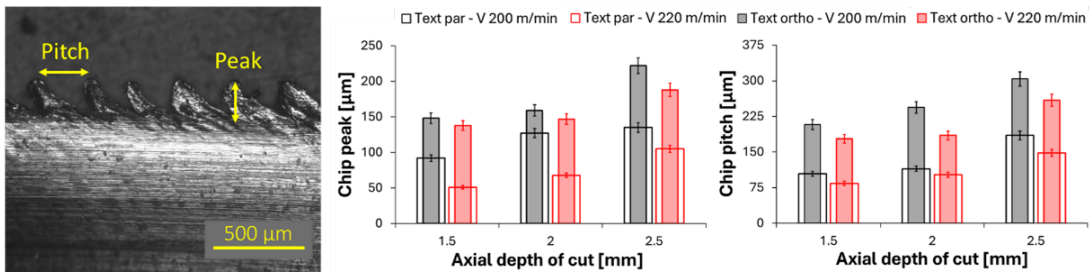

Figure 66: Analysis of chip morphology: chip peak and chip pitch [59].

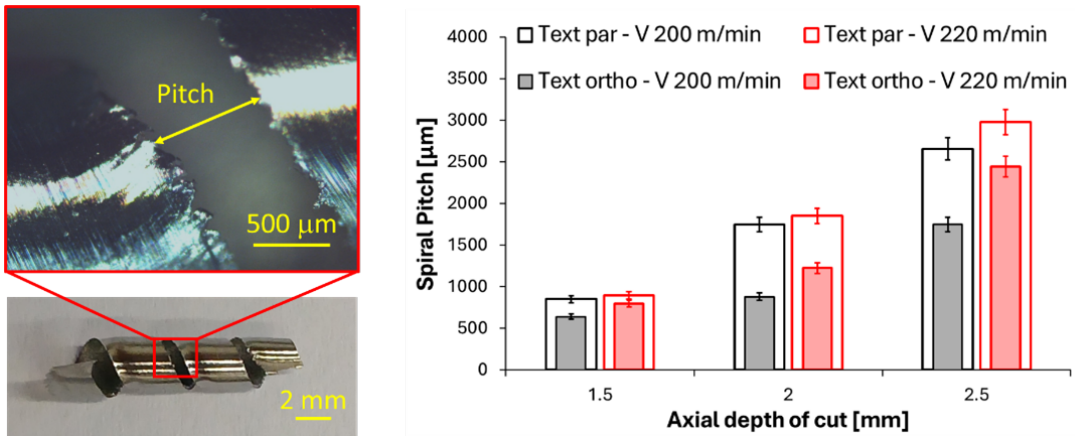

Figure 67: Analysis of chip morphology: spiral pitch [59].

Indeed, the orthogonal groove orientation enhances milling performance by slightly reducing cutting forces, improving surface quality, and promoting stable chip formation.

Although the three case studies have demonstrated that laser microtexturing can reduce friction, improve cutting stability, and enhance tool-chip interaction,

it remains clear that the mechanisms underlying these phenomena are not yet fully understood; for this reason, the work continues with further experimental and modeling analyses aimed at clarifying the remaining uncertainties and consolidating the evidence that has emerged.

5.2.3 Micromanufacturing for Optics components

The advancement of optical devices for applications in imaging, telecommunications, and photonics demands fabrication techniques that offer high precision, flexibility, and efficiency. Traditional methods such as photolithography and etching, while effective, are often time-consuming, require multiple steps, and depend on masks or photosensitive materials, limiting scalability and design freedom [60, 61]. Laser-based fabrication provides a compelling alternative by enabling maskless, direct writing of micro- and nano-scale structures with good accuracy and minimal thermal damage. While not suited for high-volume production, this technology is highly competitive for small batches and specialized components, where flexibility, precision, and rapid prototyping provide significant advantages. Ultrafast lasers, in particular, allow nonlinear absorption processes that facilitate machining of transparent and conductive materials, such as indium tin oxide (ITO), which is widely used in optoelectronic devices [62, 63, 64]. This capability reduces heat-affected zones and enables patterning without compromising substrate integrity, making it ideal for advanced photonic architectures and flexible electronics [65, 66]. Furthermore, techniques like femtosecond laser-induced solid ablation (LISA) have demonstrated rapid, single-step fabrication of diffractive elements such as Fresnel zone plates, achieving superior optical performance compared to conventional lenses [67, 68].
In this context, the first case study presents the development of a thermo-optic lens designed to exploit the temperature-dependent refractive index of transparent materials for dynamic wavefront control. The device consists of an isolated circuit patterned on an indium tin oxide (ITO) layer deposited on glass, ensuring high transparency while enabling localized heating, see Figure 68. Heat generated by microresistors modifies the refractive index of a polymer layer, shaping the transmitted wavefront. Initially, the wavefront profile is determined by the geometry of the resistors, which limits flexibility.

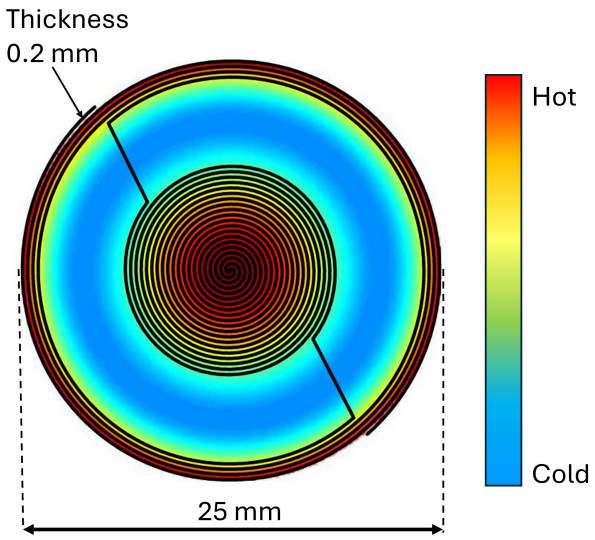

Figure 68: Design of the thermo-optical lens prototype: the black lines are the resistive traces, while the color map represents the simulation of the temperature field by passing current.

The motivation for this approach stems from the growing need for compact, reconfigurable optical components that enable precise wavefront control in miniaturized systems. Unlike bulky mechanical lenses or reflective adaptive optics, thermo-optic actuation provides broadband, polarization-insensitive phase modulation through temperature-induced refractive index changes. This approach allows dynamic adjustment of both curvature and sign, as well as independent control of multiple Zernike modes, offering a simple, transparent, and planar solution for high-resolution aberration correction in applications such as microscopy, endoscopy, and portable imaging devices.

The workpiece is a 50×50 mm, 1.1 mm-thick glass substrate coated on one side with a transparent 185 nm ITO film (10–15 Ω/sq), providing a lightweight, easily patternable, and non-solderable conductive surface suitable for research applications. Since a ceramic coating must be ablated, the wavelength chosen is 1064 nm. This wavelength is also poorly absorbed by glass unless directly focused on its surface; otherwise, it tends to transmit it. The processes to be carried out are ablation, contouring, and cutting. Laser parameters used are in Table 9.

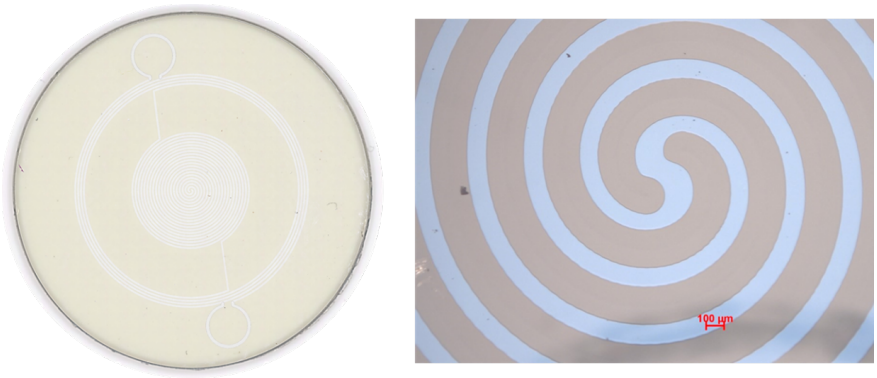

Figure 69: Spiral ablated track on the ITO.

Table 9: Laser parameters for ITO cutting and selective ablation.

IR (1064 nm)	**Scanning strategy**	**Frequency [kHz]**	**Mark speed [mm/s]**	**Overlap [%]**	**Power [W]**	**Passes [-]**	**Fluence [J/cm^2]**
Ablation	Parallel lines	500	1000	80	0.54	1	1.38
Outline	Single line	300	500	-	2.66	10	11.30
Cutting	Spiral	300	500	80	3.47	Cont.	14.70

The effectiveness of the ablation treatment is first obtained by measuring the resistance with a multimeter, and the morphological analysis is done under an optical microscope, see Figure 69. Portions of the glass have been selectively electrically insulated, and the device is ready for use: the ITO acts as an electrical resistor; when a current is applied, the coating selectively heats up and transfers heat to the glass, thus locally modifying the refractive index.

The functionality of the reconfigurable thermo-optic lens was experimentally validated from CNR-IFN of Padua by measuring its ability to generate and tune specific Zernike modes, namely defocus and primary spherical aberration. Tests were performed by applying increasing voltages to the integrated microresistive circuit, which induced controlled thermal gradients in the ITO-coated glass and polymer layer. Wavefront analysis revealed a linear relationship between applied voltage and induced aberration: defocus increased from approximately 0.28 λ at 50 V to 2.06 λ at 150 V, while spherical aberration varied from -0.11 λ to -0.88 λ over the same range. The target vs. measured aberration is shown in Figure 70. These results confirm that the lens can dynamically modulate both

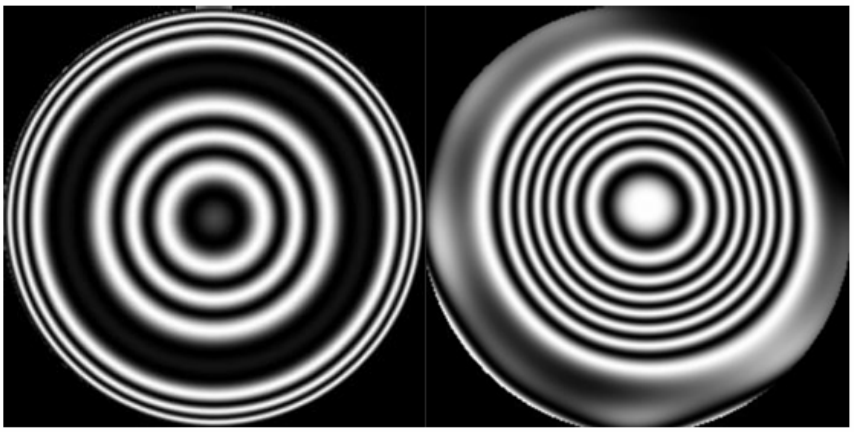

Figure 70: Target (left) versus measured (right) aberration produced by the heated thermo-optics lens.

the magnitude and sign of key aberrations, demonstrating its potential for adaptive wavefront correction. Response times to reach thermal equilibrium ranged from about 61 s at 150 V to 95 s at 50 V, indicating stable and predictable thermal behavior. Future improvements will focus on optimizing resistor geometry to minimize unwanted defocus and enable bidirectional spherical aberration control.

The second case study investigates an alternative approach to wavefront sensing that leverages the design and precise manufacturing of Zone Plates as key enabling elements for improving beam quality control in ultrafast laser-based manufacturing. Conventional solutions rely on optical relays to resize large beams before phase measurement, but these systems are expensive, occupy considerable space, and complicate integration into manufacturing environments. To overcome these limitations, we propose a compact, cost-effective design that uses custom-fabricated Zone Plate arrays combined with an imaging system inspired by the Shack–Hartmann principle, enabling direct sampling of large beams without bulky relay optics.

Zone Plates are diffractive optical elements that focus light through interference rather than refraction. They consist of concentric Fresnel zones arranged to produce constructive interference at a focal point. Their focal length depends on the outermost zone width and the wavelength of the incident light. Because the focal spot shifts with changes in the wavefront, Zone Plates can serve as effective

Table 10: Laser parameters for zone plate selective ablation.

GR (532 nm)	**Scanning strategy**	**Frequency [kHz]**	**Mark speed [mm/s]**	**Overlap [%]**	**Power [W]**	**Passes [-]**	**Fluence [J/cm^2]**
Ablation	Spiral	300	300	80	0.08	1	0.34

wavefront sensing elements. Their fabrication requires high precision, as small deviations in zone placement or duty cycle can significantly affect performance. Zone Plates can be manufactured as transmissive gratings or reflective surfaces, offering flexibility for integration into different optical architectures.

In the proposed design, an array of Zone Plates replaces the microlens array of a Shack–Hartmann sensor. Each Zone Plate focuses a portion of the beam onto a diffusive plate, creating a spot pattern that is imaged by a wide field-of-view objective and captured by a sensor. Spot positions are analyzed to reconstruct the wavefront, following the Shack–Hartmann principle. The system operates at a specific wavelength and requires calibration to correct for fabrication tolerances, speckle noise, and lens distortion. This approach eliminates the need for large-aperture lenses or mirrors, reducing cost and footprint while enabling direct measurement of large beams. Two prototypes, designed for 12 mm and 50 mm beam diameters, were developed to assess feasibility and identify critical challenges.

The Zone plate mask designed for a 50 mm diameter 635 nm wavelength laser beam, featuring four zones to be made transparent, is reported as an example. Specifications are in Figure 71.

The workpiece is a 50.8 mm-diameter, 1.1 mm-thick float-glass substrate coated on one side with a high-reflectivity enhanced aluminum layer (R $\geq$ 95% from 450 to 650 nm), providing a 4–6 λ surface flatness and a 60-40 surface quality suitable for precision optical applications. Since it is necessary to selectively remove the metal coating over an area of 50 mm, the wavelength chosen is 532 nm. This wavelength is also poorly absorbed by glass unless it is focused directly on its surface; otherwise, it tends to transmit it. The laser parameters used are listed in Table 10.

The dimensional characterization performed on a test material complies with

Zone number	Internal and External radii (µm)		Zone width (µm)
Zone 1	$r_{1,int}$	0.0	225.9
	$r_{1,ext}$	225.9	
Zone 2	$r_{2,int}$	319.5	71.8
	$r_{2,ext}$	391.3	
Zone 3	$r_{3,int}$	451.8	53.3
	$r_{3,ext}$	505.1	
Zone 4	$r_{4,int}$	553.3	44.3
	$r_{4,ext}$	597.7	

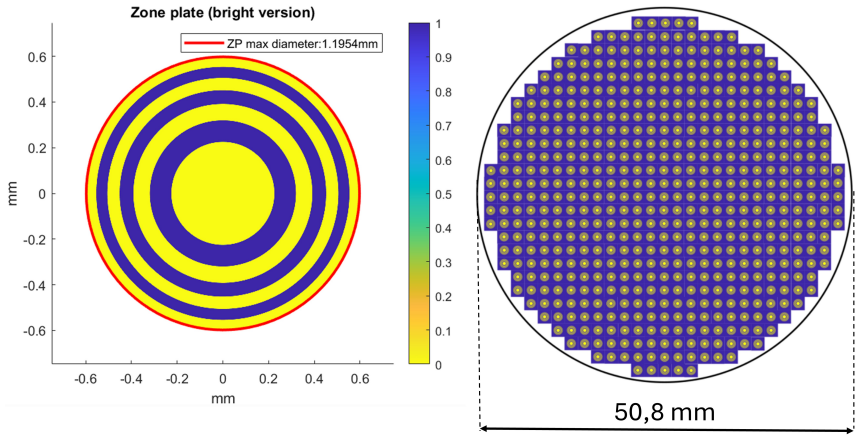

Figure 71: Zone plate design specifications: single zone plate from zone 1 to zone 4 (left), zone plate array covering a diameter of 50 mm (right).

the requirements, to within one micron. In this application, it was essential to carefully calibrate the scanning angle to avoid ellipticity away from the center of the working area, which would have compromised the proper functioning of the device. The manufactured component is shown in Figure 72, where the white portion reflects the light from the microscope, while the black emerges from the transparent exposed glass over the black table. The validation setup diagram is shown in Figure 73. It consists of a large laser beam, a zone plate array, a diffuser plate, and a large field of view imaging system. The ability to generate well-defined focal spots with correct spacing and size is verified through spot formation and uniformity, centroid regularity, focal length confirmation, and spot diameter measurements by the CNR-IFN of Padua. Because the diffuser does not scatter light uniformly and the beam has an uneven intensity profile, the resulting spots vary significantly in brightness, with lateral spots appearing dimmer due to less diffused light reaching the objective. To compensate, five images were acquired with progressively decreasing exposure as a function of radius and combined to maintain spot intensity as constant as possible, see Figure 74.

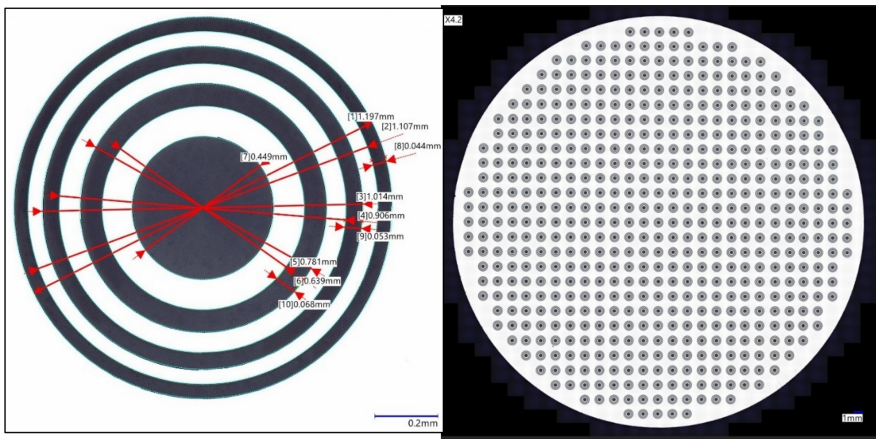

Figure 72: Manufactured zone plate characterization: single zone plate measurements (left), zone plate array covering a diameter of 50 mm (right).

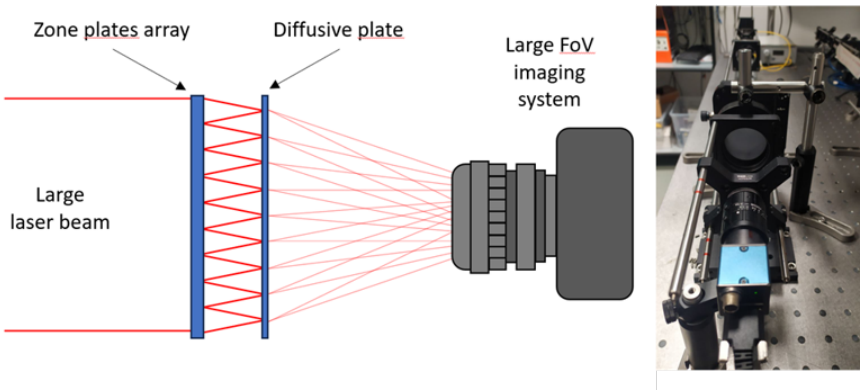

Figure 73: Zone plate functioning scheme.

Distance maps along X and Y between adjacent centroids were then analyzed to identify potential manufacturing imperfections. However, centroid measurements are affected not only by fabrication errors but also by speckle noise arising from coherent light diffusion. In some cases, systematic deviations were observed along X, likely caused by an unintended stage shift during fabrication, whereas Y-axis errors were minimal.

The column error is approximately two pixels, i.e., 95 μm. Sensor calibration performed without the diffuser and excluding defective columns yielded a pitch of Px = 1.798 $\pm$ 0.002 mm along X and Py = 1.811 $\pm$ 0.002 mm along Y, consistent with the expected value of 1.8 mm. The focal length is close to the design specification, but precise estimation is challenging because the high f-number of the Zone Plates results in minimal spot variation near focus; further measurements are planned. As can be seen from Figure 75, the measured spot profile overlaps perfectly with the expected profile, propagating a divergent wavefront from a point source at the correct distance. There is therefore compatibility with the expected results.

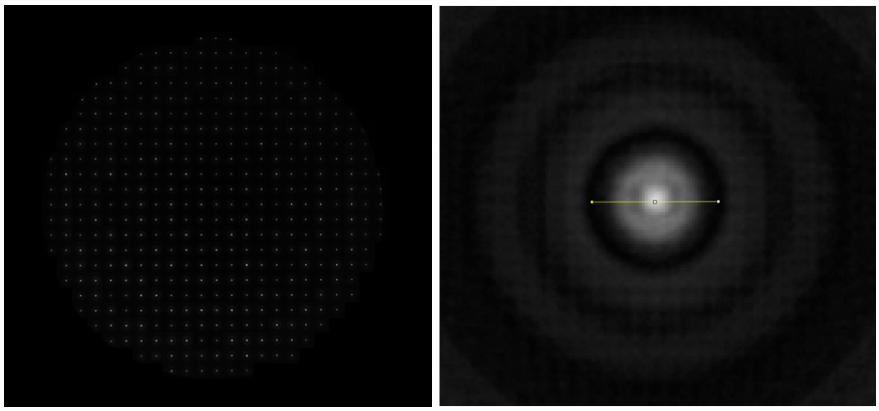

Figure 74: Multiple focused spots from irradiating the zone plate.

In summary, experimental validation with the two prototypes confirmed the concept and highlighted key challenges. Speckle noise from coherent light diffusion affects centroid accuracy, requiring mitigation through optimized diffusers or averaging techniques. Wide-field objectives introduce distortion that must be corrected through calibration models. Zone Plate manufacturing precision is critical, as errors in zone placement or duty cycle impact performance. Additionally, wavelength dependence must be carefully managed to ensure accurate

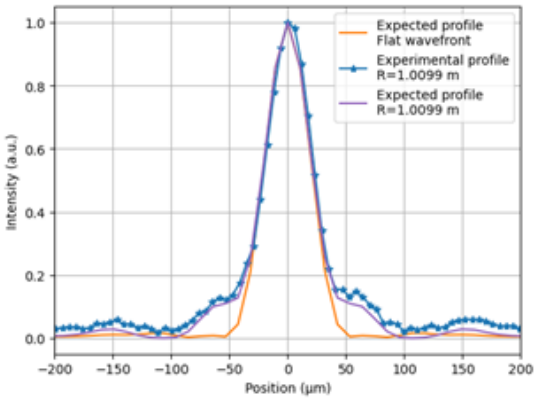

Figure 75: Experimental versus expected spot position profile.

phase reconstruction.

However, integrating this sensor with adaptive optics in ultrafast laser manufacturing offers significant benefits. For this reason, packaging the sensor into a compact industrial module with real-time adaptive optics interfaces is also a priority.

5.2.4 Colorization via Oxidation

The use of laser technology for metal coloring is a versatile and innovative alternative to traditional chemical or galvanic processes, driven by the growing demand for aesthetic customization, product identification, and anti-counterfeiting solutions. Unlike conventional methods, laser-based techniques enable localized and precise modification of surface properties without altering the bulk composition of the material, ensuring durability and environmental sustainability [69, 70]. Colorization can be achieved through two main mechanisms: controlled oxidation, which forms thin oxide layers of varying thickness, and diffractive surface structuring, which creates periodic micro- or nano-patterns that diffract light to produce iridescent effects [71, 72, 73]. Ultrafast lasers (femtosecond and picosecond) allow the generation of sub-micrometric scales LIPSS, offering high-resolution patterns and a broad palette of colors [72, 74]. These processes are single-step, maskless, and adaptable to different metals such as stainless steel, titanium, aluminum, and copper, making them suitable for industrial applications in design, branding, and functional surfaces [75, 76, 77]. Furthermore, laser

coloring combines aesthetic appeal with technical advantages and compatibility with digital workflows for image-based pattern replication [76, 78].
The proposed case study begins with the selection of suitable materials, including stainless steel, copper, brass, and aluminum. Each material responds differently to laser parameters, influencing the range and intensity of colors that can be achieved, see Figure 76 and Figure 77.

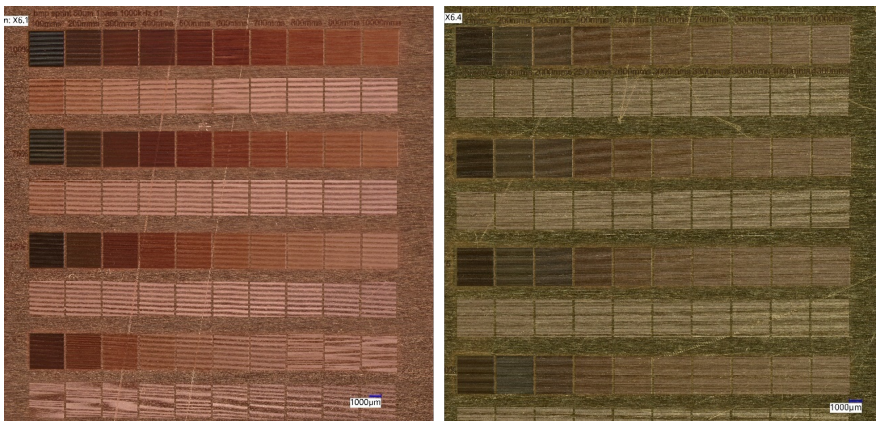

Figure 76: Color palette on copper and brass.



Figure 77: Selective oxidation with different laser parameters.

The chosen wavelength is 1064 nm, with pulse frequencies between 300 kHz and 1 MHz. The scan speed varies from 100 mm/s to 4300 mm/s, and the laser power is modulated between 4.2 W and 28.6 W. Pixel sizes used for scanning range from 25 to 200 μm, and the scanning strategy includes bitmap sprint and vector-based approaches. To generate uniform colors, the laser fluence and distance between the lines are carefully controlled. Laser parameters are summarized in Table 11.

Table 11: Laser parameters for laser coloring.

IR (1064 nm)	Scanning strategy	Frequency [kHz]	Mark speed [mm/s]	Overlap [%]	Power [W]	Passes [-]	Fluence [J/cm^2]
Oxidation	Parallel lines	300-1000	100-4300	-	23.4	1	5.35-121.44

The methodology also includes strategies to manage thermal effects to ensure uniform treatment across large areas. Laminas are processed in thermal contact with copper stacks to stabilize temperature and prevent deformation. Elastic clamps are used to maintain a consistent focal distance and avoid defocusing.
For large-scale applications, the process is extended using techniques such as Mark-On-The-Fly (MOTF), which allows continuous scanning over extended lengths by synchronizing the motion of the workpiece with the laser beam. This enables the creation of high-resolution, seamless color patterns on surfaces larger than the scanner's native field of view. In this case, it is important to carefully manage the kinematics of the process and adjust the processing parameters according to the movement of the part. To demonstrate the feasibility of processing large objects, a 120 mm long rectangle was marked.
To achieve nuanced colorization, grayscale images had to be scanned. In order to exploit the full dynamics of the laser system, image processing must be carried out by maintaining the mirror speed constant and at maximum and by modulating the source output at high speed using an Opto-Acoustic Modulator (AOM), see Figure 78.

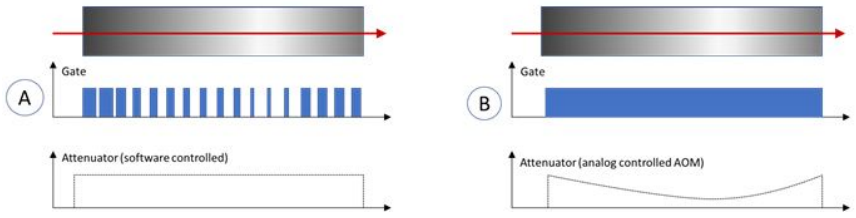

Figure 78: a) Original PWM mode of the EKSPLA 50 laser, b) Analog mode implemented using AOM.

However, to appreciate the different grayscales in a single image, the power must be linearized. The calibration process includes measuring the power in W at different percentage attenuation values set via software. At the same time, the

emitted output voltage (actual) must be evaluated to meet the power requirement (in points). Finally, a calibration file must be created that, meeting the software's requirements, contains the voltage values to be supplied (actual) as a function of the linearized power, as shown in Figure 79. Overall, the methodology

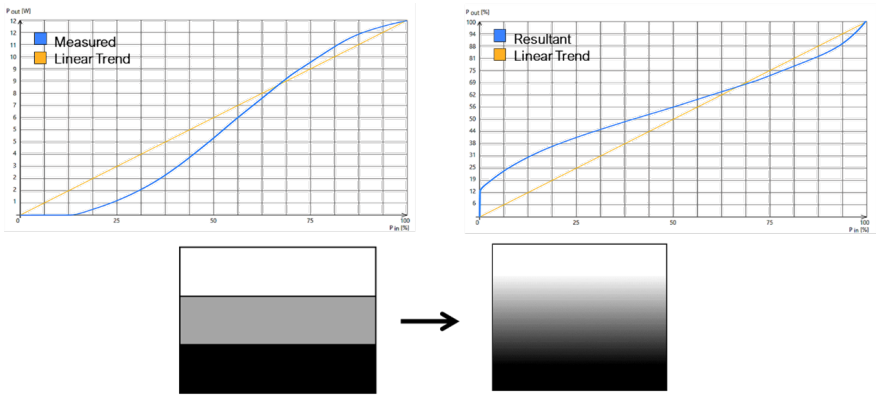

Figure 79: Power calibration curve to obtain shades.



Figure 80: Scanned bitmap example.

combines precise control of laser parameters, material-specific responses, and advanced scanning strategies to produce a wide range of colors and textures

on metal surfaces, suitable for both aesthetic and functional applications. An example of an image reproduced by laser treatment is shown in Figure 80.

5.2.5 Laser cleaning of metal-bonded joints

Structural adhesive bonding is commonly used to join components with complex geometries, as it enables uniform stress distribution, maintains material integrity, and removes the need for mechanical fasteners. Nonetheless, the irreversible behavior of traditional adhesives and the challenges associated with cleanly separating bonded parts hinder the recovery and reuse of joints, ultimately restricting recyclability and sustainability. Traditional cleaning methods, such as mechanical abrasion or chemical etching, often involve multiple steps, generate hazardous waste, and can damage the substrate or leave contaminants that compromise adhesion quality [79, 80]. Laser cleaning, based on controlled ablation, offers a highly efficient, precise, and environmentally friendly alternative by eliminating organic residues and weak boundary layers without introducing harmful chemicals or excessive thermal effects on the substrate [81, 82, 83, 84]. This process not only restores the surface to an optimal condition for subsequent bonding but also enhances physicochemical properties such as roughness, surface oxidation, and wettability, which are essential for achieving strong and durable adhesive joints [85, 86].

In addition, laser cleaning can be automated and integrated into industrial production lines, reducing processing time and improving consistency compared to conventional methods [82, 83]. Its ability to selectively remove contaminants while tailoring surface morphology makes laser cleaning a promising solution for modern manufacturing challenges where performance, sustainability, and cost-effectiveness are paramount.

In the proposed case study, laser cleaning is evaluated to remove the residual epoxy adhesive layer on Al 6061 substrates after debonding. The resulting surface morphology is analyzed, and the shear strength of the re-bonded joints is measured.

There are different mechanisms whereby radiation can remove material from the surface:

- Evaporation processes– selective vaporization, ablation;
- Impact processes– spallation, evaporative pressure, photon pressure, dry and steam cleaning, laser shock cleaning;
- Vibration processes (based on acoustic or thermoelastic forces)– transient thermal heating, angular laser cleaning.

Here, the approaches followed were mainly two: ablation of only the thermosetting epoxy resin or blowing out the resin by focusing on the Al-adhesive interface. Thus, the wavelength was selected based on two tests, the first with 355 nm and the other with 1064 nm. However, aluminum was immediately attacked by UV, and at the same time, the resin is not transparent to near-IR. At high laser energy, both the tested wavelengths had effects on epoxy resin, which was mainly visible as discoloration and ablated surfaces. In addition to the laser wavelength, the characteristics of the irradiated material also influenced the laser-induced reaction. To increase processing productivity, the wavelength chosen as definitive was 1064 nm, benefiting from greater power and energy per pulse. Laser parameters are in the Table 12.

Table 12: Laser parameters for laser cleaning.

IR (1064 nm)	**Scanning strategy**	**Frequency [kHz]**	**Mark speed [mm/s]**	**Overlap [%]**	**Power [W]**	**Passes [-]**	**Fluence [J/cm^2]**
Cleaning	Parallel lines	400	2000	60	2.0-2.2	20+	6.37-7.0

With several passes, the adhesive was removed, as visible in Figure 81, and the thickness of the substrates after laser cleaning was measured to ensure that the usable thickness of the substrate had not been reduced. Ultrashort ablation leaves a micrometric roughness on the surface, but the parameters can be tuned to obtain LIPSS structure on the exposed aluminum. LIPSS surface modifications of the substrate affect its morphology, chemical composition, and wettability, so the bonding performance.

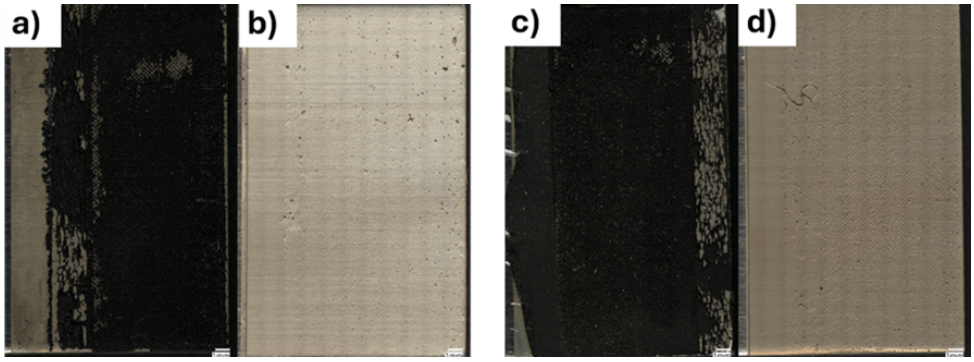

Figure 81: Untreated (a,c) versus laser cleaned (b,d) adherend surfaces. [10]

Lap shear tests were conducted to evaluate the mechanical performance of adhesively bonded joints before and after debonding treatments, and before laser cleaning treatment. The tests were performed at the DIME Laboratory of the University of Genoa using an Instron 8802 universal testing machine. The specimens were prepared in accordance with ASTM D1002. The bonding area was defined by using masking tape to ensure consistent overlap geometry. The adhesive was dispensed using a manual applicator equipped with a 2:1 ratio plunger and static mixer to ensure proper resin-hardener mixing. After assembly, the joints were subjected to uniform pressure to eliminate excess adhesive and to shape the fillet, minimizing stress concentrations at the edges. The specimens were then cured at ambient temperature for 24 hours, followed by a post-curing cycle at 80°C for 1 hour, as recommended by the adhesive manufacturer.
Lap shear tests were executed using the Blue Hill software to define the testing protocol. The specimens were loaded at a constant displacement rate of 1.3 mm/min. To ensure pure shear loading, spacers matching the specimen thickness were placed in the grips to prevent bending in the overlap region. The tensile shear strength (TSS) was calculated for each specimen, and the failure surfaces were analyzed to determine the mode of fracture (adhesive, cohesive, or substrate failure). Figure 82 shows that, across various debonding methods, laser cleaning leads to a slight increase in the tensile lap-shear strength of the re-bonded joints.

This precise, non-contact process enabled the effective rebonding of single-lap

[10]Siciliani V., Benvenuto M., Mandolfino C., Reggiani B., Orazi L., *Enabling the reuse of single-lap adhesive-bonded joints through laser cleaning and texturing*, Esaform 2026 Conference (Accepted for publication).

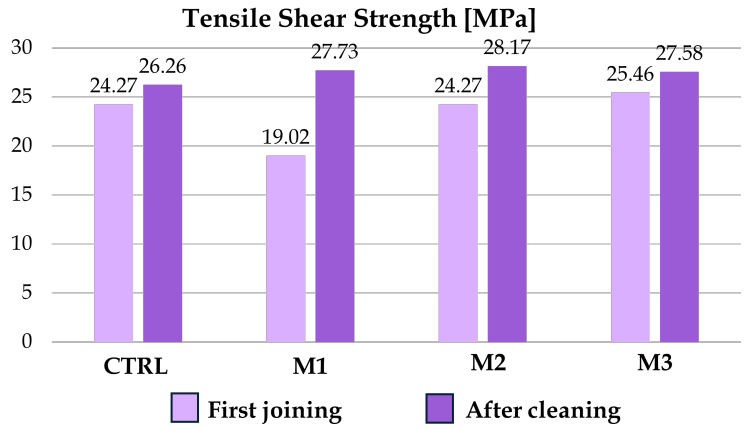

Figure 82: Shear strength before and after laser cleaning, using different debonding methods (M1, M2, M3), and with respect to the control (CTRL).

joints, supporting repair and recycling initiatives. By integrating laser cleaning into the lifecycle of adhesive-bonded assemblies, component lifespan can be extended, reducing waste and promoting a circular economy.

For comparison, laser pre-treatment before bonding was assessed to evaluate if it can increase the shear strength of the joint before bonding it for the first time. For this study, the focus was on the best debonding method among the four investigated in previous tests. After bonding and mechanical testing, joints were debonded using an electrothermal method based on Joule heating through an embedded stainless-steel mesh, which softened the adhesive without damaging the substrate. Post-debonding, laser cleaning was performed to remove residual epoxy and restore the surface. Then, after cleaning, texturing can be done on the exposed aluminum. In this way, the two processes, which are essential for improving performance, can be carried out using a single technology. The methodology scheme is presented in Figure 83. Surface characterization included wettability tests using standardized inks, optical and scanning electron microscopy for morphology, and profilometry for roughness. Mechanical performance was validated through lap shear tests following ASTM D1002 standards.

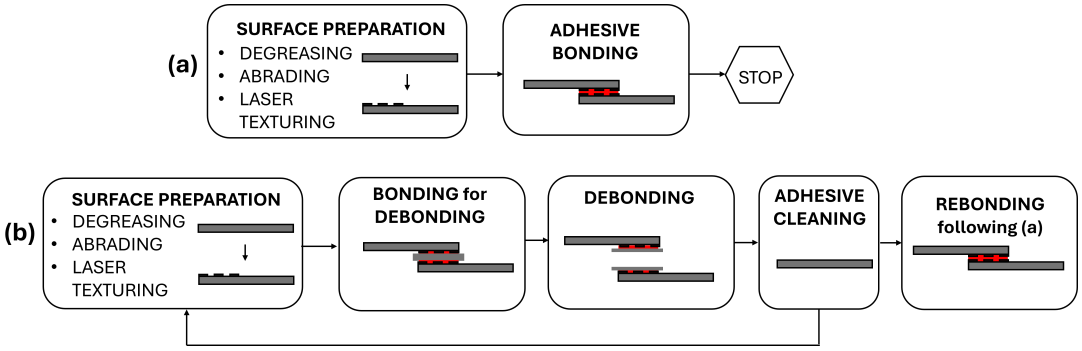

Figure 83: Laser cleaning and texturing methodology scheme. [11]

Different types of textures can be created. To take advantage of the high processing speed, LIPSS were chosen, as shown in the SEM image in Figure 84. This treatment aimed to enhance hydrophilicity, as shown in Figure 85, and mechanical interlocking. Laser parameters are in the Table 13.

Table 13: Laser parameters for texturing Aluminum substrates.

IR (1064 nm)	Scanning strategy	Frequency [kHz]	Mark speed [mm/s]	Overlap [%]	Power [W]	Passes [-]	Fluence [J/cm^2]
LIPSS texturing	Parallel lines	333	1200	50	0.3	3	0.96

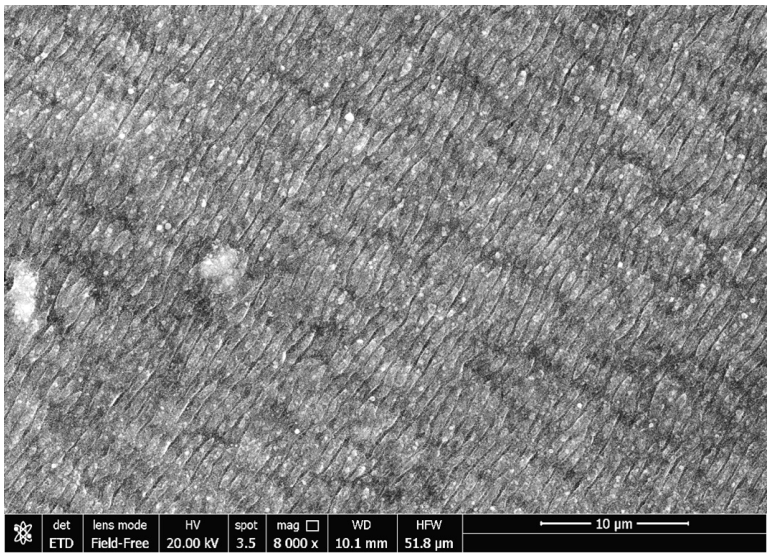

Figure 84: LIPSS structures on Aluminum surface.

[11] Ivi, p.139

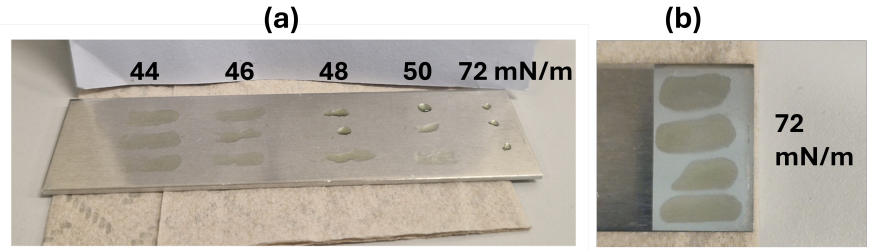

Figure 85: Surface tension evaluation on untreated versus LIPSS textured Aluminum. [12]

Laser texturing before initial bonding significantly improved joint strength, increasing lap-shear resistance and energy absorption compared to conventional abrasion and degreasing methods, see Figure 86. Fracture analysis revealed a transition from adhesive failure in untreated samples to cohesive failure in textured joints, confirming enhanced adhesion. After debonding, laser cleaning effectively removed adhesive residues and restored surface properties without chemical or mechanical damage. Wettability tests showed hydrophilic behavior with surface tension values reaching 72 mN/m, indicating excellent adhesion potential. Morphological analysis confirmed the presence of uniform LIPSS after cleaning, while roughness measurements demonstrated micrometric features favorable for bonding. Rebonded joints exhibited improved mechanical strength compared to untreated surfaces, with laser-cleaned samples outperforming those prepared by abrasion. Combining cleaning with post-treatment texturing provided additional gains in strength, although the improvement was marginal compared to cleaning alone, suggesting that laser cleaning inherently imparts beneficial surface characteristics. Overall, the approach enabled controlled debonding and effective rebonding, supporting component reuse without compromising structural integrity.

This case study demonstrates that laser cleaning and texturing are viable strategies for extending the lifecycle of adhesive joints by enabling clean disassembly and high-performance rebonding. The dual functionality of lasers—precise removal of residual adhesive and creation of optimized surface topographies—offers a sustainable alternative to conventional methods, aligning with circular economy principles. The findings highlight the potential of integrating laser-based

[12] Ivi, p.139

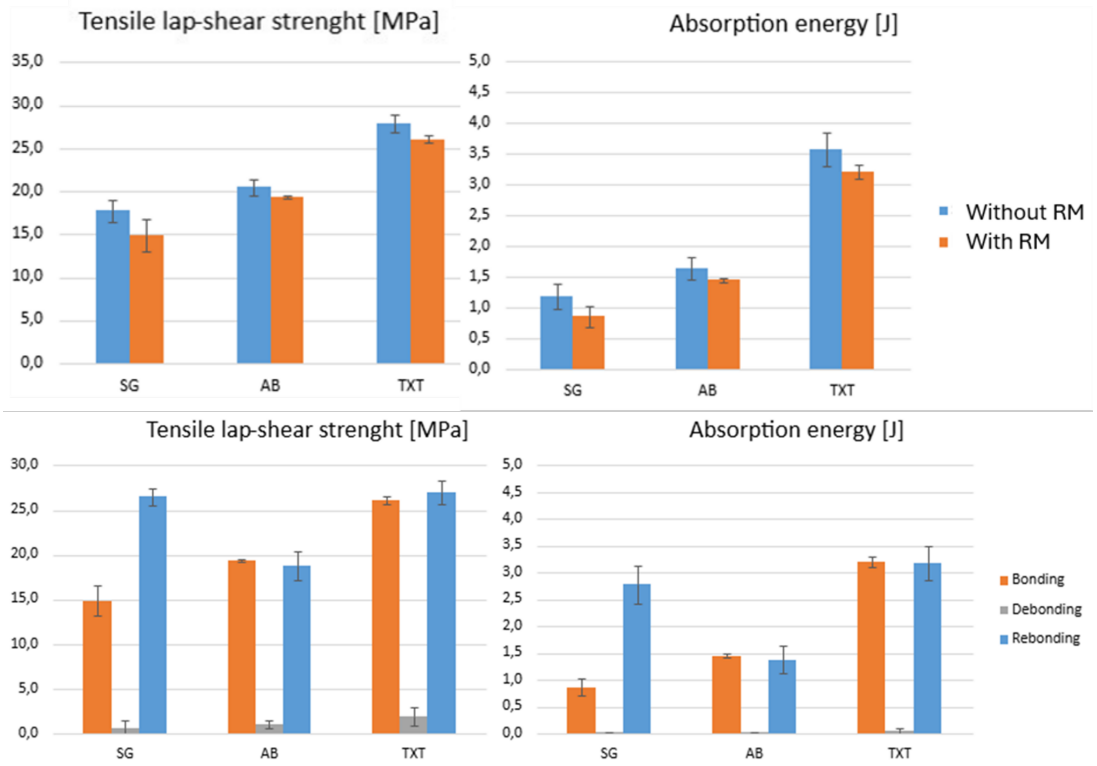

Figure 86: Shear strength and absorption energy for degreased (SG), abraded (AB), and textured (TXT) Aluminum substrates, before and after debonding.

processes into industrial repair and recycling workflows to reduce waste and improve resource efficiency.

5.3 Laser-based surface functionalization

5.3.1 Tuning polymer and metal wettability

Polyimide films such as Kapton are widely used in electronics, aerospace, and microfluidic applications due to their excellent thermal stability, chemical resistance, and mechanical properties. However, their inherently low surface energy results in poor wettability, limiting their performance in processes requiring strong adhesion or fluid interaction. Traditional methods like plasma and flame treatments can enhance wettability by inducing oxygen-containing functional groups, but they often lack precision and uniformity at the micro- and nanoscale, leading to inconsistent surface properties and potential defects [87, 88].
Ultrafast laser texturing is a favorable alternative, offering precise, controllable, and environmentally friendly surface modification. By adjusting laser parameters, it is possible to tailor both surface chemistry and morphology, creating micro- and nano-structures such as LIPSS that significantly influence wetting behavior [89]. Recent studies have demonstrated that picosecond and femtosecond laser irradiation can transform Kapton from hydrophobic to hydrophilic, reducing water contact angles by more than 20° and enabling superhydrophilic states under optimized conditions [90, 91, 92]. This approach not only improves wettability but also provides flexibility for patterning functional surfaces for advanced applications, making laser treatment a fast, repeatable, and scalable solution compared to conventional techniques [93].
In the proposed case study, thin Kapton foils (25 μm thickness) were processed using the picosecond laser irradiation at 355 nm. Two scanning strategies were tested: parallel lines spaced at 5 μm for uniform energy distribution, hereinafter also referred to as "KP1-4", and a combined approach of parallel lines followed by a perpendicular grid to generate multiscale textures, hereinafter also referred to as "KG1-2". The combination of scanning speed, pulse energy, and overlap (50% along and between scan lines) was optimized to minimize surface damage,

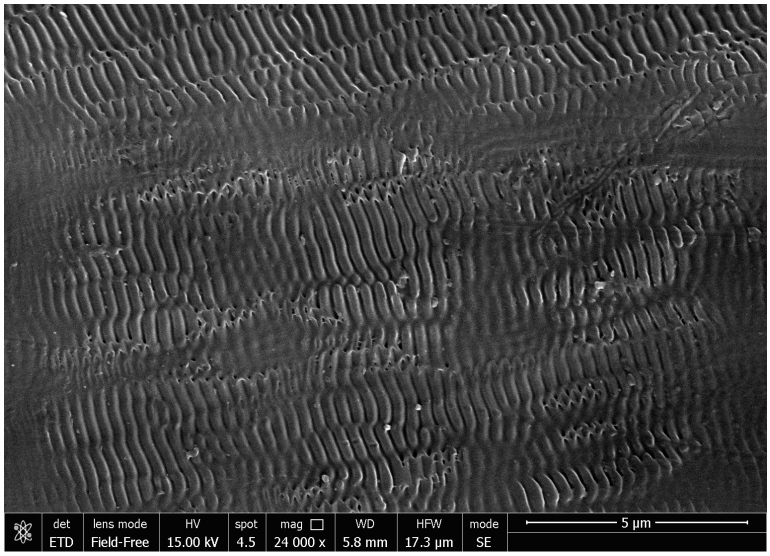

Figure 87: SEM images of LIPSS on Kapton [94].

and four energy levels (0.66–1.92 μJ per pulse) were tested from "KP1" to "KP4" to determine the threshold for effective texturing without burning, while KG1 and KG2 varied in terms of the distance between the grid lines, between 40 μm and 60 μ m. The optimal laser parameters are in Table 14. Morphological characterization was performed using SEM and AFM to analyze surface topography and roughness, while wettability was assessed through surface tension tests using standardized inks and contact angle measurements via the sessile drop method. Measurements were repeated immediately after treatment and after 24–48 hours to evaluate stability.

The threshold fluence for ablation was estimated at 1.07 J/cm^2, and the 1.92 μJ fluence condition was identified as the upper limit before visible burns and remelting occurred.

Table 14: Laser parameters for Kapton texturing.

UV (355 nm)	**Scanning strategy**	**Frequency [kHz]**	**Mark speed [mm/s]**	**Overlap [%]**	**Power [W]**	**Passes [-]**	**Fluence [J/cm^2]**
LIPSS	Parallel lines	333	1500	50	0.34	1	1.07
Texturing	Grids	333	1500	-	0.28	3	1.45

Laser texturing successfully generated LIPSS with a periodicity of approximately 338 nm, oriented along the polarization direction. These structures were classified as Long Spatial Frequency LIPSS (LSFL II), as visible in Figure 87 and

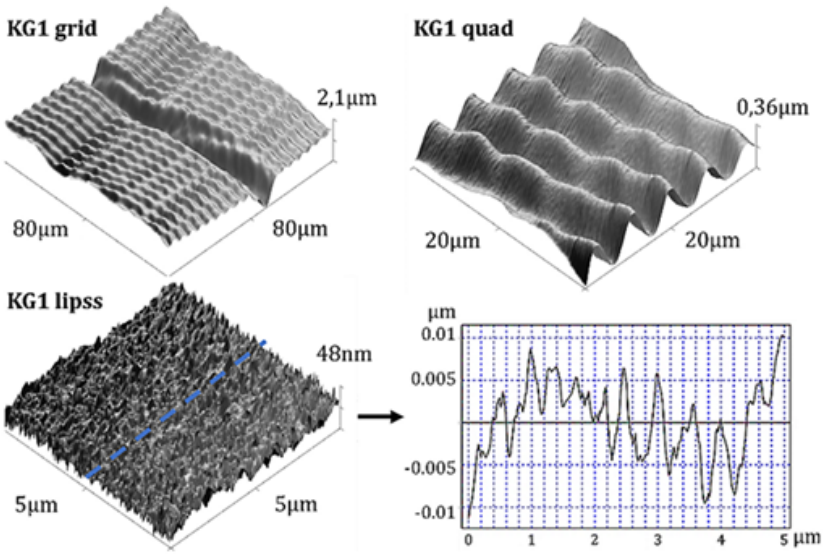

Figure 88: AFM topography of LIPSS textured Kapton: KG1 sample with a line spacing of 40 μm, at different magnifications to analyze LIPSS [94].

Figure 88. Increasing pulse energy improved wettability up to an optimal level (0.84 μJ), beyond which remelted zones appeared, reducing surface uniformity. The uniform parallel-line strategy produced highly regular LIPSS, while the grid approach created multiscale textures with increased roughness (up to 200 nm), which slightly reduced hydrophilicity compared to uniform LIPSS but remained beneficial for adhesion applications, see Figure 89 and Figure 90. Wettability tests revealed a dramatic improvement: untreated Kapton exhibited a contact angle of about 99° and a surface tension below 40 mN/m, indicating strong hydrophobicity. After laser treatment, the surface tension reached 72 mN/m (that of water), and the contact angle dropped to as low as 45.5° for parallel lines (0.84 μJ), confirming a transition to hydrophilic behavior. These effects were stable over time and attributed to both morphological changes and chemical modifications induced by laser processing. The grid strategy also improved wettability, though to a slightly lesser extent, likely due to a shift from Wenzel to Cassie-Baxter wetting regimes caused by air entrapment in the grid structures. [94]

Preliminary tests following the work have shown that the results obtained allow for better adhesion in the coupling of these components for functional performance and applications in microelectronics, biomedical devices, and advanced

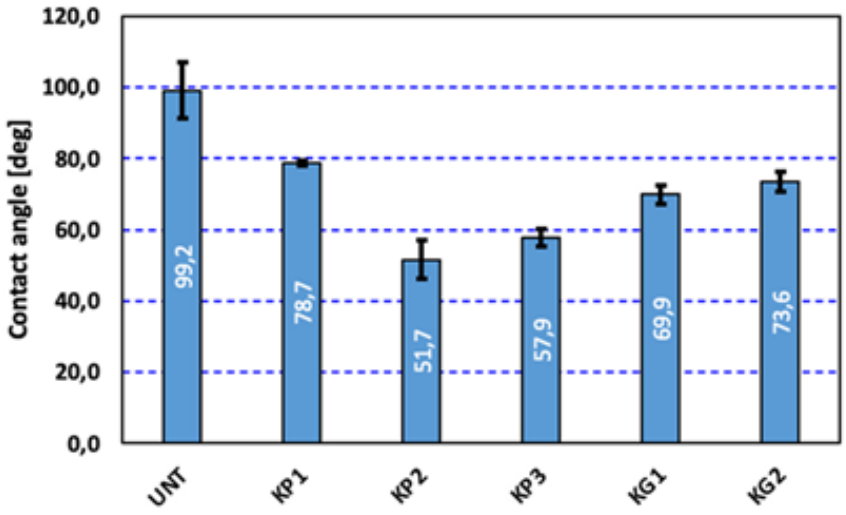

Figure 89: Contact angle measurement for evaluating wettability modification of Kapton: KP1-KP4 represent parallel lines with different energy per pulse, with the optimum in KP2 (0.84 μJ), while KG1-KG2 represent the combined structure of grid and parallel lines where the distance between the lines changes, with the optimum in KG1 (40 μm) [94].

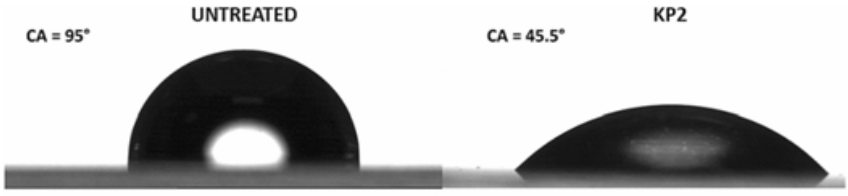

Figure 90: Contact angle measurement of untreated Kapton and Kapton with parallel line texture "KP2" [94].

manufacturing. Figure 91 shows the adhesive trapped in the surface texture created. High flexibility, repeatability, and short processing times make laser texturing a promising alternative to conventional treatments such as plasma or chemical methods.

The second case study explores the use of ultrashort pulsed laser technology to modify the surface of Ti6Al4V titanium alloy, aiming to enhance its bioactivity for dental implant applications. This application will be explained in detail in the following paragraph. Here it is reported the initial studies on the wettability of titanium.

The laser texturing process was performed using a wavelength of 532 nm to exploit the minimum available beam size. Laser parameters are in Table 15.

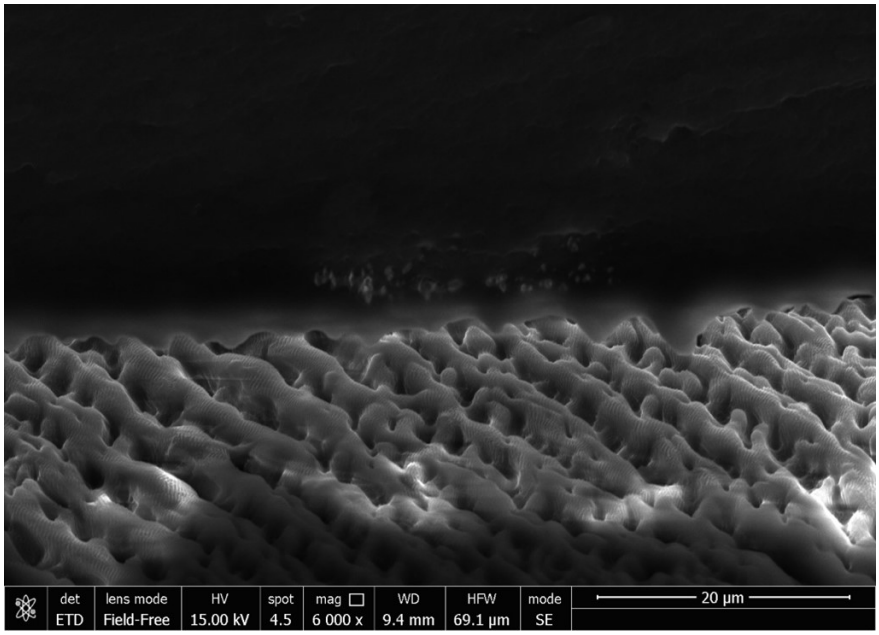

Figure 91: SEM images of adhesive penetration into the texture on the Kapton surface.

The laser was applied to 10 mm diameter titanium discs to create micro- and nanostructured textures. Three main surface designs were developed and characterized:

- Micrometric circular pockets (40 μm diameter, 5–10 μm depth), designed to mimic osteoclastic resorption pits;
- Nanometric LIPSS, applied to enhance protein adsorption and cellular adhesion;
- Hierarchical textures, combining grid-patterned grooves (100 μm wide), circular pockets, and LIPSS, which are intended to promote osteogenic and angiogenic responses synergistically.

Table 15: Laser parameters for Titanium texturing.

GR (532 nm)	**Scanning strategy**	**Frequency [kHz]**	**Mark speed [mm/s]**	**Overlap [%]**	**Power [W]**	**Passes [-]**	**Fluence [J/cm^2]**
LIPSS	Parallel lines	400	1200	70	0.04	1	0.19
Texturing (circles)	Parallel cross lines	1000	150-1000	70	0.20	2	0.25
Texturing (grid)	Parallel lines	1000	1000	70	0.20	10	0.25

Surface morphology was validated using scanning electron microscopy (SEM),

confirming the reliability and reproducibility of the laser-induced patterns, see Figure 92.

A key result of the study was the characterization of surface wettability, mea-

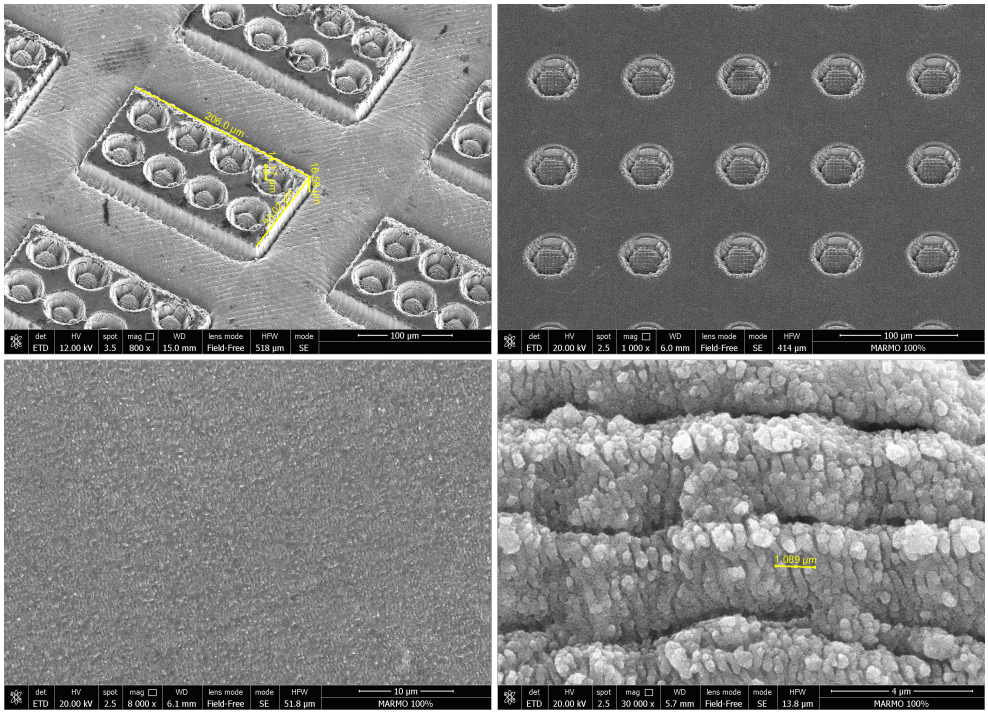

Figure 92: SEM images of Titanium texturing for increasing bioactivity.

sured via contact angle analysis and the sessile drop method. The hierarchical texture, including grooves, pockets, and LIPSS, exhibited a significantly reduced contact angle of 18.6°, indicating high hydrophilicity. In contrast, the machined control surface showed a contact angle of 65.1°, and surfaces with only pockets or LIPSS showed moderate reductions individually, see Figure 93 and Figure 94. Scientific literature indicates that moderate hydrophilic surfaces (contact angles between 60° and 80°) are optimal for promoting osseointegration. Extremely hydrophilic surfaces may enhance initial protein adsorption and cell adhesion but could hinder cellular motility. The texture combining circular pockets and LIPSS, with a contact angle of 60.6°, falls within this optimal range and was therefore selected as the final design for subsequent biological assays.

Textures	Average CA [°]
Machined	65.1
Circular Pokets	53.9
Circular Pokets + LIPSS	60.6
LIPSS	65.7
Hierarchical structure with Grids	18.6

Figure 93: Contact angle measurements of textured Titanium.

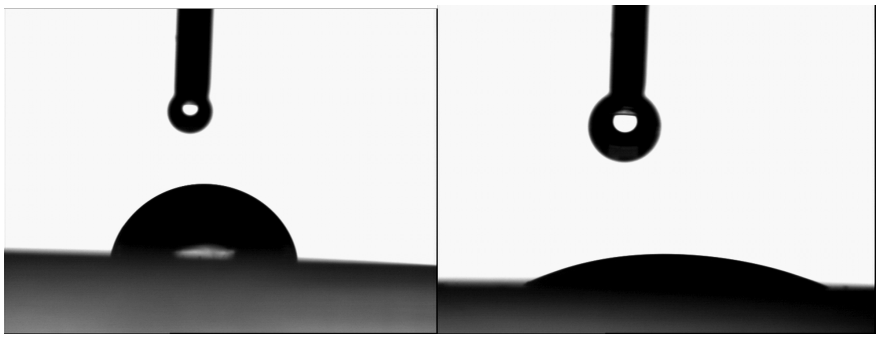

Figure 94: Deposited droplet on untreated versus textured Titanium.

5.3.2 Improving titanium biocompatibility

Laser texturing showed potential in improving the biocompatibility of titanium implants by creating controlled surface topographies that influence cellular responses. Unlike conventional methods such as grit blasting or acid etching, which produce random roughness, laser processing enables precise fabrication of micro- and nano-scale features that mimic natural bone architecture and enhance osteointegration. Experimental studies have shown that microgrooves and pits can promote vascularization and osteoblast adhesion, while nanoscale structures like laser-induced periodic surface structures and nanopillars significantly improve matrix mineralization and osteogenic differentiation of mesenchymal stem cells (MSCs) compared to polished surfaces [95, 96]. Furthermore, hierarchical patterns combining microcolumns and nanostructures have demonstrated superior performance in guiding cell motility and adhesion, supporting early bone formation [97]. Wettability and surface free energy, critical factors for cell attachment,

are also enhanced by laser texturing, with groove dimensions and intersecting angles influencing hydrophilicity and protein adsorption [98, 99]. Recent in vivo studies confirm that laser-generated μ-room and groove topographies achieve higher bone-to-implant contact and secondary stability than machined surfaces, highlighting the potential of laser texturing as a biomimetic approach to optimize implant integration and long-term success [100, 101]. In addition, femtosecond laser texturing on Ti grade 5 dental implants demonstrated that LIPSS significantly improve osteogenic cell adhesion and proliferation in vitro, with treated surfaces showing up to 98.3% resazurin reduction after 7 days compared to 82.1% on untreated controls. These improvements are attributed to the increased surface area and the presence of nanostructures that facilitate protein adsorption and cellular attachment [102].

A preliminary study investigates the use of ultra-short laser texturing to modify the surface of Ti6Al4V alloy, aiming to improve its interaction with biological environments and facilitate coating adhesion. Titanium alloys are widely used in biomedical implants due to their mechanical properties, but they face challenges such as limited tissue integration. Surface functionalization through laser processing offers a promising route to overcome these limitations by tailoring topography and chemistry without compromising bulk properties. Polished Ti6Al4V discs were textured using 1064 nm, and attenuated power below 1 W, see Table 16. Two distinct patterns were generated: a grid of protruding pillars (LTG) and a grid of recessed wobbles (LTW), both incorporating micro-scale features and nano-scale laser-induced periodic surface structures (LIPSS). Surface characterization involved 3D profilometry (Confovis), as visible in Figure 95, SEM imaging, and ISO 25178 roughness analysis. Chemical composition was assessed via EDS and Raman spectroscopy, see Figure 96, while microstructural integrity was verified through cross-sectional analysis and nanoindentation. Wettability was evaluated using static contact angle measurements with a chitosan-based solution, simulating conditions for potential bioactive coatings.

Laser texturing significantly altered surface topography, increasing roughness parameters compared to polished references (Sa rose from 0.05 μm to 2.22 μm for LTG and 3.48 μm for LTW). Both textures exhibited hierarchical structures, combining micro-channels or slots with nanoscale ripples. Microstructural anal-

ysis confirmed minimal thermal impact, with no detectable alterations beyond a few microns below the surface. Raman spectroscopy revealed localized rutile formation at peripheral zones, suggesting enhanced chemical reactivity without compromising substrate integrity. Wettability tests demonstrated that all samples were hydrophilic (contact angles <90°), but laser-textured surfaces exhibited faster spreading dynamics than polished ones. LTW promoted greater liquid penetration and lower contact angles over time, while LTG maintained slightly higher angles, indicating potential for tuning coating adhesion through topography design. Drop anisotropy on textured samples reflected directional patterns, which could influence coating uniformity and biological responses.

The findings highlight that ultra-short laser processing can effectively engineer

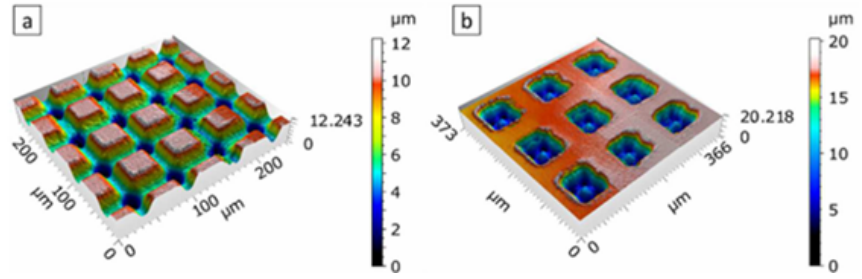

Figure 95: CNF profilometer of wobble and grid texturing on Titanium [103].

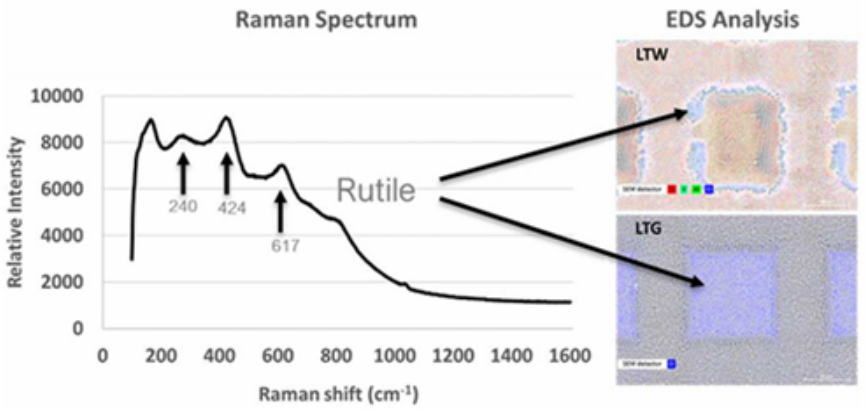

Figure 96: Raman spectrum wobble and grid texturing on Titanium [103].

surface features at multiple scales, improving conditions for mechanical interlocking and chemical bonding with polymer-based coatings such as chitosan. Enhanced wettability and controlled oxide formation suggest a favorable environment for osseointegration and coating adhesion. Importantly, these modi-

fications were achieved without inducing detrimental microstructural changes, preserving the mechanical reliability of the implant material. While wettability improvements indicate potential for better coating performance, the final biological outcome will depend on complex interactions between substrate, coating, and physiological environment, warranting further in vitro and in vivo studies [103].

The second case study aimed to optimize the surface properties of titanium alloy (Ti6Al4V) for dental implant applications by creating hierarchical micro- and nano-textures using ultrashort pulsed laser technology. The rationale was to mimic physiological bone resorption pits and collagen fiber residues, promoting osteoblast adhesion and endothelial cell organization to enhance osteointegration and angiogenesis.

Titanium discs (10 mm diameter, 3 mm thickness) were processed using the 532 nm picosecond pulsed laser. Laser parameters were tuned to produce three texture designs:

- Grid pattern with grooves and circular pits (100 μm grooves, 40 μm pits, depth 8–10 μm) combined with LIPSS of 400 nm.
- Grid with pits concentrated on raised areas, also incorporating LIPSS.
- Circular pits with LIPSS only.

The final design presented in Figure 97 was the third for the wettability results, for its reduced production time (≈12 min) and possible industrial scalability. The laser parameters are shown in Table 15, in the first two rows.

Table 16: Laser parameters for texturing titanium.

IR (1064 nm)	**Scanning strategy**	**Frequency [kHz]**	**Mark speed [mm/s]**	**Overlap [%]**	**Power [W]**	**Passes [-]**	**Fluence [J/cm^2]**
Wobble	Wobble	100	500	-	1.0	20	12.23
Grid	Grid	150	500	-	1.0	40	4.08

Surface characterization was performed via SEM to confirm dimensional accuracy and LIPSS formation, see Figure 98. Wettability was assessed using contact angle measurements, and biological performance was evaluated through in vitro assays with pre-osteoblasts (MC3T3) and endothelial cells (HUVEC) at the De-

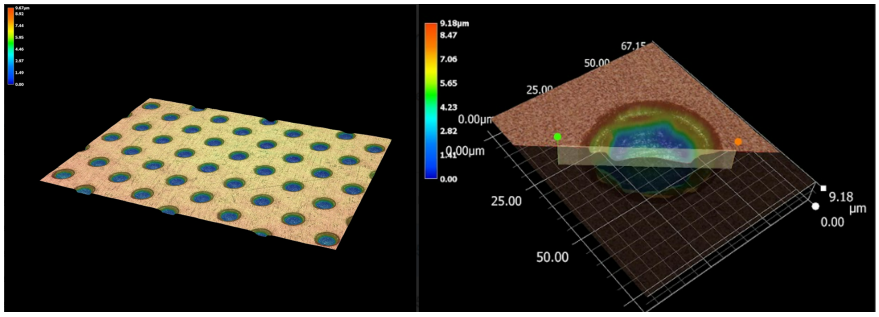

Figure 97: Profilometry of circular pockets on Titanium to increase bioactivity.

partment of Surgery, Medicine, Dentistry and Morphological Sciences with Interest in Transplant, Oncology and Regenerative Medicine of Unimore, in Modena. Cells were cultured in mono- and co-culture conditions, analyzed by confocal fluorescence microscopy and SEM for adhesion and cell morphology.

Contact angle analysis revealed that the definitive texture (pits + LIPSS)

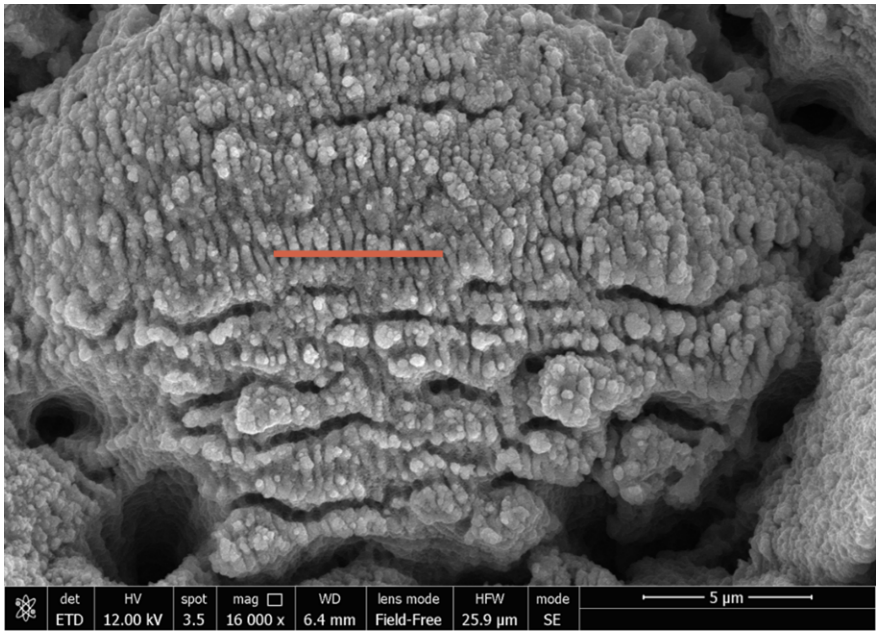

Figure 98: SEM images of LIPSS within circular pocket on titanium.

achieved moderate hydrophilicity ($\theta \approx 60.6°$), aligning with literature values favorable for osteointegration.

Osteoblasts adhered robustly to both micro- and nano-structured regions, forming numerous focal adhesions on LIPSS and extending filopodia across pits. Endothelial cells showed good affinity for nanostructured areas, but in some cases they are found inside circular pockets, organizing themselves into microcapillary-

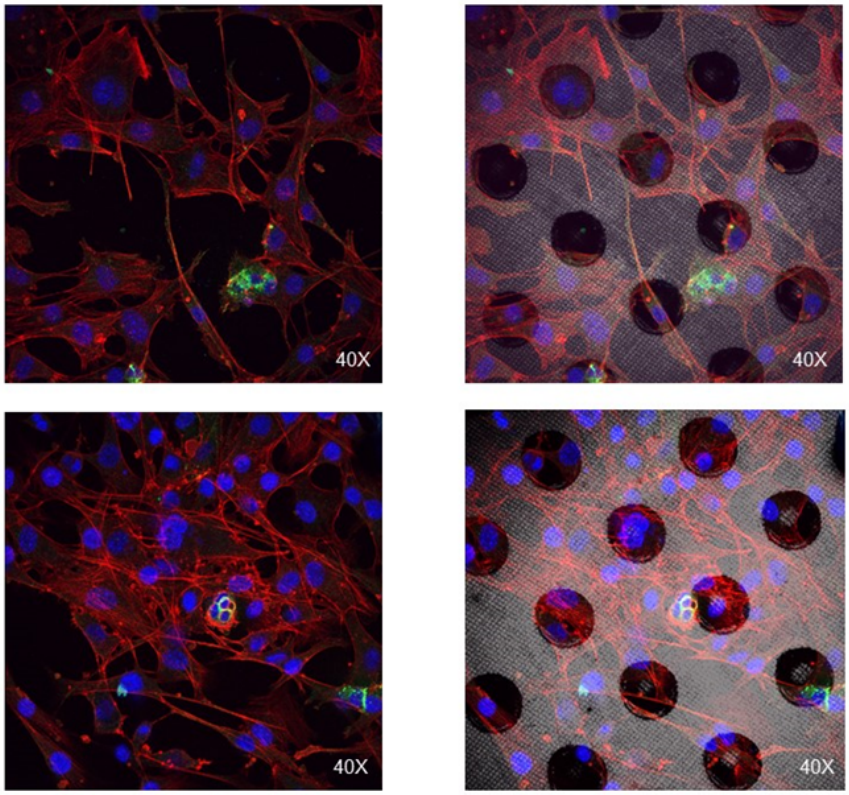

Figure 99: CNF images of osteoblast (marked in red and blue) and endothelial (marked in green) cell culture on textured titanium.

like arrangements.

Confocal imaging confirmed spatial distribution of both cell types, with osteoblasts dominating the surface and endothelial cells localizing within pits, as shown in Figure 99. SEM corroborated these observations, highlighting morphological adaptations to topography, as visible in Figure 100. The final texture combined biological efficacy with competitive processing times, supporting potential scale-up for implant manufacturing.

Laser texturing with hierarchical features promoted osteoblast adhesion and endothelial organization. The selected design demonstrated a balance between biological performance and production efficiency, suggesting strong potential for clinical translation. Future work should focus on optimizing endothelial cell density and performing differentiation assays to validate long-term functionality. Furthermore, it is necessary to evaluate the antibacterial behavior of the surface, as implants must be biocompatible for eukaryotic cells but at the same time

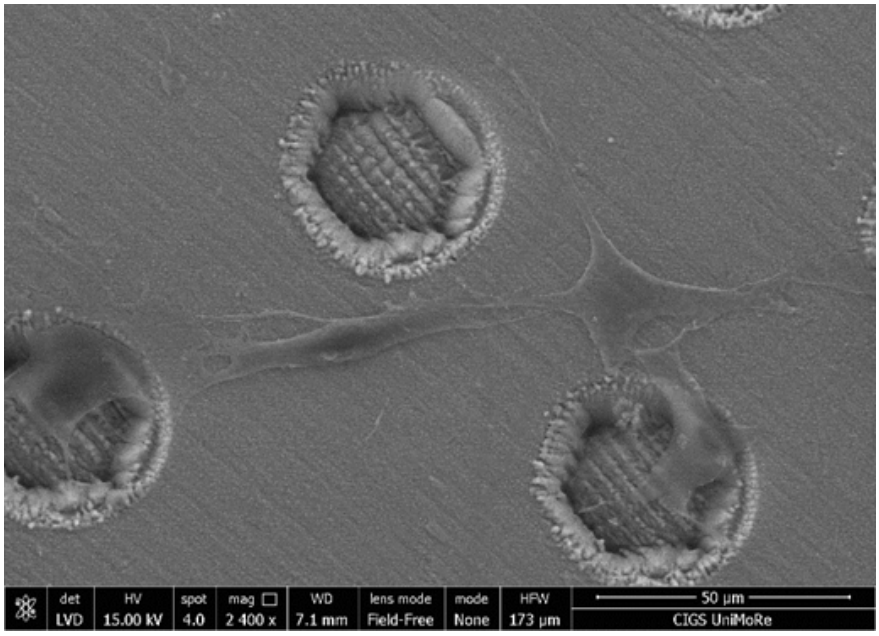

Figure 100: SEM images of osteoblast (ovoid-shaped) and endothelial (elongated shape) cells deposited on textured titanium.

inhospitable for bacteria.

The scalability and speed of the laser process must be optimized to make it suitable for industrial applications, offering a viable solution for the mass production of implants with enhanced osseointegrative properties.

5.3.3 Enhancing adhesive bonding strength

Adhesive bonding has become a preferred joining technique in aerospace, automotive, and structural applications due to its ability to reduce weight, distribute loads uniformly, and join dissimilar materials without introducing stress concentrations typical of mechanical fasteners. However, the performance of adhesive joints is highly dependent on the surface condition of the adherends. Surface pretreatment plays a critical role in enhancing adhesion by improving surface roughness, energy, and chemistry, which collectively promote mechanical interlocking and chemical bonding at the interface [104]. Traditional methods like sanding, grit blasting, and chemical etching, while widely used, often suffer from limitations including inconsistency, environmental hazards, and potential substrate damage [105]. In contrast, laser surface texturing has emerged as a superior alternative because of its precision, non-contact nature, and eco-friendly operation.

Laser texturing enables the creation of controlled micro- and nano-scale textures that significantly increase the effective bonding area and facilitate mechanical anchoring of the adhesive, while simultaneously modifying surface chemistry by introducing functional groups and removing contaminants [106]. Particularly, ultrashort pulsed laser offer significant advantages by minimizing thermal damage while enabling selective removal of contaminants and controlled surface structuring [107],[108]. For instance, IR nanosecond lasers have demonstrated the ability to remove silicone-based release agents from carbon fiber reinforced polymer (CFRP) surfaces without damaging the underlying fibers, leading to substantial improvements in adhesive joint strength and a transition from interfacial to cohesive failure [104]. Experimental studies have reported shear strength enhancements of up to 4.5 times compared to untreated or conventionally treated surfaces [108]. These improvements are attributed to the dual effect of increased surface roughness, which promotes mechanical interlocking, and the introduction of polar functional groups (e.g., hydroxyl, carbonyl) that enhance chemical bonding at the adhesive interface [109]. Moreover, laser-induced periodic surface structures (LIPSS) and microgroove patterns have been shown to further improve adhesion by increasing the effective bonding area and facilitating adhesive anchoring [107]. The durability of laser-treated joints under environmental stressors such as hydrothermal aging and water immersion has also been demonstrated, with laser-treated surfaces maintaining superior performance compared to those treated by conventional methods. These findings underscore the growing relevance of laser surface texturing as a transformative approach to surface engineering, offering a scalable and repeatable solution for enhancing the mechanical and environmental performance of adhesive-bonded joints in advanced composite structures.

The proposed case study addresses the challenge of improving adhesive bonding performance in carbon fiber reinforced polymer (CFRP) laminates produced by compression molding, where silicon-based mold release agents compromise adhesion. UV picosecond laser treatment is explored as an advanced, automated alternative surface preparation method before adhesive bonding. First, this technique is compared to conventional manual sanding. Then, two approaches were tested: cleaning treatment, with minimal matrix removal to eliminate surface

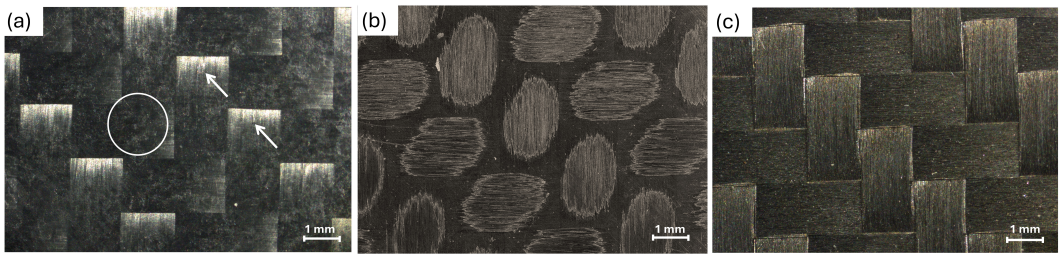

Figure 101: Stereoscope images of laser cleaning and matrix ablation treatment on CFRP [110].

contaminants; matrix ablation, to completely remove the matrix layer to expose carbon fibers.

CFRP panels were fabricated from automotive-grade prepreg and machined into single-lap joint specimens following ASTM D5868. Manual abrasion was performed using 240-grit sandpaper in a cross-hatch pattern, followed by cleaning with isopropyl alcohol. The laser treatment process involved scanning the bonding area with 45° parallel lines at 1000 mm/s, using optimized parameters (0.68 W power, 7 passes, 4 μm line spacing, fluence 2.88 J/cm^2) to ablate the matrix layer without damaging fibers, see Table 17.

Table 17: Laser parameters for CFRP composite texturing.

UV (355 nm)	**Scanning strategy**	**Frequency [kHz]**	**Mark speed [mm/s]**	**Overlap [%]**	**Power [W]**	**Passes [-]**	**Fluence [J/cm^2]**
Cleaning	Parallel lines	600	2000	60	1.5	8	3.20
Ablation	Parallel cross lines	600	2000	60	1.5	30	3.20

SEM/EDS analysis revealed that laser treatment achieved more uniform contaminant removal than manual abrasion (or manual sanding), reducing silicon content to 0.09% in the matrix and 0.02% near exposed fibers, compared to 0.21% for sanded surfaces, see Figure 102. A comparison between untreated and laser-treated surfaces, as observed under the stereoscope, is presented in Figure 101.

In matrix ablation conditions, fibers were exposed without visible damage, and laser-induced periodic surface structures (LIPSS) formed on fiber surfaces, potentially enhancing interfacial adhesion, as can be seen in Figure 103.

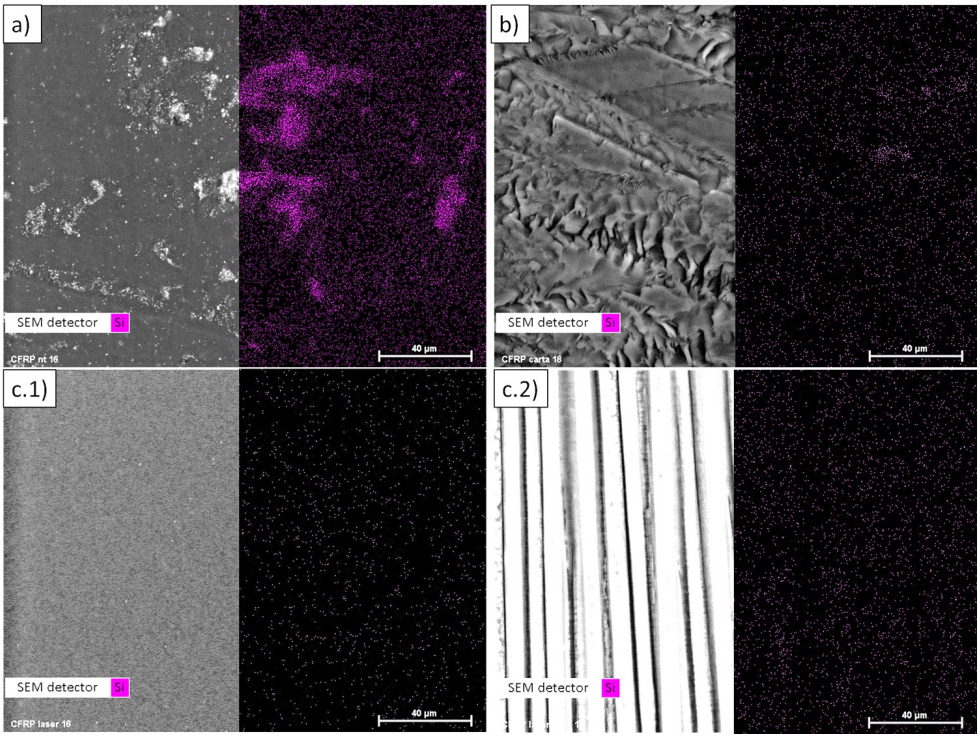

Figure 102: EDS mapping of untreated, manual abrasion, laser cleaning, and matrix ablation treatment on CFRP: Silicon is in pink colour, while Carbon is in black [111].

Mechanical performance was evaluated through tensile tests on single-lap joints bonded with a toughened epoxy adhesive (Loctite Hysol 9466), measuring load-displacement behavior and shear strength. Laser-treated joints exhibited higher maximum loads and greater displacement at failure, indicating improved energy absorption. Average shear strength increased from 14.5 ± 1.7 MPa for sanded joints to 16.8 ± 1.0 MPa for laser-treated ones—a 14% improvement. Another 16% improvement can be obtained with the matrix ablation condition. With respect to the untreated joints showing an average of 4.76 MPa, this represents up to 303% enhancement, see Figure 104. Failure mode shifted from predominantly adhesive (interface separation) in untreated samples to mixed cohesive and fiber-tearing in laser-treated joints, confirming stronger interfacial bonding, as visible in Figure 105.

The enhanced bonding performance is attributed to the laser's ability to remove release agents effectively and create a cleaner, more chemically active surface while preserving fiber integrity. Compared to manual sanding, laser treatment offers superior consistency, reduced variability, and potential for automation in

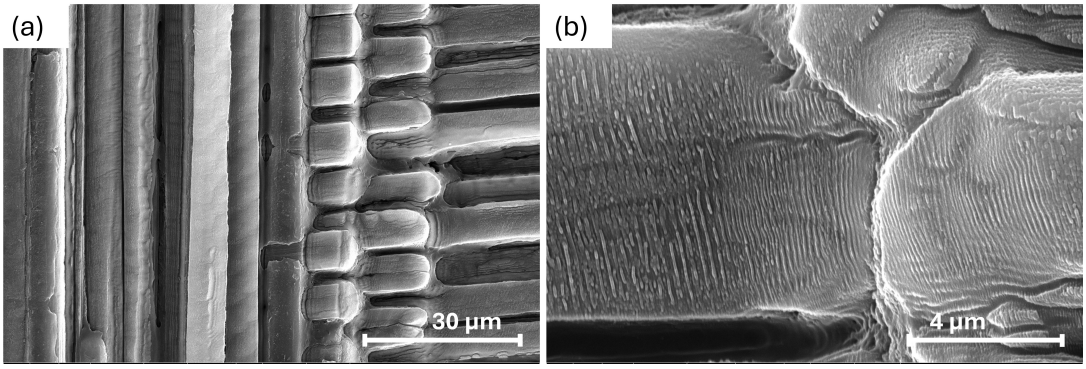

Figure 103: SEM images of LIPSS induced on the fiber of the CFRP composite [110].

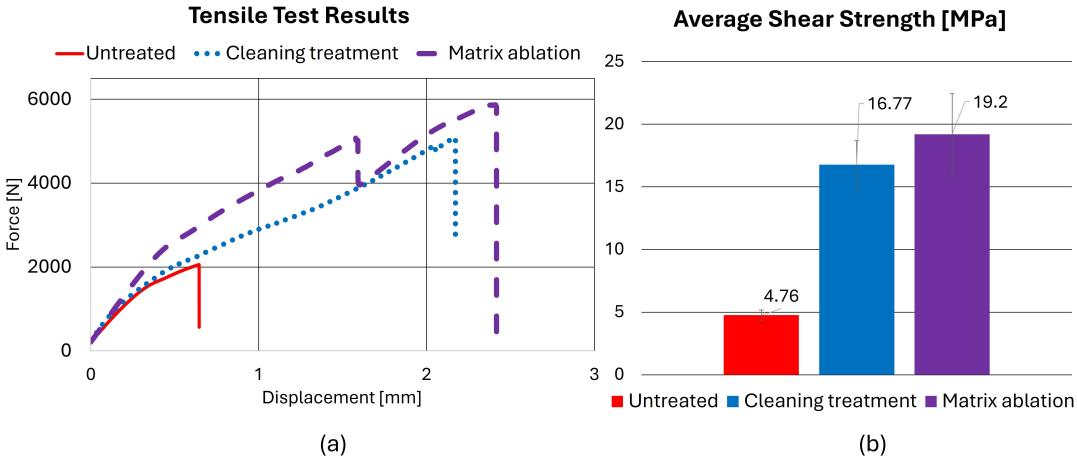

Figure 104: Shear strength of untreated versus cleaning and matrix ablation treatment on CFRP [110].

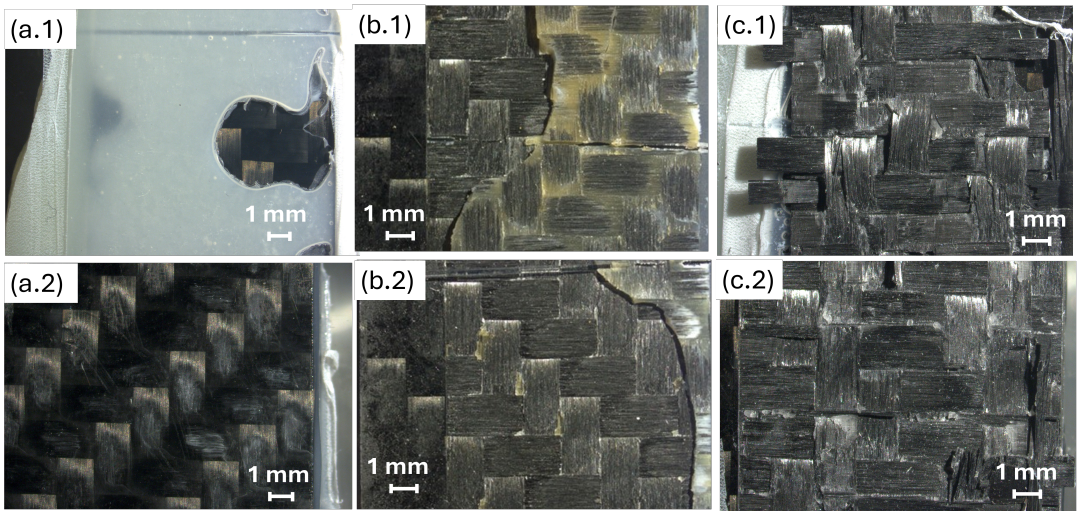

Figure 105: Fracture surfaces of untreated versus cleaning and matrix ablation treatment on CFRP [110].

industrial applications. Although the process parameters were not fully optimized, the observed improvements in shear strength and failure mode indicate significant potential for laser-based surface preparation in composite bonding. In addition, the formation of nanoscale LIPSS on exposed fibers opens new avenues for functionalizing composite surfaces, potentially improving both adhesive and interlaminar properties [111].

5.3.4 Enhancing electrochemistry: ion and solid-state batteries

Laser texturing of copper current collectors has emerged as a promising strategy to enhance the electrochemical performance of lithium-ion and zinc-based batteries by addressing limitations in interfacial adhesion and charge transport. Conventional smooth copper foils, widely used as anode current collectors, often suffer from weak bonding with active materials, leading to increased interfacial resistance, poor structural integrity, and accelerated capacity fading during cycling. Introducing micro- and nano-scale surface features through laser processing significantly improves adhesion, wettability, and electronic conductivity, thereby enabling higher rate capability and prolonged cycle life. Recent studies have demonstrated that femtosecond and nanosecond laser techniques can create hierarchical structures or crater-like morphologies on copper surfaces, increasing the effective surface area by up to 13% and reducing charge-transfer resistance by more than 50%, without compromising mechanical integrity. These modifications facilitate uniform slurry penetration, robust mechanical interlocking, and efficient ion transport, which are critical for high-energy-density systems and advanced chemistries such as silicon-based anodes. Furthermore, laser texturing offers scalability for industrial roll-to-roll processes, making it an attractive solution for next-generation batteries requiring both high power and long-term durability [112, 113, 114].

Two parallel studies were conducted to evaluate the electrochemical performance of laser-modified current collectors: a preliminary study to evaluate zinc deposition, and a more advanced study to evaluate the performance of lithium-based coin cells.

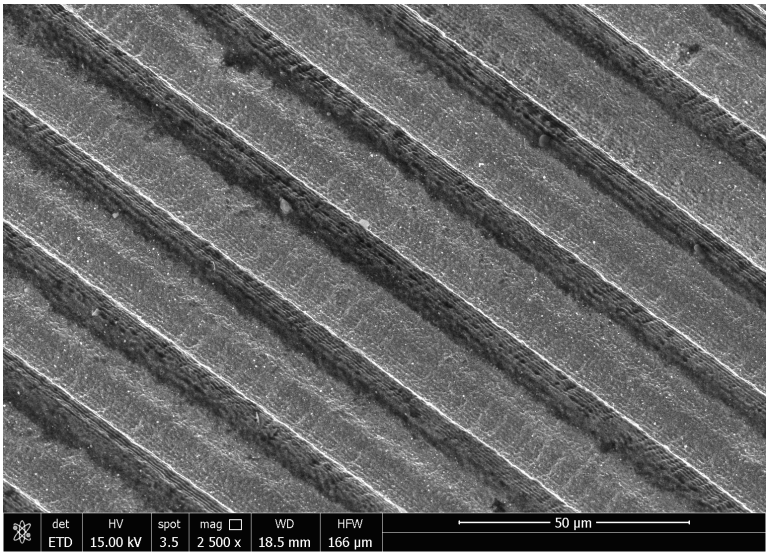

Figure 106: Groove texturing on 100 μm copper surface.

Commercial copper foils (10 and 100 μm thick) were prepared by chemical cleaning and sonication to remove oxides and contaminants. Laser texturing was done using the 1064 nm wavelength to use the maximum available power. Equispaced parallel grooves with a 20-30 μm pitch, with different depths, and LIPSS were evaluated as textures. The process parameters were chosen to impose the lowest possible heat input on the material without requiring long processing times, but they can be further optimized. For example, processing time for 39x39 mm^2 grooves is 2:30 minutes, and for LIPSS texturing is 3:40 minutes. Laser parameters for 100 μm Cu texturing are in Table 18. A SEM image of the 15 μm deep grooves is reported in Figure 106.

Table 18: Laser parameters for 100 μm Copper texturing.

IR (1064 nm)	**Scanning strategy**	**Frequency [kHz]**	**Mark speed [mm/s]**	**Overlap [%]**	**Power [W]**	**Passes [-]**	**Fluence [J/cm^2]**
Grooves	Parallel lines	500	1000	-	6.0	4-15	15.3

For zinc-based batteries, electrochemical tests were conducted using a three-electrode cell with $ZnSO_4$ electrolyte. Copper samples served as working electrodes, graphite as counter electrodes, and Ag/AgCl as the reference. Zinc deposition was performed under two conditions: 10 mA/cm^2 for 20 minutes and 20 mA/cm^2 for 10 minutes, following the scheme in Figure 107. Results show

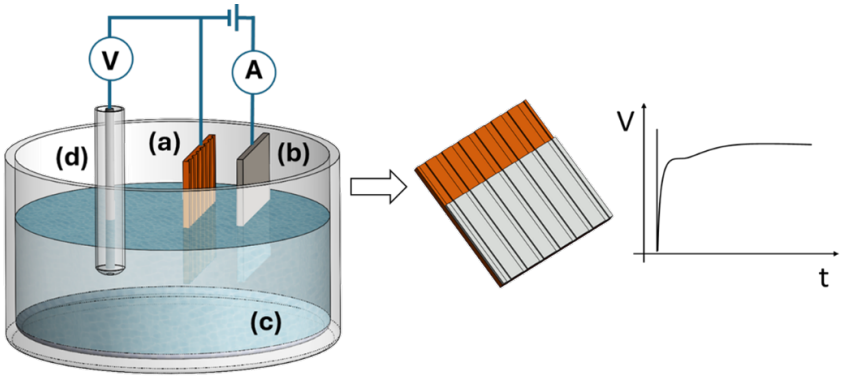

Figure 107: Zinc deposition scheme [115].

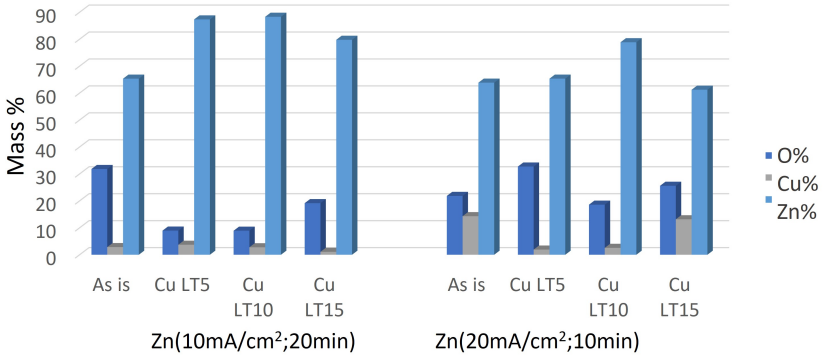

Figure 108: Mass percentage of Oxygen, Copper and Zinc of untreated and laser treated copper.

that laser texturing influenced zinc plating behavior. Untreated copper exhibited uneven zinc deposition with extensive oxidation, particularly at high current densities, leading to poor surface coverage and exposed copper regions. In contrast, laser-textured samples showed uniform zinc deposition aligned with the groove pattern, as shown in Figure 109, and increased mass percentage of Zinc, see Figure 108. Voltage profiles during plating revealed lower overpotentials for deeper textures, indicating altered deposition kinetics due to increased surface complexity.

In tests conducted on anode-free lithium-based batteries, the copper substrate was 10 μm thick, therefore, the laser parameters were slightly revised to take into account the thermal input on the material. Two distinct architectures, micrometric grooves (GR5) and laser-induced periodic surface structures (LIPSS), were designed to increase surface area and modify current distribution during lithium

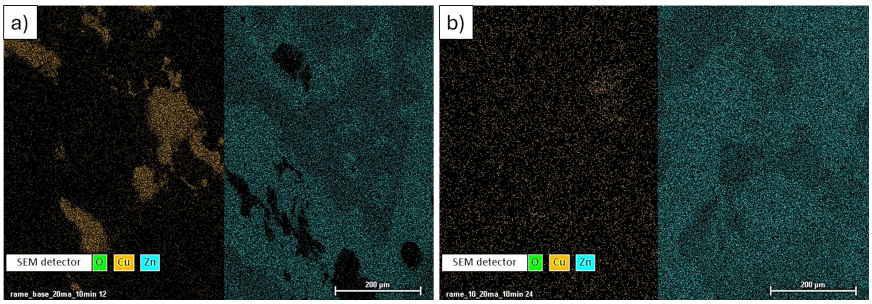

Figure 109: EDS mapping on untreated and laser-treated 100 μm copper [115].

deposition. Laser parameters are in Table 19. Profilometric and SEM analyses confirmed groove depths of approximately 5 μm for GR5 and sub-micrometer periodicity for LIPSS, with structures uniformly replicated across large areas. Electrochemical testing was performed in anode-free coin cells using LFP cathodes and commercial electrolyte, under controlled cycling protocols at capacities ranging from 0.5 to 2.5 mAh cm^{-2}. SEM/EDS in a glovebox complemented the electrochemical evaluation to correlate performances and lithium morphology with surface design.

Table 19: Laser parameters for 10 μm copper texturing.

IR (1064 nm)	**Scanning strategy**	**Frequency [kHz]**	**Mark speed [mm/s]**	**Overlap [%]**	**Power [W]**	**Passes [-]**	**Fluence [J/cm^2]**
LIPSS	Parallel lines	1000	1500	55	0.85	3	1.08
Grooves	Parallel lines	1000	2000	-	8.7	2-4	11.08

Figure 110 shows the profile and morphology of the structures obtained on the 10-micron copper sheet: even the grooves appear to be covered with LIPSS. While Figure 111 shows the deposition of lithium on copper after 6 minutes and 15 minutes.

The results confirmed that laser-induced morphology can guide lithium deposition, which deposits in greater quantities and much more uniformly in the case of laser treatment than in untreated batteries. Importantly, the performance of batteries with modified current collectors achieved a higher percentage state of health (SOH) for up to 50 cycles, while maintaining higher coulombic efficiency up to 35 cycles, as visible in Figure 112. The characterization was carried out by researchers from the Department of Chemical and Geological Sciences, in Mod-

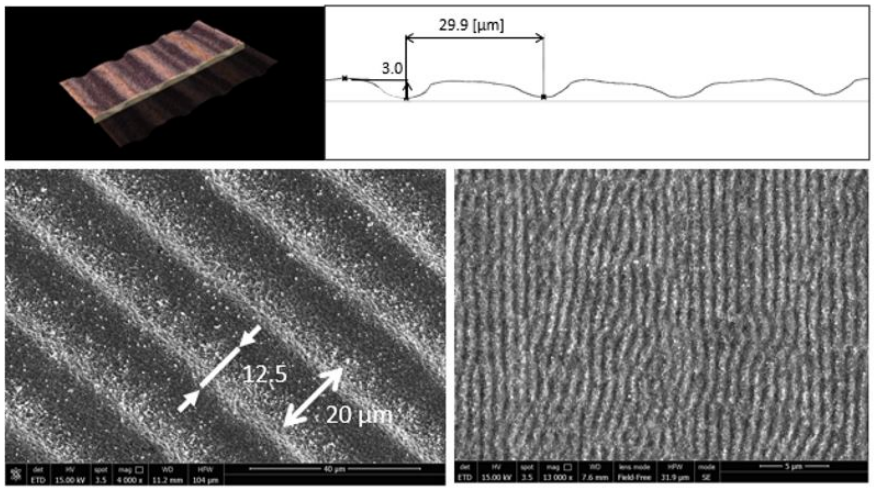

Figure 110: Profile and SEM images of 10 μm textured copper.

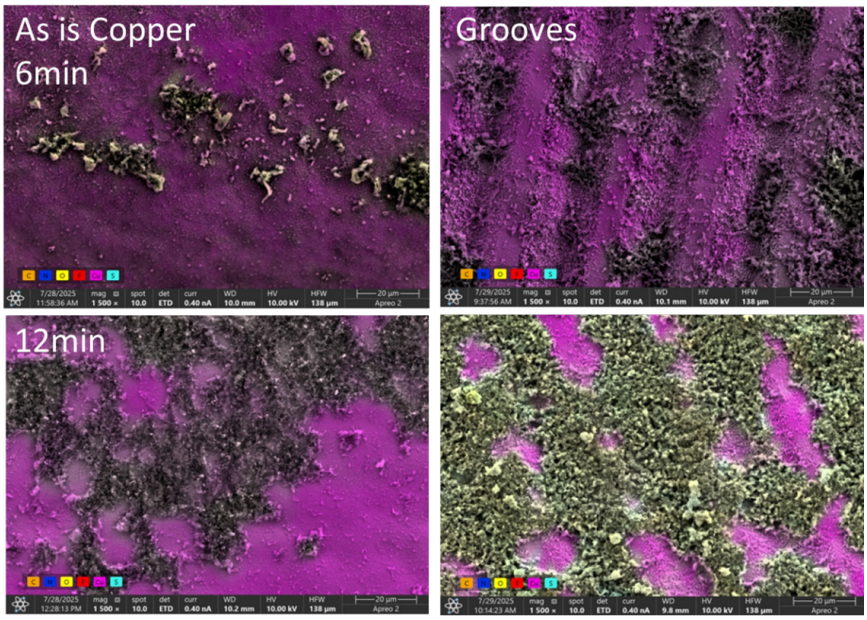

Figure 111: EDS mapping within glovebox to analyze Lithium deposition on untreated and textured Copper.

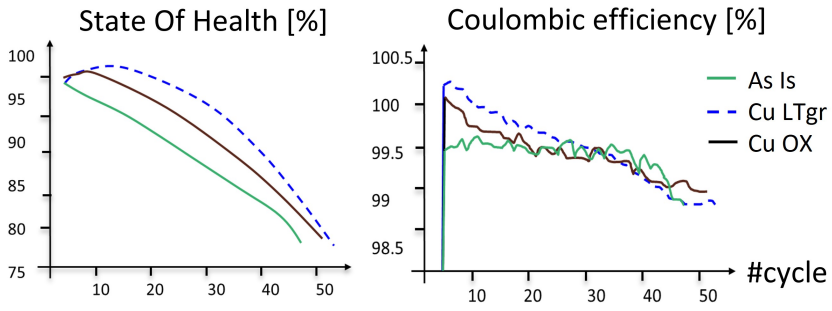

Figure 112: AFLMB battery performance of as-is and Lt laser textured copper.

ena.

The graphs show the behavior of copper oxidized in the oven, and it can be seen that the behavior lies in the middle. The results must therefore be supplemented by a series of analyses aimed at thoroughly understanding the behavior of the textured material in order to understand what improvement is provided by texturing and what by oxidation, and what type of oxidation is induced by the laser. XPS and impedance analyses have been scheduled, and the results are awaited.

5.3.5 Enhancing electrochemistry: electrolyzers and fuel cell

In production of green hydrogen, the widespread deployment of proton exchange membrane water electrolyzers (PEMWEs) is hindered by efficiency limitations and high costs associated with precious metal catalysts. A critical factor influencing performance is the interfacial transport of reactants and products at the porous transport layer (PTL)−catalyst layer (CL) interface, where inadequate water supply and oxygen removal lead to increased ohmic and mass transport losses. Laser texturing has the potential to address these challenges by tailoring PTL morphology and interfacial architecture. Femtosecond and fiber laser ablation techniques enable the creation of hierarchical structures and nanochannels that enhance electrochemical surface area, improve membrane hydration, and facilitate oxygen evacuation, thereby reducing high-frequency resistance and kinetic overpotentials [116],[117],[118]. Recent studies demonstrate that laser-structured PTLs and nanochannel electrodes achieve significant voltage reduc-

tions—up to 230 mV at 4 Acm^{-2}—and maintain durability over 100,000 accelerated stress cycles and 2,000 hours of operation, even at ultra-low iridium loadings [117],[118]. These advancements underscore the role of interfacial engineering through laser processing as a scalable and effective approach to improve PEMWE performance, reduce catalyst usage, and accelerate the transition toward cost-competitive green hydrogen production.

In the proposed case study, a 250 μm thick sintered titanium PTL is structured with LIPSS obtainable from the two wavelengths of 1064 and 532 nm, see Table 20. The sheets are cut out to be tested in the cells. The processing parameters are shown in the table.

Morphological characterization is performed using SEM, while chemical characterization is performed using EDS and Raman. The basic idea is to analyze the chemical effects of laser texturing on sintered titanium on the surface and along the thickness. To do this, the titanium sheets were cut and hot-embedded in polymeric resin, held in place by a metal clip. Surface mirror polishing was done with 180-320-600-800-1200 grit paper and 3 um and 1 um cloths. Since resins are insulating and SEM analyses require ensuring the sample's electrical conductivity, the embedded samples were also polished on the back with 80-grit paper to reveal the metal.

Finally, characterization of the Electrochemically Active Surface Area (ECSA) is performed by the company we are collaborating with for this project.

Table 20: Laser parameters for sintered Titanium texturing.

	Scanning strategy	**Frequency [kHz]**	**Mark speed [mm/s]**	**Overlap [%]**	**Power [W]**	**Passes [-]**	**Fluence [J/cm^2]**
LIPSS (IR)	Parallel lines	333	1500	55	0.86	1	3.29
LIPSS (GR)	Parallel lines	400	1200	70	0.09	3	0.67
Cut	Parallel lines	1000	500	80	7.0	250	8.92

The surface of the individual sintered particles also appears structured in depth, with the size of the LIPSS structures depending on the wavelength used, between 860 and 360 nm, as shown in Figure 113.

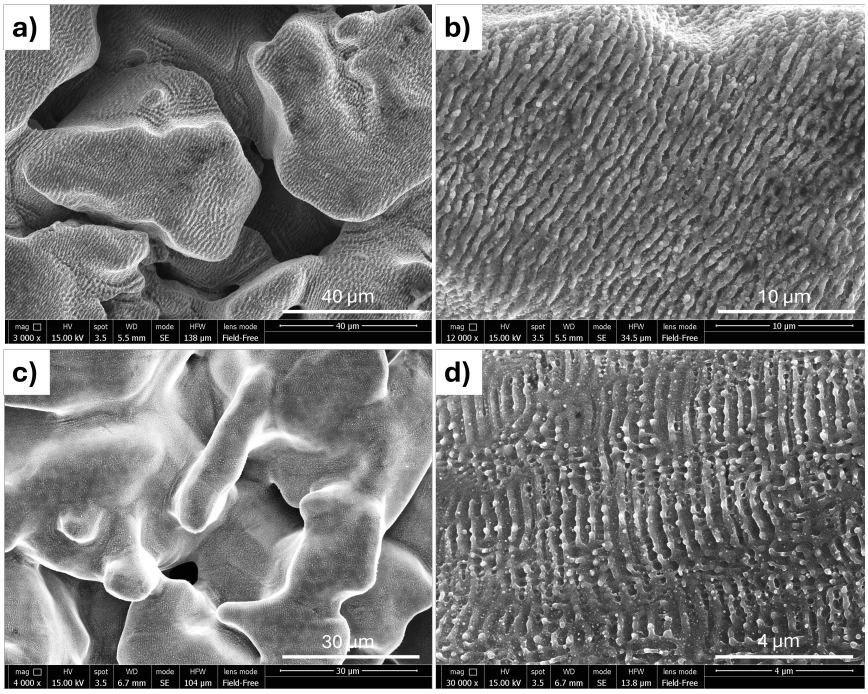

Figure 113: SEM images of LIPSS textured sintered titanium.

Raman analyses show that titanium is oxidized and contaminated (mainly with carbon) during and/or after texturing, as visible in Figure 114. Ion milling was performed after texturing. From the EDX surface analyses conducted, it can be inferred that the titanium is slightly more oxidized in the GR condition than in the IR condition, probably due to the multiple passes required to obtain it. From the EDS cross-section analyses performed, it can be inferred that the oxidation depth of the titanium is approximately 2 μm (and is slightly greater in the IR condition than in the GR condition), see Figure 115. However, the poor conductivity of the resins used does not allow for good image resolution and characterization, which are reliable with greater errors. It would be advisable to incorporate conductive resins.

ECSA measurements using cyclic voltammetry show that the increase in active area for first harmonic LIPSS is, on average, 50% greater, while for second harmonic LIPSS it is 10% greater than for untreated material, as shown in Figure 116. The tests were repeated on two samples per condition, yielding almost identical results.

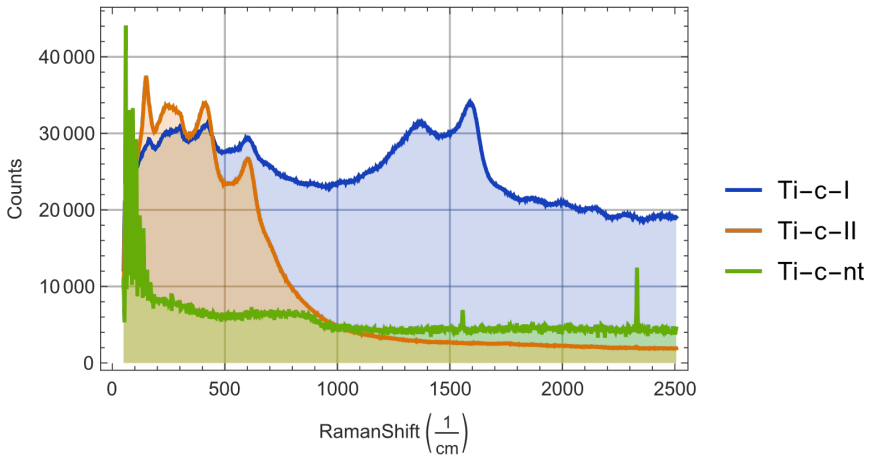

Figure 114: Raman spectrum of "nt" untreated and I/II harmonic textured sintered titanium.

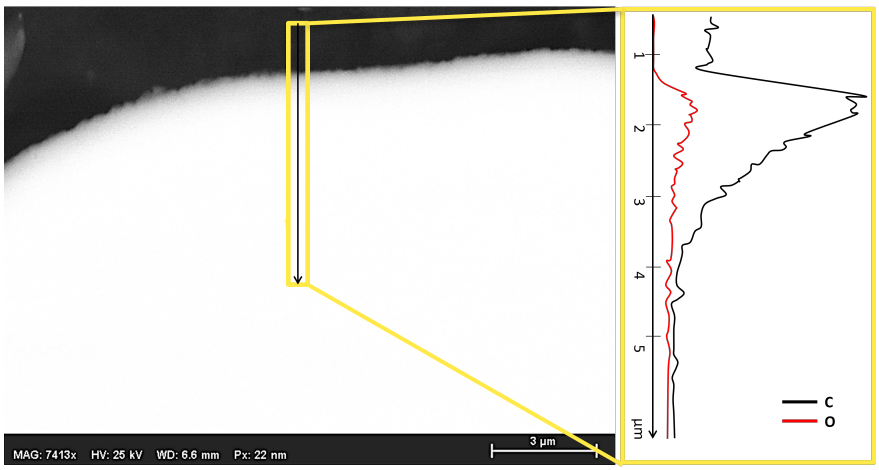

Figure 115: EDS elemental profile along the cross section: in pink is Carbon, in Red is Oxygen.

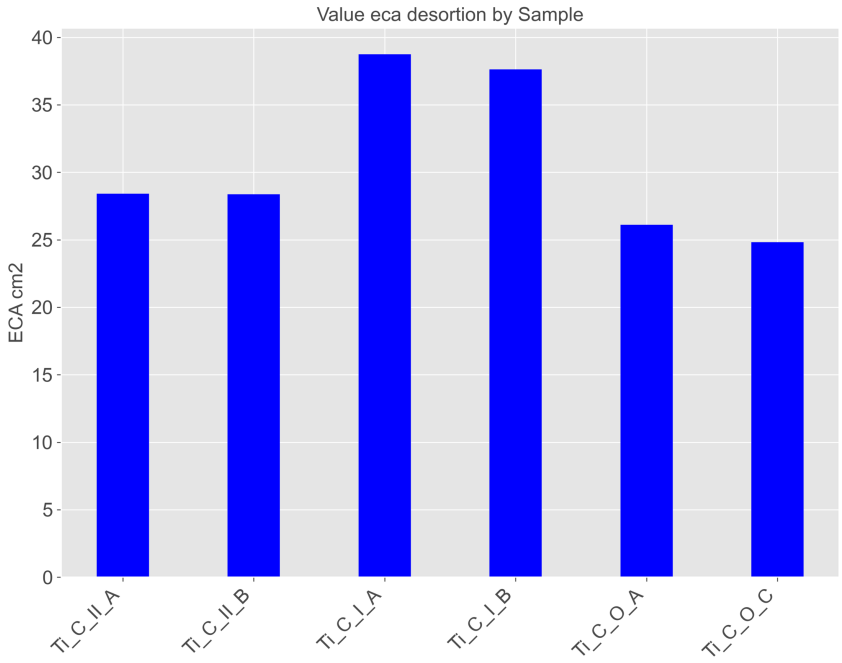

Figure 116: ECSA measurement of "O" untreated, and I/II harmonic treated sintered titanium: sample A and sample B are the two repetitions.

Enlarging this area improves catalyst utilization, reduces interfacial resistance, and promotes uniform current distribution, ultimately lowering energy consumption and boosting hydrogen output. Surface texturing represents a promising strategy to achieve these objectives by creating controlled microstructures that facilitate uniform catalyst deposition and stable adhesion. By tailoring the morphology of sintered titanium, it becomes possible to combine exceptional corrosion resistance with optimized catalytic performance, paving the way for more efficient, durable, and cost-effective PEM electrolyzers—an essential step toward large-scale deployment of green hydrogen technologies.

5.4 Adaptive Optics enhancing laser microprocessing and functionalization

5.4.1 Adaptive Optics approach for laser direct processing

The various case studies presented have demonstrated that laser texturing can impart functional properties to surfaces, such as improved wettability, antibacte-

rial properties, and enhanced tribological performance. However, when applied to large surfaces the process faces significant productivity challenges.
Traditional ultrafast laser systems employ Gaussian beams with a circular beam spot, which limits the processing speed due to the point-like nature of the energy distribution. Increasing laser power to accelerate the process often leads to undesirable effects such as debris formation, heat-affected zones, and irregular groove morphology, compromising both the quality of the texture and the durability of the mold. Similarly, increasing scan speed without modifying the beam profile reduces energy accumulation, resulting in insufficient ablation depth.
To overcome these limitations, adaptive optics has emerged as a transformative solution. AO systems enable dynamic beam shaping by modulating the wavefront through deformable mirrors. This approach allows the generation of elliptical beams elongated along the scanning direction, effectively redistributing energy over a larger area while maintaining the desired fluence. By doing so, AO facilitates a substantial increase in processing speed without sacrificing texture quality, making it a promising strategy for direct laser processing of molds and other large-scale components.
The first proof of concept performed is that of direct writing. Following the methodology described in Section 3.4, to elongate the beam, it was necessary to change the offset values of Z_2^{-2} (Astigmatism X), Z_2^2 (Astigmatism Y) and Z_2^0 (Defocus) modes. Specifically, for the elliptical beam with horizontal major axes, about 42 μm long (see Figure 117 b-1), the following values have been chosen:

- Oblique Astigmatism -0.34 waves
- Defocus 0.41 waves
- Vertical Astigmatism 0.32 waves.

For the elliptical beam with vertical major semi-axes (see Figure 117 b-2) the values are:

- Oblique Astigmatism 0.34 waves
- Defocus 0.41 waves
- Vertical Astigmatism -0.18 waves.

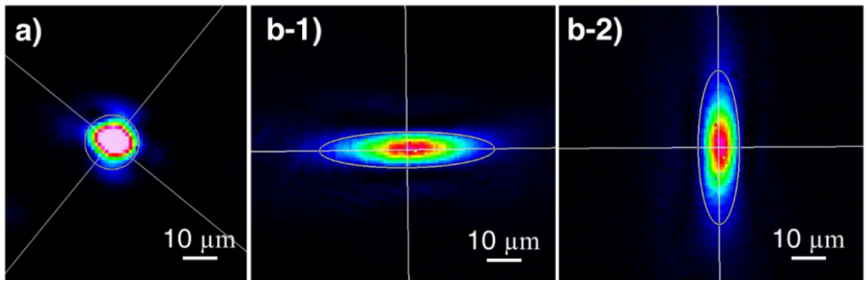

Figure 117: Circular versus 1:4 aspect ratio elliptical beam, adapted from [119].

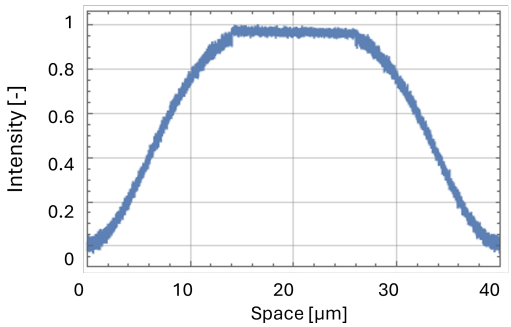

Figure 118: Measured intensity profile for the 42 μm-axis elliptical beam [119].

To achieve the 90° rotation, it was necessary to reverse the signs of the astigmatic modes $Z_2^{\pm 2}$. In addition, a slight offset, approximately equal to 0.05 waves, was also given to the primary spherical aberration Z_2^0 in both cases, because of the original shape of the circular beam.
The intensity distribution detected by the intensity sensor varies as in the graph in Figure 118.

In all processes where lasers are used to ablate or texture the surface of materials directly, beam shaping can increase productivity. In the case of linear scans, simply extending the beam in one direction, parallel to the scanning direction, is sufficient to increase speed without losing definition. In the case of very small shapes, the shape of the beam can be modified in a much more complex way to obtain the exact shape to be scanned while remaining hypothetically stationary (e.g., DOE).The only limitation is the maximum available power, because as the shape of the beam is enlarged, the emitted power must increase accordingly. However, as demonstrated in all the case studies presented, the power used was always much lower than the maximum available.

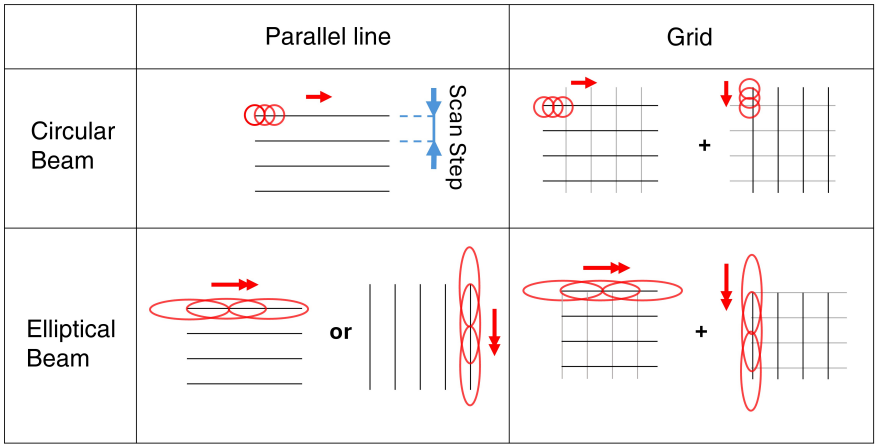

Figure 119: Laser processing scheme to obtain parallel lines or grids using a circular or elliptical beam (scan step) [119].

This methodology has been applied to 150 μm-linear and grid scans, where the problem of dynamically modifying the shape of the beam to follow the shape of the vectors to be scanned is added. To reach the desired depth of 5 μm while going faster, the starting processing parameters are 1000 kHz of laser frequency and 3 passes. In previous studies, the overlap of the circular laser beam to obtain a uniform groove was 50 %. Thus, using the circular Gaussian beam the scan speed is set to 300 mm/s, and the laser power is 5.54 W.
In the case of the 10x40 μm elliptical beam, all the parameters remain unchanged except for the scan speed, which increases to 1200 mm/s, and the power to 22.2 W, so the fluence remains the same, see Table 21. Using the four times longer beam allows scanning about three times faster while maintaining 50 % overlap, as can be seen from the schematic image in Figure 119.

Table 21: Laser parameters for direct texturing using elliptical beam.

IR (1064)	**Scanning strategy**	**Frequency [kHz]**	**Mark speed [mm/s]**	**Overlap [%]**	**Power [W]**	**Passes [-]**	**Fluence [J/cm^2]**
Circular beam	Parallel lines	1000	300	-	5.54	3	7.06
Elliptical beam	Parallel lines	1000	1200	-	22.2	3	7.06

The experimental imprint left by the circular and elliptical beam is presented in Figure 120, while Figure 121 shows the linear and grid structures obtained with the circular and elliptical beams, compared side by side. It can be seen

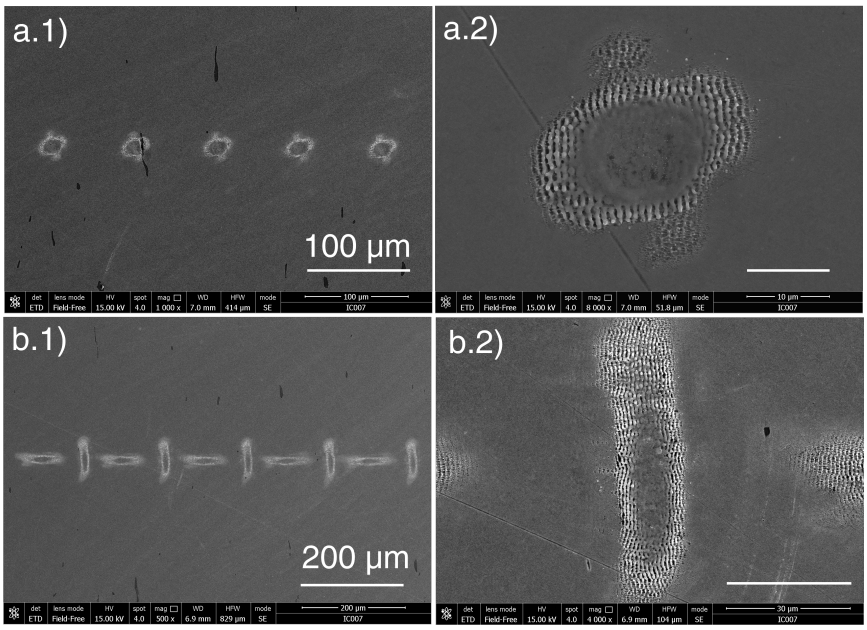

Figure 120: SEM images of the imprint left by circular (a) and elliptical beams (b) at different magnifications, adapted from [119].

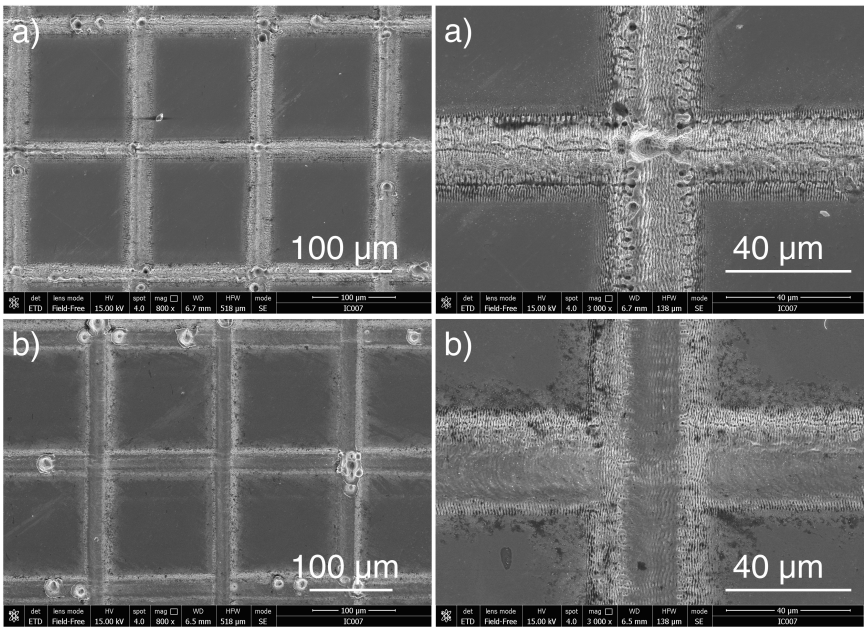

Figure 121: SEM images of the grooves obtained by circular (a) and elliptical (b) beams [119].

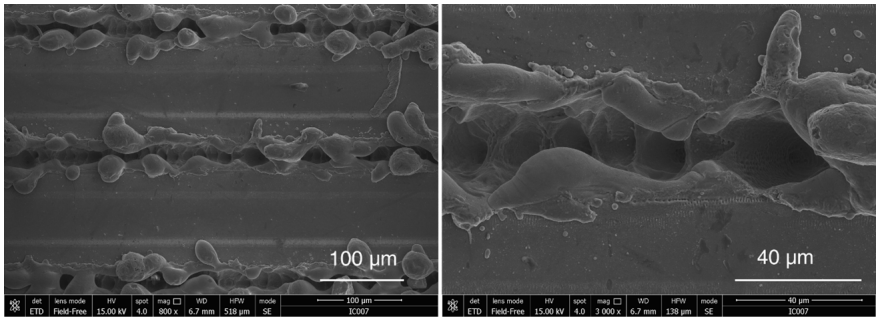

Figure 122: SEM images of grooves obtained at high power with circular beam [119].

that the quality has improved, with much smoother groove walls. Furthermore, the grooves reach an average depth of 5 ± 0.7 μm for the circular beam and 5.2 ± 0.5 μm for the elliptical beam. Processing times range from 0.580 s for the circular beam to 0.210 s for the elliptical beam on the same area of 1.5 x 15 mm^2, which is about three times faster. This is the best result ever achieved in direct processing. For more details on the methodology used, please refer to the article [119].

Going at high speed with the circular beam does not achieve the desired depth because there is not enough energy accumulation. While wanting to harness all the power of the laser by concentrating it in the circular beam, the result is in excessive heating of the material that causes melting and re-solidification, resulting in a very irregular groove morphology that cannot be used for replication purposes (see Figure 122).

5.4.2 Adaptive Optics approach for laser induced processing

The flexibility of AO-based beam shaping extends beyond simple groove formation to more complex processes, such as the generation of grids and LIPSS. In grid texturing, where lines are oriented orthogonally, AO enables rapid alternation between horizontal and vertical beam elongation, reducing the need for additional passes and minimizing downtime. This dynamic adaptability is particularly advantageous for producing hierarchical textures.

For instance, when using highly elongated beams, LIPSS can be generated over large areas in a fraction of the time required by conventional circular beams. Experimental results demonstrated that processing time for LIPSS texturing on

stainless steel molds decreased by more than 93% when employing an elongated beam, without compromising the uniformity or periodicity of the structures. These findings underscore the potential of AO not only to accelerate direct ablation processes but also to enhance induced phenomena for surface functionalization.

In all processes where lasers are used to create laser-induced structures on the surface of materials, beam shaping can increase productivity. In this case, the shape of the beam is almost irrelevant; only the area to be covered matters. If a linear scanning strategy is used to cover a regular area, simply extend the beam in a single direction, perpendicular to the scanning direction, to gain speed without losing definition, following the scheme in Figure 123.

As regards obtaining the elongated beam, by increasing the offset value of the

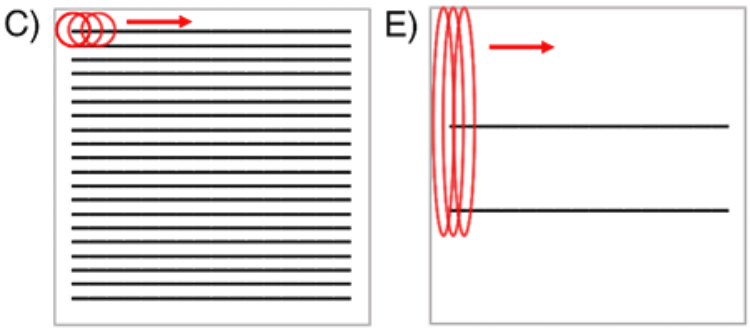

Figure 123: LIPSS texturing using circular or elliptical beam scheme, adapted from [120].

three modes seen above, a beam length of about 202 μm was made (Figure 124):

- Oblique Astigmatism 0.80 waves
- Defocus 0.65 waves
- Vertical Astigmatism 0.42 waves.

The area textured with LIPSS is 1.5x1.5 mm^2. To realize texturing with the circular beam and 55 % overlap, the scan step is 4.5 μm. Laser processing parameters are 333 kHz repetition rate, one single pass, scan speed 1500 mm/s, and 0.44 W of power. In the case of the elliptical beam, while maintaining the same fluence as used for the circular beam, the scan step can be increased to 70 μm. Since the elongated beam at 200 μm has less energetic tails, the overlap along the line becomes 65 %, see Table 22. For further details on the method-

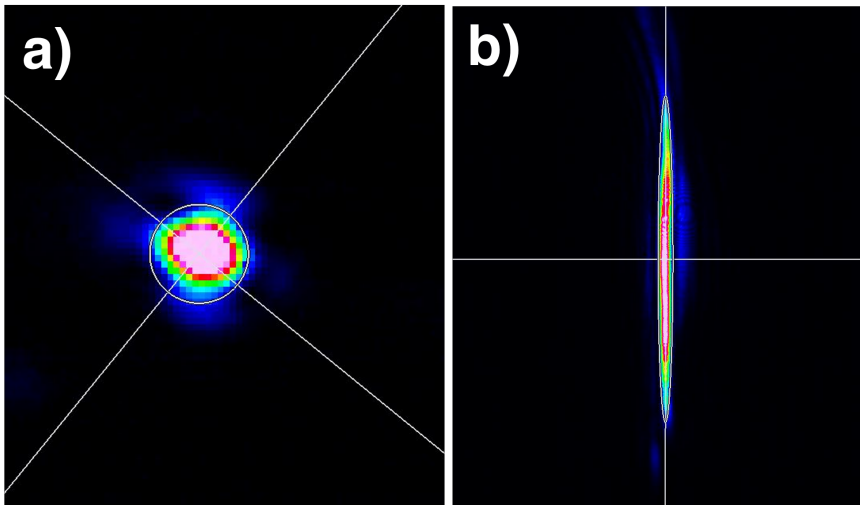

Figure 124: Circular versus 1:20 elliptical beam, adapted from [119].

ology used, please refer to the article [119]. Hence, with the same scan rate, processing time is reduced by a factor of 15, since fewer laser scans are required to process the same area. Specifically, processing times range from 1.05 s for a circular beam to 0.066 s for an elliptical beam on the same area of 1.5 x 1.5 mm^2.

Table 22: Laser parameters for LIPSS texturing using circular or elliptical beam.

IR (1064)	**Scanning strategy**	**Frequency [kHz]**	**Mark speed [mm/s]**	**Overlap [%]**	**Power [W]**	**Passes [-]**	**Fluence [J/cm^2]**
Circular beam	Parallel lines	333	1500	55	0.44	1	2.01
Elliptical beam	Parallel lines	333	1500	65	10	1	2.10

The results are shown in the SEM images in Figure 125: only the orientation changes slightly at the points where the elliptical beam overlaps.

The fact that the beam shape is different could affect the quality of the periodic structures induced by the laser. For this reason, in a very similar study [120], more specific analyses were performed. The boundary conditions change slightly, but the methodology is identical. The materials analyzed are steel and a nickel-titanium alloy. The beam used for this experiment is elliptical with an axis ratio of 1:7, obtained in the same way as described above.

The non-standard descriptor DLOA (Dispersion of LIPSS Orientation Angle)

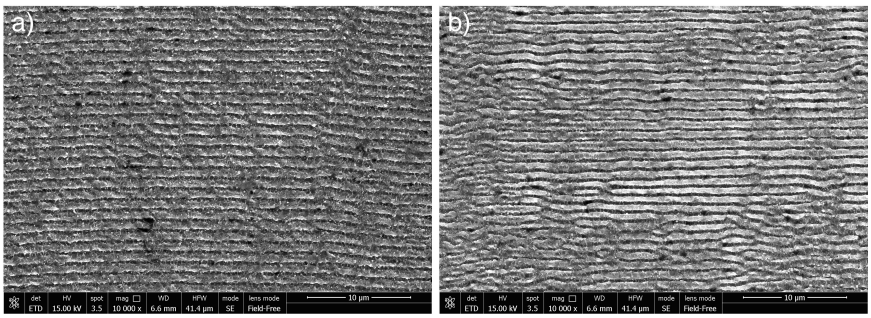

Figure 125: SEM images of LIPSS texturing using circular or elliptical beam [119].

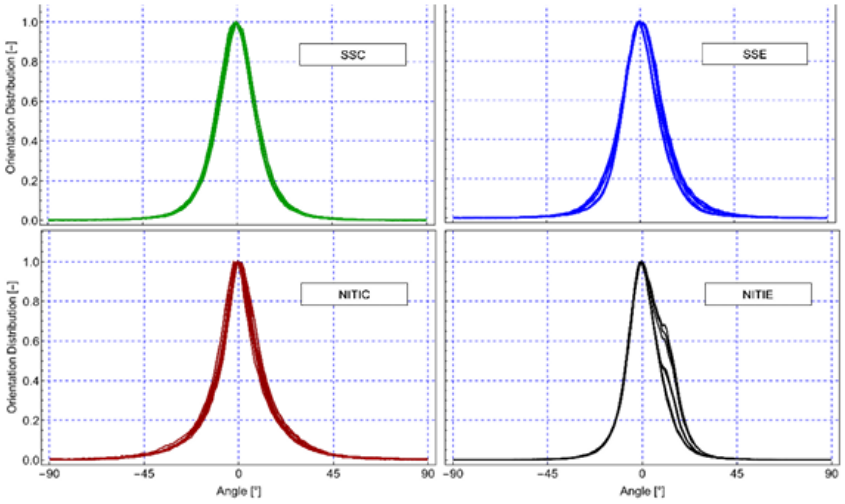

Figure 126: DLOA distribution of LIPSS obtained by circular (SSC, NITIC) or elliptical beam (SSE, NITIE) on stainless steel (SS) or Nitinol alloy (NITI) [120].

is used on SEM images, and LIPSS orientation and regularity are assessed in relation to the process parameters. The procedure has been implemented using the OrientationJ Distribution plugin implemented in the Fiji open platform for scientific image analysis distribution [121]. For each processing conditions 9 different images were extracted from SEM analysis campaign. Every image was processed thanks to a script written in ImageJ. The result distributions are then analyzed in a Mathematica notebook to obtain the DLOA indicators, which are visible in Figure 126 and Figure 127.

In the case of very small areas, the shape of the beam can be modified in a much more complex way to obtain the exact shape to be scanned while remaining hypothetically stationary, as in the case of direct processing. The limitation of the

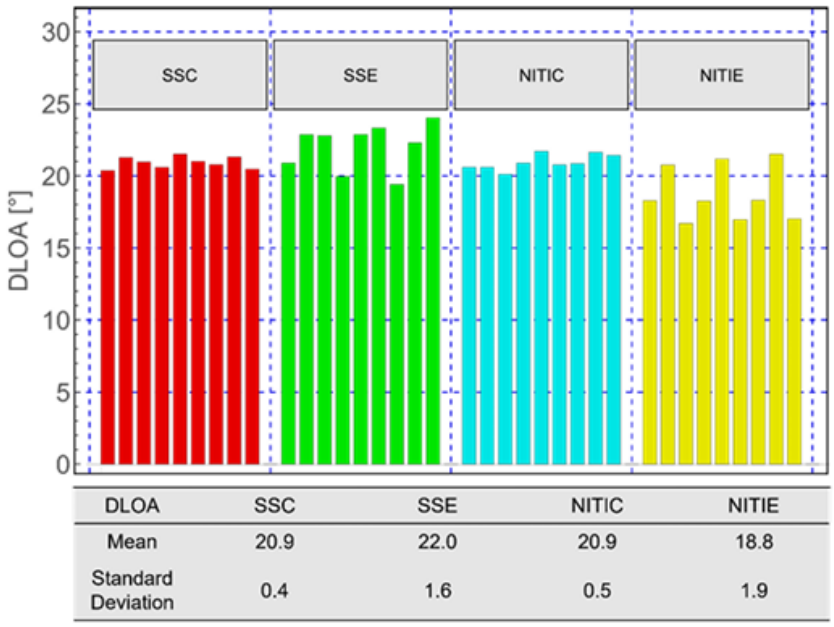

DLOA	SSC	SSE	NITIC	NITIE
Mean	20.9	22.0	20.9	18.8
Standard Deviation	0.4	1.6	0.5	1.9

Figure 127: Mean and standard deviation of LIPSS orientations for circular (SSC, NITIC) or elliptical beam (SSE, NITIE) on stainless steel (SS) or Nitinol alloy (NITI) [120].

application still lies in the maximum power available, but in this case, it benefits even more from the fact that LIPSS structures are generated at very low fluences.

5.4.3 Laser ablation simulation integrating beam shaping

The complexity of ultrashort pulse interactions with matter, where phenomena such as plasma shielding, heat accumulation, and phase explosion occur on femtosecond to microsecond timescales, makes process optimization challenging through experimental trial-and-error alone. Numerical simulation offers a powerful solution to predict ablation behavior, enabling better control of parameters such as pulse energy, repetition rate, and beam shape while reducing development costs and time. Models based on the Two-Temperature Model (TTM) have proven effective in describing the non-equilibrium heat transfer between electrons and lattice during ultrafast laser irradiation, allowing accurate estimation of temperature fields, ablation depth, and heat-affected zones [122, 123]. Recent studies have demonstrated that integrating beam motion and plasma shielding into finite element simulations can replicate real-world conditions, sup-

porting strategies like dynamic beam shaping to enhance productivity in mold texturing [124]. Similarly, fast simulation frameworks for GHz burst mode lasers have been developed to explore the interplay between pulse number, burst fluence, and thermal accumulation, which are critical for achieving high ablation efficiency without compromising surface quality [125]. These advancements highlight the role of simulation not only as a predictive tool but also as a driver for innovation in laser processing, enabling the design of adaptive optics systems and high-frequency burst regimes that significantly increase throughput while maintaining precision.

To predict and optimize the benefits of beam shaping, a numerical model based on the TTM model, which is particularly suited for ultrashort pulsed laser interactions due to its ability to separately account for the thermal behavior of electrons and the lattice, was developed and implemented in COMSOL Multiphysics®. Unlike conventional heat conduction models, TTM introduces two coupled equations: one governing the electron temperature and the other the lattice temperature. These are expressed respectively as:

$$\begin{cases} C_e \frac{\partial T_e}{\partial t} = \nabla[k_e \nabla T_e] - G(T_e - T_l) + S(x, y, t) \\ C_l \frac{\partial T_l}{\partial t} = \nabla[k_l \nabla T_l] + G(T_e - T_l) \end{cases} \tag{5.1}$$

where Ce and Cl are the specific heat capacities, ke and kl the thermal conductivities of electrons and lattice, G the electron-lattice coupling factor, and $S(x, y, t)$ the laser heat source term. All thermal properties and coupling factors are temperature-dependent, allowing the model to capture the dynamic nature of ultrafast laser-material interactions.

Table 23 summarizes the material properties of the electron and lattice as well as the parameters to define the laser source characteristics.

To simulate the effect of beam shaping, particularly the use of an elliptical beam elongated along the scanning direction (see Figure 128), the laser intensity distribution was adapted to reflect the true three-dimensional energy profile. The temporal and spatial Gaussian profile of the laser was defined as:

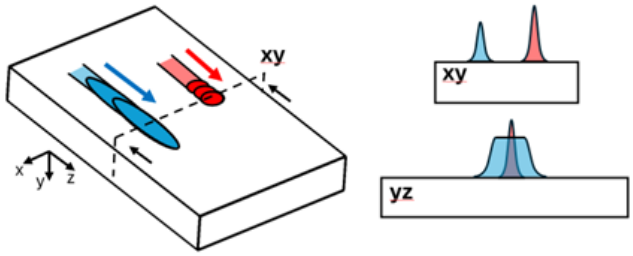

Figure 128: 3D and 2D representation of a laser pass for the circular beam (in red) and for the elliptical beam (light blue); xy plane is where laser simulation is done, yz plane is the other view.

$$I(x,t,z,t_2) = \frac{2E}{\pi w_0^2 P_w} e^{-2(\frac{x-x_0}{w_0})^2} * e^{-0.25(\frac{t-Pw-Tp*z}{Pw/4})^2} * \frac{2}{\sqrt{\pi}} * Iz_{g,e}, e(t,t_2) \quad (5.2)$$

For the z-direction, the model considered either a Gaussian distribution or an elongated distribution for the elliptical beam:

$$Iz, g(t,t_2) = e^{-2(\frac{t-Lm-Tz*t_2}{Lm})^2} \quad (5.3)$$

$$Iz, e(t,t_2) = \begin{cases} e^{-2(\frac{t-Lm-Tz*t_2}{Lm})^2} & 0 + Tz*t_2 \leq t \leq Lm + Tz*t_2 \\ 1 & Lm + Tz*t_2 \leq t \leq 1,857*Lm + Tz*t_2 \\ e^{-2(\frac{t-1.857*Lm-Tz*t_2}{Lm})^2} & t \geq 1,857*Lm + Tz*t_2 \end{cases} \quad (5.4)$$

This formulation allowed the simulation to capture the more uniform energy deposition of the elliptical beam, which contrasts with the peak-centered energy delivery of the circular Gaussian beam. The simulated intensity distribution is shown in 129; the descending and ascending traits are approximated by Gaussian functions.

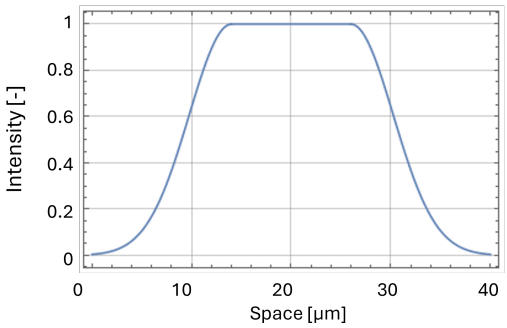

Figure 129: Simulated intensity profile in COMSOL environment [119].

The absorbed laser energy was further modulated by a temperature-dependent surface absorption coefficient A(T), absorptivity α, and a plasma shielding function, leading to the heat source term:

$$D_{well_{time}} * I(x,t,z,t_2) * (A(T) - Plasma(t_3,t_4)) * \alpha(T) * e^{(\alpha(T)*y)} - G(T_e - T_l) \quad (5.5)$$

Material removal was modeled using a deformable mesh, with the ablation velocity defined as:

$$v_{def} = \frac{HTC_z * (T_l - T_{ablate})}{\rho * H_{vap}} \quad (5.6)$$

where HTCz is a virtual heat transfer coefficient that increases steeply when the lattice temperature exceeds the ablation threshold T_{ablate}, ensuring near-constant temperature during ablation, see Figure 130. The maximum ablation velocity was capped at the speed of sound to reflect physical constraints on thermal wave propagation.

Table 23: Material parameters for ablation simulation.

Parameter type	**Parameter**	**Meas. Unit**	**Value**
Thermo-physical parameters	Density, ρ	[kg/m^3]	7850
	Average surface absorption coefficient [126]	-	0.4
	Absorptivity, α	[1/m]	7.1*10^7
	Electron heat capacity, at room temperature, C_{e0} [123]	[J/m^{3}K^2]	706.4
	Electron thermal conductivity, room temperature, k_0 [123]	[W/mK]	80.2
	Electron heat capacity	[J/Kg K]	$\frac{C_{e0}*T_e}{\rho}$
	Electron thermal conductivity	[W/mK]	$k_0 \frac{T_e}{T_l}$
	Lattice heat capacity, [127]	[J/KgK]	472 + 13.6*10^{-2} T_l - $\frac{2.82*10^6}{T_l^2}$
	Lattice thermal conductivity, [127]	[W/mK]	9.2 + 0.0175 T_l -2*10^{-6} T_l^2
	Electron-lattice coupling factor, G [123]	[W/m^3K]	130*10^{16}
	Ablation Temperature, T_{ablate} [123]	[K]	9324
	Sonic speed in solid, V_s, [123]	[m/s]	6100
	Latent heat of vaporization, H_{vap}	[kJ/kg]	500
	Surface Emissivity Coefficient, ϵ	-	0.075
Laser parameters	Laser pulse width, P_w	[ps]	10
	Wavelength, λ	[nm]	1064
	Incident pulse energy, E	[μJ]	Gaussian 16.6
			Elliptical 66.6
	Repetition Rate	[kHz]	1000
	Beam dimensions	[μm]	Gaussian 10
			Elliptical 10x40
	Laser speed	[mm/s]	Gaussian 300
			Elliptical 1200
	Dwell time	[μs]	10000
Additional parameters	Max element size - refined region	[mm]	0.00148
	Max element size - remaining domain	[mm]	0.005
	Air temperature	[K]	293.15
	Cold material temperature	[K]	293.15
	Heat transfer coefficient with air	[W/m^{2}K]	15
	Heat transfer coefficient with cold material	[W/m^{2}K]	50

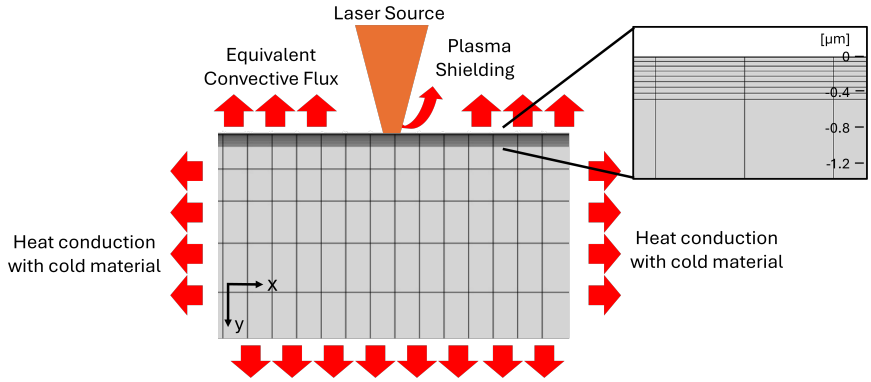

Figure 130: Heat Exchange Scheme and Mesh Refinement (top right) [119].

The simulation geometry was a 40 μm square, discretized with a refined quadrilateral mesh. Boundary conditions included convective fluxes to simulate heat exchange with surrounding cold material and air, and radiation losses from the top surface. Plasma shielding was introduced by exponentially reducing the absorption coefficient when the lattice temperature exceeded the ablation threshold, a particularly relevant phenomenon during burst-mode laser operation.

This comprehensive framework enabled accurate prediction of ablation depth and energy distribution for both circular and elliptical beams, demonstrating that beam shaping can significantly enhance laser processing efficiency without compromising quality.

The simulation was designed to compare the standard circular Gaussian beam with the elliptical beam elongated along the scanning direction, focusing on the latter due to its potential for productivity enhancement. The elliptical beam was modeled with a 10 $\times$ 40 μm profile, maintaining the same minor axis as the circular beam to preserve groove width while extending the major axis to increase interaction time.

Simulation results showed that, for three passes at a fluence of 7.06 J/cm^2, the elliptical beam achieved an average groove depth of 4.13 μm, closely matching the 4.06 μm depth produced by the circular beam. Despite operating at four times the scanning speed (1200 mm/s vs. 300 mm/s), the elliptical beam maintained comparable ablation depth, demonstrating a significant increase in processing speed without compromising quality. The groove profiles were U-shaped in both

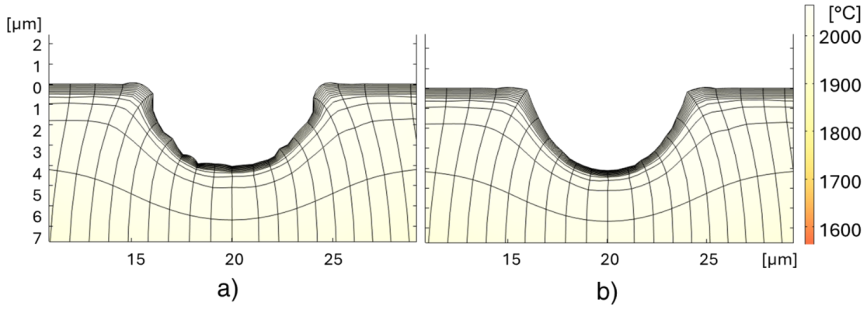

Figure 131: Depth of the simulated groove using circular (left) and elliptical (right) beam. Lattice temperature scale at right [119].

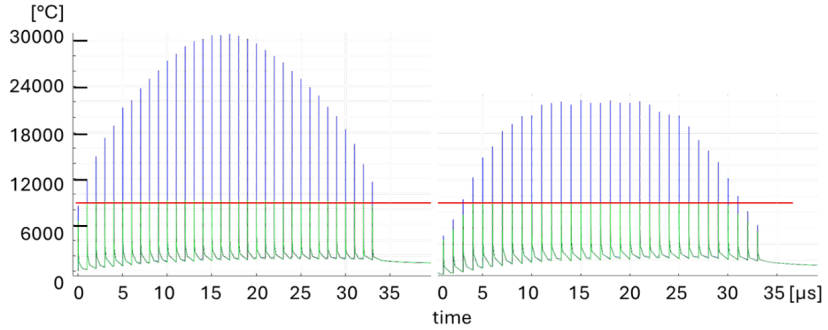

Figure 132: Plot of electron temperature (blue) and lattice temperature (green) over time, for circular (left) and elliptical (right) laser beam passage in COM SOL: ablation temperature in red [119].

cases, see Figure 131, and the simulation predicted a more consistent electron temperature plateau for the elliptical beam, while the circular beam exhibited a sharp peak. This improvement is attributed to the more constant intensity profile of the elongated beam, which maintains elevated electron temperatures over a longer interaction time, see Figure 132.

Experimental validation confirmed the simulation outcomes. Groove depths measured on AISI 420 stainless steel samples matched the predicted values, with the elliptical beam producing a depth of 4.2 ± 0.9 μm and the circular beam yielding 4.5 ± 0.6 μm, as shown in Table 24. The processing time for a 1.5 $\times$ 1.5 mm area was reduced from 0.317 s with the circular beam to 0.101 s with the elliptical beam, highlighting a threefold increase in productivity. SEM analysis of the groove cross-sections in Figure 133 revealed consistent morphology and surface quality, supporting the simulation's accuracy.

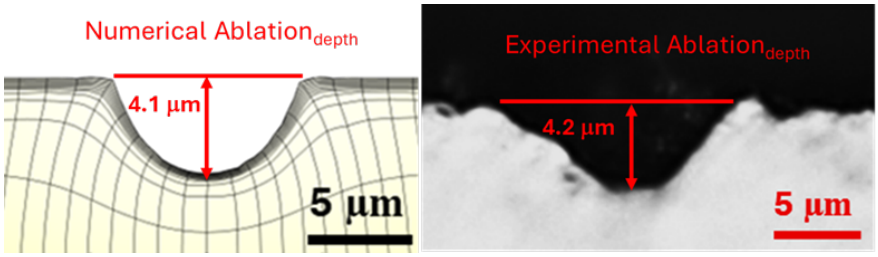

Figure 133: Example of groove section made with elliptical beam parallel scanning strategy [119].

Table 24: Mean value and depth variance comparison between simulation and experiment case.

	COMSOL Simulation		**Experimental**	
Groove type	Depth Average [um]	Variance [-]	Depth Average [um]	Variance [-]
C Parallel	4.05	-	4.5	0.6
E Parallel	4.13	-	4.2	0.9

These results validate the effectiveness of adaptive optics in enhancing laser ablation performance. By integrating beam shaping into the simulation framework, it becomes possible to optimize process parameters and fully exploit the capabilities of high-power ultrafast lasers. The elliptical beam's ability to maintain fluence while increasing scan speed offers a robust solution for high-throughput laser texturing applications, making it a valuable tool for industrial-scale surface functionalization [119].

6. Discussion

The experimental campaign conducted in the BrightLab laser processing cell confirms that adaptive optics is an enabling technology for scaling ultrafast laser manufacturing from laboratory demonstrations to industrially relevant throughput, without compromising the hallmark precision and material fidelity characteristics of picosecond and femtosecond regimes. Across the full spectrum of case studies, the same conclusion emerges: real-time beam shaping increases speed, stabilizes feature quality, and broadens the feasible process window. These gains are rooted in the meticulous set-up of the cell (source harmonics, scanning optics, diagnostics, motion control, and AO loop) and the design choices taken to couple wavefront modulation with in-situ analysis.

The cell architecture proved decisive for repeatable control of the focal intensity distribution. The instrumentation allowed a quantitative link between commanded Zernike modes and measured focal geometry, so that elliptical spot profiles could be reproduced on demand and aligned to scan vectors. This deterministic mapping is essential to avoid "black box" tuning and to industrialize recipes, e.g., setting astigmatism and defocus coefficients to obtain an axial ratio 1:n with millisecond reconfiguration latency. The cell delivered consistent focused spot sizes for the three harmonics, with known ellipticity and stability margins; when AO was introduced, the focal caustic could be tailored in real time to maximize synchronous energy coupling with the kinematics of the scanner.

A critical outcome of the study is the explicit connection between technical performance and economic sustainability. Ultrafast sources are capital intensive; however, the cost of AO (deformable mirror, wavefront sensor, driver, and software) is justified by measurable productivity gains and downstream savings:

- Throughput gains and amortization: When processing time per square centimeter is reduced by 70–93% (as observed in grid texturing and LIPSS), the same capital asset can service more jobs in a given period, improving

overall equipment effectiveness and reducing cost per unit area. Because AO reconfigures the beam in milliseconds, multiple texture families can be produced in a single set up, minimizing changeover downtime. The throughput uplift can shortly amortize AO hardware, and the combined system (ultrafast source + AO) yields a lower lifecycle cost per part than a higher power source alone operated in conventional Gaussian mode.

- Quality driven savings: AO lowers defect rates (e.g., avoiding melt recast in deep grooves or irregular LIPSS overlap), which reduces scrap, rework, and post processing. For mold texturing, maintaining groove fidelity minimizes polishing or corrective operations of replicated parts, directly affecting the cost of quality. In adhesive re bonding and composite preparation, cleaner, uniform surfaces and tuned roughness regimes reduce variability in joint strength, allowing tighter design margins and fewer destructive tests per batch. These translate into tangible savings in consumables and labor.
- Energy efficiency and cycle consolidation: By distributing energy more uniformly and matching spot geometry to scan paths, AO allows operation at lower average powers for equivalent functional outcomes. In several BrightLab runs, the process could remain within available power headroom while raising speed. In cleaning/texturing workflows (e.g., aluminum re bonding), AO helps consolidate steps—precise removal followed by functional LIPSS—so fewer machine cycles and fixture changes are required. Consolidation reduces handling time, operator interventions, and the risk of contamination between steps.
- Risk mitigation and scalability: AO contributes to process window enlargement—greater tolerance to small misalignments, part curvature, or field dependent aberrations—thus decreasing the probability of batch failures when scaling to larger areas or 3D geometries (e.g., helical threads on tools). This lowers the cost of scale up and supports standardization of recipes for production environments.

Some of the case studies were addressed to develop a working methodology, but the most suitable source for certain objectives may have been different from the

one used. However, most of them are concerned with highly effective applications, such as rapid prototyping, the creation of microfeatures on very expensive components such as optical components or special deformation and cutting tools, functionalization in terms of biocompatibility, and energy production, which are currently very hot topics.

In some of the case studies analyzed, such as increasing battery or fuel cell performance, the laser processing step can be nested into existing manufacturing lines. The gains in stack efficiency and catalyst savings outweigh texturing cost, especially when AO shortens cycle time and minimizes scrap due to non-uniform processing.

The study also revealed practical boundaries. Power headroom remains a constraint: as spot elongation grows, total power must increase to preserve fluence, and some sources may saturate or drift. The AO mirror stroke and spatial bandwidth limit the maximum aberration that can be introduced without artifacts; large field uniformity still demands careful scanner calibration and f- theta selection.

Conclusions and Future Developments

This research has addressed one of the most critical challenges in ultrafast laser-based manufacturing: the inherent trade-off between precision and productivity. Although ultrashort pulsed lasers offer unique advantages in terms of surface quality and negligible heat-affected zones, their industrial scalability has been constrained by fundamental physical and technological limitations. Increasing pulse energy or average power does not yield proportional improvements in ablation rates due to saturation phenomena and material-specific constraints, such as the maximum achievable groove aspect ratio. Likewise, raising scanning speeds at constant fluence reduces the interaction time between the laser and the material, leading to insufficient energy accumulation and compromised surface morphology. These limitations have traditionally restricted the use of ultrafast lasers to niche applications rather than large-scale manufacturing.

The work presented in this thesis demonstrates that integrating adaptive optics into ultrafast laser systems provides a viable and effective solution to these challenges. By enabling dynamic beam shaping through real-time wavefront modulation, adaptive optics allows precise control over the spatial energy distribution at the workpiece surface. This capability translates into significant improvements in process efficiency, as shown by experimental results: elliptical beam profiles achieved up to 70% faster groove texturing and more than 93% faster generation of Laser-Induced Periodic Surface Structures (LIPSS) compared to conventional gaussian beams, without compromising surface quality. These gains confirm that adaptive optics can decouple processing speed from interaction time, overcoming one of the most critical bottlenecks in ultrafast laser manufacturing.

A distinctive strength of this thesis lies in the breadth of case studies explored, encompassing microfabrication of microfluidic devices, surface functionalization for wettability and biocompatibility enhancement, tribological texturing of complex geometries, and surface preparation for adhesive bonding. Each case study illustrates the versatility of ultrafast laser technology and its potential to address

diverse industrial and scientific challenges. The integration of adaptive optics, experimentally validated on demanding materials such as stainless steel, nitinol, and zirconia, further underscores its robustness. Importantly, the principles demonstrated here are not limited to these examples: adaptive optics can be applied to all the processes investigated in this thesis, from biomedical implant texturing to electrochemical surface engineering, offering a universal strategy for productivity enhancement across multiple domains.

Beyond productivity, this research highlights the versatility of adaptive optics in supporting complex and application-specific beam profiles. The ability to reconfigure the beam shape within milliseconds opens new possibilities for multi-scale and multi-material processing, from microfluidic channel fabrication to tribological surface engineering and biomedical implant functionalization. The experimental platform developed at BrightLab, equipped with a deformable mirror and real-time wavefront sensing, proved to be a robust and flexible system for exploring these capabilities. Complementary numerical simulations based on the Two-Temperature Model further validated the experimental findings and provided predictive insights into energy deposition and ablation dynamics under different beam configurations, laying the groundwork for simulation-driven process optimization.

The implications of this work extend beyond the laboratory. Adaptive optics introduces a paradigm shift in ultrafast laser manufacturing, enabling high-throughput processing without sacrificing precision. This approach aligns with the growing demand for scalable, sustainable, and digitally integrated manufacturing solutions. Future developments should focus on industrial implementation, including the integration of adaptive optics with machine learning algorithms for real-time optimization and closed-loop control. Such advancements would allow autonomous adjustment of beam parameters based on in-process feedback, further enhancing efficiency and reliability. Additionally, expanding the scope of adaptive optics to multi-beam and burst-mode strategies could unlock new levels of productivity for large-area texturing and additive manufacturing.

In conclusion, this thesis establishes adaptive optics as a transformative technology for ultrafast laser processing. By bridging the gap between precision and

productivity, it paves the way for next-generation manufacturing systems capable of meeting the stringent requirements of advanced engineering, biomedical applications, and emerging photonic technologies. The results presented here not only demonstrate the feasibility of this approach but also provide a solid foundation for future research aimed at fully exploiting the potential of adaptive optics in industrial-scale laser manufacturing.

Appendix

A. Zernike Polynomials

Zernike polynomials constitute a complete set of orthogonal functions defined over the unit disk and are widely employed in optical engineering to represent wavefront aberrations. Their orthogonality and radial-angular decomposition make them particularly suitable for describing complex optical systems, including lenses and adaptive optics components. By expressing aberrations as a linear combination of Zernike terms, one can quantify and correct distortions with high precision, facilitating performance optimization in imaging and laser applications.

Zernike polynomials are defined over the unit disk and take values within the range -1 to $+1$, i.e. $|Z_n^m(\rho,\phi)| \leq 1$ if $\rho \leq 1$. The mathematical expression that characterizes each of them is shown below. The radial polynomials R_n^m are mathematically defined as:

$$R_n^m(\rho) = \sum_{k=0}^{\frac{n-m}{2}} \frac{(-1)^k\,(n-k)!}{k!\left(\frac{n+m}{2}-k\right)!\left(\frac{n-m}{2}-k\right)!}\,\rho^{n-2k} \tag{A.1}$$

for even n-m, while it is 0 for odd n-m, and $R_n^m(1) = 1$. As illustrative examples relevant to wavefront analysis, the first few Zernike modes, at various indices, are reported:

Piston:

$$Z_0^0 = 1; \tag{A.2}$$

Y-Tilt:

$$Z_1^1 = 2\rho sin(\phi); \tag{A.3}$$

X-Tilt:

$$Z_1^1 = 2\rho cos(\phi); \tag{A.4}$$

Oblique astigmatism:

$$Z_2^{-2} = \sqrt{6}\rho^2 sin(2\phi); \tag{A.5}$$

Defocus:

$$Z_2^0 = \sqrt{3}(2\rho^2 - 1); \tag{A.6}$$

Vertical astigmatism:

$$Z_2^2 = \sqrt{6}\rho^2 cos(2\phi); \tag{A.7}$$

Vertical trefoil:

$$Z_3^{-3} = \sqrt{8}\rho^3 sin(3\phi); \tag{A.8}$$

Vertical Coma:

$$Z_3^{-1} = \sqrt{8}(3\rho^3 - 2\rho) sin(\phi); \tag{A.9}$$

Horizontal coma:

$$Z_3^1 = \sqrt{8}(3\rho^3 - 2\rho)cos(\phi); \tag{A.10}$$

Oblique trefoil:

$$Z_3^3 = \sqrt{8}\rho^3 cos(3\phi); \tag{A.11}$$

Oblique quadrafoil:

$$Z_4^{-4} = \sqrt{10}\rho^4 sin(4\phi); \tag{A.12}$$

A complex aberrated wavefront can be approximated using Zernike polynomials, producing a set of coefficients that correspond to specific aberration types, see Equation A.13. Because these coefficients are linearly independent, the contribution of each aberration to the overall wavefront can be isolated and quantified individually.

$$\phi(x, y) = \sum a_i Z_i(x, y) \tag{A.13}$$

For example, the Piston, Defocus, and Oblique Astigmatism, multiplied by their respective fitting coefficients, are:

$$\begin{cases} a_0 \times 1 \\ .. \\ a_3 \times (2\rho^2 - 1) \\ .. \\ a_5 \times \rho^2 sin(2\phi) \end{cases} \tag{A.14}$$

where ρ is the normalized pupil radius with $0 \leq \rho \leq 1$, ϕ is the azimuthal angle around the pupil with $0 \leq \phi \leq 2\pi$, and the fitting coefficients a_0, a_3, a_5 are the wavefront errors in wavelengths.

Similar to Fourier synthesis with sines and cosines, a wavefront can be accurately represented by using a sufficiently large number of higher-order Zernike polynomials. However, wavefronts with steep gradients or high spatial-frequency features—such as those caused by atmospheric turbulence or aerodynamic flow—are poorly modeled by Zernike polynomials, which inherently act as a low-pass filter and smooth out fine spatial details. In such cases, alternative approaches like fractal-based methods or singular value decomposition may provide superior fitting performance.

Bibliography

[1] William M. Steen and Jyotirmoy Mazumder. *Laser Material Processing*. London: Springer, 2010.

[2] Alan E. Willner et al. «Optics and Photonics: Key Enabling Technologies». In: *Proceedings of the IEEE* 100 (Special Centennial Issue May 2012), pp. 1604–1643.

[3] *Le lavorazioni industriali mediante laser di potenza*. URL: `https://www.maggioli editore.it/le-lavorazioni-industriali-mediante-laser-di-potenza.html` (visited on 07/24/2025).

[4] L. Orazi et al. «Ultrafast laser manufacturing: from physics to industrial applications». In: *CIRP Annals* 70.2 (Jan. 1, 2021), pp. 543–566.

[5] Hong-Shuai Zhou et al. «Back-Scattering Suppression for Broad- Spectral High-Absorption Silicon Extended Area Blackbody». In: ().

[6] Matthias F Kling et al. «Roadmap on basic research needs for laser technology». In: *Journal of Optics* 27.1 (Dec. 2024), p. 013002.

[7] Chang Liang et al. «Laser drilling of alumina ceramic substrates: A review». In: *Optics & Laser Technology* 167 (Dec. 1, 2023), p. 109828.

[8] El-Said Salah et al. «Laser forming technology: a comprehensive review of mechanisms, process optimization, and industrial applications». In: *International Journal of Material Forming* 18.4 (Dec. 2025), p. 82.

[9] Heng Guo et al. «A review of ultrafast laser micro/nano fabrication: Material processing, surface/interface controlling, and devices fabrication». In: *Nano Research* 17.7 (July 2024), pp. 6212–6230.

[10] Di Song et al. «Microscopic Processing of Transparent Material with Nanosecond and Ultrafast Lasers». In: *Micromachines* 15.9 (Sept. 2024). Number: 9, p. 1101.

[11] Kaichang Yu et al. «Micro/nanoengineering of functionalized metal surfaces based on short/ultra-short-pulsed lasers: a review». In: *Journal of Materials Science* 59.5 (Feb. 1, 2024), pp. 1819–1866.

[12] Sibo Niu et al. «Recent Advances in Applications of Ultrafast Lasers». In: *Photonics* 11.9 (Sept. 2024). Number: 9, p. 857.

[13] Vitali V. Kononenko. «Modification of Diamond Surface by Femtosecond Laser Pulses». In: *Photonics* 10.10 (Oct. 2023). Number: 10, p. 1077.

[14] Jiecai Feng et al. «A Review of an Investigation of the Ultrafast Laser Processing of Brittle and Hard Materials». In: *Materials* 17.15 (Jan. 2024). Number: 15, p. 3657.

[15] Divyansh Patel, Vk Jain, and J Ramkumar. «Micro texturing on metallic surfaces: State of the art». In: *Proceedings of the Institution of Mechanical Engineers, Part B: Journal of Engineering Manufacture* 232.6 (May 2018), pp. 941–964.

[16] Annalisa Volpe, Caterina Gaudiuso, and Antonio Ancona. «Laser Fabrication of Anti-Icing Surfaces: A Review». In: *Materials* 13.24 (Dec. 13, 2020), p. 5692.

[17] Bo Mao et al. «Laser surface texturing and related techniques for enhancing tribological performance of engineering materials: A review». In: *Journal of Manufacturing Processes* 53 (May 2020), pp. 153–173.

[18] Bahaa E. A. Saleh and Malvin Carl Teich. *Fundamentals of photonics*. Third edition. Hoboken, NJ: Wiley, 2019. 1 p.

[19] Suresh Chandra and Mohit Kumar Sharma. *A Textbook of Optics*. Cham: Springer Nature Switzerland, 2024.

[20] *Schaum's Outline of Optics*.

[21] Sebastián Mirasol-Menacho et al. «Development of a HMD for Virtual Acoustics. Application in a World Heritage (UNESCO) Building from the Valencian Civil Gothic». In: June 15, 2016, pp. 241–250.

[22] Robert K. Tyson. *Principles of adaptive optics*. Principles of Adaptive Optics, Fourth Edition. CRC Press, 2015. 356 pp.

[23] Patrick S. Salter and Martin J. Booth. «Adaptive optics in laser processing». In: *Light: Science & Applications* 8.1 (Nov. 29, 2019), p. 110.

[24] Euan McLeod and Aydogan Ozcan. «Nano-imaging enabled via self-assembly». In: *Nano Today* 9.5 (Oct. 1, 2014), pp. 560–573.

[25] Mariusz Kłonica et al. «Selected Methods of Modifying the Surface Layer of a Carbon Composite». In: *Advances in Science and Technology. Research Journal* 18.1 (Feb. 1, 2024), pp. 270–277.

[26] Muyang Qin et al. «Ultrafast Laser Processing for High-Aspect-Ratio Structures». In: *Nanomaterials* 14.17 (Jan. 2024). Number: 17, p. 1428.

[27] T. Häfner et al. «Tailored laser beam shaping for efficient and accurate microstructuring». In: *Applied Physics A* 124.2 (Feb. 2018), p. 111.

[28] Serguei P. Murzin. «Digital Engineering in Diffractive Optics for Precision Laser Processing». In: *Photonics* 12.4 (Mar. 27, 2025), p. 306.

[29] Jong Hyun Kim and Hae Woon Choi. «Review on Principal and Applications of Temporal and Spatial Beam Shaping for Ultrafast Pulsed Laser». In: *Photonics* 11.12 (Dec. 2024). Number: 12, p. 1140.

[30] Lova Chechik and Michael Schmidt. «Identification of a descriptive beam size metric for complex beam shapes». In: *Procedia CIRP* 124 (2024), pp. 737–740.

[31] M. Schmidt et al. «Dynamic beam shaping—Improving laser materials processing via feature synchronous energy coupling». In: *CIRP Annals* 73.2 (2024), pp. 533–559.

[32] Carmelo Corsaro et al. «Adaptive Aberration Correction for Laser Processes Improvement». In: *Journal of Manufacturing and Materials Processing* 9.4 (Apr. 2025). Number: 4, p. 105.

[33] Bettina Mikulec et al. «A High Resolution, High Frame Rate Detector Based on a Microchannel Plate Readout With the Medipix2 Counting CMOS Pixel Chip». In: *Nuclear Science, IEEE Transactions on* 52 (Sept. 1, 2005), pp. 1021–1026.

[34] Stefano Bonora et al. «Design of deformable mirrors for high power lasers». In: *High Power Laser Science and Engineering* 4 (Jan. 2016), e16.

[35] I. S. Moskalev et al. «Application of Laser Beam Shaping for Spectral Control of "Spatially Dispersive" Lasers». In: *Laser Beam Shaping Applications*. Ed. by Fred M. Dickey and Todd E. Lizotte. 2nd ed. Second edition. | Boca Raton, FL : CRC Press, Taylor & Francis Group, [2017]: CRC Press, Feb. 24, 2017, pp. 357–381.

[36] Cyril Mauclair et al. «Dynamic spatial beam shaping for ultrafast laser processing: a review». In: *Opto-Electronic Science* 0.0 (2025), pp. 250002–250002.

[37] Jiaxu Huang, Kang Xu, and Shaolin Xu. «Super-resolution laser machining». In: *International Journal of Machine Tools and Manufacture* 205 (Feb. 2025), p. 104246.

[38] Salman Nisar. «Optimization of Laser Beam Geometry for Controlling Thermal Stresses in CO2 Laser Glass Cutting». In: *Lasers in Manufacturing and Materials Processing* 12.2 (June 1, 2025), pp. 298–317.

[39] Nikita Levichev et al. «Towards robust dynamic beam shaping for laser cutting applications». In: *Procedia CIRP* 111 (2022), pp. 746–749.

[40] M. Mazzonetto. «Surface micro – texturing of tapping tools with complex geometry». In: Italian Manufacturing Association Conference. Oct. 15, 2023, pp. 359–366.

[41] Jessamine Ng Lee, Cheolmin Park, and George M. Whitesides. «Solvent Compatibility of Poly(dimethylsiloxane)-Based Microfluidic Devices». In: *Analytical Chemistry* 75.23 (Dec. 1, 2003), pp. 6544–6554.

[42] W. Adamiak, D. Kałuża, and M. Jönsson-Niedziolka. «Compatibility of organic solvents for electrochemical measurements in PDMS-based microfluidic devices». In: *Microfluidics and Nanofluidics* 20.9 (Sept. 2016), p. 127.

[43] Bryan R. Benson, Howard A. Stone, and Robert K. Prud'homme. «An "off-the-shelf" capillary microfluidic device that enables tuning of the droplet breakup regime at constant flow rates». In: *Lab on a Chip* 13.23 (2013), p. 4507.

[44] Krystian L. Wlodarczyk et al. «Rapid Laser Manufacturing of Microfluidic Devices from Glass Substrates». In: *Micromachines* 9.8 (Aug. 2018), p. 409.

[45] Felix Sima and Koji Sugioka. «Ultrafast laser manufacturing of nanofluidic systems». In: *Nanophotonics* 10.9 (July 1, 2021), pp. 2389–2406.

[46] Tien-Li Chang et al. «Effect of ultra-fast laser texturing on surface wettability of microfluidic channels». In: *Microelectronic Engineering* 98 (Oct. 2012), pp. 684–688.

[47] Yafei Liu et al. «Bench scale glass-to-glass bonding for microfluidic prototyping». In: *Microsystem Technologies* 26.12 (Dec. 1, 2020), pp. 3581–3589.

[48] Yu-Jen Pan and Ruey-Jen Yang. «A glass microfluidic chip adhesive bonding method at room temperature». In: *Journal of Micromechanics and Microengineering* 16.12 (Nov. 2006), p. 2666.

[49] Leonardo Orazi et al. «Ultrafast laser micromanufacturing of microfluidic devices». In: *Procedia CIRP* 110 (2022), pp. 122–127.

[50] C Ongaro et al. «An Alternative Solution for Microfluidic Chip Fabrication». In: *Journal of Physics: Conference Series* 2385.1 (Dec. 1, 2022), p. 012029.

[51] V. Siciliani. «UV picosecond laser processing for microfluidic applications». In: Italian Manufacturing Association Conference. Oct. 15, 2023, pp. 334–341.

[52] Alice Betti et al. «Evaluating Laser-Based Microfabrication in Microfluidics: An Experimental and Computational Trial». In: *Advanced Engineering Materials* 26.21 (Nov. 2024), p. 2401105.

[53] Sudipto K De and N R Aluru. «A hybrid full-Lagrangian technique for the static and dynamic analysis of magnetostatic MEMS». In: *Journal of Micromechanics and Microengineering* 16.12 (Nov. 2006), p. 2646.

[54] Agnė Butkutė and Linas Jonušauskas. «3D Manufacturing of Glass Microstructures Using Femtosecond Laser». In: *Micromachines* 12.5 (May 2021), p. 499.

[55] Arulvel S et al. «Laser processing techniques for surface property enhancement: Focus on material advancement». In: *Surfaces and Interfaces* 42 (Nov. 1, 2023), p. 103293.

[56] Reem A. Alsaigh. «Enhancement of Surface Properties Using Ultrashort-Pulsed-Laser Texturing: A Review». In: *Crystals* 14.4 (Apr. 2024), p. 353.

[57] Raminder Singh, Manjeet Singh, and Rupinder Singh. «Impact of texture cutting tools on sustainable machining methods: a review». In: *International Journal on Interactive Design and Manufacturing (IJIDeM)* 19.5 (May 1, 2025), pp. 3121–3137.

[58] M. Mazzonetto et al. «Development of micro-texture patterns of cemented carbide cutting tools to improve cutting performance». In: *Procedia CIRP* 124 (2024), pp. 608–611.

[59] Serafino Caruso et al. «Influence of Cutting Parameters and Tool Surface Texturing on Surface Integrity in Face Milling of AISI 1050 Carbon Steel». In: *Journal of Manufacturing and Materials Processing* 9.12 (Dec. 18, 2025).

[60] T. Fujita, H. Nishihara, and Jompong Koyama. «Blazed gratings and Fresnel lenses fabricated by electron-beam lithography». In: *Optics Letters* 7 (Dec. 1, 1982), pp. 578–580.

[61] Yoshio Suzuki et al. «Fabrication and Performance Test of Fresnel Zone Plate with 35 nm Outermost Zone Width in Hard X-Ray Region». In: *X-Ray Optics and Instrumentation* 2010.1 (2010). _eprint: https://onlinelibrary.wiley.com/doi/pdf/10.1155/2010/824387, p. 824387.

[62] U. Betz et al. «Thin films engineering of indium tin oxide: Large area flat panel displays application». In: *Surface and Coatings Technology* 200.20 (May 22, 2006), pp. 5751–5759.

[63] M. Zahirul Alam, Israel De Leon, and Robert W. Boyd. «Large optical nonlinearity of indium tin oxide in its epsilon-near-zero region». In: *Science (New York, N.Y.)* 352.6287 (May 13, 2016), pp. 795–797.

[64] Rafael R. Gattass and Eric Mazur. «Femtosecond laser micromachining in transparent materials». In: *Nature Photonics* 2.4 (Apr. 2008), pp. 219–225.

[65] Koji Sugioka and Ya Cheng. «Ultrafast lasers—reliable tools for advanced materials processing». In: *Light: Science & Applications* 3.4 (Apr. 2014), e149–e149.

[66] Li Jia Jiang et al. «Femtosecond laser direct writing in transparent materials based on nonlinear absorption». In: *MRS Bulletin* 41.12 (Dec. 1, 2016), pp. 975–983.

[67] Wataru Watanabe et al. «Fabrication of Fresnel zone plate embedded in silica glass by femtosecond laser pulses». In: *Optics Express* 10.19 (Sept. 23, 2002), pp. 978–983.

[68] Kazuhiro Yamada et al. «Multilevel phase-type diffractive lenses in silica glass induced by filamentation of femtosecond laser pulses». In: *Optics Letters* 29.16 (Aug. 13, 2004), pp. 1846–1848.

[69] A Pérez del Pino et al. «Coloring of titanium through laser oxidation: comparative study with anodizing». In: *Surface and Coatings Technology* 187.1 (Oct. 1, 2004), pp. 106–112.

[70] A. Y. Vorobyev and Chunlei Guo. «Colorizing metals with femtosecond laser pulses». In: *Applied Physics Letters* 92.4 (Jan. 31, 2008), p. 041914.

[71] Z. L. Li et al. «Analysis of oxide formation induced by UV laser coloration of stainless steel». In: *Applied Surface Science*. Proceedings of the Symposium on Surface Science 2008 Festschrift in honor of Professor Şefik Süzer's 60th birthday 256.5 (Dec. 15, 2009), pp. 1582–1588.

[72] B. Dusser et al. «Controlled nanostructrures formation by ultra fast laser pulses for color marking». In: *Optics Express* 18.3 (Feb. 1, 2010), pp. 2913–2924.

[73] Md. Shamim Ahsan et al. «Colorizing stainless steel surface by femtosecond laser induced micro/nano-structures». In: *Applied Surface Science* 257.17 (June 15, 2011), pp. 7771–7777.

[74] Peixun Fan et al. «Sequential colorization of steel surface by ps laser texturing». In: ICALEO 2013: 32nd International Congress on Laser Materials Processing, Laser Microprocessing and Nanomanufacturing. AIP Publishing, Oct. 1, 2013, pp. 700–705.

[75] Erik M. Garcell et al. «Comparative study of femtosecond laser-induced structural colorization in water and air». In: *Nanoscale Advances* 2.7 (July 14, 2020), pp. 2958–2967.

[76] Hamid Roozbahani et al. «Color Laser Marking: Repeatability, Stability and Resistance Against Mechanical, Chemical and Environmental Effects». In: *IEEE Access* 8 (2020), pp. 214196–214208.

[77] Yandi Huang et al. «Mechanisms in surface coloring of titanium alloy induced by picosecond laser». In: *Journal of Manufacturing Processes* 76 (Apr. 1, 2022), pp. 304–310.

[78] He Zhao et al. «Color visual art creation on metals via multifunctional laser paintbrush». In: *Optics & Laser Technology* 159 (Apr. 1, 2023), p. 109040.

[79] Anna Rudawska. «Selected aspects of the effect of mechanical treatment on surface roughness and adhesive joint strength of steel sheets». In: *International Journal of Adhesion and Adhesives* 50 (Apr. 1, 2014), pp. 235–243.

[80] N. Saleema et al. «A simple surface treatment and characterization of AA 6061 aluminum alloy surface for adhesive bonding applications». In: *Applied Surface Science* 261 (Nov. 15, 2012), pp. 742–748.

[81] T. M. Yue, L. J. Yan, and C. P. Chan. «Stress corrosion cracking behavior of Nd:YAG laser-treated aluminum alloy 7075». In: *Applied Surface Science* 252.14 (May 15, 2006), pp. 5026–5034.

[82] Elisabeth Stammen et al. «Surface Modification with Laser: Pretreatment of Aluminium Alloys for Adhesive Bonding». In: *Plasma Processes and Polymers* 4 (S1 2007). _eprint: https://onlinelibrary.wiley.com/doi/pdf/10.1002/ppap.200730303, S39–S43.

[83] Rico Rechner, Irene Jansen, and Eckhard Beyer. «Influence on the strength and aging resistance of aluminium joints by laser pre-treatment and surface modification». In: *International Journal of Adhesion and Adhesives* 30.7 (Oct. 1, 2010), pp. 595–601.

[84] Giovanna Rotella et al. «Enhancement of static strength and long term durability of steel/epoxy joints through a fiber laser surface pre-treatment». In: *International Journal of Adhesion and Adhesives* 63 (Dec. 1, 2015), pp. 87–95.

[85] Chuanmin Zhu et al. «Application of pulsed Yb: Fiber laser to surface treatment of Al alloys for improved adhesive bonded performance». In: *Optics and Lasers in Engineering* 119 (Aug. 1, 2019), pp. 65–76.

[86] E. G. Baburaj et al. «Enhancement of adhesive joint strength by laser surface modification». In: *International Journal of Adhesion and Adhesives* 27.4 (June 1, 2007), pp. 268–276.

[87] Natalia Khomiakova et al. «Investigation of Wettability, Drying and Water Condensation on Polyimide (Kapton) Films Treated by Atmospheric Pressure Air Dielectric Barrier Discharge». In: *Coatings* 10.7 (July 2020), p. 619.

[88] P. Fabbri and M. Messori. «5 - Surface Modification of Polymers: Chemical, Physical, and Biological Routes». In: *Modification of Polymer Properties*. Ed. by Carlos F. Jasso-Gastinel and José M. Kenny. William Andrew Publishing, Jan. 1, 2017, pp. 109–130.

[89] A. Riveiro et al. «Texturing of polypropylene (PP) with nanosecond lasers». In: *Applied Surface Science*. E-MRS 2015 Spring Meeting Symposium CC: "Laser and plasma processing for advanced applications in material science", 11-15 May 2015, Lille (France) 374 (June 30, 2016), pp. 379–386.

[90] Moataz Abdulhafez, Angela J. McComb, and Mostafa Bedewy. «Tailoring Surface Hydrophobicity of Commercial Polyimide by Laser-Induced Nanocarbon Texturing». In: *Journal of Micro and Nano-Manufacturing* 8.31006 (Oct. 26, 2020).

[91] Lingxiao Wang et al. «Wetting Ridge-Guided Directional Water Self-Transport». In: *Advanced Science* 9.34 (2022). _eprint: https://advanced.onlinelibrary.wiley.com/doi/pdf/10.1002/advs.2022 p. 2204891.

[92] Qifeng Du et al. «Fabrication of superhydrophobic/superhydrophilic patterns on polyimide surface by ultraviolet laser direct texturing». In: *Journal of Materials Processing Technology* 251 (Jan. 1, 2018), pp. 188–196.

[93] Adrian H. A. Lutey and Fabrizio Moroni. «Pulsed laser texturing for improved adhesive-bonded polyethylene (PE) joints». In: *International Journal of Adhesion and Adhesives* 102 (Oct. 1, 2020), p. 102676.

[94] L. Orazi et al. «Ultrafast laser texturing to improve wettability of polyimide (Kapton) films». In: *Journal of Manufacturing Processes* 107 (Dec. 2023), pp. 368–375.

[95] Virginie Dumas et al. «Femtosecond laser nano/micro patterning of titanium influences mesenchymal stem cell adhesion and commitment». In: *Biomedical Materials* 10.5 (Sept. 3, 2015), p. 055002.

[96] Alexandre Cunha et al. «Human mesenchymal stem cell behavior on femtosecond laser-textured Ti-6Al-4V surfaces». In: *Nanomedicine* 10.5 (Mar. 2015), pp. 725–739.

[97] Antoine Klos et al. «Ultrafast Laser Processing of Nanostructured Patterns for the Control of Cell Adhesion and Migration on Titanium Alloy». In: *Nanomaterials* 10.5 (Apr. 30, 2020), p. 864.

[98] Gholam Reza Dabbagh et al. «Laser textured novel patterns on Ti6Al4V alloy for dental implants surface improvement». In: *Journal of Laser Applications* 33.4 (Nov. 2021), p. 042031.

[99] Wilhelm Pfleging et al. «Laser surface textured titanium alloy (Ti–6Al–4V): Part 1 – Surface characterization». In: *Applied Surface Science* 355 (Nov. 2015), pp. 104–111.

[100] Vadim Veiko et al. «Laser-Induced µ-Rooms for Osteocytes on Implant Surface: An In Vivo Study». In: *Nanomaterials* 12.23 (Nov. 28, 2022), p. 4229.

[101] Yong Xu et al. «Friction stability and cellular behaviors on laser textured Ti–6Al–4V alloy implants with bioinspired micro-overlapping structures». In: *Journal of the Mechanical Behavior of Biomedical Materials* 109 (Sept. 2020), p. 103823.

[102] Leonardo Orazi et al. «Fast LIPSS based texturing process of dental implants with complex geometries». In: *CIRP Annals* 69.1 (Jan. 1, 2020), pp. 233–236.

[103] Michela Sanguedolce et al. «Surface Characterization Of Ultra-Short Laser Textured Titanium For Biomedical Application». In: *Procedia CIRP* 110 (2022), pp. 128–132.

[104] Chengcheng Sun et al. «The effect of laser ablation treatment on the chemistry, morphology and bonding strength of CFRP joints». In: *International Journal of Adhesion and Adhesives* 84 (Aug. 1, 2018), pp. 325–334.

[105] Yasmina Boutar et al. «Effect of surface treatment on the shear strength of aluminium adhesive single-lap joints for automotive applications». In: *International Journal of Adhesion and Adhesives*. Special Issue on Adhesion, Surface Preparation and Adhesive Properties 67 (June 1, 2016), pp. 38–43.

[106] Muhammad Adeel Khan et al. «Influence of laser surface texturing on adhesive bonding: a comprehensive review on surface morphology and strength enhancement». In: *Optics & Laser Technology* 191 (Dec. 1, 2025), p. 113339.

[107] Ran Tao, Marco Alfano, and Gilles Lubineau. «Laser-based surface patterning of composite plates for improved secondary adhesive bonding». In: *Composites Part A: Applied Science and Manufacturing* 109 (June 1, 2018), pp. 84–94.

[108] Fatih Hayati Çakir. «Enhancing the adhesive bonding strength of Ti6Al4V sheets with fiber laser texturing». In: *International Journal of Adhesion and Adhesives* 114 (Apr. 1, 2022), p. 103117.

[109] Jianfeng Li et al. «Experimental study of adhesively bonded CFRP joints subjected to tensile loads». In: *International Journal of Adhesion and Adhesives* 57 (Mar. 1, 2015), pp. 95–104.

[110] Vincenzina Siciliani et al. «Enhancing the shear strength of adhesive bonded compression-molded CFRP laminates using selective UV picosecond laser treatment». In: *The International Journal of Advanced Manufacturing Technology* 141.9 (Dec. 2025), pp. 5697–5708.

[111] V. Siciliani. «Effect of surface preparation on adhesive bonding of CFRP compression molding laminates». In: Material Forming. 2025, pp. 2193–2202.

[112] Yaya Wang et al. «Hierarchically Micro/Nanostructured Current Collectors Induced by Ultrafast Femtosecond Laser Strategy for High-Performance Lithium-ion Batteries». In: *ENERGY & ENVIRONMENTAL MATERIALS* 5.3 (July 2022), pp. 969–976.

[113] Luca Romoli, Adrian H. A. Lutey, and Gianmarco Lazzini. «Laser texturing of Li-ion battery electrode current collectors for improved active layer interface adhesion». In: *CIRP Annals* 71.1 (Jan. 1, 2022), pp. 481–484.

[114] Wilhelm Pfleging. «Recent progress in laser texturing of battery materials: a review of tuning electrochemical performances, related material development, and prospects for large-scale manufacturing». In: *International Journal of Extreme Manufacturing* 3.1 (Dec. 2020), p. 012002.

[115] V. Siciliani. «Laser texturing of 3D Copper current collector for ultrafast Zinc metal plating». In: Italian Manufacturing Association Conference. 2025, pp. 286–293.

[116] Michel Suermann et al. «Femtosecond laser-induced surface structuring of the porous transport layers in proton exchange membrane water electrolysis». In: *Journal of Materials Chemistry A* 8.9 (2020), pp. 4898–4910.

[117] Jason K. Lee et al. «Nanochannel electrodes facilitating interfacial transport for PEM water electrolysis». In: *Joule* 8.8 (Aug. 2024), pp. 2357–2373.

[118] Jason K. Lee et al. «Interfacial engineering via laser ablation for high-performing PEM water electrolysis». In: *Applied Energy* 336 (Apr. 2023), p. 120853.

[119] Vincenzina Siciliani et al. «Increased productivity in laser texturing of molds through dynamic beam shaping». In: *Optics & Laser Technology* 192 (Dec. 2025), p. 113440.

[120] Vincenzina Siciliani et al. «Adaptive optics solution to improve laser-induced periodic surface structuring (LIPSS)». In: *Laser-based Micro- and Nanoprocessing XVIII.* Laser-based Micro- and Nanoprocessing XVIII. Ed. by Rainer Kling, Wilhelm Pfleging, and Koji Sugioka. San Francisco, United States: SPIE, Mar. 12, 2024, p. 9.

[121] L. Orazi et al. «Generation and Characterization of Laser Induced Periodic Surface Structures on Plastic Injection Molds». In: *Lasers in Manufacturing and Materials Processing* 7.2 (June 1, 2020), pp. 207–221.

[122] Vasiliki E. Alexopoulou and Angelos P. Markopoulos. «A Critical Assessment Regarding Two-Temperature Models: An Investigation of the Different Forms of Two-Temperature Models, the Various Ultrashort Pulsed Laser Models and Computational Methods». In: *Archives of Computational Methods in Engineering* 31.1 (Jan. 1, 2024), pp. 93–123.

[123] Xingsheng Wang et al. «Numerical simulation and experimental study on picosecond laser ablation of stainless steel». In: *Optics & Laser Technology* 127 (July 1, 2020), p. 106150.

[124] Manuel Mazzonetto et al. «Ablation rate assessment of GHz femtosecond laser in burst mode through fast numerical simulation». In: *Laser-based Micro- and Nanoprocessing XVIII*. Laser-based Micro- and Nanoprocessing XVIII. Ed. by Rainer Kling, Wilhelm Pfleging, and Koji Sugioka. San Francisco, United States: SPIE, Mar. 12, 2024, p. 10.

[125] Xiao Jia and Xin Zhao. «Ultrafast laser ablation of copper with GHz bursts: A numerical study on the effects of repetition rate, pulse number and burst fluence on ablation efficiency and heat-affected zone». In: *Optics & Laser Technology* 158 (Feb. 1, 2023), p. 108803.

[126] Joerg Volpp. «Laser beam absorption measurement at molten metal surfaces». In: *Measurement* 209 (Mar. 15, 2023), p. 112524.

[127] Kenneth C. Mills et al. «Equations for the Calculation of the Thermo-physical Properties of Stainless Steel». In: *ISIJ International* 44.10 (2004), pp. 1661–1668.